Developing PET/MR Imaging Probes for the *In Vivo* Tracking of Cell Therapies

Thesis submitted in accordance with the requirements of the University of Liverpool for the degree of Doctor in Philosophy

By

Niamh Emily McCallum

Institute of Systems, Molecular and Integrative Biology

March 2022

Abstract

Cell therapies hold enormous potential to treat a range of diseases and disorders. However, clinical translation of these therapies has been limited, largely due to a lack of sufficient safety and efficacy data. To obtain such data, it is necessary to track administered cells *in vivo* using non-invasive imaging techniques so that information on the fate, biodistribution and persistence of the cells can be determined. Positron emission tomography (PET) and magnetic resonance imaging (MRI) are the two most commonly used clinical imaging modalities for cell tracking; however, they each have their own limitations. For example, PET offers good temporal resolution, is highly sensitive and provides quantitative data. This means that the whole-body biodistribution of administered cells can be assessed and quantified with PET, but due to the poor spatial resolution, intra-organ distributions of cells cannot be elucidated. MRI, on the other hand, offers poor temporal resolution but excellent spatial resolution. Developing a multimodal imaging approach can help to overcome the limitations of the two modalities, and for this, hybrid imaging agents are required that can show contrast/signal in both imaging systems. The work in this thesis aimed to develop hybrid cell-specific PET/MR imaging probes for the *in vivo* tracking of macrophage-like cells, since macrophages are promising cell therapies for a number of conditions.

First, the MRI contrast agent, superparamagnetic iron oxide nanoparticles (SPIONs), were functionalised with the PET tracer, zirconium-89 (^{89}Zr). This was achieved through the functionalisation of the polymer coating of SPIONs with the ^{89}Zr chelating tetraazamacrocycles, DOTA or PCTA, generating two types of novel imaging agent: ^{89}Zr-DOTA-SPIONs and ^{89}Zr-PCTA-SPIONs **(Chapter 3)**. The effect of both hybrid particle types on cell viability and cellular uptake were assessed in RAW 264.7 cells, and were found to be non-toxic at the labelling concentrations used, and were taken up efficiently into the cells **(Chapter 4)**. Because of this, both ^{89}Zr-DOTA-SPIONs and ^{89}Zr-PCTA-SPIONs were taken forward for *in vivo* testing in mice.

^{89}Zr-DOTA-SPIONs were administered to healthy mice via systemic injection to assess the *in vivo* stability of the hybrid particles, as well as their pharmacokinetics **(Chapter 5)**. The particles were found to be unstable *in vivo*; the PET and MRI components were found to separate and produce non-corroborating signals in the body. Specifically, it was determined that free ^{89}Zr had detached from the particles and deposited in the bone. Due to this unfavourable instability, ^{89}Zr-DOTA-SPIONs were not utilised for the labelling and tracking of RAW cells *in vivo*.

Instead, the hybrid particles, ^{89}Zr-PCTA-SPIONs, were taken forward for the *in vivo* tracking of RAW cells **(Chapter 6)**. The cells were labelled with the PET/MR imaging agents and were then administered intravenously (IV) to mice that had undergone a unilateral renal ischaemia/reperfusion injury (IRI). It is already known that IV administered macrophages and macrophage-like cells preferentially home to the injured kidney in the unilateral IRI model. This model was therefore used to investigate if PET and MRI could be used to monitor the whole-body and intra-renal biodistributions of RAW cells with ^{89}Zr-PCTA-SPIONs. As well as using PET and MRI to assess the biodistribution, fate and persistence of the labelled cells, the RAWs used in the experiment also expressed firefly luciferase so that their viability could be monitored with bioluminescence imaging (BLI). ^{89}Zr-PCTA-SPIONs were found to be stable *in vivo*, producing corroborating signals in the body and displaying minor bone deposition. Through *ex vivo* PET, MRI and BLI, ^{89}Zr-PCTA-SPION-labelled and luciferase-expressing RAW cells were observed to home to injured kidneys, demonstrating the benefits of using multimodal imaging strategies for the tracking of cells to specific organs.

The information obtained from this thesis will contribute to the field of cell tracking and probe development, specifically in the area of hybrid PET/MR imaging agent development via nanoparticle radiolabelling. Additionally, the results obtained from this thesis have provided a greater understanding of the behaviour of administered macrophages and macrophage-like cells, which will be beneficial in the development of cellular therapies.

Acknowledgements

I would first and foremost like to thank my supervisors, Prof. Patricia Murray, Prof. Matthew Rosseinsky and Prof. Harish Poptani, for their help and guidance during my PhD. Thank you for providing me with the opportunity to undertake this fascinating and multi-disciplinary project, and for each of your support throughout. I would next like to thank Dr Arthur Taylor and Dr Troy Manning, without whom the work in this thesis would not be complete. Troy, thank you for all of your support on the chemistry side throughout the past 4.5 years. I am particularly grateful for our catch-ups during the 2020 COVID-19 lockdown, when a good chunk of this thesis was written. Arthur, I am extremely grateful for your help and expertise over the past few years. You have helped in so many areas of this project and I have learnt a lot working alongside you. Thank you especially for your support whilst I was writing this thesis; you kept me motivated during some tough times.

I would like to thank Dr Jack Sharkey for his help and guidance with the imaging performed in this project. Jack, thank you for sharing your imaging wisdom with me and for keeping me entertained during long imaging sessions with some interesting chats. I owe my thanks to Dr Stephen Patrick for teaching me how to be a radiochemist. Stephen, thank you so much for coming up to Liverpool from UCL to assist with my work – your help was invaluable in completing this project. Dr Ajay Verma is thanked for his assistance with the organic chemistry performed in this project. Ajay, it was a privilege to work with you and your organic expertise; you really helped to get my project on its feet in the early days. I would also like to thank Dr Ioana-Roxana Martinas for performing the IRI surgery in this project. Thank you for helping me, Ioana, even though you had just finished your own lab work!

I would like to thank Mr Stephen Moss, who provided me with analytical support throughout this project (as well as during my Master's!). I am very grateful for your knowledge, Ste, and how you are always so willing to help. Dr Wesley Surta, thank you for being a great desk buddy, for teaching me everything I know about OriginLab and for showing me how to make

pretty figures! Miss Katie Scott is thanked for conducting SQUID measurements for me, as well as for all of her lifts home over the years! To all of my friends and colleagues in both the Stem Cell groups and the MJR groups, thank you for all of your support and collaboration. I have made some life-long friends whom I will never forget.

Finally, I would like to express my sincere gratitude to my friends and family for being there for me throughout the course of my PhD. Thank you to my mum, dad, sister and Jon for being the best support network whilst I was writing up this thesis. I couldn’t have done it without you all. Thanks especially to my dad for keeping me motivated over the past few months, and for always believing in me.

Dedicated to my grandfather, Hugh C. G. McCallum.

Table of Contents

List of Figures

All schematic figures were created with BioRender.com

All chemical structures were drawn in ChemDraw

List of Tables

List of Equations

Abbreviations

ADSCs	Adipose-derived stem cells
AgNPs	Silver nanoparticles
AKI	Acute kidney injury
ALD	Alcohol-associated liver disease
AMP	Adenosine monophosphate
ANOVA	Analysis of variance
ATP	Adenosine triphosphate
AuNPs	Gold nanoparticles
BL	Bioluminescence
BLI	Bioluminescence imaging
BMDMs	Bone marrow-derived macrophages
CCD	Cooled charge-coupled device camera
CKD	Chronic kidney disease
CM	Carboxymethyl
CMC	Carboxymethyl-chitosan
CM-dex	Carboxymethyl-dextran
CNTs	Carbon nanotubes
CT	Computed tomography
DEAE	Diethylaminoethyl
DEAE-dex	Diethylaminoethyl-dextran
DFO	Desferrioxamine
DLS	Dynamic light scattering
DMEM	Dulbecco's Modified Eagle Medium
DOTA	1,4,7,10-Tetraazacyclododecane-1,4,7,10-tetraacetic acid
DOTP	1,4,7,10-Tetraazacyclododecane-1,4,7,10-tetra(methylene phosphonic acid)
DTPA	Diethylenetriaminepentaacetic acid
ED	Ethylene diamine
EDC	N-(3-Dimethylaminopropyl)-N′-ethylcarbodiimide
EDEA	2,2-(Ethylenedioxy)bis(ethylamine)
EDEA-CM-dex	2,2-(Ethylenedioxy)bis(ethylamine)-carboxymethyl-dextran
EDL	Electrical double layer

ESCs	Embryonic stem cells
ESRF	End stage renal failure
EVs	Extracellular vesicles
FBS	Foetal bovine serum
FDA	United States Food and Drug Administration
FI	Fluorescence imaging
FITC	Fluorescein isothiocyanate
FLASH	Fast Low-Angle Shot
FLuc	Firefly luciferase
[^{18}F]FDG	[^{18}F]-2-fluoro-2-deoxy-glucose
FTIR	Fourier-transform infrared spectroscopy
FWHM	Full width half maximum
GNR	Gold nanorods
HEPES	(4-(2-hydroxyethyl)-1-piperazineethanesulfonic acid)
HOBt	Hydroxybenzotriazole
ICP-OES	Inductively coupled plasma-optical emission spectrometry
IRI	Ischaemia/reperfusion injury
IV	Intravenous
MBq	Megabecquerel
MBs	Microbubbles
MES	2-(N-morpholino)ethanesulfonic acid
MGE	Multigradient echo
MPS	Mononuclear phagocyte system
MRI	Magnetic resonance imaging
MSCs	Mesenchymal stem cells
MSOT	Multispectral optoacoustic tomography
n-EG	n-ethylene glycol
NIR	Near-infrared
NMR	Nuclear magnetic resonance
NOTA	1,4,7-triazacyclononane-1,4,7-triacetic acid
OI	Optical imaging
PAA	Poly(acrylic acid)
PAI	Photoacoustic imaging
PBS	Phosphate-buffered saline

PCTA	3,6,9,15-tetraazabicyclo(9.3.1)pentadeca-1(15),11,13-triene-3,6,9-triacetic acid
PEG	Polyethylene glycol
PET	Positron emission tomography
PFA	Paraformaldehyde
PLL	Polylysine
PES	Polyethersulfone
PPi	Inorganic pyrophosphate
PVA	Polyvinyl alcohol
pXRD	Powder x-ray diffraction
QDs	Quantum dots
RCY	Radiochemical yield
ROI	Region of interest
ROS	Reactive oxygen species
SPECT	Single-photon emission computed tomography
SPIONs	Superparamagnetic iron oxide nanoparticles
SRM	Surface radio-mineralisation
TAMs	Tumour associated macrophages
TEM	Transition electron microscopy
TGA	Thermogravimetric analysis
TLC	Thin layer chromatography
TRMØ	Tissue resident macrophages
US	Ultrasound
UUO	Unilateral ureteral obstruction
VDWs	van der Waals
XPS	X-ray photoelectron spectroscopy
XRD	X-ray diffraction
ZP	Zeta potential

Chapter 1

Introduction

1.1 Cell Therapies

Cell therapies, which include stem cells, stromal cells and immune cells such as macrophages, are therapies that have the potential to replace or repair damaged tissues or organs, and could thus be used to treat a range of diseases and disorders[1, 2]. However, despite the promise of cell therapies, there has been slow progress in their translation from bench to bedside due to a lack of convincing safety and efficacy data surrounding the therapies, as well as uncertainty about their modes of action[3]. To obtain this data, it is important to monitor the biodistribution, fate and persistence of administered cells longitudinally *in vivo* using non –invasive imaging technologies[2]. In the following sections, the potential of cell therapies and the importance of imaging technologies in aiding their translation to the clinic is explored in more detail.

Stem Cells

Stem cells have the capacity to self-renew and differentiate into specialised cell types, where the extent of this differentiation is dictated by the type of stem cell[4,5]. Embryonic stem cells (ESCs) can differentiate into specialised cells from all three germ layers (the ectoderm, mesoderm and endoderm) and are known as 'pluripotent' stem cells. Adult stem cells, on the other hand, have a more limited differentiation potential and are typically 'unipotent' or 'multipotent'.

Embryonic Stem Cells

Human ESCs (hESCs) have unlimited proliferation ability. They are derived from the inner cell mass (ICM) of 4-5 day old blastocyst-stage embryos (Figure 1.1)[6, 7]. Since the first report of their derivation in 1998 by Thomson *et al.*, hESCs have sparked much interest in scientific research due to their pluripotent, regenerative properties[6]. For example, retinal pigmented epithelial cells derived from hESCs have been tested in clinical trials for their potential to treat macular degeneration[8, 9]. Despite the therapeutic promise of hESCs, their use has been restricted in some countries due to ethical concerns, since the process of deriving hESCs results in destruction of the embryo[10]. Due to these issues, other stem cell types such as mesenchymal stromal cells (MSCs) have been investigated.

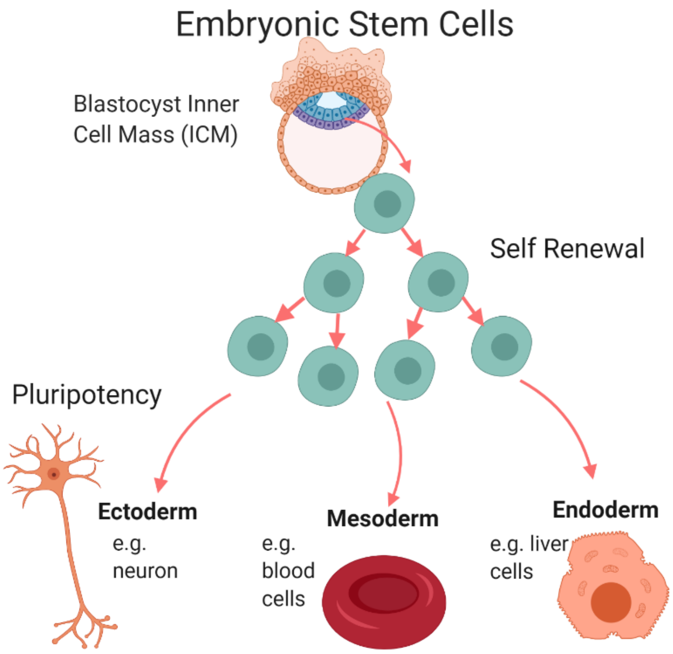

Figure 1.1: Embryonic stem cells (ESCs) are derived from the inner cell mass (ICM) of blastocyst-stage embryos. ESCs can self-renew for a prolonged period of time without differentiating. ESCs are pluripotent and can give rise to cells from all three germ layers: the ectoderm, the mesoderm, and the endoderm, meaning that ESCs can differentiate into cells of all adult tissues. The ectoderm gives rise to the skin and nervous system. The mesoderm gives rise to cells from the muscle, blood, blood vessels, connective tissue and the heart. The endoderm gives rise to the intestine, liver and lungs.

Mesenchymal Stromal Cells

MSCs are derived from a number of adult tissue sources including bone marrow, adipose tissue and the human umbilical cord[11]. This cell type has been found to show efficacy in preclinical models of kidney injury[12], lung injury[13, 14] and acute myocardial infarction[15], to name a few. MSCs are plastic adherent and can be readily grown and expanded *in vitro*. Because of this, and the fact that bone marrow and adipose-derived MSCs can be sourced from the patients themselves, they are commonly used in clinical trials. MSC-based therapies currently make up approximately 14% of all cell therapy trials in the UK[16].

Limitations of ESCs and MSCs

The main safety concern surrounding ESCs is the risk of tumourigenicity, resulting from the fact that they do not undergo senescence and are highly proliferative[17]. With MSCs, although they were originally described as multipotent, there is little evidence that they can generate differentiated cell types following implantation *in vivo*[18]. Moreover, they can sometimes result in adverse effects following direct administration in some organs. This is exemplified in the case of three patients who underwent intravitreal injection of autologous adipose tissue-derived 'stem cells' and developed severe bilateral visual loss[19].

A problem with systemic administration is that MSCs are entrapped in the first vascular bed that they encounter. For instance, after intravenous (IV) injection, MSCs tend to become entrapped in the pulmonary vasculature, which can potentially lead to pulmonary embolism[20]. A further limitation of cell therapies is that up to 90% can be lost due to factors such as physical stress and immune rejection. To combat this, patients are often administered high cell doses, which can increase the risk of tumour formation[21].

Mechanisms of Action of MSCs

It was originally believed that MSCs exert therapeutic effect by migrating to the site of injury or disease, engrafting, and finally, differentiating into healthy cells that can replace cells of the damaged tissue[10, 22]. However, an increasing number of studies, in a variety of disease and injury models, have reported that MSCs often do not engraft onto tissue in large enough numbers to cause the observed regeneration[23-25].

Novel hypotheses are emerging that suggest it is paracrine or endocrine activity that allows MSCs to sustain the growth and survival of the cells of tissues that they interact with[26, 27]. It is proposed that the release of cytokines, hormones, growth factors and extracellular vesicles (EVs), as well as mitochondrial transfer, could all be involved in immunomodulatory roles of MSCs[28]. Through such activity, MSCs can influence the distribution, polarisation, and function of innate macrophages of the immune system, as shown schematically in Figure 1.2.

MSCs have been shown to interact with macrophages at sites of inflammation, causing macrophages to switch from their pro-inflammatory 'M1' phenotype to their anti-inflammatory/tissue repairing 'M2' phenotype[29]. Some studies suggest that it is macrophages themselves that are mediating the therapeutic effects associated with MSC infusion[27, 30]. With fewer safety concerns associated with them than their MSC counterparts, interest in the direct use of macrophages as a therapy has increased in recent years, with macrophages showing efficacy in various mouse models of kidney disease[31]. Additionally, macrophages are currently being used in clinical trials, which is exemplified in the ongoing phase I/II clinical trials of macrophages for liver cirrhosis (MATCH study)[32], as well as in the completed phase I clinical trial of M2 macrophages as a treatment for non-acute stroke[33].

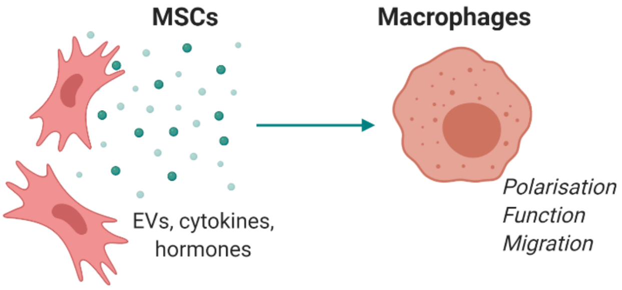

Figure 1.2: MSCs have been proposed to interact with macrophages at sites of inflammation, releasing cytokines, extracellular vesicles (EVs) and hormones, which affect the polarisation, function and migration of macrophages.

Macrophages

Macrophages are a type of immune cell that exist in all organs in the body and maintain homeostasis in adult tissues[34]. Macrophages have several important roles including phagocytosis[35], maintaining T cell tolerance[36] and initiating immune responses to bacterial infection[37]. As well as this, macrophages have shown great potential in regenerative medicine applications due to their regulatory roles in all stages of tissue repair. This is due to the unique plasticity of macrophages – the cells exhibit a range of phenotypes during tissue regeneration[38].

During the healing process, macrophages adopt a pro-inflammatory M1 phenotype and progress to an anti-inflammatory M2 phenotype[39]. Whilst the exact roles of M1 and M2 phenotypes are not very well understood, it is believed that M1 macrophages initiate the healing process[40] and M2 macrophages induce stabilisation and tissue maturation, and overall tissue repair is a careful balance between the two phenotypes[38]. This is displayed schematically in Figure 1.3.

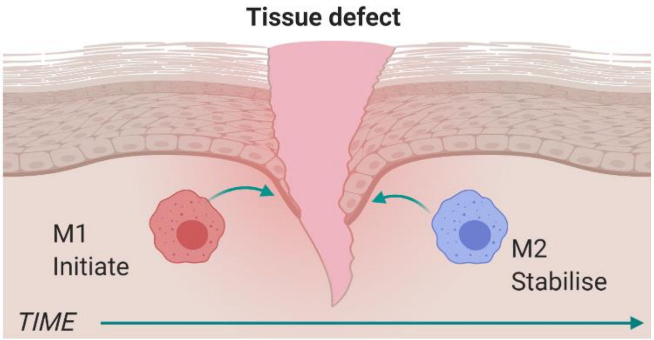

Figure 1.3: The time scale of macrophage-induced tissue repair. Pro-inflammatory M1-type macrophages reach the site of injury and initiate the healing process. Following this, anti-inflammatory macrophages induce stabilisation, tissue maturation and tissue repair.

The use of macrophage therapy dates back to as early as the 1980s, when *ex vivo* activated M1 macrophages were used in the treatment of cancer[41]. In recent years, on top of showing promise in the treatment of liver cirrhosis and non-acute stroke, macrophages have shown therapeutic efficacy in models of lung[42], heart[43], and renal injuries[27, 44]. The efficacious results brought about by macrophages in models of acute kidney injury (AKI) are of particular significance since there are currently no effective therapies available for AKI[27]. In addition to this, AKI can develop into chronic kidney disease (CKD), and even end stage renal failure (ESRF), which is only treatable by dialysis or kidney transplantation[45, 46]. There is a clear need for novel therapies to treat AKI and to prevent its manifestation into more severe renal disease, which macrophage therapy could provide.

Limitations of Macrophages

A few studies have reported that macrophages, like MSCs, tend to become entrapped in the lungs, liver and spleen upon systemic administration[47-51]. It is important to monitor the fate and biodistribution of administered macrophages to ensure that they do not become entrapped in these organs, and instead, engraft onto the desired site of injury. Another issue associated with macrophage therapy, that must be monitored, is the rapidly changing phenotypes of the cells. It is not clear if *ex vivo* activated macrophages maintain their phenotype when administered *in vivo*[38]. If M2-type macrophages are used to treat inflammatory disease but M1 macrophages are associated with a pro-inflammatory response, a change in phenotype from M2 to M1 could have serious deleterious effects on the damaged tissue or organ. It would be desirable to track the fate of administered macrophages *in vivo*, to ensure that they maintain their phenotype.

Non-invasive *in vivo* imaging technologies are vital for assessing the fate and biodistribution of administered macrophages. Using these technologies can help in the visualisation of where macrophages home to, what type of macrophage is acting on the site of injury and how long they survive for. Obtaining such data will aid the development of more safe and efficacious macrophage therapies for inflammatory disease.

1.2 Non-Invasive Imaging Technologies for Cell Tracking

The successful clinical translation of cell therapies has been largely limited by a lack of convincing data on the safety and efficacy of administered cells. Despite this, a number of commercial clinics offering stem and other cell-based therapies have emerged globally, offering unregulated and unproven therapies, which are potentially dangerous and raise ethical concerns[52, 53]. The concerns over cell therapies are centred on the potential for tumourigenicity, immunogenicity and emboli formation, as well as uncertainties in the mechanisms of action of the administered cells[2]. To monitor these issues and assess the risk: benefit ratio associated with cell therapies, animal models and pre-clinical imaging must be used. Imaging can allow for the visualisation of cells *in vivo*, ascertaining longitudinal information on the biodistribution, fate and safety profile of administered cells.

Pre-clinical imaging encompasses a wide array of modalities, some of which can only be applied in the pre-clinical imaging of small animals, and others which can be used to image larger animals and humans[54]. This section will discuss the basic principles and advantages and disadvantages of the most popular imaging modalities, which are optical, photoacoustic, magnetic, and nuclear imaging, as depicted in Figure 1.4 and summarised in Table 1.1.

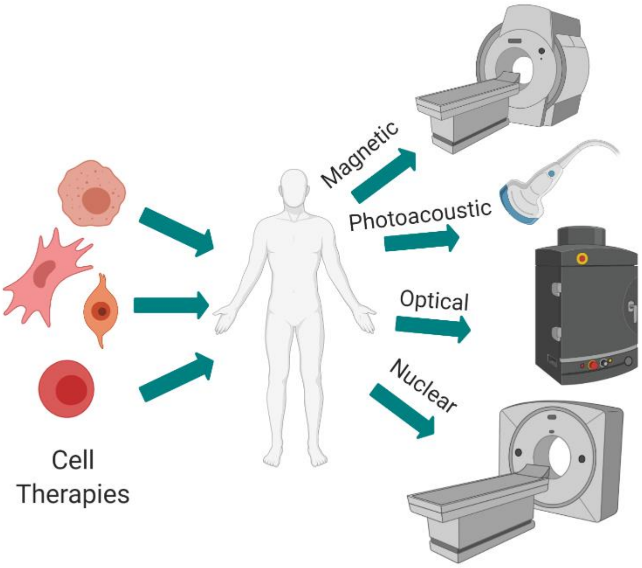

Figure 1.4: Imaging cell therapies using non-invasive imaging technologies. Common modalities for imaging cells are magnetic, photoacoustic, optical and nuclear imaging.

Optical Imaging

Optical imaging (OI), which covers bioluminescence imaging (BLI) and fluorescence imaging (FI), is a commonly used imaging modality that relies on the detection of emitted light. For cell tracking with OI, cells are either genetically modified to express genetic reporters, or are labelled with molecular probes[55].

As seen in Figure 1.5, for BLI, cells must express a luciferase enzyme, which can react with its substrate to produce light (details of this reaction are provided in Chapter 2.) For FI, light of a particular wavelength is absorbed by fluorescent proteins encoded by reporter genes, fluorescent dyes or other materials with fluorescent properties, which results in excitation of the fluorophore, followed by emission of light. In both types of imaging, the emitted light is detected by a photon detector known as a cooled charge-coupled device (CCD) camera[56]. Excitation and emission occur in the visible range (400 – 700 nm) or near-infrared range (800 – 1900 nm) of the electromagnetic spectrum[2]. However, longer wavelengths of ~ 650 – 1100 nm are typically applied for preclinical *in vivo* imaging since tissues of the body absorb less light in this range, allowing the light to penetrate more deeply. This is because tissues of animals contain many different light-absorbing molecules such as haemoglobin, deoxyhaemoglobin and water, and these molecules have the lowest absorption coefficient at longer wavelengths, particularly in the range of 700-900 nm, which is known as the ‘optical window’[57].

The main advantage of OI is good temporal resolution and for cell tracking purposes, this means that whole-body biodistributions of cells can be obtained. Additionally, OI is a relatively cheap imaging modality, which has contributed to its widespread use. An advantage of BLI is excellent sensitivity; however, this is not the case for FI, mainly due to the issue of autofluorescence (fluorescent signals from endogenous tissues). The main disadvantage of OI, that affects both BLI and FI, is its low penetration depth (< 1 cm for FI, 1 – 2 cm for BLI)[56] due to light scattering and tissue attenuation. This, in turn, reduces the spatial resolution of OI and limits its quantification capabilities[58].

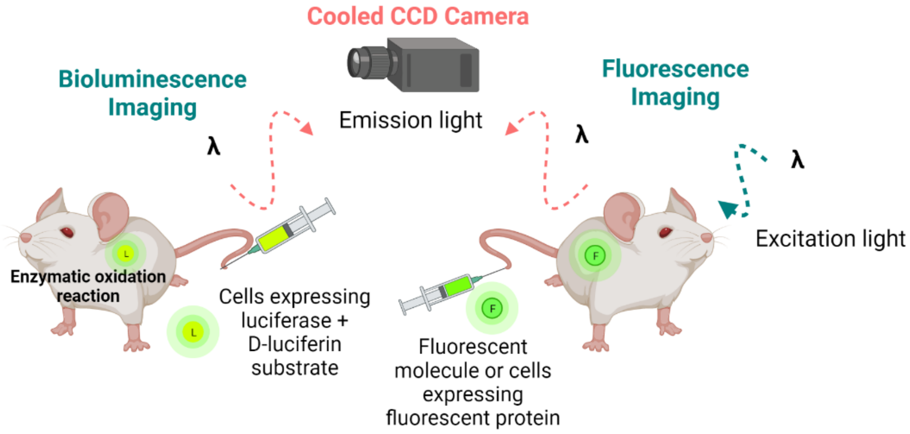

Figure 1.5: Optical imaging involves the detection of light and encompasses bioluminescence imaging (BLI) and fluorescence imaging (FI). BLI requires the administration of cells that express a luciferase enzyme, as well as an appropriate exogenous substrate (D-luciferin if firefly luciferase (FLuc) is expressed) that can react with luciferase in an enzymatic reaction to produce light. For FI, animals can be administered a fluorophore or cells expressing a fluorescent protein, which leads to absorption of light, excitation and subsequent emission of light. In both types of imaging, the emitted light is detected by a cooled charge-coupled device (CCD) camera.

Photoacoustic Imaging

Photoacoustic imaging (PAI), also known as optoacoustic imaging, is a relatively new imaging modality. PAI is a hybrid technology; it is a combination of optical imaging and acoustic imaging (i.e. ultrasound (US)) and relies on the detection of sound waves, which result from the absorption of light[59]. The modality works by firing a short pulse of non-ionising laser energy at the tissue of interest. This results in heating of the tissue, which causes thermoelastic expansion and ensuing relaxation, followed by the production of US waves (Figure 1.6)[60]. The resulting waves are detected on the surface of the skin and the time it takes for them to reach the detector depends on the depth of the tissue of origin, as well as the characteristics of the tissue. By measuring the amplitude of the waves and their times of arrival, an image can then be reconstructed[56].

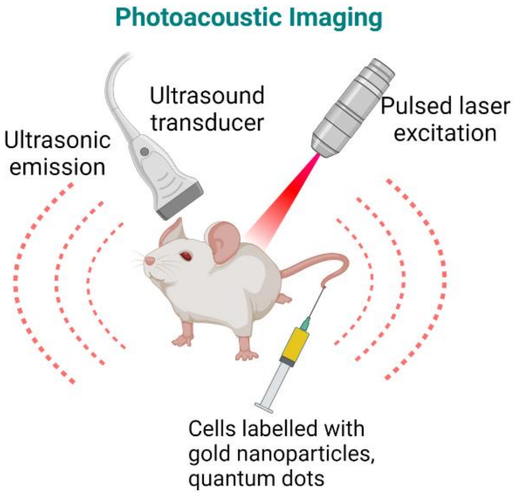

Figure 1.6: Photoacoustic imaging (PAI) combines the benefits of optical imaging (OI) with ultrasound (US), where light is converted to sound waves. Following the administration of an appropriate contrast agent (e.g. gold nanoparticles, organic dyes or quantum dots, discussed later in this chapter), a laser is irradiated on the subject, which results in heating due to the absorption of photons, thermoelastic expansion, and the subsequent emission of sound waves. These waves are detected via an ultrasound transducer.

The main advantage of PAI is its ability to convert light to sound waves, which results in significantly less scattering (1000 x less than with OI[61]) and provides the modality with a good penetration depth of ~ 4 – 5 cm. Because of this, PAI offers very good spatial resolution (20 – 300 µm), temporal resolution (seconds to minutes) and sensitivity, which permits whole-body imaging of small animals[2]. For cell tracking purposes, PAI can be used to assess intra-organ distributions of cells, as well as whole-body biodistributions. A key drawback of PAI is that it is not possible to image the lungs using this technology due to the presence of air[62]. Since many therapeutic cells become entrapped in the lungs upon systemic administration, the inability of PAI to image this organ and assess the distribution of cells there is a clear disadvantage. Additionally, PAI is not routinely used in the clinic, although the modality is clinically translatable[63] and is being tested in clinical trials for a variety of applications, for example in the detection of head and neck cancers[64] and in the detection of chronic rheumatoid arthritis[65].

Magnetic Resonance Imaging

Magnetic resonance imaging (MRI) is a clinical and preclinical imaging technology that uses a strong magnet (1.5 – 10.5 T) and radiofrequency energy to visualise soft tissue structures *in vivo* (Figure 1.7). Exogenous contrast agents such as superparamagnetic iron oxide nanoparticles (SPIONs) or gadolinium-(Gd)-based agents, including Gd-DOTA and Gd-DOTP, can be administered to enhance contrast in the body. The principles of MRI are described in greater detail in Chapter 2.

MRI is used extensively due to its excellent spatial resolution (40 – 100 µm)[2], which allows for the provision of anatomical information, particularly detailed examinations of organs. Additionally, MRI has an unlimited penetration depth and is completely safe. MRI; however, lacks in sensitivity (10^{-3} – 10^{-5} M)[66] and has poor temporal resolution, meaning that it can be difficult to acquire a full body image due to long acquisition times[56]. Because of this, tracking the body-wide distribution of administered cells is not feasible with MRI, and the modality is more suited in ascertaining information on the intra-organ distributions of cells. However, imaging cells in regions with inherently variable MR contrast, such as the lungs, spleen, gut and bone, is difficult[2]. Additionally, tracking SPION-labelled cells in the lungs is not possible using MR because SPIONs produce negative contrast (darkening) and the lungs appear black on MR images due to being filled with air[67].

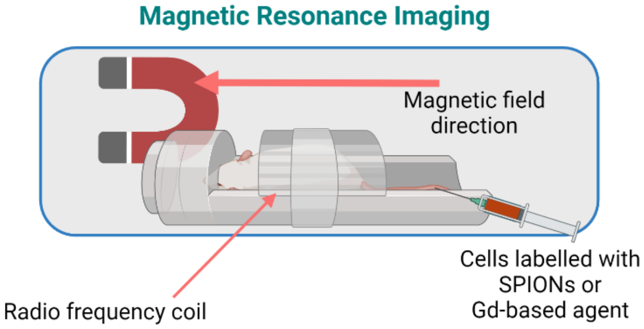

Figure 1.7: Magnetic resonance imaging (MRI) is based on the utilisation of radiofrequency pulses to excite hydrogen nuclei from within a subject that is positioned inside a magnet. Contrast is generated through the varying rates of relaxation of the excited protons that reside in different tissues of the body. Contrast can be enhanced through the administration of exogenous contrast agents, such as superparamagnetic iron oxide nanoparticles (SPIONs) or gadolinium (Gd)-based agents.

Nuclear Imaging

Nuclear imaging, which includes positron emission tomography (PET) and single-photon emission computed tomography (SPECT), is a type of imaging modality that relies on the decay of structurally unstable radioisotopes (Figure 1.8). To rectify their instability, PET radioisotopes, such as fluorine-18 (^{18}F) or zirconium-89 (^{89}Zr), emit a positron upon radioactive decay that collides with an electron close to this site of decay within the subject. This results in the release of two high energy gamma photons that travel 180° apart and are detected by a closed ring PET camera[56] (the principles of PET are described in more detail in Chapter 2). SPECT imaging, in contrast, employs a rotating gamma camera to detect gamma photons that are directly released by unstable SPECT tracers such as indium-111 (^{111}In) and technetium-99 (^{99m}Tc)[56].

Since the photons emitted by PET and SPECT tracers are in the high energy gamma range, this increases their chance of leaving the body and being detected by their respective cameras[56]. Thus, nuclear imaging offers unlimited depths of penetration, very high sensitivity and quantification capabilities[62]. This means that for cell tracking purposes, PET and SPECT can be very useful techniques for quantifying the proportion of cells that have reached an organ of interest. However, only PET and not SPECT, is fully quantitative since PET provides the opportunity for attenuation correction[56]. These nuclear imaging modalities also provide very good temporal resolution (seconds to minutes)[2], which means that whole-body images can easily be obtained with PET and SPECT and, for cell tracking purposes, the biodistributions of administered cells can be easily determined.

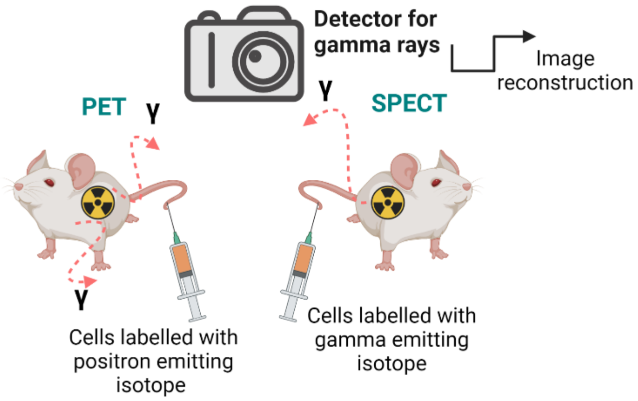

Figure 1.8: Nuclear imaging, which includes positron emission tomography (PET) and single-photon emission computed tomography (SPECT), relies on the administration of unstable radioactive isotopes to a subject. Upon decay of the isotope, gamma photons are emitted from the subject and are subsequently detected by a gamma camera. An image is then reconstructed.

The main disadvantage of PET and SPECT is that the spatial resolution is poor (1 – 2 mm in preclinical applications)[56], meaning that organs cannot be imaged in detail using nuclear modalities and the intra-organ distributions of administered cells cannot be visualised. Another important issue with nuclear imaging is the safety concern over using radioactive probes. However, due to the very high sensitivity of PET and SPECT, the concentrations of radiotracers that are used for imaging are very low and the risks of using such probes are carefully monitored. Although both PET and SPECT are popular imaging technologies in both clinical and preclinical settings, PET has the edge over SPECT due to being more sensitive (10^{-11} – 10^{-12} M for PET vs 10^{-10} – 10^{-11} M for SPECT)[56] and being fully quantitative.

Table 1.1: Summary of the key advantages and disadvantages of the most commonly used modalities in preclinical imaging (optical, photoacoustic, magnetic and nuclear)

Modality	**Advantages**	**Disadvantages**
Optical Imaging: Bioluminescence Imaging (BLI) and Fluorescence Imaging (FI)	• Completely safe • Good temporal resolution (seconds to minutes) • BLI is highly sensitive	• Poor spatial resolution (a few mms) • Limited penetration depth (< 1 cm for FLI, 1-2 cm for BLI) • Not clinically translatable • FI lacks in sensitivity due to host tissue autofluorescence
Photoacoustic Imaging (PAI)	• Completely safe • Good spatial resolution (20 – 300 µm) • Good temporal resolution (seconds to minutes) • Clinically translatable	• Limited penetration depth (4 – 5 cm), although this is an improvement on optical imaging
Magnetic Resonance Imaging (MRI)	• Unlimited penetration depth • Completely safe • Good spatial resolution (40-100 µm) • Used clinically	• Poor temporal resolution (minutes to hours)
Nuclear Imaging: Positron Emission Tomography (PET) and Single-Photon Emission Computed Tomography (SPECT)	• Unlimited penetration depth • Good temporal resolution (seconds to minutes) • High sensitivity • PET is fully quantitative • Used clinically	• Poor spatial resolution (1 – 2 mms) • Some safety concerns over the use of radiotracers, although very low doses are administered

Multimodal Imaging Techniques

There are clear advantages and disadvantages to each of the main imaging modalities. Thus, to improve diagnostic performance and to compensate for the weaknesses of individual imaging systems whilst harnessing their strengths, the current trend in medical imaging is to combine technologies to produce ‘multimodal’ or ‘hybrid’ imaging strategies[68].

The most common example of a multimodal imaging system is PET and x-ray computed tomography (CT) (PET/CT). The fusion of PET with CT was considered such a breakthrough in medical imaging that now none of the major manufacturers of medical imaging devices provide stand-alone PET scanners[69]. Following the success of PET/CT, SPECT/CT devices were developed shortly afterwards. The advent of these combined imaging systems was driven by one of the main shortfalls of nuclear imaging: the modality lacks an anatomical reference frame, which can create difficulties in accurately interpreting acquired images[70]. Thus, CT is now used to provide such an anatomical reference to complement the molecular information that PET or SPECT can provide. The success of PET/CT and SPECT/CT has led researchers in the medical imaging community to trial different combinations of imaging technologies, for example, US and MRI[71].

Prototype PET/MRI scanners are also currently under development, which is driven by the complementary nature of the two imaging technologies[69]. PET provides information at the molecular level and offers good temporal resolution and quantification, but the technology lacks in spatial resolution. Equally, MRI provides information at the anatomical level due to its excellent spatial resolution but has poor temporal resolution. Combining PET and MRI will offer excellent spatial resolution, temporal resolution, quantification capabilities and high sensitivity[68].

Applying PET/MRI in cell tracking could allow for the whole-body biodistributions of administered cells to be imaged and quantified using PET, whilst information on the intra-organ distributions of cells could be determined using MRI. In parallel with the emergence of novel PET/MRI systems, hybrid imaging probes that have the ability to generate signal and contrast in both PET and MRI are also under development. The next section will discuss common imaging probes and contrast agents that are used for the labelling and *in vivo* tracking of cells, with a particular focus on probes for PET and MRI.

1.3 Imaging Probes for Cell Tracking

Imaging probes, also known as contrast agents or imaging agents, are agents that are administered to a host prior to imaging that can exhibit a traceable signal in their respective imaging modality. For tracking cells *in vivo*, labelling probes can be employed, or cells can be genetically modified to express reporter genes[2], as summarised in Figure 1.9.

Cell Labelling with Reporter Genes

Reporter gene labelling involves the incorporation of genetic information into cells, which allows them to express genes that encode for reporter proteins[72]. Such proteins include enzymes, fluorescent proteins, transmembrane pumps and cell surface receptors, to name a few[73]. The non-native protein then exerts a function, which can be light production via fluorescence, the catalysis of a reaction, such as in the case of BLI, or the uptake of tracers via surface receptors, among others. The advantage of using reporter gene labelling over direct cell labelling is that the genetic modification of the cells is passed onto daughter cells during cell division. Thus, upon cell death, there is an accompanying loss of signal, whilst when cells proliferate, the signal intensity increases. Because of this, reporter gene imaging is an excellent tool for tracking cell fate[62]. The main disadvantage of reporter gene imaging is that weaker signals are generated compared to imaging with probes[74] (with the exception of luciferase enzymes for BLI), which is limited by factors such as the levels of expression of the reporter gene and the biodistribution of the administered exogenous substrate[2]. There are also some concerns over immunogenic and mutagenic responses in hosts[75].

The most commonly used genetic reporters are for OI, although reporter genes exist for all four of the common imaging modalities discussed above. PET and SPECT genetic reporter systems involve the administration of PET or SPECT tracers, which are transported inside of or bind to the target cells via the reporter gene. An example of a reporter gene for radionuclide imaging is the herpes simplex virus type 1 thymidine kinase (HSV1-tk) gene[72]. The advantage of nuclear reporter systems like the HSV1-tk gene is high sensitivity; however, they are very expensive and require the use of a potentially cytotoxic radioactive isotope[76]. Magnetic reporter systems work by utilising genes of which code for proteins that generate contrast upon the application of pulse sequences. Examples of these include the tyrosinase reporter, which results in T_1 contrast, and the transferrin receptor, which leads to T_2 contrast[2]. However, these reporters suffer from limited sensitivity and produce poor contrast compared to direct cell labelling with MRI probes, thus, have limited use in cell tracking applications[77]. There are even reporter systems for PAI based on near-infrared fluorescent protein reporters, such as iRFP[78], despite this imaging technique being relatively new. However, these systems suffer from low photostability and detection sensitivity[79].

Reporter genes for OI include fluorescence and bioluminescence reporter genes. An advantage of FI with reporter genes is that the technique does not require the use of an exogenous substrate, and instead relies on the absorption of light of a particular wavelength to excite the fluorescent protein[80]. A disadvantage of fluorescent reporter imaging, particularly for cell tracking, is background autofluorescence of endogenous tissue, which reduces the signal-to-noise ratio[81]. As mentioned earlier, BLI requires the use of genetically modified cells that can express luciferase. Since endogenous mammalian cells do not express luciferase, and background luminescence in animals is negligible, BL reporter gene imaging produces high signal-to-noise in contrast to fluorescence imaging[82]. Because of this, BLI reporter gene imaging has grown to be the method of choice for the optical tracking of cells in small animals[58].

The most widely used BLI reporter for cell tracking purposes is firefly luciferase (FLuc), which requires the presence of the substrate D-luciferin (as well as ATP, Mg^{2+} and oxygen) to emit light. The advantages of FLuc are that ~60% of the emitted light is of wavelengths > 600 nm, and FLuc has an emission at 620 nm when collected at 37°C. Since these wavelengths are close to the optical window, these emissions avoid being absorbed and scattered by surrounding tissues, which improves sensitivity and detection[82]. Additionally, the substrate, D-luciferin, has a long half-life since it is poorly catalysed by mammalian tissues[83]. Other commonly used luciferases include the sea pansy and marine cope-pod luciferases; however, both of these luciferases produce shorter wavelengths of light (peaking at 480 nm), which results in greater tissue attenuation and poorer sensitivity compared to FLuc[84].

Cell Labelling with Probes

Applying imaging probes is a direct and facile way to label cells since there is no requirement for genetic modification. Labelling involves the co-incubation of cells with a probe using tissue culture methods, which allows cells to internalise the probes, effectively ‘tagging’ them and allowing them to generate signal/contrast that is distinct from unlabelled cells. Cell labelling can be achieved in high yields, which produces intense signals, improves sensitivity and allows for the detection of low numbers of cells[2]. The main issue with using direct cell labelling over genetic reporters is signal dilution, which occurs when cells divide. Probes can also leach from the administered cells upon cell death, which can then be sequestered by endogenous cells of the host, leading to false positives[72, 85]. Cell labelling probes are, therefore, best utilised for the short-term tracking of cells. Common optical probes include luminescent particles, fluorophores and quantum dots (QDs). Such probes can also be used for PAI, which also has its own photoacoustic-specific agents, including gold nanoparticles (AuNPs) and carbon nanotubes (CNTs)[2]. The next sections will discuss in detail the cell labelling probes that are used for PET and MRI, since they are most relevant to this thesis.

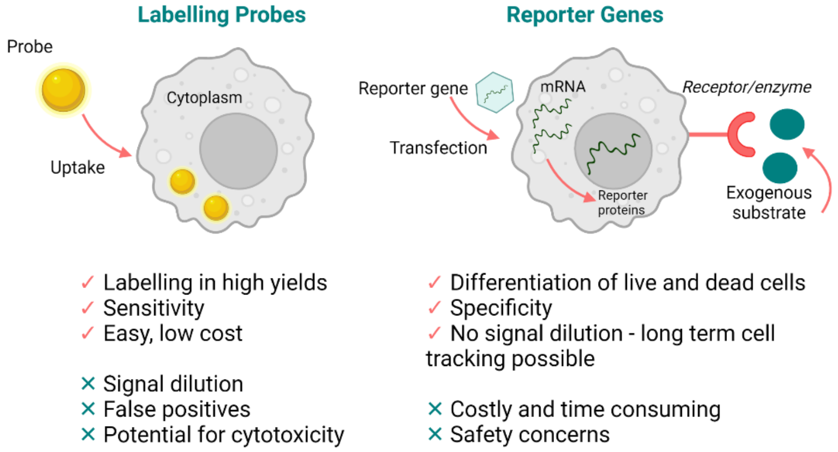

Figure 1.9: Comparing direct cell labelling using probes with reporter gene imaging. Cell labelling with exogenous probes, such as SPIONs, quantum dots (QDs) and gold nanoparticles (AuNPs), is time and cost-effective, sensitive and results in high labelling yields. However, the drawback of the technique is that signal dilution occurs upon cell division, and probes can leach from cells when they die, leading to false positives. There is also a risk of cytotoxicity when cells uptake the probes. Typically, probes are taken up by endocytosis and become localised within the endosomes and lysosomes of cells. Reporter gene imaging involves the uptake of foreign DNA into the cell's own DNA, which results in the expression of a reporter protein. The reporter protein can then generate signal upon administration of an exogenous substrate or via other mechanisms discussed in the text. The advantage of this technique is that information on the viability of the cells can be obtained, and no signal dilution occurs since the genetic modification is passed onto daughter cells upon cell division. Drawbacks to the technique include cost and the safety concerns over introducing foreign genetic material into cells.

Probes for PET Imaging

For the past few decades, radiopharmaceutical cell labelling has been used to systematically monitor cells *in vivo*. Clinically, PET is used to accurately detect the presence and location of cancerous cells. For this application, the tracer [^{18}F]-2-fluoro-2-deoxyglucose ([^{18}F]FDG) is used since cancer cells have increased metabolic demands; thus, [^{18}F]FDG accumulates in cancerous cells more significantly than it does in normal host cells, serving as an effective marker for cancer[86]. For long-term cell tracking purposes; however, fluorine-18-(^{18}F)-based radiotracers are not ideal since they have a short half-life of 109.8 min[56]. Radioisotopes such as copper-64 (^{64}Cu) and bromine-76 (^{76}Br) could be more suitable PET tracers for cell tracking due to having half-lives of 12.7 h and 16.2 h, respectively[56]. However, recent advances in cell tracking with PET have involved the labelling of cells with ^{89}Zr-oxine (Figure 1.10), which is owed to the long half-life of zirconium-89 (^{89}Zr, 3.3 days)[87], allowing for the tracking of cells for up to 3 weeks[88]. For example, ^{89}Zr-oxine has been employed in the labelling and imaging of immune cells, including dendritic cells and T cells[89], and there is a clinical trial currently ongoing that is investigating the ability of ^{89}Zr-oxine to track lymphocytes[90].

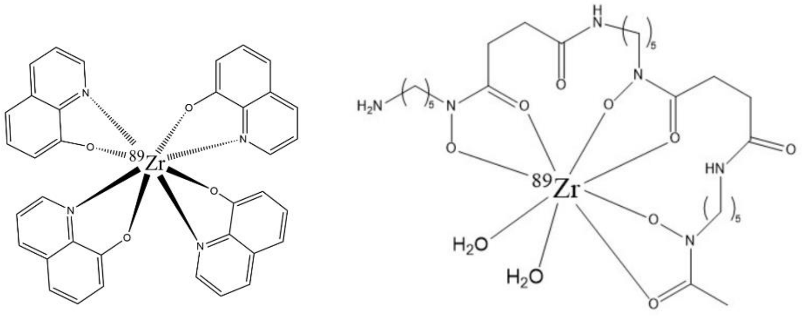
^{89}Zr-oxine **^{89}Zr-DFO**

Figure 1.10: Structures of some common PET tracers. ^{89}Zr-oxine has been used for the *in vivo* tracking of cells and ^{89}Zr-DFO is frequently used for the labelling of monoclonal antibodies.

Despite the promise of ^{89}Zr-oxine, there are a number of disadvantages to this PET tracer; current methods for its production result in low radiochemical yields (RCY) and involve numerous cumbersome steps[91]. Additionally, ^{89}Zr-oxine is a hydrophobic molecule, thus, can diffuse across the cell membrane. Once internalised in cells, ^{89}Zr is trapped by non-specific binding to cytoplasmic components, where it loses its oxine molecule tracers[91]. This is unfavourable, since free ^{89}Zr is known to deposit in the bone[92], leading to unspecific PET signals there and requiring the administration of higher doses of ^{89}Zr to produce signals in the organ of interest, which can lead to toxicity.

The importance of the *in vivo* stability of bound ^{89}Zr is well recognised and radiochemists have trialled various different tracers in an attempt to find the most stable ^{89}Zr-complexes for *in vivo* applications. A popular chelator for ^{89}Zr is desferrioxamine (DFO) (Figure 1.10), which is used to chelate ^{89}Zr to antibodies for ^{89}Zr-immuno-PET, and is currently the only ^{89}Zr chelator used in clinical studies[93]. The synthesis of ^{89}Zr-DFO and its functionalised derivatives is comparatively much simpler than the synthesis of ^{89}Zr-oxine and initial reports on its high *in vivo* stability have led to its increasing popularity[94]. However, there have been reports describing the accumulation of ^{89}Zr radioactivity in bone tissue following administration of ^{89}Zr-DFO[95]. It is believed that the observed *in vivo* instability of ^{89}Zr-DFO is due to the complex having an unsaturated coordination sphere; zirconium favours octadentate coordination but is only offered hexadentate coordination by DFO, which leaves ^{89}Zr exposed to solvent molecules and at risk of hydrolysis[96]. It is also thought that the unsaturated coordination sphere of ^{89}Zr-DFO is responsible for its transchelation by bone tissue, and its subsequent deposition there[97] (this is discussed further in Chapter 5).

Tetraazamacrocyclic Zirconium-89 Complexes

A class of chelator compounds that have been explored in recent years for the chelation of ^{89}Zr is the tetraazamacrocyclic ligands. These ligands, which include 1,4,7,10-tetraazacyclododecane-1,4,7,10-tetraacetic acid (DOTA) and 1,4,7,10-tetraazacyclododecane-1,4,7,10-tetra(methylene phosphonic acid) (DOTP), incorporate all eight binding sites for ^{89}Zr^{4+}, which confers additional preorganisation and results in enhanced stability[96]. Additionally, tetraazamacrocyclic ligands demonstrate heightened stability compared to acyclic ligands due to the macrocyclic effect. Another advantage of this class of chelator compound is that many are bifunctional chelators, which means that they have a metal binding moiety function, as well as chemically reactive functional groups. This could allow them to be easily conjugated to nanoparticles, polymers and antibodies for combined biomedical applications[98].

In 2016, Pandya *et al*. reported the synthesis of ^{89}Zr-DOTA (Figure 1.11), and noted its superior *in vivo* behaviour compared to ^{89}Zr-DFO, which is believed to be due to the ability of DOTA to form an octa-coordinate complex with the ^{89}Zr^{4+} ion[98]. Noteworthy, ^{89}Zr-DOTA displayed significantly less *in vivo* bone deposition than ^{89}Zr-DFO. A key drawback to the use of DOTA; however, is that high temperatures (> 60°C) are required to label the macrocycle with ^{89}Zr, which could be a disadvantage in the synthesis of ^{89}Zr-labelled nanoparticles or antibodies, due to the risk of thermal decomposition. To address this issue, Pandya *et al*. more recently reported the synthesis of some analogous compounds including ^{89}Zr-1,4,7-triazacyclononane-1,4,7-triacetic acid (^{89}Zr-NOTA) and ^{89}Zr-3,6,9,15-tetraazabicyclo(9.3.1)pentadeca-1(15),11,13-triene-3,6,9-triacetic acid (^{89}Zr-PCTA) at physiological temperature, with the latter complex (Figure 1.11) displaying remarkable stability *in vitro* and *in vivo*[93].

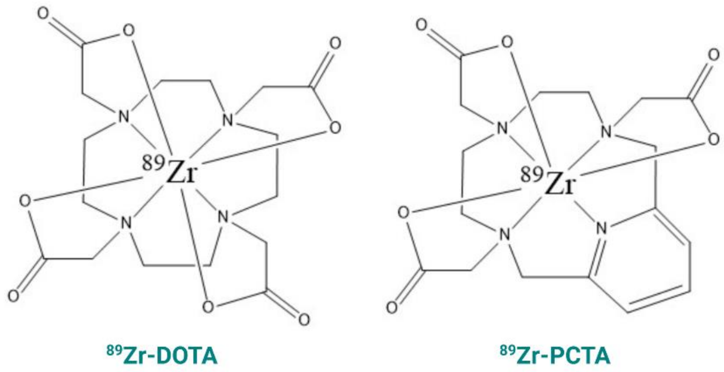

Figure 1.11: Tetraazamacrocyclic ligands yield ^{89}Zr complexes of remarkable stability, with ^{89}Zr-DOTA and ^{89}Zr-PCTA demonstrating superior *in vivo* stability compared to ^{89}Zr-DFO[93, 98].

To the best knowledge of the author, there have been no specific reports on the use of ^{89}Zr-DOTA or ^{89}Zr-PCTA for cell labelling and tracking *in vivo.* However, a report detailing the use of ^{64}Cu-DOTA derivatives for the *in vivo* tracking of adipose-derived stem cells (ADSCs) with PET noted efficient cell labelling with the probes and observed no significant reductions in cell viability[99]. PET tracers based on ^{89}Zr-labelled tetraazamacrocyclic compounds, such as ^{89}Zr-PCTA, could also be invaluable in the development of hybrid PET/MRI probes for cell tracking, since they can be prepared under mild conditions and could easily be conjugated to the surface of MRI agents, for example, SPIONs.

Probes for MR Imaging

Conventional MRI is performed on the ^{1}H nucleus, which is present in abundance in the water of tissues in the body. The different environments in which protons reside in the body leads to varying T_1 and T_2 relaxation times (the mechanisms of T_1 and T_2 relaxation are described in Chapter 2), which generates endogenous image contrast. External agents can be administered for ^{1}H MRI to alter the relaxation times of surrounding water protons and thus enhance local contrast in the body. For cell tracking, these agents can be introduced into cells *ex vivo* prior to transplantation in a host, which enables them to generate a contrast different to that of the surrounding host tissue[100].

Generally, contrast agents can be separated into T_1 and T_2 type contrast agents, with T_1 agents covering paramagnetic metal complexes and T_2 agents broadly covering SPIONs, as well as dysprosium-based agents. Furthermore, agents for ^{19}F MRI exist and are based on perfluorocarbons; however, these are technically not 'contrast agents' since there is an absence of MRI detectable endogenous ^{19}F in tissues of the body to contrast with, and are referred to as 'tracers'[101]. Although it is possible to carry out MRI on various other active nuclei, including ^{13}C and ^{23}Na, only ^{19}F has been applied in the field of cell tracking (in addition to ^{1}H) since it offers the next highest sensitivity following ^{1}H MRI[102].

Paramagnetic T_1 Contrast Agents

Paramagnetic T_1 contrast agents are widely used in clinical MRI and these cover gadolinium-based (Gd^{3+}) and manganese-based (Mn^{2+}) agents. Such agents primarily affect the T_1 relaxation time of the tissue, leading to hyperintense, positive contrast, which appears as a bright image. Gd^{3+} itself is toxic, so it is often paired with chelates, such as DOTA and DOTP (Figure 1.12), to reduce transmetallation *in vivo*[103]. Gd^{3+} chelates have been applied in the labelling and tracking of various types of cells, including endothelial progenitor cells[104] and MSCs[105]. However, barriers to the wide-spread use of Gd^{3+} chelates for cell tracking lie in their overall low sensitivity and their low uptake by cells, which often requires the use of transfection agents[106]. Most importantly, there are concerns over whether the long-term use of Gd^{3+} contrast agents can lead to toxicity to the cells that they label or to surrounding host tissue. This is illustrated in reports of Gd^{3+} chelates causing severe fibrosis and even death in patients with impaired kidney function[107]. Mn^{2+} contrast agents are also useful positive contrast agents but their utility as cell tracking agents has been limited, which is likely due to the cellular toxicity that Mn^{2+} can also exhibit[108]. Despite this, there have been reports on the use of manganese (II) chloride ($MnCl_2$)[109] for the labelling of lymphocytes, and manganese oxide nanoparticles have been used to track cells *in vivo*[110]. The most popular nanoparticle-based contrast agents for cell tracking with MRI; however, are SPIONs.

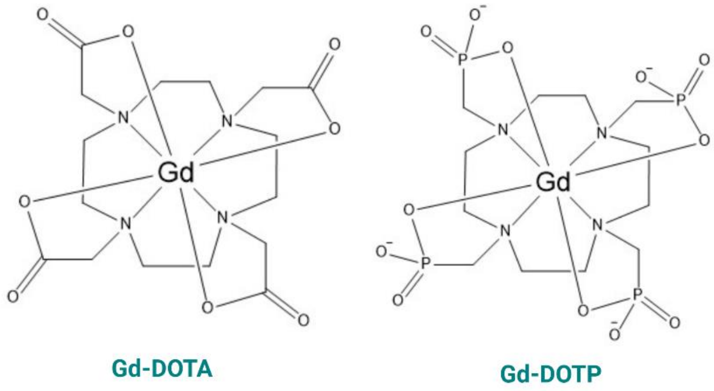

Figure 1.12: Gadolinium chelates, which include Gd-DOTA and Gd-DOTP, are widely used as T_1 MRI contrast agents.

Superparamagnetic Iron Oxide Nanoparticle T_2 Contrast Agents

SPIONs affect the T_2 relaxation time of water protons, leading to hypointense, negative contrast, which appears dark on images. Compared to Gd^{3+}-based contrast agents, SPIONs possess a much stronger MR relaxivity and offer higher sensitivity, which allows them to image small numbers of cells[111]. This, along with their low cytotoxicity and established synthetic procedures, has led SPIONs to become the gold standard in the labelling and tracking of cells[100]. However, to date, there have been no clinically approved SPIONs available for the specific labelling of therapeutic cells. The two iron oxide based products that were commercially available as contrast agents for the liver (Feridex® and Resovist®) were subsequently removed from the market, and their lack of specificity for cell labelling meant that transfection agents were required to facilitate their uptake into cells[112]. The use of transfection agents to label cells is far from ideal since they can add extra cost, have the potential to impart toxicity[100] and have been shown to cause particle aggregation[85].

SPIONs are small synthetic particles that have core sizes ranging from 10 to 100 nm, comprising either Fe_3O_4 (magnetite), γ-Fe_2O_3 (maghemite) or α-Fe_2O_3 (hematite), which is responsible for generating MR contrast. However, maghemite and magnetite type SPIONs are the most widely used for biomedical purposes[113]. For such applications, SPIONs are typically coated with a polymer, forming a core/shell structure, which confers stability and biocompatibility. A number of hydrophilic polymer-coated SPIONs have been developed in recent years to help improve the uptake of SPIONs into therapeutic cells. Such polymer coatings have included synthetic polymers, like polyvinyl alcohol (PVA)[114], polylysine (PLL)[115] and polyethylene glycol (PEG), as well as a number of naturally-derived polysaccharides like chitosan, pullulan and dextran (Figure 1.13)[100].

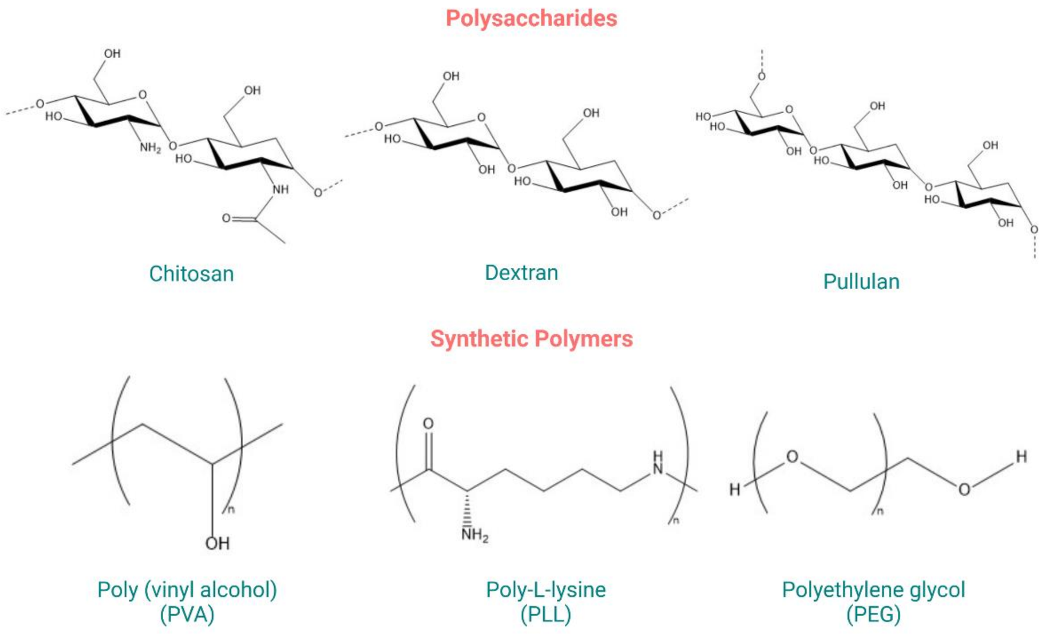

Figure 1.13: The structures of some widely used polymer coatings for SPIONs.

Of the synthetic polymers, PEG is widely used as a SPION coating due to being hydrophilic and highly biocompatible. PEG is often referred to as a ‘stealth’ polymer, owed to its long circulation time in the blood, since PEG-coated SPIONs avoid opsonisation and sequestration by cells of the mononuclear phagocyte system (MPS)[116]. Because of this, the uptake of PEG-coated SPIONs by stem/stromal cells and other therapeutic cells is often poor. However, this can be improved by functionalising PEG with groups that can become charged, such as NH_2 or hyaluronic acid[117]. PLL is a polycationic polymer, which has been used as a transfection agent, as well as a coating for SPIONs, with PLL-SPIONs demonstrating good uptake and viability in rat macrophages[118].

Of the polysaccharides, chitosan is a biocompatible polymer that contains amine groups thus the polymer carries an overall slight positive charge[100]. Chitosan-coated SPIONs have demonstrated good viability in hMSCs; however, their uptake has required the use of PLL as a transfection agent[119]. Chitosan has been functionalised with carboxymethyl groups, to generate a negatively charged polymer, carboxymethyl-chitosan (CMC), and CMC-coated-SPIONs have been shown to take up very efficiently into hMSCs without a transfection agent, owing to their high overall negative charge[120]. Pullulan is another polysaccharide that has also been widely investigated as a coating for SPIONs. However, pullulan itself is a neutral polymer, so it has been functionalised with ethylene diamine (ED) to generate the polycationic, ED-pullulan. SPIONs coated with ED-pullulan have demonstrated efficient MSC labelling[121].

Out of all of the polysaccharide polymers, dextran is the most commonly used as a coating for SPIONs, with the first report of SPIONs synthesised via the coprecipitation method using dextran as the stabilising polymer[122]. SPIONs coated with dextran alone; however, lead to low uptake in stem/stromal cells and require the use of transfection agents to enable sufficient uptake[123]. Dextran can be functionalised with charged groups such as fluorescein isothiocyanate (FITC) to render the polymer anionic, or diethylaminoethyl (DEAE), to make dextran polycationic. A recent study published by our group demonstrated how the surface charge of dextran SPIONs could be tailored by coating the particles with different ratios of DEAE-dextran to FITC-dextran[124]. A number of particles were synthesised with varying surface charges that ranged from -1.5 mV to +18.2 mV. The particles of surface charge +18.2 mV afforded a 6-fold uptake in mouse MSCs compared to neutral dextran particles, enforcing the idea that high positive charges on SPIONs result in very efficient uptake in stem cells. A further study from our group demonstrated that the positively charged DEAE-dextran-coated SPIONs could also safely label macrophages at least 10 times more efficiently than a clinically approved brand of SPION, which had a surface charge of -24.2 mV[125]. Since the polymer shell of SPIONs can have a significant influence in facilitating uptake into cells, it is an important factor to consider in the design of cell tracking probes. Additionally, for the development of hybrid PET/MRI cell tracking probes, it is useful if a polymer is selected that contains functional groups that can enable the binding of PET tracers.

1.4 Summary and Research Aims

In summary, cellular therapies, including macrophage therapy, hold great promise in the treatment of a wide range of diseases. However, to assist in their translation from bench to bedside, it is important to gather more safety and efficacy data surrounding such therapies. Non-invasive imaging technologies are invaluable tools for assessing the biodistribution, fate and persistence of administered cells, as well as for providing information on their mechanisms of action. Nevertheless, each of the main imaging technologies have their own strengths and limitations. Developing hybrid or multimodal imaging approaches can help to improve the performance of the individual imaging technology. The complementary nature of PET and MRI is recognised, as is the ease at which hybrid PET/MR imaging probes can be synthesised.

Thus, the main aims of this thesis were to:

1. Develop a hybrid imaging agent that could show signal and contrast in both PET and MRI, via the attachment of the PET tracer, ^{89}Zr, to dextran-coated SPIONs.
2. Optimise the *in vitro* colloidal stability of the hybrid particles, as well as their uptake and toxicity profiles in RAW 264.7 cells.
3. Assess the pharmacokinetics and *in vivo* stability of the hybrid particles following a systemic injection in mice using PET and MRI.
4. Assess the biodistribution, fate and persistence of IV administered luciferase expressing RAW 264.7 cells that are labelled with the hybrid particles using BLI, PET and MRI in a murine model of renal ischaemia/reperfusion injury (IRI).

Chapter 2

Materials and Methods

2.1 Materials

All chemical and biological reagents were purchased from Merck, UK, unless stated otherwise. All chemical reagents used were of > 96% purity. Deionised water from a Milli-Q system (Merck, Dorset, UK) (resistivity 15 mΩ cm^{-1} at 25 °C) was used for all experiments.

2.2 Imaging

2.2.1 Magnetic Resonance Imaging

^{1}H magnetic resonance imaging (MRI) relies on a strong magnetic field and the inherent spin properties of the body's water protons. Hydrogen nuclei consist of a single proton that carries a positive charge. Protons are spherical and spin constantly thus the spinning positive charge generates a magnetic field known as the magnetic moment of the proton.

The magnetic moments of protons are randomly orientated but in the presence of an external magnetic field, the magnetic moments align with the magnetic field. The direction of this alignment can be either parallel (in the same direction) or antiparallel to the external magnetic field (in the opposite direction). Lower energy protons align their magnetic moments parallel to the external field, whilst higher energy protons align their magnetic moments antiparallel to the magnetic field. Protons also precess in the presence of an external magnetic field and the speed of this precession is defined as the precession frequency (ω_0)[126]. This is determined by the Larmor equation (Equation 2.1), where γ is the gyromagnetic ratio (the ratio of angular momentum to magnetic moment) and B_0 is the strength of the external magnetic field.

$$\omega_0 = \gamma B_0 \quad \textbf{(2.1)}$$

Protons that are precessing parallel to the magnetic field in opposing directions begin to cancel one another out. There is; however, always a larger number of protons aligned parallel to the magnetic field at thermal equilibrium since these are of lower energy. Therefore, the magnetic moments of the nuclei aligned parallel to the magnetic field cancel out the smaller number of higher energy magnetic moments aligned antiparallel to the magnetic field, which leaves a net number of protons precessing parallel in the direction of the z-axis, along B_0. The result is a sum of the magnetic field and is called the longitudinal magnetisation, as shown in Figure 2.1 and represented by a net magnetisation vector (NMV) in the z-axis.

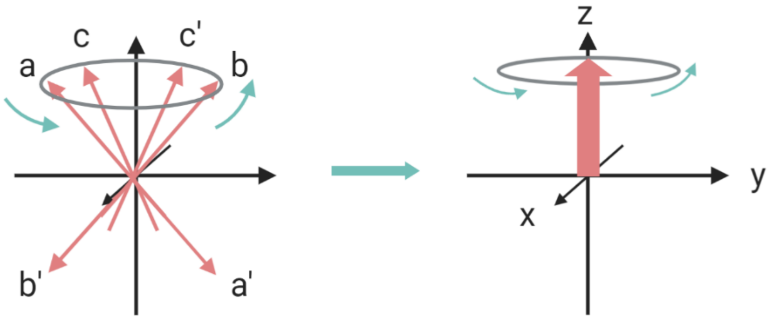

Figure 2.1: Some of the magnetic moments of protons spinning in the magnetic field cancel one another out, leaving a net magnetisation in the z plane along B_0 – parallel to the magnetic field, known as the longitudinal magnetisation. Here shown as a net magnetisation vector (NMV) in pink.

Upon application of a radiofrequency, the spin alignment of the protons is disturbed so that they fall out of alignment with the magnetic field. This is achieved through the transfer of energy from the radiofrequency to the protons and can only occur if the radiofrequency is of the same energy as the Larmor frequency (precessional frequency, ω_0), a phenomenon known as resonance[127]. Absorbing the radiofrequency causes the protons to move from their relaxed state to their excited state, which is antiparallel to the magnetic field. This results in transverse magnetisation; the sum of the magnetisation tilts 90°, creating a new magnetisation vector in the x-y plane, as shown in Figure 2.2. Once this radiofrequency pulse is removed, the protons relax back to their aligned spin state and longitudinal magnetisation is restored.

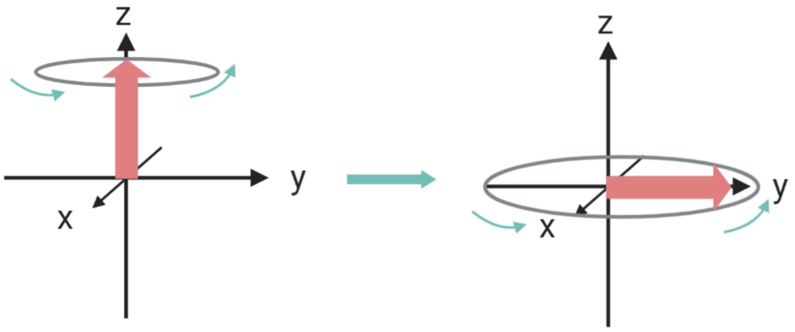

Figure 2.2: Application of a radiofrequency causes the net, longitudinal magnetisation to flip into the x-y plane, creating a new NMV, known as the transverse magnetisation.

There are two mechanisms of proton spin relaxation: T_1 and T_2 relaxation. T_1 relaxation is also known as longitudinal relaxation and is a process by which protons exchange energy with their surroundings to return to the low energy state thus restoring the longitudinal magnetisation. T_2 relaxation is a time constant for the dephasing/decay of the transverse magnetisation: it is the time in which protons fall out of phase with the x-y plane, via the exchange of energy with neighbouring protons. It is also known as 'spin-spin relaxation'[128]. T_2* relaxation refers to the dephasing/decay of the transverse magnetisation caused by a combination of spin-spin (T_2) relaxation and inhomogeneities in the magnetic field. T_2* decay is what the receiver coil actually detects following the removal of the RF excitation pulse. This decay is much more rapid and greater in magnitude than T_2 decay due to the inherent inhomogeneities of the magnetic field. If the magnetic field was perfectly uniform, then T_2 and T_2* would be equivalent[129]. The effects of T_2* are observed and applied in gradient echo imaging.

Protons of different tissues relax to the equilibrium state at different rates, which gives rise to MR contrast[130]. Contrast agents can also be administered to enhance MR contrast, and this is achieved through accelerating the proton relaxation rate, providing a more informative image. Superparamagnetic iron oxide nanoparticles (SPIONs) accelerate the T_2 relaxation rate through altering the T_2 values of water protons surrounding the particles. When SPIONs are used *in vivo*, they experience the external magnetic field from the MRI scanner, causing their magnetic moments to align. This results in the generation of large heterogeneous magnetic field gradients, which water protons can diffuse through. As a consequence, the magnetic moments of SPIONs and water protons experience dipolar coupling, which causes spin dephasing and T_2 relaxation[131]. In MRI, protons with a high T_2 relaxation rate give negative (dark) contrast, whereas protons of low T_2 relaxation rate give positive (bright) contrast. Hence, areas containing SPIONs will usually show as dark contrast in MR images.

In this work, all MR data were acquired with a Bruker Avance III spectrometer interfaced to a 9.4 T magnet system (Bruker Biospec 90/20 USR) (Bruker, MA, USA). For *in vivo* imaging, all data were acquired with a 4-channel surface coil designed for the mouse abdomen. For imaging of phantoms containing SPIONs and SPION-labelled cells, data were acquired using a 40 mm transit/receive quadrature volume coil, and for imaging the kidneys *post-mortem*, data were acquired using a 20 mm transit/receive quadrature volume coil. All imaging was carried out using gated Fast Low-Angle Shot (FLASH) T_2* sequences, whilst relaxation times were calculated from a T_2* map obtained with a multigradient echo (MGE) sequence. All MRI work performed in this thesis was assisted by Dr Arthur Taylor, University of Liverpool.

Table 2.1: MR acquisition parameters applied for the *in vivo* imaging of mice abdomens

	FLASH T_2* (mouse abdomen)	**B_0 Map**	**MGE T_2* Map (mouse abdomen)**
Echo Time (ms)	5.5	3.6	N/A
Repetition Time (ms)	290	10	988
Flip Angle (°)	20	15	50
Matrix Size (pixels)	386 x 386	64 x 64 x 64	256 x 256
Field of View (mm)	35 x 35	45 x 45 x 45	35 x 35
Averages	3	3	2
Slices	22	1	22
Slice Thickness (mm)	0.5	45	0.5
Echo Images	N/A	N/A	8
Echo Spacing	N/A	N/A	4.5 ms, start at 4.5 ms
Acquisition Time	5 m 36 s	2 m 3 s	6 m 19 s

Table 2.2: MR acquisition parameters applied for the *post mortem* imaging of the kidneys, SPION-labelled cells and phantoms containing SPIONs

	FLASH T_2* (kidneys *post mortem*)	**FLASH T_2* (labelled cells, phantoms)**	**MGE T_2* Map (phantoms)**
Echo Time (ms)	6.3	4.1	4.5, 10, …, 43 (8 echoes)
Repetition Time (ms)	1800	220	800
Flip Angle (°)	20	20	50
Matrix Size (pixels)	400 x 400	256 x 256	256 x 256
Field of View (mm)	17 x 17	30 x 30	30 x 30
Averages	24	5	2
Slices	100	10	1
Slice Thickness (mm)	0.2	0.5	0.5
Echo Images	N/A	N/A	8
Echo Spacing	N/A	N/A	5.5 ms, start at 5.5 ms
Acquisition Time	4 h 48 m	4 m 42 s	5 m 7 s

2.2.2 Positron Emission Tomography

Positron emission tomography (PET) involves the administration of an unstable, radioactive isotope to a host. To rectify their instability, PET isotopes undergo positron, or beta plus (β^+) decay *in vivo*, where the extra proton they carry transforms into a neutron, a positron and a neutrino. When the positron, also known as an anti-electron, is rapidly ejected from the nucleus, it undergoes inelastic interactions with electrons in surrounding tissues. The positron begins to lose kinetic energy and collides with an electron in an event known as annihilation (Figure 2.3)[132].

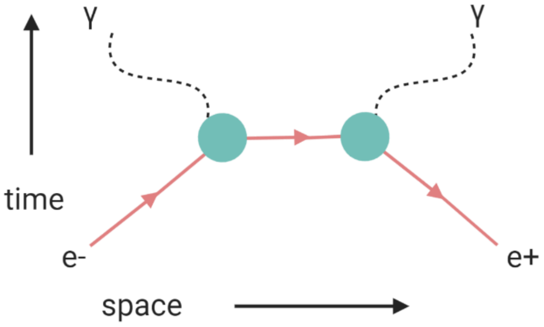

Figure 2.3: A positron (anti-electron, e+) collides with an electron (e-) at the site of radioactive decay, generating two gamma photons, γ, that travel in opposite directions to one another and are detected by a PET camera.

To conserve energy and momentum, the annihilation reaction produces two high energy photons that travel away from each other in opposite directions, 180° apart. The photons have an energy of 511 keV each, which puts them in the gamma region of the electromagnetic spectrum. The gamma rays produced are detected by a PET camera, which consists of a scintillation crystal coupled to photomultiplier tubes (PMTs)[133].

The PET tracer, zirconium-89 (^{89}Zr), is generated in a cyclotron in which its starting material, yttrium-89 (^{89}Y), which is 100% naturally abundant, is bombarded with high energy protons. These interact with the nucleus of ^{89}Y causing a neutron to be emitted, producing ^{89}Zr, in what is known as a (p,n) nuclear reaction[134]. ^{89}Zr used in this thesis was obtained from Perkin Elmer via BV Cyclotron VU (Amsterdam, NL) and arrived as the species, ^{89}Zr-oxalate, dissolved in

1M oxalic acid. The radiochemistry performed in Chapter 5 was assisted by Dr Stephen Patrick, University College London.

To provide an anatomical reference for PET images, x-ray computed tomography (CT) was performed prior to PET imaging. CT was undertaken on a Molecubes X-Cube (Molecubes NV, Ghent, BE), which has a resolution of 50 µm and delivers a dose < 4 mGy to obtain a rapid full-body scan. PET imaging was performed on a Molecubes β-cube (Molecubes NV, Ghent, BE), which has a resolution of 850 µm. All PET scans, unless stated otherwise, were performed over a period of 30 minutes. After imaging, the scans were reconstructed with an iterative construction at 400 µm. All PET/CT imaging performed in this thesis was assisted by Dr Jack Sharkey, University of Liverpool.

2.2.3 Bioluminescence Imaging

Bioluminescence detects light produced from the enzymatic oxidation reaction of luciferase with its substrate[132]. Luciferase enzymes can be introduced into cells through transduction with the gene that encodes them (see section 2.3 for more details). North American firefly luciferase (FLuc) was transduced into macrophages used in this project. FLuc oxidises its substrate, D-luciferin, in the presence of the co-factors, oxygen, adenosine triphosphate (ATP) and magnesium. First, the carboxyl group of luciferin is activated by ATP in an adenylation reaction. An intermediate forms that reacts with molecular oxygen, eliminating adenosine monophosphate (AMP) and inorganic pyrophosphate (PPi), and forming a further intermediate, dioxetanone. Dioxetanone then decomposes, yielding CO_2 and an excited oxyluciferin, which emits light (hν) to relax back to its ground state[135]. The overall reaction is summarised in Figure 2.4.

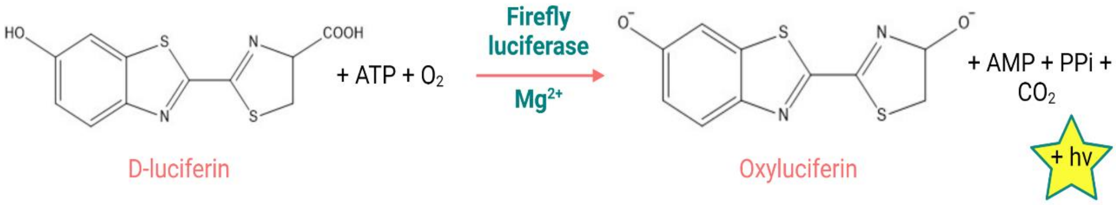

Figure 2.4: Overall representation of the bioluminescence reaction. Cells expressing firefly luciferase catalyse the substrate, D-luciferin, in the presence of oxygen, ATP and Mg^{2+} to produce oxyluciferin, CO_2, inorganic pyrophosphate (PPi) and light (hν).

Bioluminescence imaging (BLI) data were obtained on an IVIS spectrum system (Perkin Elmer, Buckinghamshire, UK). Imaging data were normalised to the acquisition conditions and expressed as radiance (photons/s/cm^2/sr). Bioluminescence imaging analysis was performed on Living Image® software (Perkin Elmer, Buckinghamshire, UK). All BLI performed in this thesis was assisted by Dr Jack Sharkey, University of Liverpool.

2.3 RAW 264.7 Cell Culture

RAW 264.7 murine cells, a macrophage/monocyte-like cell line, originally derived from BALB/c mice, were acquired from the European Collection of Authenticated Cell Cultures (#91062702)[136]. RAW cells were transduced with lentiviral vectors encoding a bicistronic construct of firefly luciferase (FLuc) and ZsGreen, as previously described[137]. The RAW Luc_Zs cell line was grown in Dulbecco's Modified Eagle Medium (DMEM) cell culture medium supplemented with 10% foetal bovine serum (FBS), 1 x glutamine and 1 x penicillin/streptomycin. Cells were maintained at 37°C in a humidified incubator with 5% CO_2.

To harvest RAWs, the cells were detached from the surfaces of low attachment dishes by scraping with a cell scraper. Cell suspensions were transferred to falcon tubes and centrifuged (1500 rpm, 2 min) then resuspended in medium for counting. Cells were counted on a haemocytometer (Hawksley, Lancing, UK) then plated in dishes or multi-well plates at the appropriate seeding density for regular cell line maintenance and all experiments involving

RAW cells. Details on methods used for cell labelling and the assays used for measuring SPION uptake and cytotoxicity are presented in the relevant chapters.

2.4 General Animal Methods

7 – 11 week-old male albino C57BL/6 mice were housed in individually ventilated cages under a 12 h light/dark cycle, with *ad libitum* access to standard food and water. For cell administration and imaging experiments, mice were anaesthetised with isoflurane prior to the procedure. After scanning, animals were recovered in a heat box and then returned to their cages.

All animal experiments were performed under a home office license granted under the UK Animals (Scientific Procedures) Act 1986 (Project License: PP3076489) and were approved by the University of Liverpool ethics committee. ARRIVE guidelines were followed to report animal experiments. All animal work performed in this thesis was assisted by Drs Arthur Taylor and Jack Sharkey, University of Liverpool, both of whom possess a personal license for the tasks that they undertook. More information of the design of animal studies are presented in the relevant chapters.

2.5 SPION Synthesis

A number of methods have been employed to synthesise SPIONs, with the two most common being coprecipitation and thermal decomposition. Other less popular methods include pyrolysis, sol-gel methods, and flow-injection synthesis. While thermal decomposition is an advantageous technique for SPION synthesis due to its high control over core size and crystallinity, these reactions are costly and not very scalable since they require high boiling solvents. Coprecipitation synthesis methods, on the other hand, are performed in aqueous solutions so are facile and produce large quantities of SPION. Although there is less degree of control over monodispersity in coprecipitation, this can be achieved by optimising variables such as reaction time and pH[100, 138, 139].

2.5.1 Coprecipitation

Coprecipitation occurs when iron ions (Fe^{2+} and Fe^{3+}) are mixed in solution in the presence of base, under an inert atmosphere and at an elevated temperature to form magnetite nanoparticles, Fe_3O_4 (Equation 2.2a)[140, 141]. According to thermodynamics, complete precipitation of magnetite occurs at pH 8 – 14, with a 2:1 stoichiometric ratio of ferric to ferrous ion (Fe^{3+}/Fe^{2+}).

$$2\mathrm{Fe}^{3+} + \mathrm{Fe}^{2+} + 8\mathrm{OH}^- \rightarrow \mathrm{Fe}_3\mathrm{O}_4 + 4\mathrm{H}_2\mathrm{O} \quad \textbf{(2.2a)}$$

Magnetite nanoparticles can be unstable in air and can convert to maghemite, γ-Fe_2O_3. The potential for oxidation can be impractical for long-term storage and use *in vivo*, therefore, magnetite nanoparticles are often subjected to deliberate oxidation to convert them to maghemite (Equation 2.2b). Both phases of SPION are ferrimagnetic, so conversion between the two does not affect superparamagnetic properties. Maghemite particles are stable in air, as well as in basic and weakly acidic conditions[142].

$$\mathrm{Fe}_3\mathrm{O}_4 + 2\mathrm{H}^+ \rightarrow \gamma\mathrm{Fe}_2\mathrm{O}_3 + \mathrm{Fe}^{2+} + \mathrm{H}_2\mathrm{O} \quad \textbf{(2.2b)}$$

Coprecipitation of SPIONs can be considered in three main stages: stage 1) is nucleation, which occurs in a short burst where species concentration reaches critical supersaturation and stage 2) is slow growth of the nuclei by diffusion of solutes to the crystal surface. Stage 3) is the optional step, which is forced oxidation of precipitated magnetite[140].

Our group has recently described a method for the synthesis of pure phase maghemite SPIONs by a coprecipitation method based off that described by Molday[143] and Paul[144]. In this reaction, pure phase magnetite is first accessed by using a 1:1 polymer to iron salt (mass to mass) ratio. DEAE-dextran and Fe^{3+}/Fe^{2+} salts are mixed in water then degassed to remove oxygen. The nucleation phase is achieved by the addition of base at 0°C, then nuclei growth is achieved by incubating the reaction mixture at high temperature for one hour. Following successful precipitation of magnetite, the reaction vessel is exposed to oxygen to allow for step 3, the forced oxidation to maghemite. Since this reaction is facile, reproducible and gives SPIONs of a very narrow size distribution, this protocol was utilised for synthesising SPIONs in this thesis, changing only the polymer system[143, 145, 146].

2.5.2 SPION Synthesis Protocol

To synthesise the mixed dextran SPIONs described in Chapter 3, the mass to mass ratio of total polymer to total iron salt was kept at ~ 1:1. The ratios of the polymers EDEA-CM-dextran (synthesis described in Chapter 3) to DEAE-dextran (MW 40,000) were varied but the total mass of the polymers was kept at 0.05 g. The stoichiometric ratio of ferric to ferrous iron (Fe^{3+}/Fe^{2+}) remained as 2:1, as per Equation 2.2a.

Therefore, 0.05 g total of EDEA-CM-dextran and DEAE-dextran, 0.015 g ferrous chloride tetrahydrate ($FeCl_2.4H_2O$) and 0.03 g ferric chloride hexahydrate ($FeCl_3.6H_2O$) were added in 25 ml water to a two-necked flask fitted with a non-magnetic PTFE overhead stirrer through an air-tight connection. The reaction mixture was purged with nitrogen on ice and then 1 ml 28 – 30% ammonium hydroxide (NH_4OH) was added dropwise over 120 s with constant stirring (200 ± 5 RPM). The solution was then transferred from ice to a 60°C oil-bath and the temperature was increased to 80°C over a period of 15 min, then kept at this temperature for 1 h. Following this, the solution was exposed to air to allow for oxidation and was then refluxed for 5 h at 110°C.

The solution was cooled to room temperature post reflux and poured into a 7K MWCO cellulose dialysis bag (ThermoFisher, Runcorn, UK). The solution was then dialysed for approximately 24 hours, until the pH of the particle solution was neutral. Finally, the particle solution was washed twice with DI water and concentrated to around 2 – 5 ml post dialysis using 100K MWCO polyethersulfone (PES) membrane spin filters (ThermoFisher, Runcorn, UK). Water volumes were adjusted to obtain SPION concentrations of around 1 mg ml^{-1}. To sterilise and remove any fine particles, such as dust, SPIONs were passed through 0.22 µm PES syringe filters prior to cell labelling experiments and dynamic light scattering (DLS)/zeta potential (ZP) measurements.

2.6 EDC Couplings

To synthesise DOTA-SPIONs and PCTA-SPIONs, the polymer, CM-dextran, was first functionalised with the linker, 2,2′-(ethylenedioxy)-bis-(ethylamine) (EDEA), which would serve as a site for the macrocycles, 1,4,7,10-tetraazacyclododecane-1,4,7,10-tetraacetic acid (DOTA) (Macrocyclics, TX, USA) or 3,6,9,15-tetraazabicyclo[9.3.1]pentadeca-1(15),11,13-triene-3,6,9-triacetic acid (PCTA) (CheMatech, Dijon, FR). Both of these reactions (joining of the linker and the macrocycles) were achieved through N-(3-Dimethylaminopropyl)-N′-ethylcarbodiimide (EDC) couplings.

2.6.1 Mechanism of EDC Coupling

EDC coupling reactions are a one-pot method for the production of amides from their corresponding carboxylic acids and amines in the presence of an activating agent such as hydroxybenzotriazole (HOBt). Such couplings are facile since their products are easily purified and reactions can be performed at room temperature and in aqueous solutions[147, 148]. In the reaction, the carboxylic acid first attacks the carbodiimide of EDC, forming an *O*-acylurea intermediate[149]. The additive, HOBt, then attacks the intermediate to form the OBt activated ester, eliminating the acylurea side product. HOBt is added in at this stage to enhance the reactivity of the intermediate ester and to reduce epimerisation, resulting in greater yields of the amide product[150]. Following this, the amine attacks in at the carbonyl centre of the activated ester, eliminating the good leaving group, HOBt, producing the amide product. The mechanism of EDC/HOBt coupling is summarised in Figure 2.5.

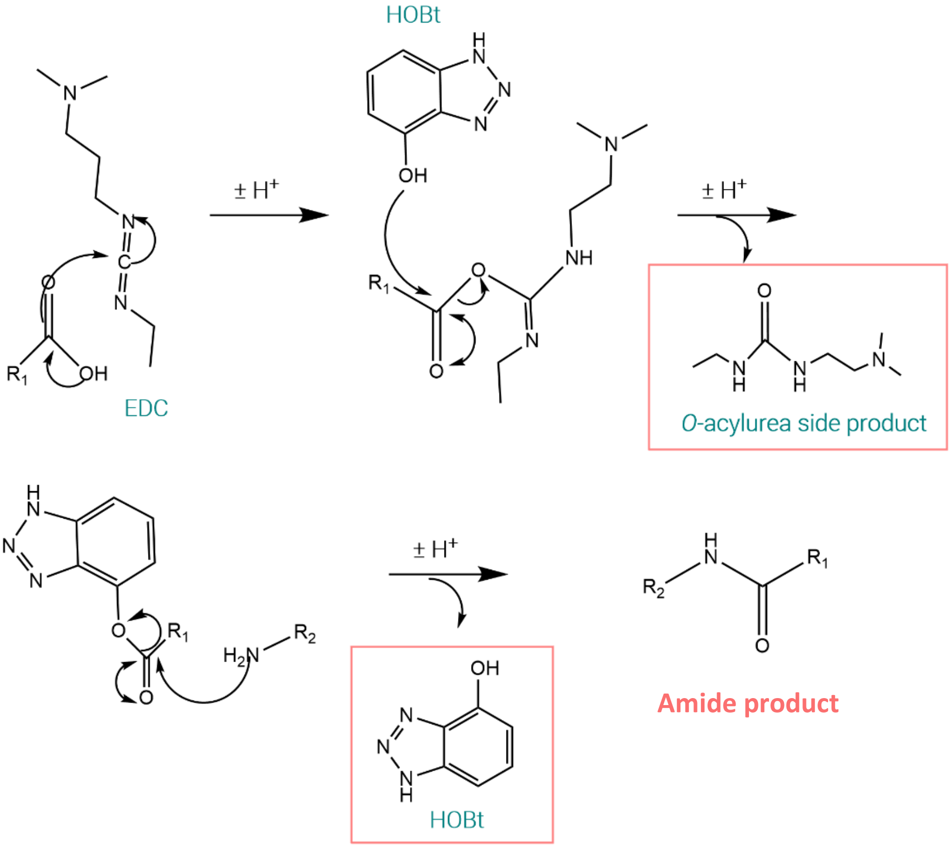

Figure 2.5: Amide formation from its corresponding carboxylic acid and amine via EDC coupling. The carboxylic acid attacks at the carbodiimide centre of EDC forming an acylurea intermediate. This is eliminated when the additive, HOBt, attacks in at the carbonyl centre to form an activated ester intermediate. Finally, the amine attacks in at the carbonyl centre, eliminating the good leaving group, HOBt, and forming the amide product.

2.6.2 EDC Coupling Protocol

In both the functionalisation of CM-dextran with EDEA and SPIONs with the DOTA or PCTA macrocycles, EDC couplings were employed. In the first instance, CM-dextran was the carboxylic acid whilst EDEA was the amine, and in the second instance, DOTA or PCTA were the carboxylic acids whilst the EDEA-CM-dextran-coated SPION was the amine. The reactions were performed in MES buffer (a none-carboxylate or amine containing buffer) to maintain pH ~ 4 – 5. To ensure maximum amide bond formation, reactions were performed for 3 h at ambient temperature.

Following each reaction, the products were dialysed through 7K MWCO cellulose tubing (ThermoFisher, Runcorn, UK) to allow for removal of the low molecular weight side products and unreacted starting materials.

2.7 Freeze Drying

EDEA-CM-dextran and SPION samples were freeze dried for chemical characterisations using a Labconco Freezone 4.5 freeze-dryer (Labconco, MO, USA) with a condenser temperature of -50°C and a shelf temperature of 20°C.

2.8 Chemical Characterisations

To characterise functionalised polymers and SPIONs, a number of analytical techniques were employed, the details of which are described below.

2.8.1 DLS

DLS measurements were performed on a ZetaSizer Nano ZSP instrument (Malvern Panalytical, Malvern, UK) at ambient temperature. SPIONs for DLS measurements were diluted to approximately 1 mg ml^{-1} in 10 mM NaCl solution.

2.8.2 Zeta Potential

Zeta potential measurements were performed on a ZetaSizer Nano ZSP instrument (Malvern Panalytical, Malvern, UK) at ambient temperature. SPIONs for zeta potential measurements were diluted to approximately 1 mg ml^{-1} in 10 mM NaCl solution.

2.8.3 Powder X-Ray Diffraction

To determine the mean core diameter of SPIONs synthesised in this project, powder x-ray diffraction (pXRD) and the Scherrer equation were applied (Equation 2.3). pXRD patterns were collected in transmission geometry at 25°C on a Panalytical X'pert Pro diffractometer (Malvern Panalytical, Malvern, UK) with Co Kα radiation (λ = 1.788965 Å). Data were collected over 1 hour in the $10^{o} < 2\theta < 80^{o}$ range with a step size of 0.0133^{o}. To determine mean core diameter, peaks in the pXRD pattern were fit using the pseudo Voight peak profile on X'Pert Highscore plus software (Malvern Panalytical, Malvern, UK). This determined the FWHM, β_d, of the reflections which were then put into the Scherrer equation. This allowed the average domain size, D, to be calculated. pXRD measurements and calculations were assisted by Dr Troy Manning, University of Liverpool.

$$D = \frac{0.9\lambda}{\beta_d} \cdot \frac{1}{cos\theta} \quad \textbf{(2.3)}$$

2.8.4 Fourier-Transform Infrared Spectroscopy

Fourier-transform infrared spectroscopy (FTIR) measurements were performed on a Bruker Vertex 70 Fourier Transform Infrared Spectrometer (Bruker, MA, USA) in transmission mode. SPION samples were freeze dried prior to FTIR analysis.

2.8.5 Quadrupole Time-of-Flight Mass Spectrometry

Quadrupole time-of-flight mass spectrometry (q-TOF-MS) was performed by Mr Stephen Moss, University of Liverpool, on an Agilent 6450 quadrupole LC/MS system (Agilent, CA, USA) using a direct injection into the q-TOF and positive ion electrospray ionisation (ESI+) to ionise the samples. SPION samples for q-TOF-MS were prepared at a concentration of 1 mg ml^{-1}.

2.8.6 ^{13}C Nuclear Magnetic Resonance

Samples for ^{13}C nuclear magnetic resonance (NMR) were performed in D_2O on a Bruker Avance II 400MHz-WB spectrometer (Bruker, MA, USA) at 25°C. All chemical shifts (δ) in this thesis are quoted in ppm.

2.8.7 Elemental Analysis

Samples for elemental analysis were performed by Mrs Jean Ellis, University of Liverpool, on a Thermo EA1112 Flash CHNS-O Analyzer (ThermoFisher, Runcorn, UK). SPION samples were freeze dried prior to elemental analysis.

2.8.8 Thermogravimetric Analysis

Thermogravimetric analysis (TGA) Measurements were performed on a TA Instruments Q600 machine (TA Instruments, DE, USA) under a constant air flow of 50 ml min^{-1}. Samples were heated up to 120°C at a heating rate of 20°C min^{-1}, then were incubated at 120°C for 20 min to ensure complete removal of water. Heating was then ramped up to 1000°C at a rate of 10°C min^{-1}. SPION samples were freeze dried prior to thermogravimetric analysis.

2.8.9 Inductively Coupled Plasma-Optical Emission Spectrometry

Inductively coupled plasma-optical emission spectrometry (ICP-OES) measurements in this thesis were performed by Mr Stephen Moss, University of Liverpool, on an Agilent 5110 spectrometer. Zr-SPION samples for ICP-OES were spun down via spin filtration until they were dry, then were digested in 1M HCl (1 ml) at 80°C for 2 h. They were then diluted 10 fold with Milli-Q H_2O.

2.8.10 Transmission Electron Microscopy

Transmission Electron Microscopy (TEM imaging) was performed on a JEOL JEM 2100Plus Electron Microscope (Oxford Instruments, Oxford, UK). SPION samples were prepared for TEM by depositing a drop (10 µl) of solution on a carbon coated TEM grid and allowing it to dry overnight. Data analysis was carried out on AZtecOne software (Oxford Instruments, Oxford, UK).

2.8.11 Superconducting Quantum Interference Device

Magnetic isotherm data were collected at 300 K in VSM scan mode (scan length 30 mm, scan time 4 seconds, 2 scans per measurement) using an MPMS3 superconducting quantum interference device (SQUID) magnetometer (Quantum Design, Surrey, UK). 1.5 mg freeze-dried samples were packed in a size 4 gelatine capsule and fixed in a plastic drinking straw.

Chapter 3

Synthesis and Characterisation of Hybrid PET/MRI Cell Tracking Probes

3.1 Introduction

As interest in multimodal imaging systems increases, there is a greater demand for safe and effective hybrid imaging agents. The nature of a hybrid imaging agent is a single probe that can show signal in two types of imaging modality. Regarding their pharmacokinetic properties, hybrid imaging agents are typically handled *in vivo* as single entities, unlike if one were to inject a cocktail of imaging agents to a host, meaning that the probe can colocalise to the area of interest in a single injection. This results in more accurate signal quantification[151].

This chapter will review some of the synthetic strategies that could be employed to generate hybrid positron emission tomography/magnetic resonance (PET/MR) imaging agents, focusing on the methods available to radiolabel superparamagnetic iron oxide nanoparticles (SPIONs). Furthermore, the work in this chapter will show how the hybrid PET/MR imaging agents used in this project were synthesised and characterised.

Design of Hybrid PET/MR Imaging Probes

In the world of multimodal imaging, PET and magnetic resonance imaging (MRI) are considered to be the two most complementary modalities[151]. As detailed in Chapter 1, MRI is widely recognised for its high spatial resolution, whereas spatial resolution is lower with PET, and unlike MRI, PET offers high sensitivity and good temporal resolution[152]. PET is fully quantitative, whilst MRI is only semi-quantitative at best. For cell tracking purposes, MRI could be used to track the intra-organ distribution of administered cellular therapies due to its excellent spatial resolution, whilst PET could image the whole-body biodistribution of cells due to its high temporal resolution and unlimited penetration depth. For multimodal cell tracking with PET/MRI to be realised, it is important that hybrid PET/MR imaging agents are developed that can show signal/contrast in both imaging systems. Furthermore, an ideal hybrid cell tracking agent is biocompatible, confers high *in vitro* and *in vivo* stability and is taken up efficiently by cells.

In 2010, *Frullano et al.* developed a hybrid PET/MR imaging agent based on a modified gadolinium-DOTA complex (T_1 contrast agent) that was functionalised with the PET tracer, fluorine-18[153]. This agent was used successfully for *in vivo* pH measurements; however, it would be unsuitable for cell tracking applications due to the short half-life of fluorine-18, the potential for gadolinium-associated cytotoxicity and the low relaxivity of the Gd^{3+} ion when internalised in cells[154]. Because of the issues centred on Gd^{3+}, much of the research into hybrid PET/MR imaging agents has been based on the radiolabelling of SPIONs with common PET tracers.

Methods for Radiolabelling SPIONs

Harnessing the versatile surface chemistry of SPIONs can lead to facile and efficient radiolabelling; isotopes can easily attach to the nanoparticle. However, there are many factors to consider when radiolabelling SPIONs for PET/MR applications. Ideal radiolabelling reactions are quick; this is important because radionuclides used in PET tend to have a short half-life, and so a rapid post-modification step on the SPIONs is best to maximise radiochemical yields (RCY). The technique must be reproducible, and radiolabelling must not change the physical and biological properties of the particles[155]. The next section will outline three methods that could be employed to radiolabel SPIONs.

Physisorption

Physisorption is a non-classical radiolabelling technique that exploits the surface zeta potential of nanoparticles. Many polymer-coated SPIONs have high net surface charges (either negative or positive) since this confers high colloidal stability to the particles and can increase their cellular uptake[156]. A radioactive ion, which carries a charge opposite to that of the nanoparticle system, could become entrapped on the Stern layer between the SPION surface and the dispersion medium via an electrostatic attachment, as shown in Figure 3.1. The advantages of this physisorption method are that few steps are required, and the reaction can be performed at room temperature. However, the key feature of physisorption is that no discrete or dative covalent bond forms thus the electrostatic linkage between the radiolabel and SPION may not be strong enough for the hybrid components to remain joined *in vivo*[155].

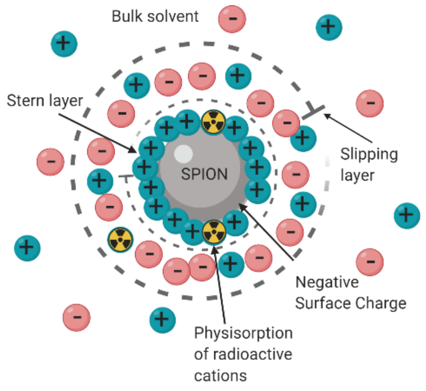

Figure 3.1: Radiolabelling via physisorption. In this example, radioactive cations bind to the negative surface of SPIONs via entrapment on the particle's Stern layer.

There are few reports detailing electrostatic-based radiolabelling techniques, suggesting that this method is not a commonly used approach. One of these was published in 2013 by Abou *et al.*[157], who reported a chelator free method of radiolabelling the negatively charged heads of Gd-functionalised liposomes with the cationic PET tracer, zirconium-89 ($^{89}Zr^{4+}$), for combined PET/MR imaging. The resultant radiolabelled liposomes were found to be unstable *in vitro* and *in vivo*; the particles lost 50% of their activity following a 48 h incubation in serum, and a significant radioactive bone uptake was observed following administration of the particles in mice. This suggests that physisorption is not the most robust method for radiolabelling nanoparticles. To the best of the author's knowledge, there are no specific reports on electrostatically radiolabelling SPIONs and, instead, techniques such as chemisorption and particle coating modifications have been investigated more extensively.

Chemisorption

Chemisorption is another non-classical radiolabelling technique that involves direct chemical bond formation between a radionuclide and the SPION surface[155]. The technique was first generalised by the Holland Lab[158], who reported a heat-induced, chelate-free method of labelling the iron oxide core of SPIONs with ^{89}Zr, which is displayed schematically in Figure

3.2. In 2019, Patrick *et al.*[159] established the mechanism of chemisorption as a mineralisation of ^{89}Zr-oxide on the surface of SPIONs, as determined by characterisation techniques such as x-ray photoelectron spectroscopy (XPS), and named the method 'surface radio-mineralisation' (SRM).

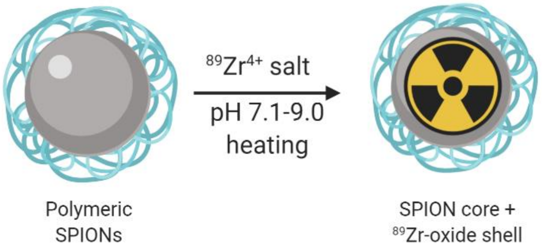

Figure 3.2: Chemisorption of the ^{89}Zr radiotracer as a layer of ^{89}Zr-oxide onto the surface of the SPION core via surface radio-mineralisation (SRM).

The main advantage of the SRM method is that it avoids the use of bulky radiometal chelating ligands, which can impact on the pharmacokinetics of particles, producing hybrid particles that display the same *in vivo* behaviour as non-radiolabelled SPIONs[155]. The method is rapid and results in high RCYs. Additionally, it produces hybrid particles of high *in vivo* stability that appear to remain bound following systemic administration, displaying little radioactive bone uptake[159, 160]. Drawbacks to the SRM method include the requirement of high temperatures (40 – 100°C) to label the particles, which could decompose the polymer shells that coat SPIONs, reducing their colloidal stability. As well as this, the method may not be suitable for all nanoparticle systems; in order for the radiometal to reach the SPION surface for SRM, it must penetrate the, often charged, polymer shell. This means that radiotracers of like charge to the polymer coating may be repelled and may not reach the particle surface for mineralisation.

Noteworthy, there are additional non-classical radiolabelling techniques that have been reported in the literature, such as radiochemical doping and isotopic exchange[155]; however, these are not relevant to the work performed in this thesis, and thus, will not be discussed.

Particle Coating Modifications with Chelator Compounds

The most widely used, classical nanoparticle radiolabelling method is coating based metal ion chelation. Here, the polymer coating of SPIONs is modified with functional groups that can form a covalent bond with a radiometal. There are many examples of this method in the literature, with one being reported by Thorek *et al.*[161], who utilised the chelating compound, desferrioxamine (DFO), to covalently link ^{89}Zr-oxalate with Feraheme®, a formerly clinically approved SPION. To achieve this, the carboxymethyl-dextran coating of Feraheme® was first functionalised with the linker, 1,2-ethylenediamine, then a modified version of the DFO chelator (DFO-pBN-SCN) was conjugated to the functionalised particles (Figure 3.3). Finally, DFO was radiolabelled by ^{89}Zr in a metal ion chelation reaction, producing a PET/MR probe for imaging of the sentinel lymph nodes. Feraheme® particles were radiolabelled with high efficiency (> 90%) and yielded particles of high stability when challenged in serum. This highlights the key advantage of the particle coating modification method: a strong covalent or dative covalent bond forms between the radiolabel and the nanoparticle, meaning the two are likely to remain bound *in vitro* and *in vivo*. However, the main disadvantage to this technique is the addition of bulky chelating groups onto the surface of SPIONs, which risk altering the physiochemical properties of the particles and thus their pharmacokinetic and toxicity profiles[162].

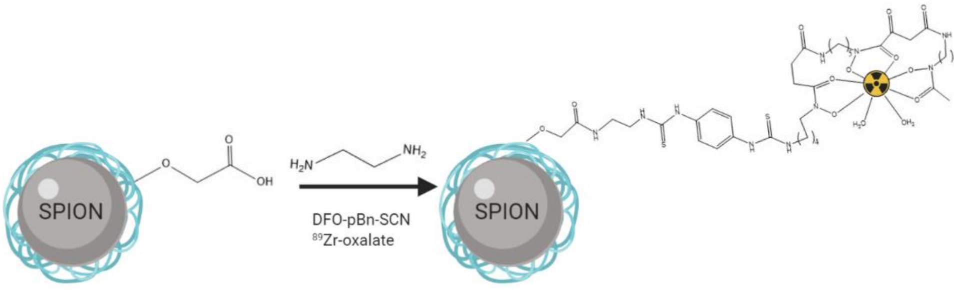

Figure 3.3: Radiolabelling with ^{89}Zr via a particle coating modification with the chelator compound, DFO, on the carboxymethyl-dextran-coated SPION, Feraheme®, as reported by Thorek *et al*[161].

Experimental Plan

While physisorption could be a fast radiolabelling technique that does not expose SPIONs to harsh synthetic conditions, it is unlikely that the radiolabel would remain attached to the particle under physiological conditions. This is because physiological medium contains many large, charged proteins and biomacromolecules that can adsorb to the particle and form a protein corona[163]. Such molecules could preferentially adsorb to the SPION and displace the radiolabel. This would mean that the components of the hybrid particle would not colocalise *in vivo* and could potentially give signals in different areas of the body.

In our group we have developed SPIONs that are coated with the polycationic polymer, DEAE-dextran (DEAE-dex). We have shown that this polymer confers high colloidal stability to the particles and allows for efficient uptake into stem cells and macrophages[124, 125]. Since most common PET radiotracers exist as positive ions, it is possible that the tracer would not penetrate through the positive polymer shell for SRM.

Because of these potential issues, neither physisorption nor chemisorption was performed in this project as the radiolabelling method. Instead, a simple covalent method was employed to modify the SPION particle coating with a chelator compound. As mentioned above, DEAE-dex is a biocompatible polymer, so we aimed to keep this polymer as part of the SPION coating. However, DEAE-dex is very difficult to modify since the polymer's terminus is a stable tertiary amine. Because of this, the more easily modifiable polymer, carboxymethyl-dextran (CM-dex) was selected to be functionalised with the ^{89}Zr chelating macrocycles, 1,4,7,10-tetraazacyclododecane-1,4,7,10-tetraacetic acid (DOTA) or 3,6,9,15-tetraazabicyclo(9.3.1)pentadeca-1(15),11,13-triene-3,6,9-triacetic acid (PCTA). DOTA was chosen as a macrocycle to chelate the PET tracer since ^{89}Zr-DOTA complexes have been found to be more stable than their ^{89}Zr-DFO and ^{89}Zr-DOTP counterparts[98]. Due to the high temperatures required to label DOTA with ^{89}Zr metals salts, the macrocycle PCTA was also chosen to be coupled to SPIONs, since PCTA can be labelled by ^{89}Zr at temperatures as low as 37°C[164]. CM-dex was first functionalised with a small organic linker compound to allow it to bind the different macrocycles.

SPIONs were synthesised using a mixture of the two dextran polymers. Functionalised CM-dex has an overall neutral charge meaning that the mixed dextran SPIONs had an overall positive charge due to the presence of DEAE-dex on the surface, which is beneficial for cell labelling and colloidal stability[124].

The first step in the hybrid particle synthesis was to functionalise CM-dex with the n-ethylene-glycol linker, 2,2′-(ethylenedioxy)-bis-(ethylamine) (EDEA) by 1-ethyl-3-(3-dimethylaminopropyl)carbodiimide (EDC) coupling (more details in Chapter 2) to make EDEA-CM-dex, as shown schematically in Figure 3.4.

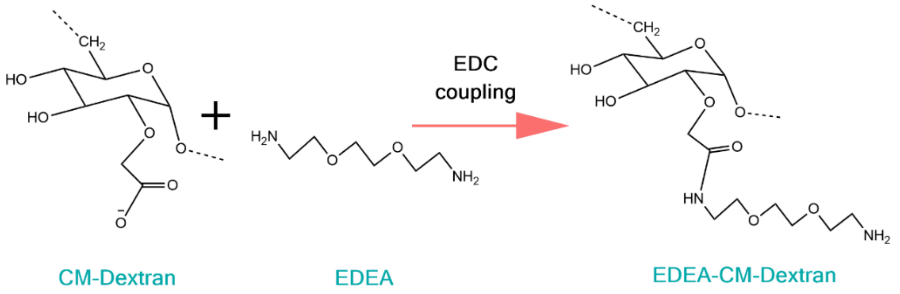

Figure 3.4: Schematic representing the synthesis of 2,2′-(ethylenedioxy)-bis-(ethylamine)-carboxymethyl-dextran (EDEA-CM-dex) from 2,2′-(ethylenedioxy)-bis-(ethylamine) (EDEA) and carboxymethyl-dextran (CM-dex) via 1-ethyl-3-(3-dimethylaminopropyl)carbodiimide (EDC) coupling.

Initially, it was considered to then coordinate the different macrocycles to EDEA-CM-dex in subsequent EDC coupling reactions. However, there is a potential for iron to favour sitting in the pores of the macrocycles during SPION synthesis instead of coprecipitating with polymer and forming nanoparticles, since iron ions have a high affinity for tetraazamacrocyclic structures[165]. Therefore, it was decided to form nanoparticles from EDEA-CM-dex and DEAE-dex first and to couple each macrocycle onto the SPION surface post nanoparticle synthesis.

The experimental steps are outlined in the following schematics:

Step 1 – SPION Synthesis

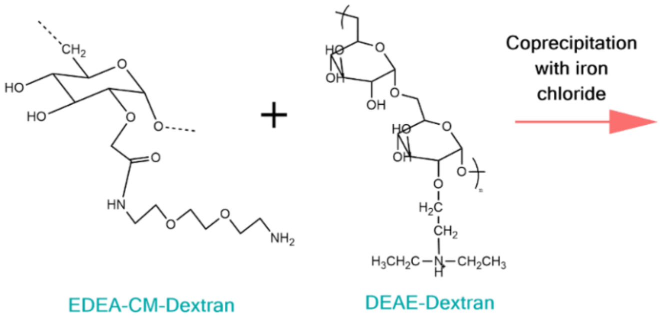

Step 2 – Macrocycle Coupling

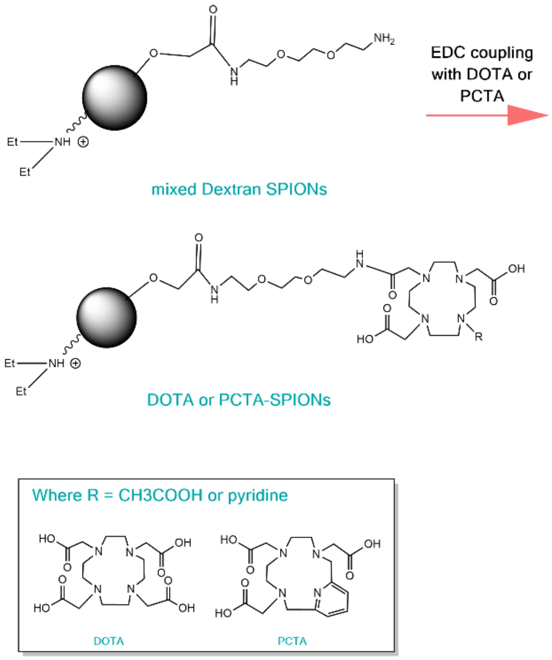

Figure 3.5: Synthesis of mixed dextran polymer-coated SPIONs via coprecipitation of dextran polymers and iron (II/III) chloride under basic conditions followed by EDC coupling of the macrocycles, DOTA or PCTA, to make DOTA-SPIONs or PCTA-SPIONs.

Macrocycle-bound SPIONs were then labelled with zirconium (Zr). In this chapter, non-radioactive zirconium chloride ($ZrCl_4$) was initially used as the Zr source to prove that the chemistry is viable.

Step 3 – Zirconium Labelling

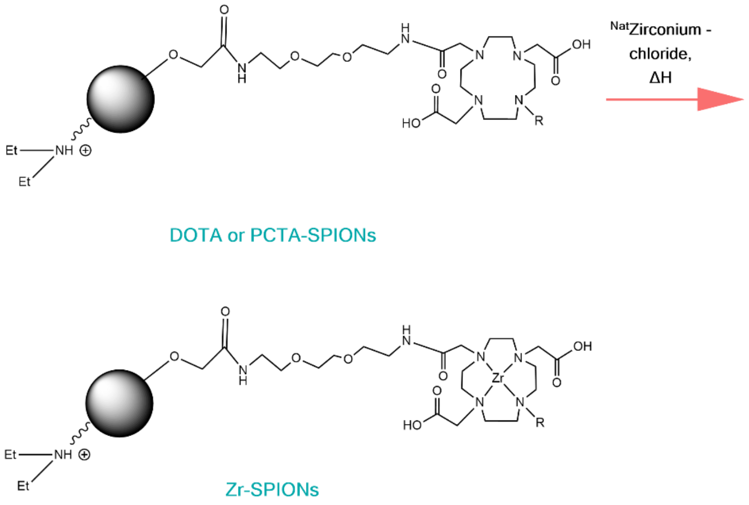

Figure 3.6: Schematic displaying the zirconium labelling of the macrocycle bound-SPIONs, DOTA-SPIONs or PCTA-SPIONs, to make Zr-DOTA-SPIONs or Zr-PCTA-SPIONs (Zr-SPIONs).

3.2 Methods

3.2.1 Synthesis and Characterisation of EDEA-CM-Dex

The polymer, CM-dex (MW 20,000), was functionalised with EDEA on its carboxymethyl terminus via amide bond formation in an EDC coupling reaction. A large excess of EDEA was used in this reaction to ensure there was maximum coverage of the linker on the dextran polymer. CM-dex (0.5 g, 1.26 mmol) was dissolved in 0.1 M MES buffer (50 ml). To this, EDC (2.2 ml, 12.6 mmol) was added followed by HOBt (1.70 g, 12.6 mmol). The mixture was stirred for 10 min at room temperature, then EDEA was added (2.2 ml, 12.6 mmol). The resulting reaction mixture was left to stir at room temperature for 4 h.

Following this, the white solution was dialysed overnight and then was freeze dried for 48 h to yield a fine, cream powder. EDEA-CM-dex was characterised by nuclear magnetic resonance (NMR), Fourier-transform infrared spectroscopy (FTIR) and elemental analysis (instruments described in Chapter 2).

3.2.2 Mixed Dextran SPION Synthesis and Characterisation

SPIONs were synthesised as described in Chapter 2. A ratio of 1:4 by mass of the two polymers, EDEA-CM-dex to DEAE-dex was used since this conferred the most colloidal stability out of the range of polymer ratios tested (this work is shown in Chapter 4). SPIONs were characterised by dynamic light scattering (DLS) and zeta potential measurements, thermogravimetric analysis (TGA), FTIR, powder x-ray diffraction (pXRD), transmission electron microscopy (TEM), superconducting quantum interference device (SQUID) measurements and elemental analysis. The instruments used for these measurements are described in Chapter 2.

3.2.3 Macrocycle Coupling to SPIONs

Following SPION synthesis and characterisation, the macrocycles, DOTA or PCTA, were coupled to the surface of the particles, shown schematically in Figure 3.5. DOTA (Macrocyclics Inc., USA) (10 mg, 0.025 mmol) or PCTA (CheMatech, FR) (10 mg, 0.026 mmol) were dissolved in MES buffer (500 µl, 0.1 M). To the macrocycle-MES mixture, EDC (13.5 µl, 0.08 mmol) and HOBt (10 mg, 0.08 mmol) were added and the resultant mixtures were adjusted to pH 5 and left to stir at room temperature for 10 min. Following this, 1 ml mixed dextran SPIONs (2 – 4 mg ml^{-1}, Fe basis) was added and the reaction mixture was left to stir overnight at room temperature on a rocker. Macrocycle-bound SPIONs were then dialysed overnight then washed three times with ultrapure water via spin filtration using 100K MWCO polyethersulfone (PES) membrane spin filters (ThermoFisher, Runcorn, UK). The particles were then characterised by DLS and zeta potential measurements, TGA, quadrupole time-of-flight mass spectrometry (q-TOF-MS) and elemental analysis. The instruments used for these measurements are described in Chapter 2.

3.2.4 Zirconium Labelling

Following purification, DOTA-SPIONs were labelled with non-radioactive zirconium chloride ($ZrCl_4$) (Figure 3.6). $ZrCl_4$ (5 mg, 0.02 mmol) was dissolved in HEPES buffer (20 mM, 1 ml) and 10 µl of the Zr-HEPES solution was added dropwise to 1 ml SPION (2 – 4 mg ml^{-1}, Fe basis). The mixture was reacted at room temperature overnight on a rocking incubator.

Following purification, PCTA-SPIONs were labelled with non-radioactive Zr. $ZrCl_4$ (5 mg, 0.02 mmol) was dissolved in oxalic acid (1 M, 1 ml). 10 µl of the Zr-oxalic acid solution was added to 1 ml SPION (2 – 4 mg Fe) and the pH of the SPION solution was adjusted to ~ 7 with 1 M Na_2CO_3. 100 µl TRIS buffer (100 mM, pH 7.4) was then added to the reaction mixture, which was left to shake at 37°C overnight.

Following both reactions, Zr-SPIONs were washed 3 times with ultrapure water via spin filtration. Zr-SPIONs were then characterised by DLS and zeta potential measurements and q-TOF-MS. Zr metal content was measured using inductively coupled plasma-optical emission spectrometry (ICP-OES), as described in Chapter 2 and the % binding was calculated using Equation 3.1 below.

$$\%\,Zr\ binding = \frac{amount\ of\ zirconium\ measured\ on\ particles}{total\ zirconium\ (on\ particles + in\ \ supernatant\ of washes)}\ x\ 100 \quad (\mathbf{3.1})$$

3.3 Results

3.3.1 Characterisation of EDEA-CM-dex

^{13}C NMR

To attach the Zr chelating macrocycles, DOTA or PCTA, onto the polymer, CM-dex, a small organic n-ethylene glycol (n-EG) linker, EDEA, was first attached onto the polymer. EDEA was joined to CM-dex in an EDC coupling reaction via amide bond formation on the carboxymethyl terminus of the polymer. ^{13}C NMR was performed on the functionalised polymer to confirm successful amide bond formation. The spectrum displayed an amide stretch at δC(400 MHz; D_2O) 154.89, 154.96, shown in Figure 3.7.

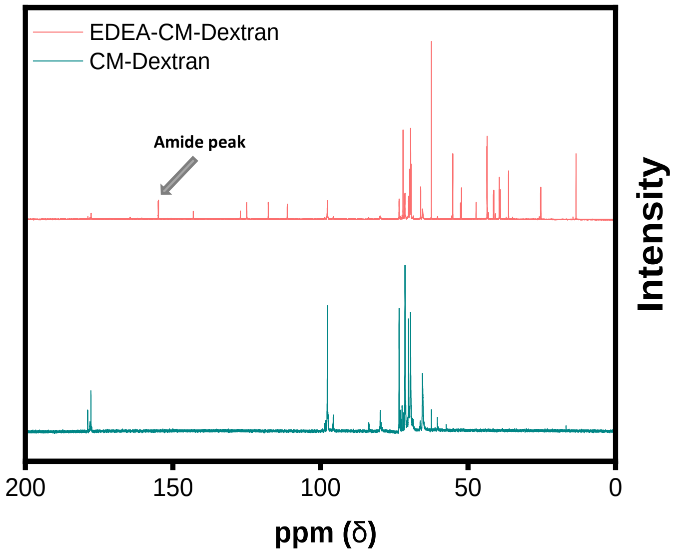

Figure 3.7: ^{13}C NMR spectra of EDEA-CM-dex and CM-dex. The top spectrum, which corresponds to EDEA-CM-dex, displays a new amide peak at δC(400 MHz; D_2O) 155.02, 154.94. This peak is not present in the starting material, CM-dex (bottom spectrum).

Elemental Analysis

Elemental analysis was also performed on the functionalised polymer as a complementary analytical technique (Table 3.1). In the starting material, no nitrogen content was measured, which is expected, since CM-dex contains only carbon, hydrogen and oxygen. In the functionalised polymer, nitrogen content increased to 10.75%, suggesting that the nitrogen containing EDEA had successfully coupled to the polymer.

Table 3.1: Elemental analysis results for EDEA-CM-dex, which show an increase in nitrogen content from the starting material, indicating the successful coupling of EDEA to CM-dex.

Sample	% Carbon	% Hydrogen	% Nitrogen
CM-dex	39.51	6.54	0.00
EDEA-CM-dex	45.06	7.66	10.75

FTIR

To further confirm amide bond formation, FTIR was employed, as seen in Figure 3.8. The spectrum for EDEA-CM-dex (top) demonstrated a large stretch at ν_{max}/cm^{-1} 1635, which corresponds to ν(CO) of CONH, and small shoulders at ν_{max}/cm^{-1} 1593 and ν_{max}/cm^{-1} 1456. These smaller peaks correspond to the symmetric and asymmetric ν(CO) stretches of the COOH groups[166] that have not reacted with EDEA and can be seen in the spectrum of the starting material, CM-dex (bottom). Since the CONH stretch is very intense in the FTIR spectrum of EDEA-CM-dex, this indicates that most CM-dex units have formed amide bonds and have been functionalised with EDEA, which should allow for significant macrocycle coverage.

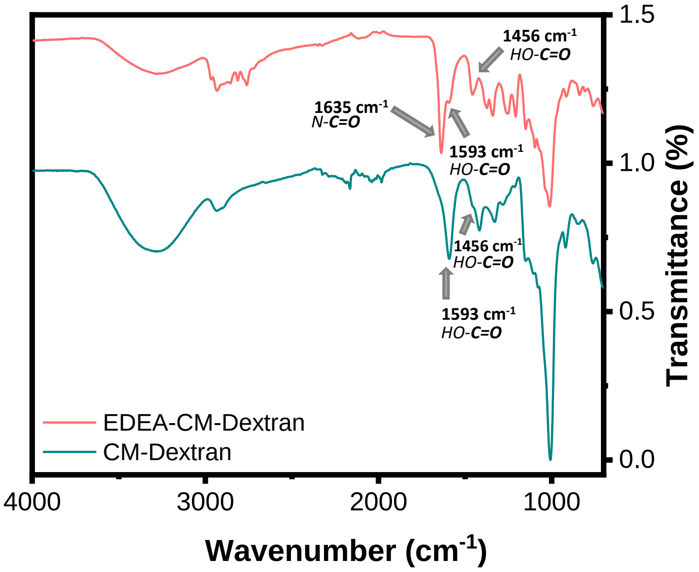

Figure 3.8: FTIR spectra of EDEA-CM-dex and CM-dex. EDEA-CM-dex (top spectrum) displays a large amide stretch at ν_{max}/cm^{-1} 1635, confirming the successful functionalisation of CM-dextran with the EDEA linker. There is also a small shoulder on the EDEA-CM-dex spectrum at ν_{max}/cm^{-1} 1593 which corresponds to the carbonyl stretch of the unfunctionalised COO$^-$ groups of CM-dex. This stretch is also present in the starting CM-dex spectrum (bottom).

3.3.2 Characterisation of Mixed Dextran SPIONs

Particle Size and Surface Charge

Polymer-coated nanoparticles were synthesised using a method that we have previously employed, a coprecipitation protocol similar to that described by Molday[143] and Paul[144]. The resultant SPIONs were colloidally stable with a Z-average of 107 ± 3 nm, as determined by DLS (Figure 3.9a). Zeta potential measurements were also performed on the particles to ensure that the mixed dextran SPIONs maintained a positive surface charge with the addition of the new polymer, EDEA-CM-dex. As mentioned previously, positive zeta potentials are favourable for labelling cells. Zeta potential measurements revealed the surface charge of mixed dextran SPIONs to be +16.6 ± 0.8 mV. (Figure 3.9b).

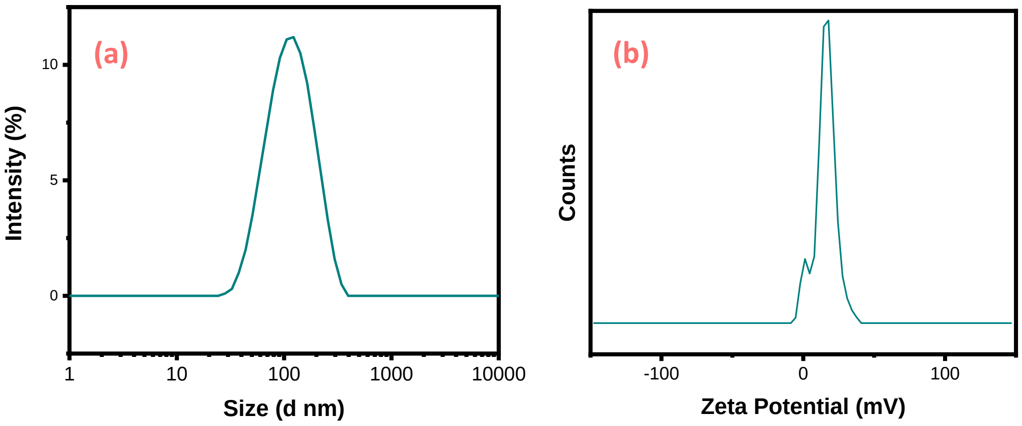

Figure 3.9: (a) Particle size distribution of mixed dextran SPIONs, which displays a population of particles of Z-average = 107 ± 3 nm and **(b)** zeta potential distribution of mixed dextran SPIONs, which displays a surface charge of +16.6 ± 0.8 mV.

FTIR

A 1:4 ratio of EDEA-CM-dex to DEAE-dex was selected to coat SPIONs, since this ratio provided the highest colloidal stability (see Chapter 4). FTIR was performed to confirm the presence of both polymers on the particle surface, which showed peaks corresponding to the ν(CO) stretch of EDEA-CM-dex at ν_{max}/cm^{-1} 1597 and the ν(NH) bond of DEAE-dex at ν_{max}/cm^{-1} 1642 (Figure 3.10). These peaks matched those associated with the free polymers[167]. This indicates that in the mixed dextran SPION synthesis, both polymers were anchored onto the particle surface.

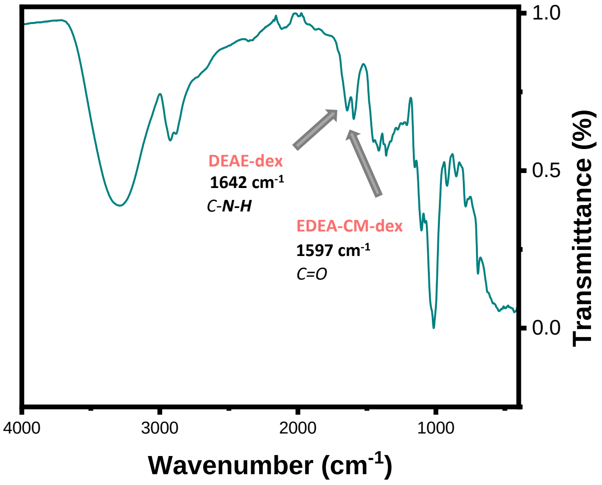

Figure 3.10: FTIR spectrum of mixed dextran SPIONs, which shows peaks corresponding to both EDEA-CM-dex and DEAE-dex at ν_{max}/cm^{-1} 1597 and ν_{max}/cm^{-1} 1642, respectively.

Magnetic Properties

Mixed dextran SPIONs were further characterised using TEM and SQUID. Figure 3.11a displays a TEM image of the particles, which shows their spherical morphology. The TEM micrograph also revealed that the particles have domains of less than 20 nm, suggesting their superparamagnetic properties. This was confirmed by SQUID measurements (Figure 3.11b), which showed that the particles had remnant magnetisation at room temperature, characteristic of their superparamagnetic behaviour.

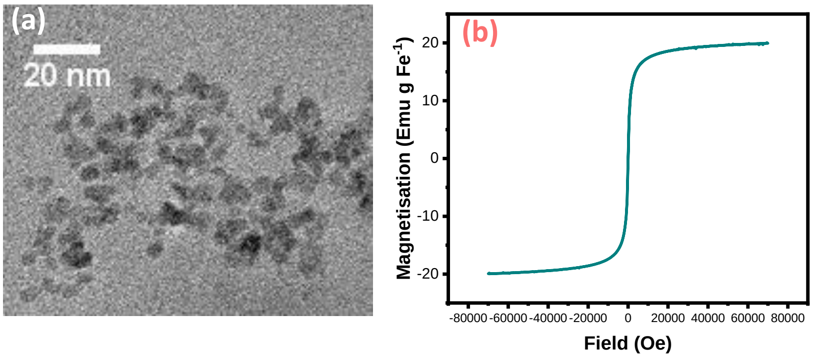

Figure 3.11: (a) TEM image of γ-Fe_2O_3 mixed dextran SPIONs showing that the particles are less than 20 nm and **(b)** magnetisation curve measured at 300K on freeze dried mixed dextran SPIONs.

pXRD

pXRD was performed on mixed dextran SPIONs to further study their domain size and, with applying the Scherrer equation (details in Chapter 2), the average core diameter was determined to be 10.1 ± 0.3 nm (Figure 3.12). Applying the same method, the domain size for DEAE-dex only SPIONs was calculated as 9.5 ± 0.8 nm, which is in close agreement with the size for mixed dextran SPIONs.

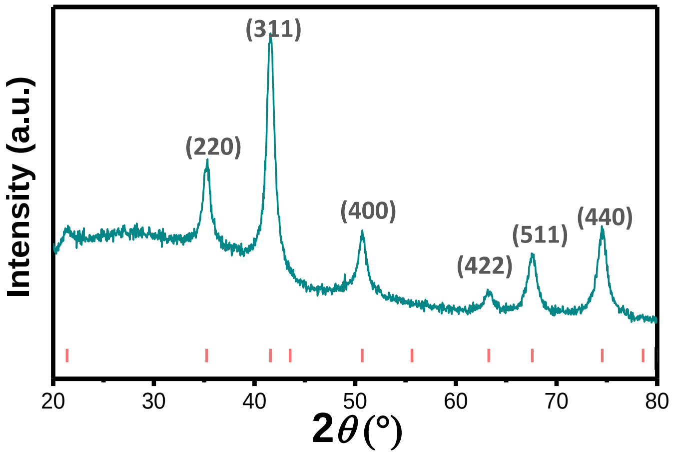

Figure 3.12: pXRD pattern for mixed dextran SPIONs which is in close agreement with the pattern displayed for DEAE-dex only SPIONs. Using the Scherrer equation, the core size of mixed dextran SPIONs was calculated as 10.1 ± 0.3 nm.

Characterisation of Macrocycle-Functionalised SPIONs

Elemental Analysis

Following successful mixed dextran SPION synthesis, PCTA or DOTA were coupled to the surface of the particles, to eventually serve as hosts for Zr chelation. An excess of each macrocycle was reacted to ensure a good coverage on the particle surfaces.

Elemental analysis was employed to determine the particles' composition after macrocycle modification (Table 3.2). In the mixed dextran SPION, there was a small amount of nitrogen present (2.24%), due to the tertiary amine terminus of DEAE-dex. The nitrogen content of DOTA-SPIONs increased to 8.65%, indicating the presence of the nitrogen rich, tetraazamacrocycle on the particle surface, whilst the nitrogen content of PCTA-SPIONs increased to 5.11%.

Table 3.2: Elemental analysis results for PCTA-SPIONs and DOTA-SPIONs that both show an increase in nitrogen content from the starting mixed dextran SPIONs, indicating the successful coupling of the nitrogen rich macrocycles, PCTA and DOTA.

Sample	% Carbon	% Hydrogen	% Nitrogen
Mixed Dextran SPIONs	27.92	5.17	2.24
PCTA-SPIONs	32.92	5.21	5.11
DOTA-SPIONs	34.73	6.00	8.65

q-TOF-MS

q-TOF-MS was performed on macrocycle-bound SPIONs to determine whether masses for PCTA or DOTA could be found in the samples. Figures 3.13a and 3.13b show mass spectra for mixed dextran-SPIONs, with no distinct peaks at *m/z* = 381.1 or 405.2, the masses of (PCTA-H)$^+$ or (DOTA-H)$^+$. Figure 3.13c shows the mass spectrum of PCTA-SPIONs, which contains peaks at *m/z* = 381.1 and 419.3, corresponding to (PCTA-H)$^+$ and (PCTA-K)$^+$, respectively, confirming that the macrocycle was present in the SPION sample. Figure 3.13d shows the mass spectrum of DOTA-SPIONs, displaying peaks at *m/z* = 405.2 and 443.0, which correspond to (DOTA-H)$^+$ and (DOTA-K)$^+$, respectively. q-TOF-MS confirmed that both macrocycles had coupled to SPIONs.

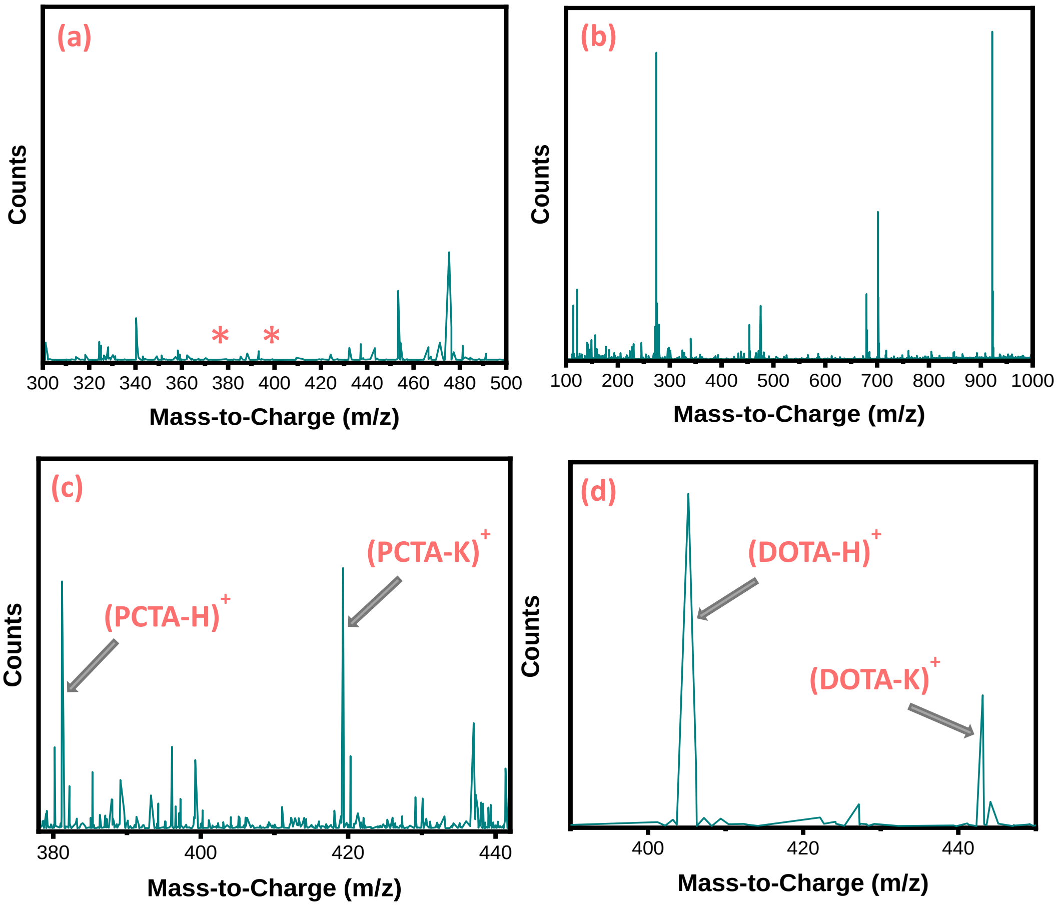

Figure 3.13: q-TOF-MS (positive ion mode) analysis of mixed dextran SPIONs, PCTA-SPIONs and DOTA-SPIONs. **(a)** q-TOF mass spectrum of mixed dextran SPIONs in the *m/z* range 300 – 500 showing no masses at *m/z* = 381.1 or 405.2, which would correspond to (PCTA-H)$^+$ or (DOTA-H)$^+$, respectively. **(b)** Full q-TOF mass spectrum of mixed dextran SPIONs from *m/z* = 100 to 1000. **(c)** Mass spectrum of PCTA-SPIONs in the *m/z* range = 380 – 440 showing a clear mass at *m/z* = 381.1 corresponding to (PCTA-H)$^+$ and a mass at *m/z* = 419.3

corresponding to PCTA associated with a potassium ion. **(d)** Mass spectrum of DOTA-SPIONs in the *m/z* range 390 – 450 showing a clear mass at *m/z* = 405.2 corresponding to $(DOTA\text{-}H)^+$ and a mass at *m/z* = 443.0 corresponding to DOTA associated with a potassium ion $(DOTA\text{-}K)^+$.

Particle Properties

DLS and zeta potential measurements were conducted on PCTA-SPIONs and DOTA-SPIONs at pH 7.0 to check for any changes in particle size and surface charge (Table 3.3, Figures A3.1 and A3.3). SPION particle size was found to increase from 107 ± 3 nm to 136 ± 5 nm upon reaction with DOTA, suggesting that the macrocycle was decorating the SPION surface. However, the size of PCTA-SPIONs did not change upon macrocycle coupling. Zeta potential measurements were also conducted on PCTA-SPIONs and DOTA-SPIONs to check for any changes to the particles. As expected, there were no significant changes in the surface charges upon macrocycle coupling, since DOTA and PCTA are neutral macrocycles.

TGA was also performed on macrocycle-bound SPIONs to check for changes in polymer (organic) content (Table 3.3, Figure A3.2). Polymer content was found to increase for both PCTA and DOTA-SPIONS compared to mixed dextran SPIONs, which have a polymer content of 66.6%. For PCTA-SPIONs, polymer content increased to 77.2%, whilst DOTA-SPIONs afforded an increase in polymer content to 80.2%. The increase in organic content for both particle types suggests the presence of coordinated macrocycle.

Table 3.3: Properties of the three types of SPIONs, including hydrodynamic diameter as measured by DLS, surface charge as measured by zeta potential measurements and polymer content, measured by TGA.

Sample	**Hydrodynamic *Z*-avg in 0.01 M NaCl (nm)**	**Zeta Potential in 0.01 M NaCl (mV)**	**Polymer Content by TGA (%)**
Mixed Dextran SPIONs	107 ± 3	+16.6 ± 0.8	66.6
PCTA-SPIONs	107 ± 1	+14.9 ± 2.5	77.2
DOTA-SPIONs	136 ± 5	+17.1 ± 0.3	80.2

Characterisation of Zirconium-Labelled SPIONs

q-TOF-MS

q-TOF-MS was performed on PCTA-SPIONs and DOTA-SPIONs to determine whether Zr had successfully labelled the particles. As seen for PCTA-SPIONs in Figure 3.14b, there is a mass at *m/z* = 470.3, which corresponds to $(Zr\text{-}PCTA\text{-}H)^+$. There is also a small peak at *m/z* = 492.3, which corresponds to $(Zr\text{-}PCTA\text{-}K)^+$. Neither of these peaks are present in mixed dextran-SPIONs (Figure 3.14a). Figure 3.14c displays DOTA-SPIONS following Zr labelling. There is a peak present at *m/z* = 405.2, which corresponds to the unlabelled macrocycle. However, there is no peak in the spectrum that corresponds to $(Zr\text{-}DOTA\text{-}H)^+$, which we would expect at around *m/z* = 491, suggesting that Zr had not labelled DOTA under these conditions. Figure 3.14d displays the q-TOF mass spectrum of free Zr-DOTA that had been synthesised by reflux in methanol. There is a clear peak here at *m/z* = 491.1, which corresponds to $(Zr\text{-}DOTA\text{-}H)^+$ that is not present for DOTA-SPIONs in Figure 3.14c. This suggests that harsher conditions than what were employed (see section 3.2.4) are required for Zr-DOTA labelling.

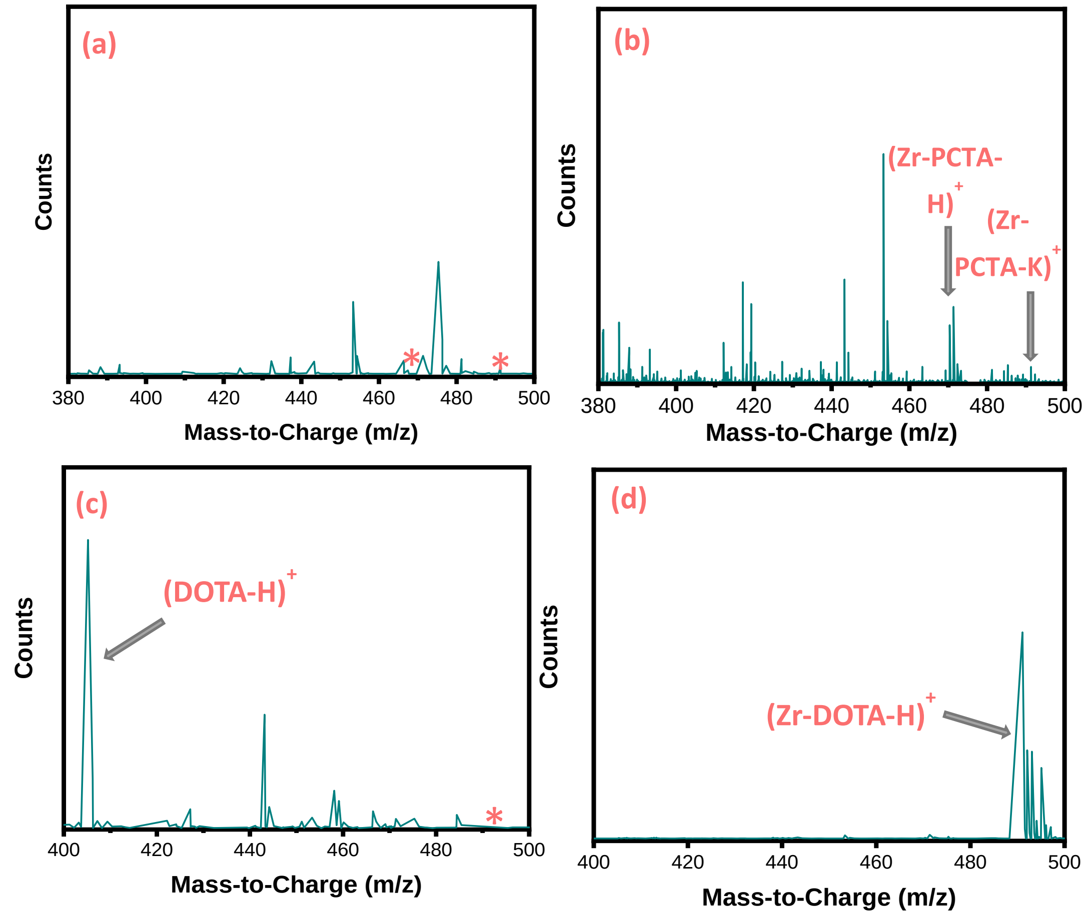

Figure 3.14: q-TOF-MS (positive ion mode) analysis of mixed dextran SPIONs, Zr-PCTA-SPIONs, DOTA-SPIONs and Zr-DOTA. **(a)** Mass spectrum of mixed dextran SPIONs in the *m/z* range 380 – 500 showing no masses at around *m/z* = 470 or 491, which would correspond to $(Zr\text{-}PCTA\text{-}H)^+$ or $(Zr\text{-}DOTA\text{-}H)^+$, respectively. **(b)** q-TOF mass spectrum of Zr-PCTA-SPIONs from *m/z* = 380 to 500 displaying peaks at *m/z* = 470.3 and 492.3 which correspond to $(Zr\text{-}PCTA\text{-}H)^+$ and $(Zr\text{-}PCTA\text{-}K)^+$. **(c)** q-TOF mass spectrum of DOTA-SPIONs in the *m/z* range 400 – 500, which shows no mass at *m/z* = 491, the mass of $(Zr\text{-}DOTA\text{-}H)^+$. **(d)** Mass spectrum of Zr-DOTA synthesised via reflux in methanol. There is a clear peak at *m/z* = 491.1, which corresponds to $(Zr\text{-}DOTA\text{-}H)^+$.

Particle Properties

DLS and zeta potential measurements were performed on the functionalised Zr-SPIONs to assess for changes in hydrodynamic diameter and surface charge (Table 3.4, Figures A3.1 and A3.3). Functionalising both DOTA-SPIONs and PCTA-SPIONs with Zr^{4+} afforded an increase in surface charge, suggesting the presence of the cationic metal on the particles. The surface charge of DOTA-SPIONs increased from +17.1 ± 0.3 mV to +19.1 ± 0.7 mV whilst the surface charge of PCTA-SPIONs increased from +14.9 ± 2.5 mV to +19.1 ± 0.7 mV. As well as this, the hydrodynamic diameters of the particles increased upon Zr labelling. The size of DOTA-SPIONs increased from 136 ± 5 nm to 141 ± 7 nm, whilst the size of PCTA-SPIONs increased from 107 ± 1 nm to 122 ± 2 nm.

Table 3.4: Properties of Zr-SPIONs, including hydrodynamic diameter as measured by DLS and surface charge as measured by zeta potential measurements.

Sample	Hydrodynamic Z-avg in 0.01 M NaCl (nm)	Zeta Potential in 0.01 M NaCl (mV)
Zr-PCTA-SPIONs	122 ± 2	+19.1 ± 0.7
Zr-DOTA-SPIONs	141 ± 7	+23.5 ± 4.8

ICP-OES

ICP-OES was employed to quantify Zr uptake into macrocycle-bound SPIONs (Figure 3.15), and this was compared to uptake in control SPIONs (mixed dextran only SPIONs that contain no macrocycle). Zr labelling reactions for PCTA-SPIONs and DOTA-SPIONs were performed using different methods, as described in section 2.3.4. In the PCTA reaction, which took place at 37°C, 64 ± 9% of the reacted Zr bound to PCTA-SPIONs whereas just 35 ± 1% of the reacted Zr bound to the control SPIONs. However, in the case of the DOTA reaction, which took place at 25°C, DOTA-SPIONs bound with 98 ± 3% of the reacted Zr, with close to the same amount (100 ± 0%) measured on control SPIONs, suggesting that a strong, non-specific interaction is occurring under these conditions.

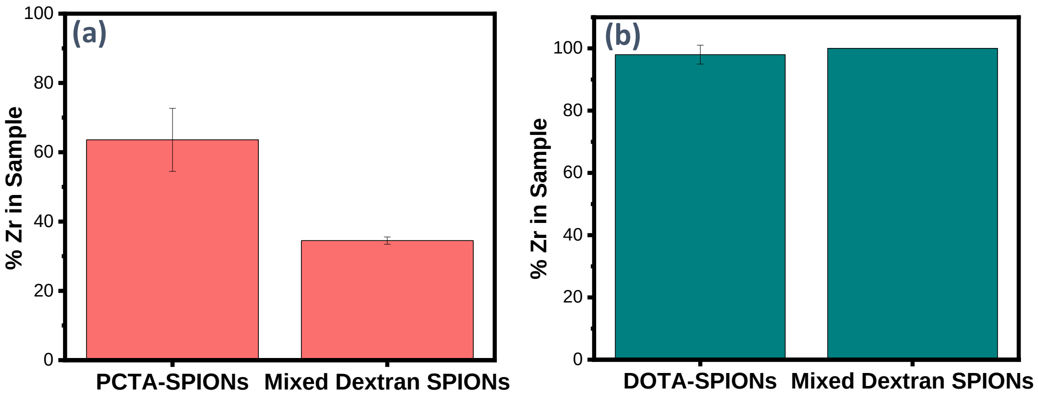

Figure 3.15: Percent binding of Zr to **(a)** PCTA-SPIONs and **(b)** DOTA-SPIONs, both compared to control SPIONs (mixed dextran SPIONs containing no macrocycle), as quantified by ICP-OES. Zr labelling reactions for PCTA-SPIONs and DOTA-SPIONs were performed using different methods, as described in section 3.2.4.

3.4 Discussion

CM-dex was selected to be functionalised with the n-ethylene glycol linker, EDEA, for eventual macrocycle coordination. CM-dex is a biocompatible polymer that is used to coat the commercially available Feraheme®[168]. A recent study in our group found that CM-dex-coated SPIONs displayed no toxicity to bone marrow derived macrophages (BMDMs); however, a negligible amount of the particles was taken up into the cells. DEAE-dex-coated SPIONs, on the other hand, were endocytosed up to 9 times more efficiently into BMDMs than CM-dex SPIONs and also displayed no significant cytotoxicity[125]. We propose that synthesising SPIONs with a mix of CM-dex and DEAE-dex would combine the benefits that both polymers offer, producing a SPION that shows no toxicity to macrophages and macrophage-like cells, but which also shows very efficient cellular uptake.

Mixed Dextran Nanoparticle Synthesis

The approach taken to functionalise CM-dex was a modified method based on that reported by Zaw Thin *et al*.[169], who showed that the commercially available, fluidMAG, another CM-dex-coated SPION, could be functionalised with EDEA followed by the DOTA macrocycle. We have employed this similar method to free CM-dex and found that the polymer successfully coupled to the amine group of EDEA to form EDEA-CM-dextran (EDEA-CM-dex) via the carboxymethyl terminus of the polymer, forming a strong amide bond. This was confirmed by ^{13}C NMR, which showed peaks in the amide region (Figure 3.7). Interestingly, each peak in the spectrum is split in two, which may be due to differences in the conformations of each individual glucose residue[170]. Since the amide peak at δC(400 MHz; D_2O) 155.02, 154.94 is also split, this provides strong evidence that the peak belongs to the amide functionalised polymer.

Elemental analysis and FTIR measurements were also employed to confirm successful amide bond formation (Table 3.1 and Figure 3.8). The nitrogen content increased from CM-dex to EDEA-CM-dex (0.00% to 10.75%), suggesting that the nitrogen containing EDEA had coupled to CM-dex. FTIR measurements revealed a large amide stretch in the polymer's spectrum (ν_{max}/cm^{-1} 1635), indicating successful coupling of EDEA. There are also some peaks at ν_{max}/cm^{-1} 3000, which are typical of primary amides. There is a small shoulder next to the amide stretch at ν_{max}/cm^{-1} 1593, which represents the symmetric stretch of the ν(CO) group of COO^-. This indicates that some units of the CM-dex polymer had not been functionalised with EDEA. This is noteworthy because DEAE-dex is polycationic so may interact with the free COO^- units on EDEA-CM-dex and cause aggregation during SPION synthesis. The amide stretch is very large in intensity compared to this minor COO^- peak; however, suggesting that most of the polymer is, in fact, functionalised with EDEA.

By adopting a coprecipitation approach, mixed dextran SPIONs were synthesised using a 4:1 ratio of DEAE-dex to EDEA-CM-dex and a 1:1 ratio of total polymer to total iron content. No aggregation or sedimentation was observed, despite the presence of some free COO^- units on EDEA-CM-dex. Evidence of this is shown in the DLS measurement (Figure 3.9a), which displays a monodisperse population of SPIONs with a Z-average of 107 ± 3 nm. No large aggregate populations were detected.

Pure DEAE-dex SPIONs, which we have synthesised in our group with a 1:1 ratio of polymer to total iron content, have a mean particle size of 47.3 nm[125], over half the size of the mixed dextran SPIONs. Recently, Mohamaddi *et al.* reported the synthesis of SPIONs comprising a double dextran/PEG polymer layer[171] which was achieved through the synthesis of dextran-coated SPIONs via coprecipitation, followed by the immobilisation of a second PEG layer around the dextran SPIONs. The researchers noted a marked increase in hydrodynamic diameter from their singly-coated dextran SPIONs to their doubly-coated PEG/dextran SPIONs. A potential explanation for the increase in particle size of DEAE-dex only to mixed DEAE/EDEA-CM-dex SPIONs is that a similar, double polymer coat comprising one DEAE-dex layer and a second EDEA-CM-dex layer forms during synthesis.

The effect of particle size on biocompatibility is less clear than the effect of zeta potential. Some research groups suggest that a particle size of around 50 nm is desired[172], possibly because more than one particle can fit in the vesicles formed from the endocytic pathways that are employed to internalise the particles. What is more important is the colloidal stability of SPIONs in physiological medium, which will be investigated in Chapter 4, since aggregated particles have different cellular uptake profiles to their colloidally stable counterparts, and can exhibit cytotoxic effects[173].

The core of mixed dextran SPIONs was also investigated using pXRD (Figure 3.12). Iron oxide nanoparticles are considered to be superparamagnetic if their core sizes are less than 20 nm[174]. The mixed dextran SPIONs were found to have a domain size of 10.1 ± 0.3 nm. pXRD measurements proved that modifying the particle's core-shell structure with the new EDEA-CM-dex polymer maintained the superparamagnetic properties of the SPIONs and this was confirmed with SQUID measurements. Pure DEAE-dex SPIONs have a core diameter of 9.5 ± 0.8 nm. Although not significant, there is a slight difference between the two particles' core sizes. This is expected since the different polymer systems which were used may have unique affinities for precipitating nanoparticles[175]. This means that the polymers will graft onto the iron oxide surface at different densities, resulting in varying core-shell sizes.

The pattern obtained for mixed dextran SPIONs matched that of the maghemite phase, which is anticipated, since the particles undergo an oxidation step in their synthesis, which converts magnetite to maghemite[146] (more details in Chapter 2). Magnetite and maghemite are both used for SPION cell labelling; however, we have used the maghemite phase for this study since it has been reported that magnetite can oxidise *in vivo*, releasing Fe^{2+} ions in the labelled cells. These ions can catalyse Fenton-type reactions, releasing toxic radicals and causing cytotoxicity[176]. There are also practical implications associated with the two phases of the SPIONs; magnetite particles must be kept under inert conditions to prevent oxidation to maghemite, which is not always feasible, hence why maghemite was used. We expect the maghemite particles to be stable, biocompatible and to show good MRI contrast, which will be examined in Chapters 4, 5 and 6.

Zeta potential measurements were performed on the mixed dextran SPIONs and the average zeta potential was measured as +16.6 ± 0.8 mV (Figure 3.9b). As mentioned previously, high surface charges, whether positive or negative, are highly beneficial to nanoparticles since they improve colloidal stability[156]. In our group, we have shown that SPIONs bearing high positive surface charges (> 15 mV) are taken up very efficiently into various cell types, including macrophages. This is thought to be due to an interaction of the polycationic shell of the SPIONs with the negatively charged cell membrane, which promotes absorptive endocytosis[138]. The high surface charge on the particles should allow for very effective cellular uptake into cells, which will maximise cell contrast in MRI.

FTIR was employed to determine whether both polymers were present on the SPION surface (Figure 3.10). Mixed dextran SPIONs produced stretching frequencies in their FTIR spectrum at ν_{max}/cm^{-1} 1642, which matches with the ν(NH) bond in free DEAE-dex's FTIR spectrum, stretching at ν_{max}/cm^{-1} 1640. The other stretching frequency observed in the FTIR spectrum of SPION at ν_{max}/cm^{-1} 1597 corresponds to the ν(CO) stretch of EDEA-CM and matches with the ν(CO) stretch of CM-dex (ν_{max}/cm^{-1} 1593). Infrared measurements proved that both polymers were present on the surface and because of this, SPIONs could be coupled with the macrocycles for Zr chelation.

Macrocycle Labelling

DOTA or PCTA were coupled to EDEA-CM-dex, which was anchored on the surface of SPIONs, via amide bond formation from the acetate arms of the macrocycles to the free amine group of the polymer. Elemental analysis was performed on DOTA-SPIONs, which revealed an increase in nitrogen content from 2.24% to 8.65%, which indicates the presence of the nitrogen-rich tetraazamacrocycle on the particle surface (Table 3.2). PCTA-SPIONs also displayed an increase in nitrogen content, from 2.24 to 5.11%. The increase in organic content observed in elemental analysis of macrocycle-bound SPIONs was matched in TGA measurements – PCTA-SPIONs afforded an increase in organic content from 66.2% to 77.2% while DOTA-SPIONs afforded an increase from 66.2% to 80.2%.

DLS measurements were performed on macrocycle-bound SPIONs to investigate for any changes in hydrodynamic diameter (Table 3.3). Particle size increased upon DOTA coordination, from 107 ± 3 nm to 136 ± 5 nm. This could be due to DOTA decorating the particle surface, which increases the overall hydrodynamic diameter of the particles. However, the same increase in hydrodynamic diameter was not observed for PCTA chelation; the particle size remained the same (107 ± 3 nm before coordination, 107 ± 1 after PCTA coordination).

q-TOF-MS was used to detect the macrocycles PCTA and DOTA in SPION samples (Figure 3.13). Measured in positive ion mode, the q-TOF mass spectrum of PCTA-SPIONs revealed masses at $m/z = 381.1$ corresponding to $(\text{PCTA-H})^+$ and at $m/z = 419.3$ corresponding to $(\text{PCTA-K})^+$. The q-TOF mass spectrum of DOTA-SPIONs also revealed masses corresponding to the DOTA macrocycle at $m/z = 405.2$ $(\text{DOTA-H})^+$ and $m/z = 443.0$ $(\text{DOTA-K})^+$.

Zirconium Chelation

Following incubation with Zr, q-TOF-MS was also performed on SPIONs to detect the masses corresponding to Zr-PCTA and Zr-DOTA. In Zr-DOTA-SPION samples, no masses were detected at around $m/z = 490$, which would correspond to $(\text{Zr-DOTA-H})^+$. DOTA-SPIONs were labelled with Zr based on a method described by Zaw Thin *et al.*[169], who used $InCl_3$ dissolved in 20 mM HEPES buffer to generate In-DOTA-SPIONs. This reaction occurred at 70°C and further studies into radiolabelling SPIONs have shown that at temperatures greater than 40°C, the chemisorption method, SRM, can occur[160]. To avoid this competing mechanism, and since SRM is not observed at room temperature[160], Zr labelling was performed at 25°C. Therefore, $ZrCl_4$ was dissolved in 20 mM HEPES and added to DOTA-SPIONs, then shaken overnight at room temperature.

DOTA is a macrocycle that offers pre-organised donor atoms that yield metal complexes of high thermodynamic stability. However, these reactions require elevated temperatures and extended reaction times, which suggest that there is a kinetic barrier to labelling DOTA with metal ions[177]. This was exemplified in a study by Tsionou *et al.*[178] who showed that in the radiosynthesis of ^{68}Ga-DOTA at pH 3.5 and with a ligand concentration of 5 µM, the radiochemical yield of ^{68}Ga-DOTA increased from 21% at 25°C to 90% at 90°C.

Using the free DOTA macrocycle, Zr-DOTA was synthesised following a method described by Pandya *et al*[98]. DOTA was labelled at 65°C using ZrAcAc dissolved in methanol as the Zr source. As seen in Figure 3.14d, there is a large peak in the q-TOF mass spectrum of Zr-DOTA at $m/z = 491.1$, which corresponds to $(\text{Zr-DOTA-H})^+$. Since this peak was not observed in the mass spectrum of DOTA-SPIONs after Zr labelling at room temperature, this suggests that DOTA does require high temperatures to form metal ion complexes.

Another chemical aspect that may hinder Zr-DOTA labelling is the instability of the Zr^{4+} ion in aqueous environments. Zr (IV) undergoes strong hydrolysis across the entire pH range due to the high polarity of the ion and the low solubility product of $Zr(OH)_4$. This means that all Zr^{4+} species have a strong tendency to hydrolyse *in aquo* and form colloidal species, which can prevent the diffusion of free Zr ions into macrocycles like DOTA[179]. Since the DOTA-SPION reaction with Zr (IV) chloride occurred in aqueous HEPES buffer, it is possible that the Zr cations formed colloidal species instead of remaining in solution and labelling the macrocycle.

Despite there being no masses corresponding to Zr-DOTA present in the mass spectrum of Zr-DOTA-SPION, a large amount of Zr was detected on DOTA-SPIONs by ICP-OES. The % binding of Zr was calculated by dividing the amount of Zr measured on DOTA-SPION particles after three ultrapure water washes by the sum of the measured amount of Zr in the supernatant of the washes and on DOTA-SPIONs and multiplying by 100. 98 ± 3.0% of the measured amount of Zr was found on the particles, with very little Zr content measured in the washes. The same amount of Zr (100 ± 0%) was measured on control particles, suggesting that there is a strong, non-specific interaction occurring between SPIONs and Zr. This could possibly be attributed to an electrostatic interaction between Zr^{4+} ions and any non-functionalised CM-dex chains on SPIONs that bear a negative charge, or due to the presence of colloidal Zr species in DOTA-SPION samples that are challenging to wash away.

Due to the difficulties encountered with the labelling of DOTA, the labelling of PCTA by Zr was performed at an elevated temperature of 37°C, in accordance with the method reported by Pandya *et al*[164]. Figure 3.14b displays the q-TOF mass spectrum of PCTA-SPIONs following Zr labelling. There is a large peak at *m/z* = 470.3, which corresponds to $(\text{Zr-PCTA-H})^+$, proving the successful labelling of PCTA by Zr^{4+} at physiological temperature. PCTA, along with macrocycles of similar chemical structure (NOTA, THP) have been investigated as radiometal chelators to overcome the limitations of DOTA. This is because they have been reported to conjugate radiometal ions at ambient temperatures due to the ligands providing rigid and kinetically inert metal-chelator complexes[164, 178]. In 2006, Tircsó *et al*. reported that the formation of Ln(PCTA) proceeds at least 10 times faster than corresponding Ln(DOTA) complexes, with the fast labelling kinetics of PCTA being attributed to the pre-organisation of the ligand that is offered by the pyridine ring[180]. This result was mirrored in studies by Ferreira *et al*., who demonstrated the superior binding kinetics of PCTA complexes with the radiometals ^{64}Cu and ^{68}Ga compared to their corresponding DOTA complexes[181, 182]. The ability of Zr^{4+} to label PCTA and not DOTA at reduced temperatures is likely due to the extra organisation and rigidity of the PCTA ligand provided by the pyridyl ring, that is not present in DOTA.

Another difference in the Zr-PCTA reaction vs the Zr-DOTA reaction is the medium in which the PCTA reaction took place. As mentioned above, the Zr^{4+} ion is extremely sensitive to hydrolysis, forming aggregated clusters or multinuclear hydroxylate complexes in aqueous media[183-185]. Thus, to mitigate the formation of such entities and promote the labelling of the PCTA macrocycle, $ZrCl_4$ dissolved in 1 M oxalic acid was used in the synthesis to form Zr-oxalate *in situ.* Oxalate ligands have been shown to stabilise the Zr^{4+} ion against hydrolysis and colloid formation over a wide pH range since these powerful didentate ligands can be thermodynamically and kinetically difficult to displace[186, 187]. Despite the high stability of Zr-oxalate, it was hypothesised that the now stabilised Zr^{4+} ions would preferentially bind to PCTA due to the chelate effect and the favourable increase in entropy that results from macrocycle binding[188]. It is likely that the heightened stability of the Zr species resulted in the successful binding of the metal to PCTA.

Despite the successful labelling of PCTA by Zr, there was still a large degree (35 ± 1%) of Zr binding to control SPIONs compared to the 64 ± 9% Zr binding that was measured for PCTA-SPIONs by ICP-OES (Figure 3.15). This suggests that there are some non-specific interactions occurring between the particles and Zr. A study by Kobayashi *et al.*[185] revealed that the speciation of Zr^{4+} ions in oxalic acid is of the chemical formula $[Zr(C_2O_4)_4]^{4-}$. The observed non-specific interaction between SPIONs and Zr may be due to a strong electrostatic interaction between $[Zr(C_2O_4)_4]^{4-}$ and the polycationic DEAE-dex chains that encapsulate SPIONs and provide a high positive zeta potential. With chelated Zr, we would expect a strong bond between the metal and PCTA-SPIONs. However, with non-specific, electrostatically bound Zr, the bond is most likely weaker and we might expect the metal to separate from SPIONs *in vivo* and deposit in undesired areas like the bones (see Chapter 5 for more details). Despite this, as long as there is still a significant amount of chelated Zr on SPIONs, even with some of the metal being bound non-specifically, the particles could still be very beneficial for use as cell tracking agents.

DLS and zeta potential measurements performed on Zr-SPIONs also suggest the presence of bound Zr^{4+}; both particles afforded an increase in particle size and surface charge upon Zr labelling. The surface charge of DOTA-SPIONs increased from +17.1 ± 0.3 mV before Zr labelling to +19.1 ± 0.7 mV after labelling. At the same time, PCTA-SPIONs increased from +14.9 ± 2.5 mV pre-labelling to +19.1 ± 0.7 mV post-labelling. There was an increase in particle size for DOTA-SPIONs (136 ± 5 nm) to Zr-DOTA-SPIONs (141 ± 7 nm) as well as for PCTA-SPIONs (107 ± 1 nm) to Zr-PCTA-SPIONs (122 ± 2 nm). This is likely due to the entrapment of non-specifically bound Zr ions on the Stern layer of the particles, which results in an expanded hydrodynamic diameter.

Although there are uncertainties in the modes of binding of Zr to PCTA and DOTA particles, there is clearly a large degree of Zr associated with SPIONs in both particle types, as observed from ICP-OES measurements. Thus, both particles types will be assessed for their respective stabilities *in vitro* and *in vivo* in the coming chapters.

3.5 Conclusions

In this chapter, a hybrid PET/MR imaging probe was successfully synthesised through the functionalisation of dextran-coated SPIONs with Zr. Non-radioactive Zr was used in these initial studies to prove that the chemistry is viable, which was achieved.

To produce the PET/MRI cell tracking probe, the polymer CM-dex was functionalised with a small n-ethylene glycol linker, EDEA, which would eventually be used to coordinate the Zr-chelating macrocycles, DOTA or PCTA. Mixed dextran SPIONs were synthesised from a mixture of DEAE-dex and EDEA-CM-dex via a coprecipitation method. The resultant SPIONs were colloidally stable and bore a high surface charge (> 15 mV).

DOTA or PCTA were coupled to the surface of SPIONs using an EDC-coupling approach to make DOTA-SPIONs or PCTA-SPIONs, which maintained the particles' colloidal stability. The macrocycles then served as hosts for Zr^{4+} chelation, which yielded the hybrid PET/MR imaging probes (Zr-SPIONs). In the next chapter, the colloidal stability and biocompatibility of the resultant Zr-SPION particles will be assessed.

Chapter 4

Optimising the *In Vitro* Colloidal Stability and Biocompatibility of Hybrid PET/MRI Cell Tracking Probes

4.1 Introduction

There are many factors that affect the *in vitro* properties of nanoparticle-based imaging agents, particularly for their use as cell labelling probes. Nanoparticles must display good colloidal stability in physiological media and resist aggregation. They must also be stable to enzymatic degradation and pH changes. As well as this, nanoparticles must show minimal toxicity and be taken up efficiently into cells so as to provide sufficient contrast and allow them to be detected *in vivo* using an appropriate imaging modality.

This chapter will review the factors that affect the *in vitro* properties of nanoparticles and assess the uptake, stability and toxicity of the hybrid PET/MR imaging probes, Zr-SPIONs, in RAW 264.7 cells.

Nanoparticle Colloidal Stability

SPIONs typically remain as a colloidal suspension in water, but are not always stable in cell culture medium or phosphate-buffered saline (PBS), causing the formation of aggregates or sediment due to the complexity of the physiological environment[189]. It is important for nanoparticles to have high colloidal stability *in vitro*, in order to retain their physicochemical properties.

A colloid consists of two phases, where one solid phase is dispersed in a second, often liquid, phase. Colloidal stability can be defined as the ability of nanoparticles to resist aggregation or sedimentation in their suspension media. When nanoparticles are dispersed in suspension media, they experience a range of attractive and repulsive forces, the balance of which determines the overall stability of the system[173].

The attractive forces that nanoparticles experience are governed by intermolecular forces known as van der Waals (vdWs) forces (Figure 4.1). These forces are due to dipole-dipole interactions in the interatomic bonds between nanoparticles, and result in destabilisation of the colloidal system[190].

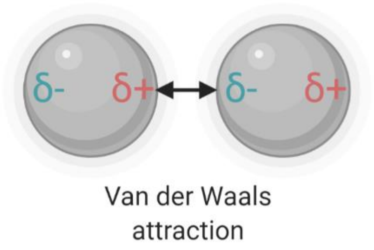

Figure 4.1: Permanent or induced dipoles in nanoparticles can result in van der Waals (vdWs) attractive forces between the particles, which can destabilise the colloidal system and result in aggregation.

As well as attractive forces between nanoparticles, there are also repulsive surface forces acting, which contribute to the overall stability of colloidal systems. Repulsions are caused by both the electrical double layer (EDL) and steric effects. In regard to the former type of repulsive forces, most nanoparticles carry a surface charge, which can be due to the adsorption of ions onto the particle surface, or the ionic association/dissociation of surface groups. This results in the formation of a cloud of oppositely charged ions surrounding the particles known as the Stern layer. The Stern layer then attracts more ions of opposite charges around it, which are collectively known as the diffuse layer. The overall combination of the Stern and diffuse layers is referred to as the EDL. When two EDLs formed from particles of like charge interact with one another, they repel. This, combined with steric repulsions between bulky molecules adsorbed on the nanoparticle surface, results in an overall stabilisation of colloidal systems (Figure 4.2 and Figure 4.3)[191].

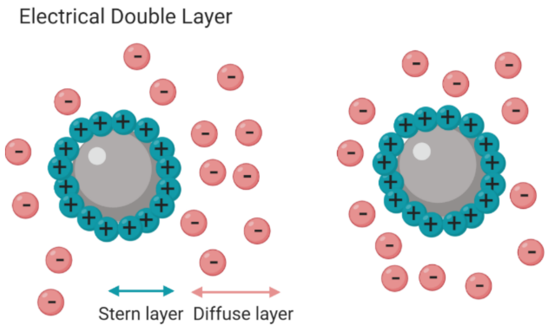

Figure 4.2: The electrical double layer (EDL) of two anionic nanoparticles. The particles' EDL is comprised of a cationic Stern layer and an anionic diffuse layer. The two diffuse layers repel one another, meaning that the nanoparticles cannot come close to one another and remain colloidally stable. Distances not to scale.

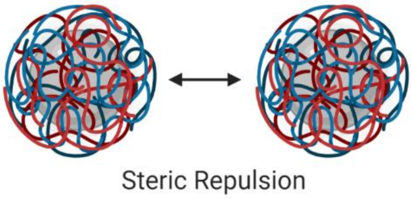

Figure 4.3: Steric repulsions between large molecules and polymers adsorbed on nanoparticle surfaces contribute to colloidal stability.

To predict the overall stability of a colloidal system, the Derjaguin-Landau-Verwey-Overbeek (DVLO) theory can be applied, which weighs up the overall effect of the attractive and repulsive forces acting on nanoparticles[192]. Classical DVLO theory predicts that nanoparticle systems of high surface charges will be colloidally stable and that systems stabilised by bulky polymers will also be colloidally stable, due to dominating steric repulsions.

Colloidal stability of nanoparticle-based imaging agents in aqueous medium is essential for effective transfer into physiological medium, and stability in serum-containing media is advantageous for use *in vivo*[100]. On top of this, aggregated nanoparticles exhibit different sizes and morphologies to their stable counterparts, which can result in different rates of diffusion and different interactions with cells, changing their uptake and toxicity profiles[193].

Nanoparticle Chemical Stability

As well as colloidal stability, the chemical stability of nanoparticles is also highly important for their function, particularly for SPIONs. This is because when nanoparticles are internalised inside cells, they typically become localised within endosomes and lysosomes, which have an acidic environment (pH 4.5 – 5.5). This can digest SPIONs, which are acid labile, resulting in loss of MRI signal[100]. In order to track cells over long periods of time (up to 4 weeks) following administration, nanoparticle-based imaging agents must show long-term stability *in vivo*. As well as signal loss, degraded SPIONs can leach iron ions into cells, resulting in toxicity, which is discussed further in the next section.

To improve chemical stability, SPIONs are often coated with biocompatible polymers, such as those described in Chapter 1, which shield the iron oxide core from the physiological environment and prevent degradation of the nanoparticles.

Nanoparticle Cytotoxicity

Most nanoparticles, when taken up into cells, display some degree of cytotoxicity, the effects of which are summarised in Figure 4.4. Nanoparticles can be bulky due to their various polymer coatings, and this can physically impact on the cytoskeleton of cells upon entry. The cytoskeleton is highly important in regulating cell morphology, cell division and interactions with the cellular environment. Disrupting the cytoskeleton could impact largely on the cell's biological function, resulting in toxicity[194-196].

Internalised nanoparticles can also impact on cell signalling pathways, interfering with intracellular signalling cascades and transcription/translation machinery. This can affect the physiological function of cells as well as their differentiation, phenotype and proliferation potential[197-199].

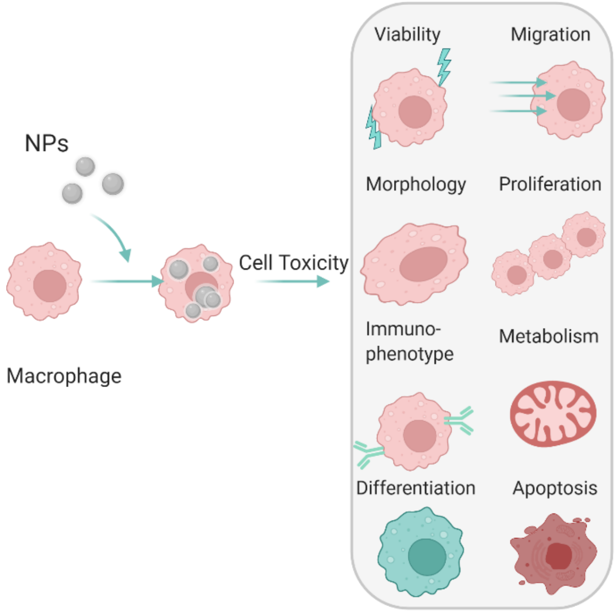

Figure 4.4: When nanoparticles are taken up into cells, they can impact on the cell's viability, migration, morphology, proliferation capabilities, immunophenotype, metabolism, differentiation and rate of apoptosis, which can all lead to cytotoxicity.

The most common cause of cytotoxicity is oxidative stress due to the production of reactive oxygen species (ROS)[200]. As mentioned previously, when SPIONs and other common synthetic nanoparticles are internalised into cells, they tend to accumulate in lysosomes or late endosomes[201, 202]. It is believed that the acidic environment of these cytoplasmic vesicles can cause the dissolution of SPIONs over time, which can lead to the leaching of iron ions (Fe^{2+} and Fe^{3+}) from the particles[112].

Mitochondria are continuously producing the ROS, superoxide ($\bullet O_2^-$) and hydrogen peroxide (H_2O_2)[203]. When catalysed by iron ions, $\bullet O_2^-$ can react with H_2O_2 to form the extremely reactive radical, •OH, in a Haber-Weiss type reaction (Equation 4.1). This is achieved when Fe^{3+} ions (ferric iron) are reduced to Fe^{2+} (ferrous ion) by the super oxide species, $\bullet O_2^-$ (Equation 4.2). Fe^{2+} can then be oxidised back to Fe^{3+} by H_2O_2, forming $^{\bullet}OH$ in a Fenton type reaction (Equation 4.3)[203]. This is summarised in Figure 4.5.

$$\cdot O_2^- + H_2O_2 \xrightarrow[Fe^{3+}/\,Fe^{2+}]{} \cdot OH + OH^- + O_2 \qquad \textbf{(4.1)}$$

$$Fe^{3+} + \cdot O_2^- \longrightarrow Fe^{2+} + O_2 \qquad \textbf{(4.2)}$$

$$Fe^{2+} + H_2O_2 \longrightarrow Fe^{3+} + \cdot OH + OH^- \qquad \textbf{(4.3)}$$

Figure 4.5: Equations detailing the iron catalysed reaction of superoxide, $\bullet O_2$-, with hydrogen peroxide, H_2O_2, to form the highly reactive radical, •OH.

A consequence of ROS production is increased oxidation of proteins, nucleic acids and lipids. Increased protein oxidation can lead to denaturation and thus proteolysis, while DNA base oxidation can lead to more serious genetic mutations, which can cause carcinogenesis. The lipid bilayer of cell membranes is comprised of polyunsaturated fatty acids, the double bonds of which are susceptible to attack by the ROS, $^{\bullet}OH$, which can impair the lipid structure. Once one double bond is attacked, a free radical chain reaction can cascade across the cell membrane, breaking down the lipid bilayer and damaging transport and ion channels[203].

Studies have shown that the addition of antioxidants to cell culture medium can reduce SPION cytotoxicity[204] and the addition of the iron chelating compound, deferrioxamine (DFO), to medium has been shown to reduce the toxic effects of SPIONs in mesenchymal stromal cells (MSCs)[205]. This reinforces the idea that Fe^{3+}/Fe^{2+} induced oxidative stress is a major contributing factor in SPION cellular toxicity.

Cellular Uptake of Nanoparticles

It is important that enough nanoparticle-based imaging agent enters a cell to produce a detectable signal in its respective imaging system. However, despite the small size of nanoparticles, they tend not to cross the cell membrane and are typically taken up by endocytosis[206, 207]. Endocytosis is a form of active transport that involves the engulfing of a material within the cell membrane to form a membrane-bound vesicle called an endosome[208]. Endocytosis can be subcategorised into phagocytosis, which engulfs large materials and debris, and pinocytosis, which involves the uptake of materials in the nano-range. Due to the size of nanoparticles, the latter pathway is mostly employed in their uptake[209, 210].

During pinocytosis, nanoparticles are taken into small vesicles called pinosomes, which then fuse with lysosomes, the pH of which leads to the degradation of the vesicle content[211, 212]. Pinocytosis can be broken down into four subsets: clathrin-mediated endocytosis, caveolae-mediated endocytosis, clathrin- and caveolae-independent endocytosis and macropinocytosis[213, 214].

Clathrin-mediated endocytosis is a receptor-mediated form of pinocytosis, while caveolae-mediated endocytosis involves invagination of particles within the caveolae (‘little caves’) of cell membranes of certain cell types[215-217]. Clathrin and caveolae-independent endocytosis is an uptake pathway that occurs in cells that lack clathrin and caveolae, while macropinocytosis is a pathway that engulfs micron sized particles, forming a micron sized vesicle called a macropinosome[209, 218]. These pathways are summarised and shown schematically in Figure 4.6.

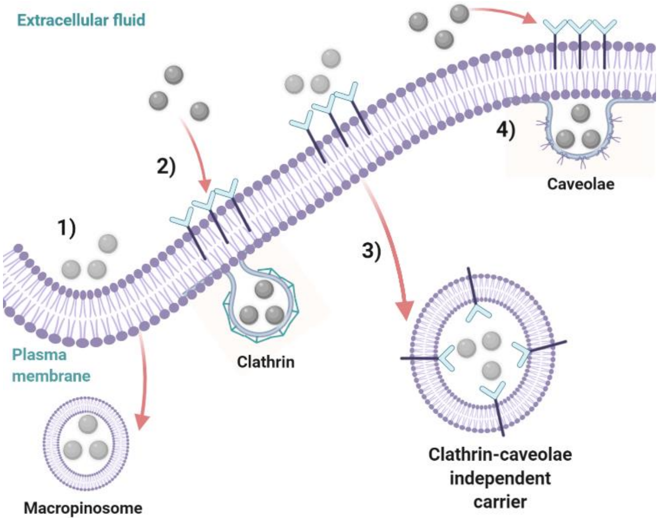

Figure 4.6: The four main pathways of pinocytosis that nanoparticles can be involved in. Pathway 1 is macropinocytosis, which allows for the uptake of larger particles. 2 and 4 are clathrin-mediated and caveolae-mediated endocytosis, respectively. 3 is clathrin-caveolae-independent endocytosis.

The size of nanoparticles can be important in determining their efficiency of uptake, as well as the uptake pathway[219]. In one particular study, particles over the size of 250 nm were found to be taken up via a macropinocytosis pathway, while nanoparticles in the range of 120 – 150 nm were found to be internalised by caveolae-mediated endocytosis[220]. In another study, nanoparticles in the range of 30 – 50 nm were internalised by clathrin-mediated endocytosis[221]. This last pathway has been found to increase the efficiency of particle uptake by more than a hundredfold, showing the importance of size in nanoparticle design[222]. It is worth mentioning that despite these findings, the mechanisms of nanoparticle-cellular uptake can be difficult to elucidate since it is almost impossible to inhibit all of the other potential uptake pathways while studying only one.

Surface charge is another important factor when considering the efficiency and pathway of nanoparticle-cellular uptake. Positively charged nanoparticles are taken up more effectively into cells than neutral or negatively charged particles[223, 224]. This is possibly due to an interaction with the negatively charged cell membrane. A study has shown that positively charged nanoparticles are taken up into cells by macropinocytosis, whilst negatively charged nanoparticles are internalised by clathrin-/caveolae independent endocytosis pathways[225]. In this report published by Dausend et *al*., the cationic particles had a diameter of 113 nm, small enough to be taken up by pathways other than macropinocytosis. However, the clathrin-mediated pathways showed very little input in the uptake of these nanoparticles, suggesting a greater influence of charge than size on the pathway of nanoparticle-cellular uptake.

Nanoparticle-Protein Corona Formation

When nanoparticles are placed in biological fluid, a 'protein corona' is formed spontaneously (Figure 4.7). This is where highly abundant proteins, such as serum albumin and globulins, adsorb onto the particle surface. These are eventually replaced by more specific proteins, which have a higher affinity for the polymer system, an effect known as the Vroman effect[226, 227]. As well as proteins, biological fluid, particularly cell culture medium, contains a number of biomolecules that are essential for cellular growth and survival. These include amino acids and ionic salts, which can also be incorporated into the corona. Protein coronas can have a variety of effects on nanoparticles, ranging from affecting cellular uptake to influencing particle stability[228].

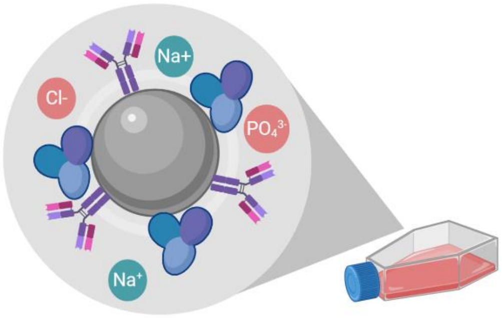

Figure 4.7: Schematic representation of the protein corona formed when nanoparticles are placed into cell culture medium. Nanoparticles become enveloped by proteins such as globulins and albumin, as well as ionic salts.

It is well documented that nanoparticles bearing high surface charges can improve cellular uptake; however, the mechanism behind this is not well understood. It is proposed that due to these high surface charges, particularly positive ones, more specific proteins can be incorporated into the corona, which can lead to enhanced uptake. Most studies suggest it is the protein corona that cells recognise and respond to upon uptake, as opposed to the charged polymer itself[100].

In contrast to this, some researchers have found that protein coronas can actually lead to decreased cellular uptake. Cheng *et al*. discovered that when placed into cell culture medium, gold nanoparticles (AuNPs) were immediately enveloped in a corona formed from serum proteins[229]. The presence of this corona prevented direct adhesion of particles onto proteins in the cell membrane, reducing uptake in RAW 264.7 cells.

Generally, when nanoparticles are placed in cell culture medium, serum helps to stabilise the particles and prevent aggregation[173]. However, there are some reports of nanoparticle systems becoming destabilised in culture medium, forming aggregates and eventually sedimenting. Culture medium mostly has a higher ionic strength than water due to the higher concentration of ionic salts. These ions are strongly attracted to the particles, forming a smaller ionic cloud in the diffuse layer and compressing the EDL, which brings the particles closer together. This allows the attractive vdWs forces to dominate, causing aggregation[230, 231].

Electrostatically stabilised nanoparticles are generally very unstable in culture medium and require bulky coatings to provide steric stability. Despite this, sterically stabilised nanoparticles can also be subject to destabilisation in cell culture conditions. This is due to the competitive adsorption of proteins and large biomolecules onto the surface of nanoparticles, which exchanges with, or removes the nanoparticle's protective coating. This causes a reduction in steric repulsive forces between particles and an increase in attractive vdWs forces, which results in aggregation[232]. As well as this, the adsorbed molecules can act as a physical bridge between particles, and add to the vdWs attractive forces, also resulting in aggregation[173, 228].

The extent at which stabilising polymers are exchanged/removed depends largely on the nature and robustness of the coat[232]. Nanoparticles coated with hydrophilic polymers, such as naturally derived dextrans and synthetic PEGs, have demonstrated a marked reduction in protein adsorption, resulting in greater steric stabilisation[233]. As mentioned in Chapter 1, such polymers have also been functionalised to carry charge, adding electrostatic repulsive forces to the already present steric forces and augmenting stabilisation, an effect known as electrosteric stabilisation. It is also theorised that since the protein corona contributes to the overall hydrodynamic diameter of the nanoparticle system, this can increase the steric bulk surrounding the particle, increasing the repulsive forces between nanoparticle-protein coronas in solution and bringing about stabilisation[234]. Nanoparticle-protein corona formation is a natural phenomenon that cannot be avoided in protein-containing media, but if particles are designed cleverly and are carefully monitored under *in vitro* conditions, the protein corona can improve the biological performance of the particles.

Experimental Plan

The aims of the work in this chapter were to study the colloidal stability and biocompatibility of the hybrid PET/MR imaging probes, Zr-SPIONs, which were synthesised in Chapter 3. To achieve the aims, a library of mixed dextran SPIONs were synthesised with varying ratios of the polymers, EDEA-CM-dextran (EDEA-CM-dex) to DEAE-dextran (DEAE-dex) (2:1,1:1, 1:2, 1:4). The colloidal stabilities of each of the hybrid particles in the library were then screened using serum incubation assays, to determine the optimum dextran polymer ratio. Once established, the cellular uptake and toxicity profiles of the hybrid PET/MRI probes, Zr-SPIONs, were then assessed in RAW 264.7 cells. The aims are summarised in Figure 4.8.

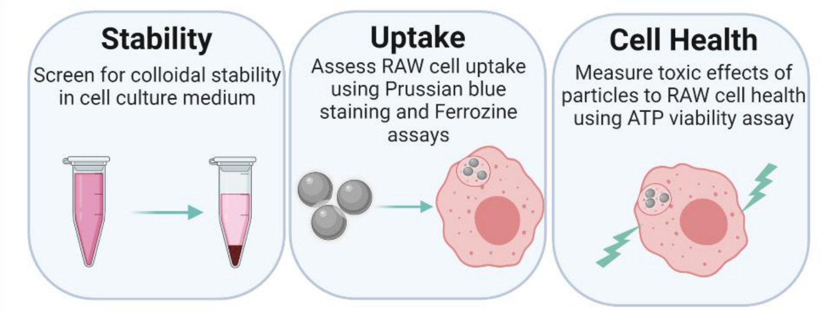

Figure 4.8: Assessing the biocompatibility of SPIONs and Zr-SPIONs. Particles were assessed for colloidal stability using serum incubation assays, then their toxicity and uptake profiles were determined in RAW 264.7 cells, a macrophage-like cell line, using various assays.

4.2 Methods

4.2.1 Stability Screening

To assess the colloidal stability of mixed dextran SPIONs in cell culture medium, particles were immersed in phenol red-free Dulbecco's Modified Eagle Medium (DMEM) at a concentration of 50 µg ml^{-1} (Fe basis) containing either 10% or 0% foetal bovine serum (FBS). The serum concentration used for these studies was selected since the cells used in this work were cultured in 10% FBS. The suspensions were incubated at 37 °C for a maximum of 24 h in a plastic cuvette.

4.2.2 Prussian Blue Staining Assay

The Prussian blue staining assay was employed to qualitatively assess iron uptake in RAW 264.7 cells (culture details described in Chapter 2). 10^{5} RAW cells were seeded overnight in a 24-well plate, to allow for growth and attachment. The cells were then dosed with increasing concentrations of SPION (mixed dextran SPIONs or Zr-SPIONs) (0 – 50 µg ml^{-1}, Fe-basis) containing DMEM (+ 10% FBS) for a maximum of 24 h. Cells were washed with phosphate-buffered saline (PBS) to remove excess SPION. Cells were then fixed with 4% paraformaldehyde (PFA) and were stained with a Prussian blue Iron Stain Kit (Sigma Aldrich, Dorset, UK), according to the manufacturer's instructions. Images were captured using a Leica DM IL inverted microscope attached to a DFC420C camera.

4.2.3 Viability (ATP) Assay

To assess the effects of the SPION particles on cell viability, an adenosine triphosphate (ATP) assay was employed. Here, 4 × 10^{4} RAW cells were seeded in a 96-well plate overnight to allow for growth and attachment. Following this, the culture medium was removed from each well and replaced with SPION containing DMEM (+10% FBS) up to a concentration of 50 µg ml^{-1} (Fe-basis). RAWs were dosed for 24 h. Following labelling, the medium was aspirated, replaced with fresh medium and 20 µl CellTiter-Glo Luminescent Cell Viability reagent (Promega, Hampshire, UK) was added to each well. A luminescent protocol in line with the manufacturer's instructions was then applied to quantify levels of cellular ATP using a FLUOstar® Omega microplate reader (BMG LABTECH, Ortenberg, DE).

4.2.4 Ferrozine Assay

To quantify iron uptake in RAW cells, a modified method of a previously reported ferrozine assay was employed[235]. Briefly, 10^5 RAWs were seeded overnight in a 24-well plate to allow for growth and attachment. The cells were then dosed with increasing concentrations of Zr-SPION (0 – 50 µg ml^{-1}, Fe-basis) for 24 h. Following labelling, the medium was aspirated, and cells were washed, scraped, counted then transferred to microfuge tubes. The cells were then pelleted and lysed in 1.2 M HCl (50 µl) at 80°C for 2 h. Upon cooling, lysates were diluted 1:1 with distilled water and then 30 µl ferrozine reagent was added (5 M ammonium acetate, 2 M ascorbic acid, 6.5 M 3-(2-pyridyl)-5,6-diphenyl-1,2,4-triazine, 15 M neocuproine). Colour was allowed to develop for 30 min. Absorbance was then measured at 570 nm on a FLUOstar® Omega microplate reader (BMG LABTECH, Ortenberg, DE) and was compared to a standard curve prepared with an iron standard to quantify iron content per cell.

4.3 Results

4.3.1 Improving the Colloidal Stability of Mixed Dextran SPIONs

Stability Screening

Prior to labelling SPIONs with the Zr-chelating macrocycles, the mass-to-mass ratio of the particles' polymer coatings, EDEA-CM-dex and DEAE-dex, was varied to determine whether this influenced the colloidal stability of the particles. A library of SPIONs was synthesised by varying the polymer ratios while keeping the mass-to-mass ratio of total polymer to total iron salt at 1:1. Dynamic light scattering (DLS) and zeta potential measurements were performed on the particle library in aqueous medium, which resulted in varying hydrodynamic diameters and zeta potentials (Figures A4.1 and A4.2). The properties of the library are summarised in Table 4.1.

Table 4.1: Properties of the library of synthesised mixed dextran SPIONs and their respective colloidal stabilities in serum-supplemented (10% FBS-containing) and serum-depleted DMEM after 4 and 24 h. All particles sedimented instantly when immersed in serum-depleted DMEM. *2:1 SPIONs were unstable in aqueous medium thus were not utilised in bioassays.

EDEA-CM-dex: DEAE-dex Ratio	Hydrodynamic Diameter (nm)	Zeta Potential (mV)	Stable in 0% serum after 4 h	Stable in 10% serum after 4 h	Stable in 10 % serum after 24 h
1:4	107 ± 3	+16.6 ± 0.8	x	✓	✓
1:2	135 ± 3	+26.8 ± 0.7	x	x	x
1:1	100 ± 1	+27.6 ± 1.0	x	✓	x
2:1*	81 ± 1	+23.9 ± 0.7	x	x	x

The library of particles was tested for colloidal stability in DMEM supplemented with 10% FBS or FBS-depleted DMEM. The particles were dispersed in each media type at a concentration of 50 µg ml^{-1} and were incubated for 4 and 24 h. The extent of aggregation was assessed visually. As seen in Figure 4.9, each particle in the library sedimented instantly in serum-depleted medium. In serum-supplemented medium, only the 1:1 and the 1:4 particles remained as a colloidal suspension after 4 h. The particles were incubated for a further 20 h and it was found that only the 1:4 EDEA-CM-dex: DEAE-dex particles remained colloidally stable. Therefore, this ratio was selected and the results from hereon are from 1:4 EDEA-CM-dex: DEAE-dex particles.

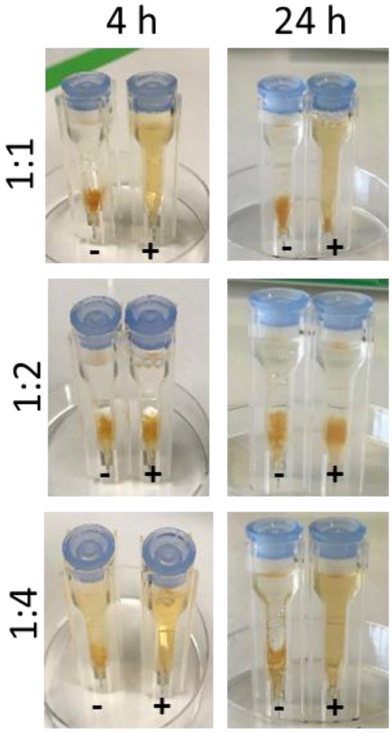

Figure 4.9: Particles of varying polymer ratios were incubated in serum-depleted (-) and serum-supplemented (+ 10% FBS) cell culture medium for 4 and 24 h. All particles aggregated in serum-depleted medium after both time points. Only the 1:1 and 1:4 particles remained colloidally stable in serum-containing medium after 4 h and only the 1:4 particles remained colloidally stable in serum-containing (10% FBS) medium after 24 h.

Prussian Blue Staining Assay

To assess the *in vitro* behaviour of mixed dextran SPIONs synthesised with a 1:4 ratio of EDEA-CM-dex to DEAE-dex, an initial Prussian blue (PB) staining assay was performed on the particles in RAW cells. This was done to assess SPION uptake by RAWs, but the assay also provided an insight into the colloidal stability of the particles under cell labelling conditions.

RAWs were dosed with mixed dextran SPIONs at a concentration of 50 µg ml^{-1} since this was the highest concentration used in the stability screening. As seen in Figure 4.10, RAWs appeared healthy following the 24 h dosing period and displayed a good uptake of mixed dextran SPIONs into cells, with minimal extracellular aggregates, as indicated by the blue pigment. Blue staining was observed in all cells, with some stained more intensely than others.

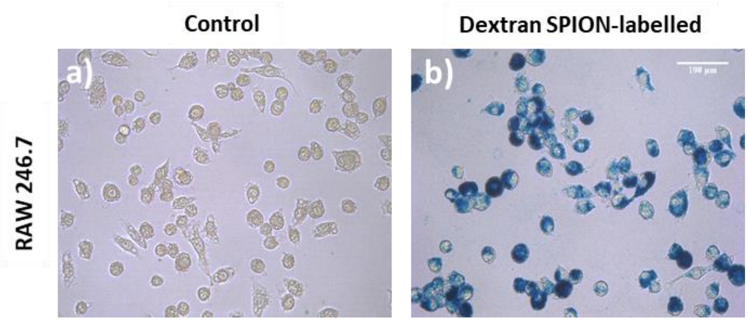

Figure 4.10: Prussian blue staining of RAW 264.7 cells after 24 h labelling with **(a)** just media (no SPIONs) and **(b)** mixed dextran SPIONs at a concentration of 50 µg ml^{-1}. Scale bar = 100 µm.

4.3.2 Cellular Uptake of Zr-SPIONs in RAW 264.7 Cells

Once the optimum EDEA-CM: DEAE-dex ratio of SPIONs had been established, the particles were labelled with the macrocycles, PCTA or DOTA, then were chelated with Zr, as described in Chapter 3. The properties of the Zr-SPION particles are shown in Table 4.2 and the particle size distributions of Zr-SPIONs are displayed in Figure 4.11 Both particle types were colloidally stable in serum-supplemented media.

Table 4.2: Hydrodynamic diameter (particle size) and zeta potential (surface charge) values for Zr-PCTA-SPIONs and Zr-DOTA-SPIONs.

Sample	Hydrodynamic Z-avg in 0.01 M NaCl (nm)	Zeta Potential in 0.01 M NaCl (mV)
Zr-PCTA-SPIONs	122 ± 2	+19.1 ± 0.7
Zr-DOTA-SPIONs	141 ± 7	+23.5 ± 4.8

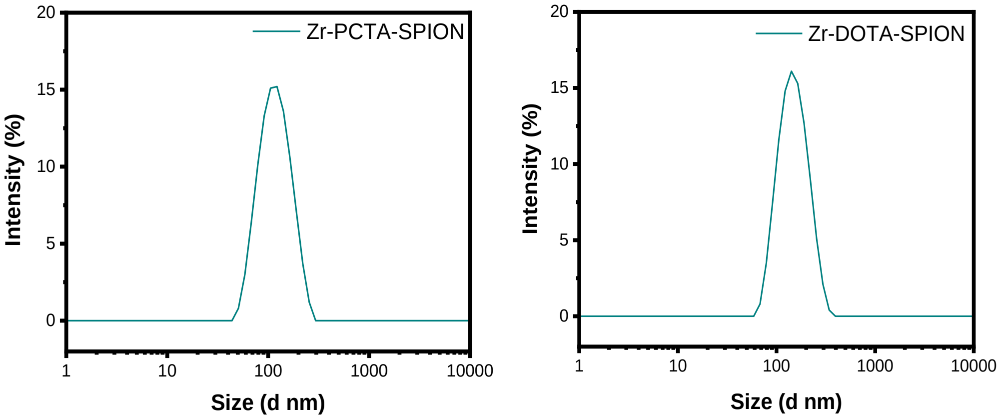

Figure 4.11: Particle size distribution of **(a)** Zr-PCTA-SPIONs and **(b)** Zr-DOTA-SPIONs.

Prussian Blue Staining Assay

The biocompatibility of the particles, Zr-DOTA-SPIONs and Zr-PCTA-SPIONs, were next assessed. The PB assay was first performed to evaluate particle uptake into RAW cells, as well as to gauge any further aggregation due to the cellular environment (Figure 4.12).

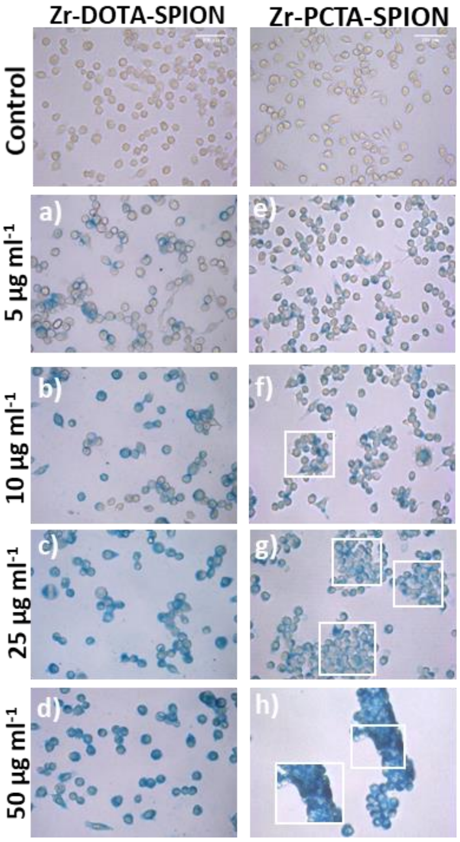

Figure 4.12: Prussian blue staining performed on (1:4 EDEA-CM-dex to DEAE-dex) Zr-SPION dosed RAW 264.7 cells compared with control (just media/no SPIONs). Images (a) – (d) display intracellular iron after a 24 h incubation with increasing concentrations of Zr-DOTA-SPIONs (5, 10, 25, 50 µg ml^{-1}). Images (e) – (h) display

intracellular iron after a 24 h incubation with increasing concentrations of Zr-PCTA-SPION (5, 10, 25, 50 µg ml^{-1}). Scale bar = 100 µm.

RAWs were dosed with increasing concentrations of Zr-SPION for a 24 hour period. Zr-DOTA-SPIONs were well tolerated by RAWs, showing a dose dependent increase in cellular iron uptake, as indicated by blue staining. Minimal extracellular aggregates were observed. Zr-PCTA-SPIONs were tolerated by RAWs at lower particle concentrations, displaying good cellular uptake with no extracellular aggregation. However, at concentrations of 10, 25 and 50 µg ml^{-1}, cells became less adherent and began to float in the culture dish, settling in clumps towards the end of the dosing period, as seen in Figures 4.12 (f), (g) and (h) and indicated by the white boxes on images.

Because of this, RAWs were dosed with lower concentrations of Zr-PCTA-SPION (1, 2.5, 5 and 12.5 µg ml^{-1}), as seen in Figure 4.13. Particles were well tolerated by RAWs at these concentrations, with cells remaining adherent and appearing healthy. Prussian blue staining indicated a high degree of iron internalisation compared to control images.

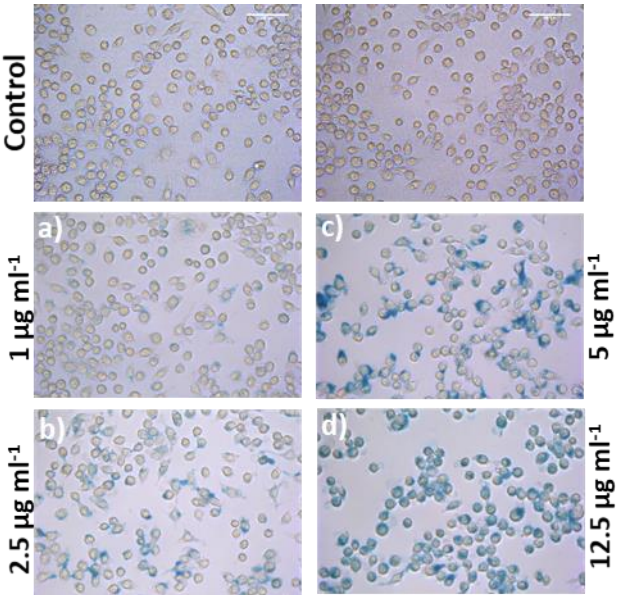

Figure 4.13: Prussian blue staining performed on Zr-PCTA-SPION dosed RAW 264.7 cells compared with control (just media/no SPIONs). Images **(a)** – **(d)** display intracellular iron after a 24 h incubation with increasing concentrations of Zr-PCTA-SPIONs (1, 2.5, 5, 12.5 µg ml^{-1}). Scale bar = 100 µm.

Ferrozine Assay

To quantify RAW cell Zr-SPION uptake, a colorimetric method known as the ferrozine assay was employed following a 24 h labelling period. As Zr-SPION labelling concentration increased, the amount of intracellular iron increased, shown in Figure 4.14. Zr-PCTA-SPIONs (Figure 4.14b) displayed a significant increase in cellular iron uptake at concentrations of 5 µg ml^{-1} and greater, with respect to controls (cells dosed with 0 µg ml^{-1} Zr-SPION) ($P < 0.03$, one-way ANOVA, Tukey's post-hoc test). Meanwhile, Zr-DOTA-SPIONs (Figure 4.13a) displayed a significant increase in cellular iron uptake at concentrations of 25 µg ml^{-1} and greater, with respect to controls ($P < 0.002$, one-way ANOVA, Tukey's post-hoc test).

Zr-DOTA-SPIONs displayed a peak intracellular iron content of 7 ± 1 pg Fe cell^{-1} at a concentration of 50 µg ml^{-1}. Zr-PCTA-SPIONs, meanwhile, displayed a peak intracellular iron content of 5 ± 0.6 pg Fe cell^{-1} at the much lower concentration of 12.5 µg ml^{-1}. We have recently reported in our group that 4.8 pg Fe cell^{-1} is a sufficient intracellular iron concentration to provide MRI contrast[125].

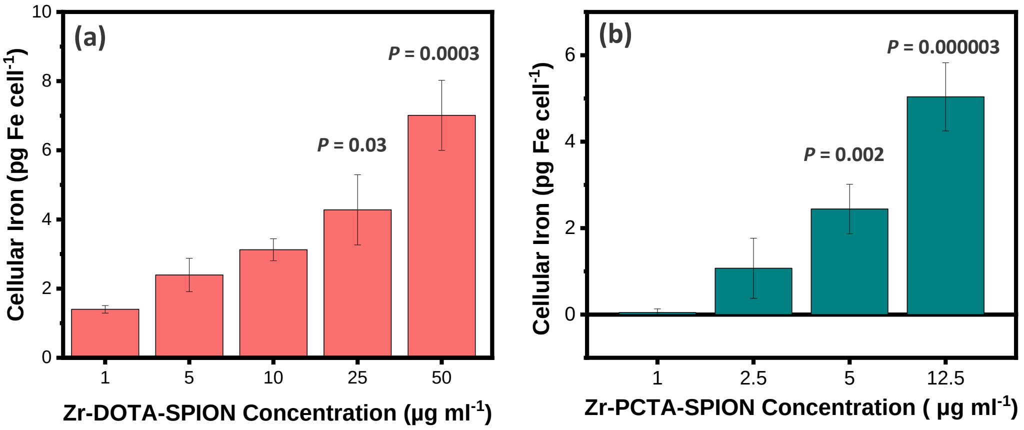

Figure 4.14: Intracellular iron content of RAW 264.7 cells labelled for 24 h with increasing concentrations of **(a)** Zr-DOTA-SPIONs and **(b)** Zr-PCTA-SPIONs. Error bars correspond to the SD obtained from three repeat measurements. Statistical significance (*P)* to respective controls (0 µg ml^{-1} Zr-SPION) was determined by applying a one-way ANOVA followed by a Tukey's post-hoc test. Concentrations that have a *P* value next to it are statistically different to controls.

4.3.3 Viability of RAW 264.7 Cells with Zr-SPIONs

To determine if the two particle types were toxic to RAW cells, ATP viability assays were performed. This assessed how viable the cells were after being dosed with Zr-SPIONs, by measuring the levels of ATP (Figure 4.15). Zr-DOTA-SPIONs caused no significant reduction in cell viability compared to control (0 µg ml^{-1}) at all labelling concentrations (P = 0.36, one-way ANOVA). However, there was a non-significant reduction in viability of the cells following labelling with 5 µg ml^{-1} Zr-DOTA-SPIONs, which may have been due to losses of the cells during washing steps. Zr-PCTA-SPIONs, on the other hand, caused reductions in cell viability at all labelling concentrations with a significant decrease in cell viability at 50 µg ml^{-1} (74% viable) (P = 0.02, one-way ANOVA, Tukey's post-hoc test). This is likely due to significant losses of labelled cells that detached during the assay.

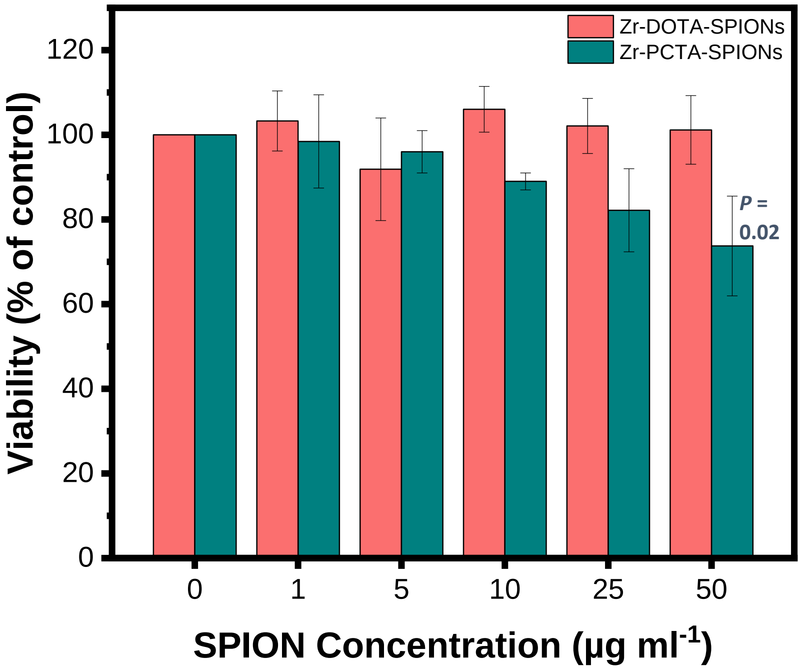

Figure 4.15: Cell viability of RAW 264.7 cells labelled with increasing concentrations of Zr-DOTA-SPIONs and Zr-PCTA-SPIONs for 24 h. Error bars correspond to the SD obtained from three independent measurements. Statistical significance of Zr-PCTA-SPIONs (*P)* to respective controls (0 µg ml^{-1} Zr-PCTA-SPION) was determined by one-way ANOVA followed by a Tukey's post-hoc test. Concentrations with a *P* value next to it are statistically different to controls.

Due to the reduction in viability seen for Zr-PCTA-SPIONs at higher labelling concentrations (10 – 50 µg ml^{-1}) and the non-adherence of labelled RAW cells under these conditions, the lower Zr-PCTA-SPION concentrations that were used in iron uptake assays were applied in a subsequent ATP assay.

As seen in Figure 4.16, under all Zr-PCTA-SPION conditions, the viability of the RAW cells was above 100% and there were no statistically significant differences in viability compared to control, as determined by one-way ANOVA ($P = 0.08$). Zr-PCTA-SPION labelled RAW cells also remained adherent under these conditions.

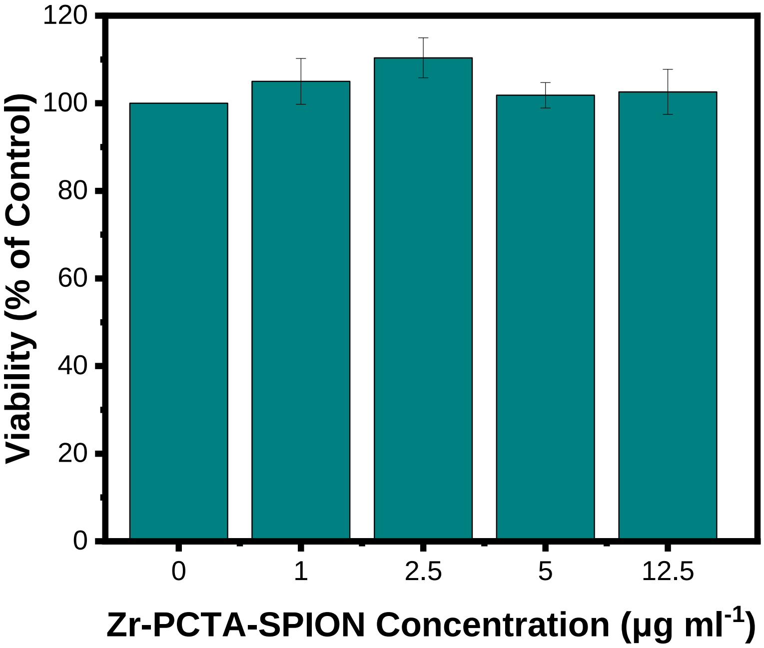

Figure 4.16: Cell viability of RAW 264.7 cells labelled with increasing concentrations of Zr-PCTA-SPIONs for 24 h. Error bars correspond to the SD obtained from three independent measurements.

4.4 Discussion

The stability of nanoparticle-based imaging agents plays a crucial role in determining their *in vitro* behaviour. In a practical aspect, nanoparticles must remain colloidally stable and resist aggregation in cell culture medium so that they can label cells effectively, and so labelled cells can be easily injected into a host. Colloidally unstable nanoparticles can also exhibit cytotoxic effects. Therefore, it is important to assess the stability of nanoparticle-based imaging agents *in vitro* before they are used to label cells and are ultimately administered *in vivo*.

Colloidal Stability of Mixed Dextran SPIONs

Mixed dextran SPIONs were synthesised from the polymers EDEA-CM-dex and DEAE-dex, as described in Chapter 3, using varying ratios of the two polymers in order to determine which ratio provided the greatest colloidal stability. The library of particles was synthesised with mass ratios of EDEA-CM-dex: DEAE-dex of 1:4, 1:2 and 1:1 (Table 4.1). Each particle was incubated in both 10% FBS-containing DMEM and 0% FBS DMEM to assess which particles were colloidally stable and how this was affected by the presence of FBS.

All particles were found to be unstable in serum-depleted medium; each particle immediately aggregated and subsequently sedimented upon dispersion (Figure 4.9). This result suggests the importance of serum proteins in the stabilisation of SPIONs. A number of reports have demonstrated that FBS at a concentration of 10% greatly improves the colloidal stability of nanoparticles, which may be due to the electrosteric stabilisation provided by the adsorbed serum proteins. Depleting FBS from DMEM may have removed this extra degree of stabilisation, resulting in the sedimentation of mixed dextran SPIONs[234, 236-238].

Despite this observation, not all SPIONs in the library remained colloidally stable in serum-supplemented media. When dispersed in 10% FBS-containing DMEM, the 1:2 (EDEA-CM-dex to DEAE-dex ratio) particles sedimented instantly, whilst the 1:1 particles sedimented after the 24 h incubation period. Only the particles with the 1:4 polymer mass ratio remained colloidally stable after 24 h in 10% FBS-containing DMEM. From DLS and zeta potential measurements (Table 4.1), we can see no clear trend in properties of the particles in relation to their polymer ratio. The medium sized particle (107 ± 3 nm) was the most colloidally stable, while the smallest and largest particles (100 ± 1 nm and 135 ± 3 nm, respectively) sedimented, suggesting there is no effect of hydrodynamic diameter on colloidal stability. As well as this, the particles all bore highly positive surface charges.

A problem with the size and surface charge measurements obtained in this chapter is that they were all conducted in salt, while it is well recognised that the properties of nanoparticles can change drastically when immersed in cell culture medium. Measuring the DLS of nanoparticles in serum-containing cell culture medium is very challenging due to the inherent characteristics of light scattering. Light scattered by a particle is proportional to the sixth power of its size[173]. This means that large matter will scatter light greatly, producing large signals and dominating over the signals that the smaller particles produce. Because of this, nanoparticle aggregates and free proteins in the suspension, which scatter light greatly, can prevent the size of the nanoparticle-protein corona complex from being accurately measured.

Nanoparticle-protein coronas can be separated from their protein rich matrix by a variety of techniques such as magnetic separation, centrifugation and chromatography. However, these rather rigorous isolation methods can often cause desorption of weakly bound serum proteins from the nanoparticle surface[123, 239], which can result in inaccurate size and surface charge data for the nanoparticle-protein corona. It is not possible to draw conclusions on whether nanoparticle size and surface charge has influenced colloidal stability in serum-containing cell culture medium in this work, since these measurements could not be obtained accurately.

A possible reason for the varying size of the nanoparticles within the mixed dextran SPION library, and their subsequent colloidal stabilities, is the conformation of the core-shell structures of SPIONs. In 2010, Veiseh *et al.* proposed a ‘wrapping’ conformation for dextran-coated SPIONs, in which the carbohydrate polymer is tightly wrapped around the iron oxide core[240]. As outlined in a recent publication by our group, an issue with this model is that not all polymer chains will be bound in the same way and it is difficult to control this in syntheses, resulting in variability between particles and batches of particles[124]. If this is the case for particles of the same polymer system, it is almost certain that particles of different polymer systems, i.e., mixed dextran SPIONs with different ratios of EDEA-CM-dex to DEAE-dex, will have completely different core-shell conformations to one another.

It is possible that the different polymer conformations adopted by the 1:1, 1:2 and 1:4 (EDEA-CM-dex to DEAE-dex) SPIONs had different affinites for serum proteins, and therefore, different capabilities of forming a uniform monolayer of proteins around the nanoparticle. Some studies have shown that surfaces that are only partially covered with protein, i.e. not in a uniform monolayer, can approach one another and experience attractive forces[241]. Perhaps in the case for the 1:1 and 1:2 particles, whose conformations may be very different to the colloidally stable 1:4 particles, there was only partial nanoparticle surface coverage of serum proteins from 10% FBS-containing DMEM, which resulted in attraction between the particles, causing destabilisation and sedimentation.

The most colloidally stable mixed dextran SPION (1:4) was applied in a Prussian blue staining assay at a concentration of 50 μg ml^{-1} and the particles were endocytosed well by the RAWs, as indicated by the blue pigment displayed in Figure 4.10. In the assay, RAW cells appeared healthy and their morphology looked normal following the 24 h incubation with mixed dextran SPIONs. In addition to this, minimal extracellular aggregates formed under these conditions.

Viability of RAW 264.7 Cells with Zr-DOTA-SPIONs and Zr-PCTA-SPIONs

Due to the good biocompatibility of mixed dextran SPIONs, the biocompatibility of the further functionalised particles, Zr-DOTA-SPIONs and Zr-PCTA-SPIONs, was assessed *in vitro*. Following a 24 h incubation of RAW 264.7 cells with Zr-DOTA-SPIONs at concentrations of 1, 5, 10, 25 and 50 μg ml^{-1}, there was no significant change in the viability of the cells.

In 2009, Huang *et al.* reported the proliferative effect of Ferucarbotran in human MSCs characterised by increased cell growth and acceleration in the cell cycle process[242]. There is growing evidence to suggest that magnetic nanoparticles can catalyse the breakdown of the

ROS, H_2O_2, due to the intrinsic peroxidase-like behaviour of the particles[243]. Huang *et al*. showed that Ferucarbotran dramatically reduced intracellular H_2O_2 levels, after incubating for just 1 h, which resulted in increased cell growth. On top of this, the report showed how Fe ions produced from lysosomal metabolism of SPIONs can accelerate cell cycle progression through alteration of the expression of protein regulators of the cell cycle.

Contrary to the points discussed above, leached Fe ions from SPIONs have also been found to increase the formation of ROS, causing cytotoxicity[100]. Zr ions are also known to exhibit cytotoxic effects but there has been little research into the mechanisms of cytotoxicity of Zr-based nanomaterials. However, there have been reports of zirconium oxide nanoparticles inducing significant ROS generation and oxidative stress effects[244]. As well as this, some research has shown that zirconium oxide nanoparticles accumulate in the lysosomes of liver and spleen macrophages when administered *in vivo*[245]. It is possible that, like their iron oxide nanoparticle counterparts, zirconium oxide nanoparticles can be degraded by lysosomes, leaching free Zr ions, which can impart toxicity.

Since dosing RAW cells with Zr-DOTA-SPIONs resulted in a good cytotoxicity profile, it is possible that the maintenance of cell viability is caused by a balance of the material's beneficial, proliferative properties e.g., breaking down ROS and the material's detrimental, cytotoxic properties e.g., catalysing the formation of ROS.

Although Zr-DOTA-SPIONs displayed no toxicity to RAW cells in the 24 h dosing period, Zr-PCTA-SPIONs caused reductions in cell viability compared to control (RAWs labelled with 0 µg ml^{-1} SPIONs/just media) at concentrations of 10 (89% viable), 25 (82% viable) and 50 µg ml^{-1} (72% viable) as displayed in Figure 4.15. The reduction in cell viability at 50 µg ml^{-1} was significant ($P = 0.02$). The main issue with dosing RAW cells with Zr-PCTA-SPION particles at these concentrations was a loss of adherence of cells to their culture dish following the 24 h incubation period. This meant that during washing steps of the bioassays, a high proportion of labelled cells was lost, which impacted the results of the viability assay specifically. Despite this, the RAWs that were harvested (*i.e.* not lost due to detachment) appeared healthy. This observation is consistent with other groups who have reported an inhibition of *in vitro* attachment of astrocytes and fibroblasts following dosing with high concentrations of SPION[246, 247].

Because of the detachment of RAW cells following dosing with 25 and 50 µg ml^{-1} Zr-PCTA-SPIONs, lower dosing concentrations of the particles were used in further bioassays, with the highest concentration of Zr-PCTA-SPION at 12.5 µg ml^{-1}. At concentrations of 1, 2.5, 5 and 12.5 µg ml^{-1}, Zr-PCTA-SPIONs caused no cell detachment or significant reductions in RAW cell viability, as displayed in Figure 4.16.

Cellular Uptake of Zr-SPIONs

Zr-DOTA-SPIONs and Zr-PCTA-SPIONs differ structurally only in that each particle is functionalised with a different macrocycle, DOTA or PCTA, respectively. Therefore, it may be surprising that the two particle types have such different effects on RAW cell attachment, with Zr-PCTA-SPIONs causing the cells to detach at concentrations as low as 10 µg ml^{-1}.

In the ferrozine assay (Figure 4.14), which quantifies cellular iron uptake, Zr-DOTA-SPIONs afforded a maximum uptake of 7 ± 1 pg iron per cell at the highest concentration of 50 µg ml^{-1} whilst Zr-PCTA-SPIONs afforded a maximum uptake of 5 ± 0.6 pg iron per cell at the highest concentration of 12.5 µg ml^{-1}. It is possible that Zr-PCTA-SPIONs detached *in vitro* because they endocytosed so much iron at the higher concentrations of 25 and 50 µg ml^{-1}. This effect was seen qualitatively in the Prussian blue assay (Figure 4.12(g) and (h)), which displays a very intense blue staining at these concentrations. Of note, it was not possible to quantitatively measure Zr-PCTA-SPION uptake at the higher particle concentrations via the ferrozine assay due to the high degree of RAW cell detachment and the ensuing losses during washing steps.

The differences in RAW cell uptake between the two particle types may be attributed to differences in their physicochemical properties, namely the size of each SPION. Zr-DOTA-SPIONs are larger than Zr-PCTA-SPIONs, with hydrodynamic diameters of 141 nm and 122 nm, respectively. RAW cells, due to their inherent macrophage/monocyte-like nature, can endocytose and engulf large amounts of foreign material. Some attempts in the literature have been made to elucidate the exact mechanisms of SPION uptake into macrophage-like cell lines.

In 2019, Guggenheim *et al.* studied the uptake of the commercially available Sienna+® SPIONs into THP-1 cells[248], a human monocytic cell line. When the AP2 protein, a cargo protein that facilitates clathrin-mediated endocytosis, was inhibited, SPION internalisation into THP-1 cells was significantly reduced. When the phagocytosis pathway in THP-1 cells was inhibited, SPION uptake also decreased. However, when phagocytosis functionality was reduced to 20-30%, 50-70% SPIONs were taken up into the cells, suggesting that the particles can enter into macrophages by more than one route.

In a report by Gu *et al*, the internalisation pathways of dimercaptosuccinic acid (DMSA)-coated SPIONs into RAW 264.7 cells were investigated[249]. When clathrin-mediated endocytosis inhibitors were administered to the cells, SPION uptake was drastically reduced. A similar result was observed when caveolin-mediated endocytosis and macropinocytosis inhibitors were applied.

The results from both studies suggest that macrophage-like cells apply several endocytic pathways to facilitate SPION uptake. However, the pathways that appear to contribute the most to SPION uptake are those that employ vesicular structures e.g., clathrin-mediated and caveolin-mediated endocytosis, as well as macropinocytosis. Since these endosomal vesicles are typically fixed in their sizes, it is possible that more Zr-PCTA-SPIONs were able to fit into the vesicles upon cellular uptake due to their smaller size of 122 nm, whilst fewer Zr-DOTA-SPIONs were able to fit into the vesicles due to being larger (141 nm). In addition to this, Zr-DOTA-SPIONs bore a higher surface charge (+23.5 mV) than Zr-PCTA-SPIONs (+19.1 mV) so may have adsorbed more serum proteins into the Zr-DOTA-SPION protein corona, resulting in a larger hydrodynamic diameter and thus less endocytic uptake. This may explain why just 12.5 μg ml^{-1} Zr-PCTA-SPION was able to provide a peak RAW cell iron concentration of 5 pg cell^{-1} whilst upwards of 25 μg ml^{-1} Zr-DOTA-SPIONs was required to achieve the same amount of intracellular iron.

The superior uptake capabilities of Zr-PCTA-SPIONs were observed in the Prussian blue staining assay seen in Figure 4.13. Iron uptake, which is indicated by blue pigment, increased with increasing concentration of SPION and an intense blue staining was imaged at the highest concentration of 12.5 μg ml^{-1}, indicating high cellular SPION uptake.

4.5 Conclusions

Two types of hybrid PET/MR imaging agent, Zr-DOTA-SPIONs and Zr-PCTA-SPIONs, were synthesised and their *in vitro* behaviour was assessed in this chapter.

At the labelling concentrations used here, both particle candidates offered a good cytotoxicity profile in RAW 264.7 cells and provided substantial iron labelling (> 5 pg Fe cell^{-1}). Because of this, both Zr-DOTA-SPIONs and Zr-PCTA-SPIONs were utilised in *in vivo* studies and this work will be discussed in Chapters 5 and 6. First, Zr-DOTA-SPIONs were investigated *in vivo* to determine their stability and pharmacokinetics, since these particles had shown the ability to bind high quantities of zirconium.

Chapter 5

Multimodal Imaging of ^{89}Zr-DOTA-SPIONs Following Systemic Injection

5.1 Introduction

The use of zirconium-89 (^{89}Zr) in medical imaging has become increasingly popular in recent years, particularly for the application of immunoPET and the labelling of monoclonal antibodies[92]. In addition to this, ^{89}Zr has become a favourable radiotracer for cell tracking via positron emission tomography (PET) since the isotope has a long half-life of 78.4 h, making it suitable for long-term studies[250].

Studying the pharmacokinetics (biodistribution, metabolism, excretion) of ^{89}Zr is of great importance since the radioactive metal can display toxic effects *in vivo* and accumulate in areas of the body that are not of clinical relevance. It is particularly pertinent to study the biodistribution of ^{89}Zr when attached to superparamagnetic iron oxide nanoparticles (SPIONs), since the two entities could separate *in vivo*, resulting in non-corresponding PET and magnetic resonance imaging (MRI) signals, which could create confusion when tracking labelled cells.

This chapter will examine the pharmacokinetic properties of ^{89}Zr labelled DOTA-SPIONs following an intravenous (IV) injection in mice. This will help us to better understand how the particles behave *in vivo* and allow us to optimise the particles for cell labelling and tracking. DOTA-SPIONs were studied first since these particles had shown the ability to bind a high quantity of non-radioactive zirconium.

Pharmacokinetics of Zirconium-89 Complexes

To better understand the safety profile of ^{89}Zr for use in PET imaging, the pharmacokinetics of $^{89}Zr^{4+}$ complexes have been studied extensively. Zirconium is a chemical element of atomic number 40 with an atomic mass of 91.224. The metal exists at low concentrations (< 5 ppb) in a variety of foods, including plums, parsley and carrots. Small amounts of Zr are found in the body, predominantly in fat, liver and gall bladder tissue, with trace amounts found in the brain[251]. Excretion of dietary Zr is thought to go through the hepatobiliary system, which results in faecal excretion[252]. However, the fate of non-dietary Zr is less well understood and is thought to largely depend on the chemical speciation of the metal[253].

Biodistribution

In a study conducted by Abou *et al.*[92], the chemical and biological fates of ^{89}Zr-oxalate, ^{89}Zr-chloride, ^{89}Zr-phosphate, ^{89}Zr-desferrioxamine (^{89}Zr-DFO) and ^{89}Zr-citrate in mice following IV injection were investigated. The structures of some of these complexes are displayed in Figure 5.1. It was reported that, for ^{89}Zr-DFO and ^{89}Zr-citrate, the activity had completely excreted after the first day of injection. In the rest of the ^{89}Zr species, activity remained in the bodies of mice for six days and, after this period, 20% of the activity for ^{89}Zr-oxalate and ^{89}Zr-chloride had been cleared, whilst only 5% ^{89}Zr-phosphate clearance was achieved.

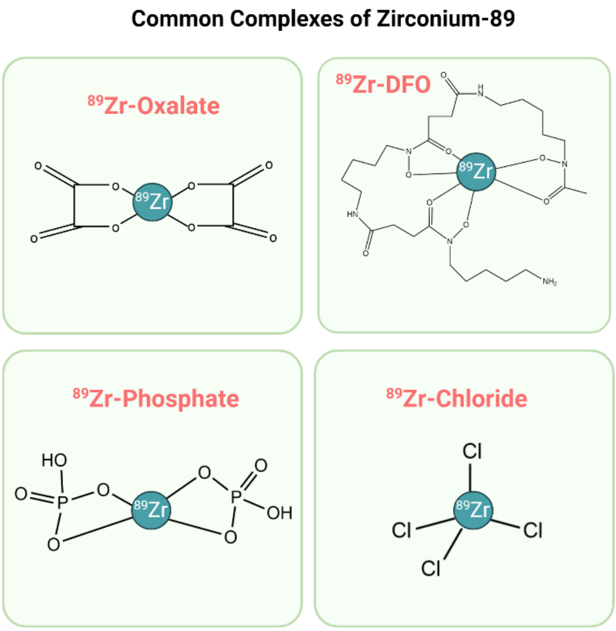

Figure 5.1: Complexes of zirconium-89 (^{89}Zr) that are commonly used as PET radiotracers

In Abou's study, both ^{89}Zr-oxalate and ^{89}Zr-chloride exhibited similar biodistribution profiles, with the heart and lungs accumulating some activity within 3 h of injection due to the high vascularity of these organs. Bone analysis performed by the researchers displayed high accumulation (about 20% of the injected dose) of ^{89}Zr-oxalate and ^{89}Zr-chloride in mineralised constituents of bone, specifically the epiphyses. It is likely that ^{89}Zr is chelated by the phosphate-containing mineral, hydroxyapatite (Figure 5.2), which is prevalent in this part of the bone. Unlike its chloride and oxalate counterparts, ^{89}Zr-phosphate displayed very little bone activity and instead, preferentially homed to the liver and spleen[92]. This result highlights the affinity of Zr for phosphate and, thus, the high stability of Zr-phosphate complexes.

Since Zr is a bone seeker, it is important that bone uptake by ^{89}Zr is monitored when administering such radiotracers *in vivo*; bone deposition is prevalent when ^{89}Zr is not tightly bound to a chelate. Since ^{89}Zr-DFO was shown by Abou *et al*. to be the least osteophilic of the radiotracer complexes, releasing the least amount of ^{89}Zr^{4+}, followed by ^{89}Zr-phosphate, ^{89}Zr-citrate, then ^{89}Zr-chloride and ^{89}Zr-oxalate, this demonstrates how bone uptake by ^{89}Zr is affected by the denticity and, thus, the stability of the ^{89}Zr complex. This is a factor that should be considered when selecting a Zr-based radiotracer for PET; greater bone uptake means that more radiotracer is required to provide a specific PET signal, which could result in toxicity[252].

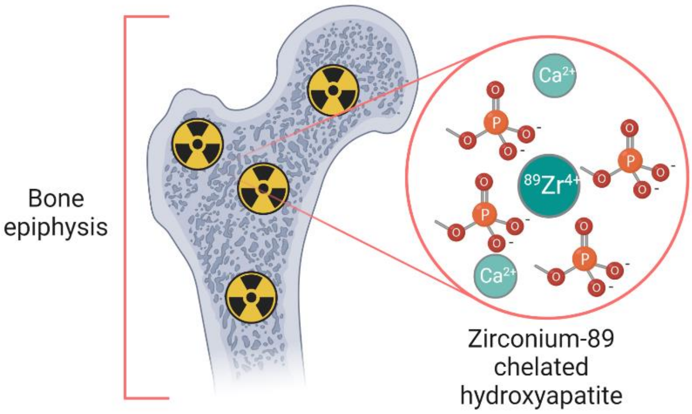

Figure 5.2: ^{89}Zr has a high affinity for bone *in vivo* due to the high concentration of hydroxyapatite present there. Hydroxyapatite, which is rich in phosphate groups, preferentially chelates ^{89}Zr, resulting in bone deposition of the radiometal.

Clearance

The stability and complexation of ^{89}Zr affects not only its *in vivo* biodistribution, but also its mechanism and rate of clearance. Studies suggest that the rate and mechanism of ^{89}Zr clearance depends on the physical size of the Zr species (whether it is colloidal or polymeric), since larger Zr aggregates have been shown to clear slowly from the blood[254]. In one murine study, ^{89}Zr-chloride was administered to animals and was found to accumulate in the livers of mice, suggesting that the tracer had precipitated there in colloidal form[187]. However, in another study where ^{89}Zr-chloride was prepared using a different method, no accumulation in soft tissue was observed, meaning that the complex is likely to have remained in polymeric form[92]. In a handful of studies, the high denticity complex, ^{89}Zr-DFO, was shown to clear and excrete rapidly from the kidneys through the urine, suggesting that ^{89}Zr-DFO is not subject to colloidal aggregation[187, 255].

In summary, the biodistribution, metabolism and clearance of ^{89}Zr complexes largely depends on the stability and speciation of the metal cation and is something that should be carefully considered when utilising this radiotracer *in vivo*.

Pharmacokinetics of SPIONs

The wide-spread biomedical use of SPIONs started in the 1980s[256, 257], and over the past 30 years, the use of SPIONs as a contrast agent has grown increasingly popular due to their favourable properties such as magnetic functionality and high biocompatibility[258]. SPIONs have been clinically available for a number of years, with the first contrast agent, Endorem, gaining FDA approval in 1996, which was shortly followed by Resovist® (Ferucarbotran)[85].

Despite the notion that SPIONs are biocompatible, they are also known to catalyse Haber-Weiss and Fenton-type reactions, which can produce cytotoxic free radicals (discussed in greater detail in Chapter 4 of this thesis). Therefore, it is pertinent to assess the fate, biodistribution and clearance of novel SPIONs to ensure they maintain a sound safety profile *in vivo*. The overall pharmacokinetic profile of SPIONs is summarised in Figure 5.3.

Biodistribution

SPIONs that are administered intravenously must cross the vascular endothelium in order to reach their target sites. This is achieved through sequestration of the particles by macrophages of the mononuclear phagocyte system (MPS)[113, 259] and the rate at which this occurs can depend on the hydrodynamic diameters of the SPIONs. It has been suggested that particles that have diameters of less than 50 nm can evade opsonisation by the MPS, so circulate in the bloodstream for longer before being taken up by macrophages in the lymph tissue, liver and bone marrow. Meanwhile, particles of diameters greater than 100 nm are taken up rapidly by Kupffer cells from the liver and macrophages of the spleen. Particles of sizes greater than 200 nm have been reported to have higher rates of uptake in the spleen than in the liver[260, 261]. Another factor that affects the rate of blood clearance by the MPS is the surface charge of SPIONs. Negatively charged and neutral nanoparticles adsorb fewer opsonin plasma proteins, which reduces their rate of uptake by the MPS and thus their rate of blood clearance[262].

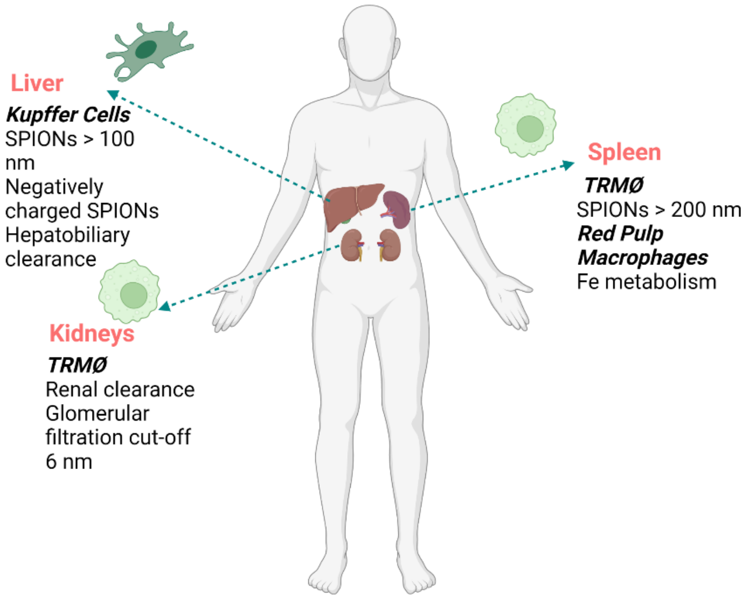

Figure 5.3: Typical *in vivo* biodistribution and clearance pathways of SPIONs following intravenous (IV) injection. SPIONs of hydrodynamic diameters greater than 100 nm and negatively charged SPIONs are rapidly sequestered by Kupffer liver cells and spleen macrophages from the mononuclear phagocyte system (MPS). SPIONs that accumulate in the liver undergo hepatobiliary clearance. SPIONs of less than 50 nm can evade rapid opsonisation so circulate in the blood for longer before being taken up by tissue resident macrophages (TRMØ) of the spleen, other lymphatic tissue, the kidneys and the liver. SPIONs of hydrodynamic diameters greater than 200 nm have higher rates of uptake in the spleen than in the liver. Red pulp macrophages that are localised in the spleen can phagocytose SPIONs and are involved in iron metabolism. SPIONs greater than 6 nm avoid renal clearance due to the size exclusion limit for glomerular filtration.

In a study by Wang *et al*., researchers evaluated the tissue distribution of uncoated, 20 nm sized SPIONs by atomic absorption spectrometry following an intragastric injection in mice[263]. A wide distribution of SPIONs was found in the heart, liver, spleen, lungs, kidneys, small intestine and bone marrow, with the highest concentration of particle found in the liver and spleen. Interestingly, Wang *et al*. also measured significant concentrations of SPIONs within the brain tissue[263]. The liver and spleen are highly ferruginous, with more iron found in these organs than anywhere else in the body[264], which may explain why macrophage-SPION activity is most prevalent in these areas. In addition to this, the spleen produces red-pulp macrophages, which are specifically involved in iron metabolism[265].

Clearance

Iron is a widely distributed element in the body that has many important uses, including oxygen transport and cellular respiration. The metabolism of iron, therefore, is part of a closed system, which allows for little iron loss from the body.[266-268].

Lysosome-mediated degradation is considered to be the main intracellular mechanism of SPION metabolism (Figure 5.4). Following uptake into circulating macrophages, particles are transferred from early to late endosomes, which then fuse with lysosomes. SPIONs are digested into their corresponding free iron ions within these lysosomes, which have a pH of 4.5 – 5.5[269]. The resulting ions are then sequestered and stored in ferritin and hemosiderin protein cages[270]. In our group, we have replicated the lysosomal microenvironment using acidic buffers in the presence of sodium citrate, and found that the commercially available SPIONs, Molday Ion and Feratrack, underwent full dissolution within four days under these conditions[271].

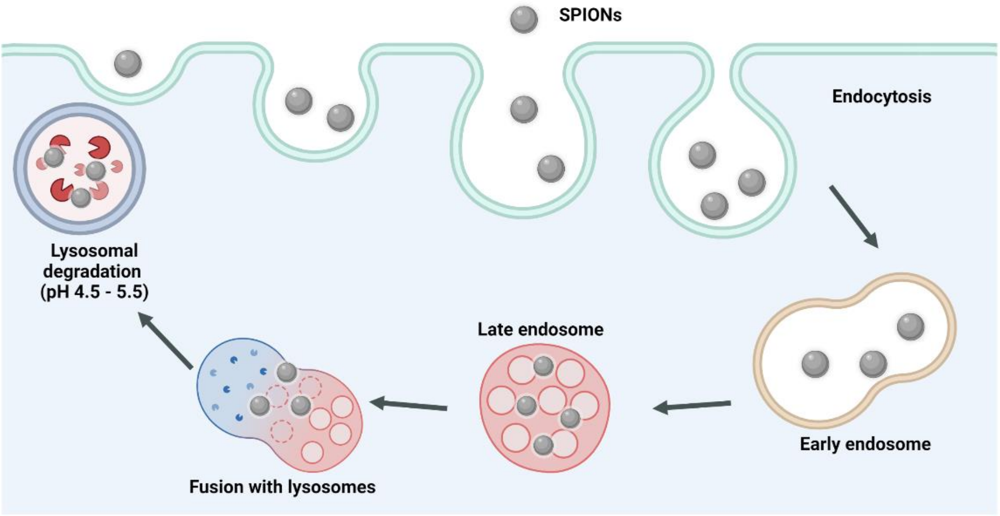

Figure 5.4: SPION metabolism via lysosome-mediated degradation. SPIONs are endocytosed into cells, where they are taken up into early endosomes before being transferred into late endosomes. These endosomes then fuse with lysosomes, forming an endolysosome, before undergoing acidic dissolution within the lysosomes, which have a pH of 4.5 – 5.5 Iron ions (Fe^{3+}/Fe^{2+}) that are released upon lysosomal digestion are stored in ferritin and hemosiderin protein cages for later use.

The main routes of SPION excretion are via the renal pathway or through the hepatobiliary system[272]. However, the least toxic SPION elimination route is via the kidneys, since this involves minimal intracellular catabolism and thus reduces the probability of generating reactive oxygen species (ROS)[113]. Despite this, dextran-coated SPIONs have been reported to undergo just 1% elimination via the urine of rats, over a period of 12 weeks. 21.8% SPIONs were found to be excreted via the faeces (hepatobiliary system) and the rest were incorporated into the body's iron stores[273]. The size of SPIONs determines whether the particles will be cleared via the kidney. This was demonstrated in a study by Leal *et al.*[259], who reported the accumulation and retention of PEG-SPIONs in the renal corpuscles due to their hydrodynamic diameters being much larger than the 6 nm exclusion limit for glomerular filtration[274-276].

Pharmacokinetics of Radiolabelled Nanoparticles

Altering the synthesis of SPIONs and other nanoparticles can affect their size, shape and material composition, which, in turn, can affect the biological properties of the particles. Thus, labelling SPIONs with radiotracers can result in altered tissue biodistribution, biological targeting and excretion and clearance profiles[277]. To better understand how radiolabelling

SPIONs can affect these important parameters, this section will analyse the pharmacokinetics of some radiolabelled nanoparticles using examples from the literature.

In 2018, McDonagh *et al.* investigated the behaviour of ^{89}Zr-labelled cerium oxide nanoparticles (CONPs) in mice[277]. Uncoated ^{89}Zr-CONPs displayed high radioactive signal in the lungs, as well as in the liver and spleen following IV injection. Coated nanoparticles displayed a more general biodistribution, with enhanced uptake in the liver and spleen. All coated particles displayed bone uptake, suggesting that the ^{89}Zr tracer had leached from the particles. The coating of the particles also affected their biodistribution, with PAA and citrate-coated ^{89}Zr-CONPs displaying PET signal in the kidneys which led to 75% of the injected dose being excreted in the urine. This was likely due to the smaller particle sizes of PAA and citrate-coated nanoparticles of 3.8 nm and 3.1 nm, respectively. All other, larger ^{89}Zr-CONPs showed a significant uptake in the gallbladder and faeces, which indicates that the particles were excreted via the hepatobiliary system.

Similarly, Zhan *et al.* investigated the biodistribution of intravenously injected ^{89}Zr-labelled manganese oxide nanoparticles (^{89}Zr-Mn_3O_4-NPs) in mice[278]. A strong uptake of particles was observed in the liver and spleen. Since the 8 nm particle sizes were too large for renal filtration, the main route of clearance observed for ^{89}Zr-Mn_3O_4-NPs was via the hepatobiliary system, which reflects the high uptake observed in the liver.

As detailed in Chapter 3, the first report of chelate-free SPION radiolabelling with ^{89}Zr was by Boros *et al.*, who modified the surface of Feraheme® particles with ^{89}Zr to generate ^{89}Zr-Feraheme[158]. Following an IV injection in mice, ^{89}Zr-Feraheme circulated in the blood stream for 6-8 h before rapidly accumulating in the liver, spleen and lymph nodes of mice. This long circulation time suggests that the particles, which had small hydrodynamic diameters of 17 – 31 nm, evaded opsonisation and, thus, rapid sequestration by the MPS. The highest uptake of ^{89}Zr-Feraheme was observed in the liver, indicating hepatobiliary clearance. The pharmacokinetic profile of ^{89}Zr-Feraheme was consistent with the reported pharmacokinetics data for FDA approved Feraheme[279-282], demonstrating that labelling the particles with the radiotracer does not affect their biological behaviour.

In summary, the literature suggests that labelling nanoparticles with radiometals, including ^{89}Zr, does not appear to affect the pharmacokinetics (biodistribution, metabolism, excretion) of the particles, on the condition that the two entities remain bound *in vivo*. Weakly associated ^{89}Zr has the potential to separate from SPIONs in the body, resulting in unfavourable bone deposition.

Experimental Plan

The aim of the work in this chapter was to study the biodistribution of ^{89}Zr-DOTA-SPIONs via PET and MRI following an IV injection in healthy mice. This was to assess whether the PET radiotracer remains bound to SPIONs *in vivo*, and to check for any toxic effects to animals. The data acquired helped to determine whether ^{89}Zr-DOTA-SPIONs would be suitable for cell labelling and tracking *in vivo*. Since the study at hand was a short pilot study, only the DOTA-SPIONs, and not PCTA-SPIONs were radiolabelled and administered *in vivo*. DOTA-SPIONs were selected first to study since they had shown the ability to bind more zirconium than PCTA-SPIONs.

To achieve the aims, DOTA-SPIONs were synthesised as described in Chapter 3 and then were radiolabelled with ^{89}Zr via mixing with ^{89}Zr-oxalate overnight at room temperature. The particles were purified by spin filtration, then were injected into the tail vein of 11 week-old healthy male C57BL/6 mice. These mice were selected since there were spare animals available within our group’s colony at the time of the study. Animals were imaged immediately by PET (day 0) then on days 1, 5 and 7. MR imaging took place on days 1, 5 and 7. Mice were then sacrificed, and their organs were harvested. The study plan is summarised in Figure 5.5.

Prior to conducting *in vivo* imaging by PET and MR, ^{89}Zr-DOTA-SPIONs were also imaged *in vitro* using phantoms. This was to ensure that the particles were able to show signal/contrast in both PET and MR.

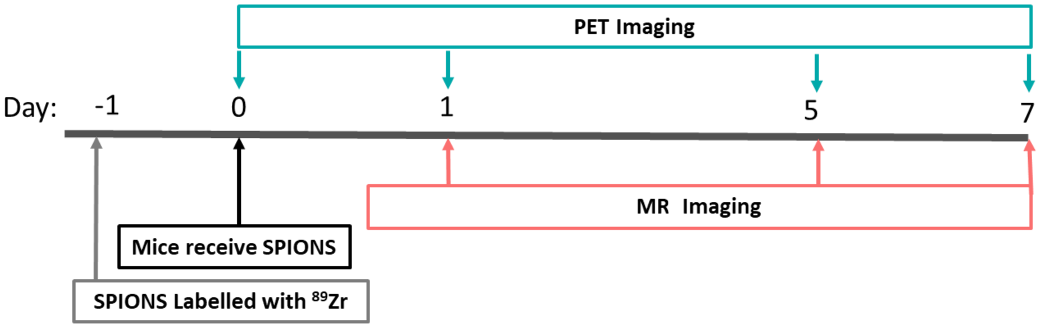

Figure 5.5: Summary of Chapter 5 study plan. DOTA-SPIONs were first radiolabelled with ^{89}Zr to generate ^{89}Zr-DOTA-SPIONs. Mice received radiolabelled SPIONs via intravenous injection on day 0 and were immediately imaged by PET. PET imaging was repeated on days 1, 5 and 7. MR imaging occurred on days 1, 5 and 7. Animals were culled on day 7 and their organs were collected.

5.2 Methods

5.2.1 Radiolabelling DOTA-SPIONs with Zirconium-89 Oxalate (^{89}Zr-oxalate)

DOTA-SPIONs and mixed dextran SPIONs were synthesised as described in Chapter 3 and were purified to concentrations of 1 mg ml^{-1}. 25 megabecquerel (MBq) ^{89}Zr-oxalate (Perkin Elmer, Amsterdam, NL) was added in 20 mM HEPES (100 µl) and the pH was adjusted to ~ 8.0 with 1 M Na_2CO_3 to yield a total volume of 135 µl. 20 MBq ^{89}Zr-oxalate in HEPES (110 µl) was added to 1 ml DOTA-SPIONs. Mixed dextran SPIONs (200 µl) were utilised as control particles to which 20 µl ^{89}Zr-oxalate in HEPES was added. The remaining ^{89}Zr-oxalate activity in HEPES was used as a control in thin layer chromatography (TLC).

Both particle mixtures were shaken for 24 hours at room temperature and radiolabelling yields of the particles were determined at 1, 3, 4 and 24 hours after incubation using TLC. A pencil line was drawn on a silica TLC strip and 2 µl aliquots of radioactive particles were applied to the line. As a control, 2 µl free ^{89}Zr-oxalate (without particles) was applied to the TLC strip. After the spots of radioactivity dried, the lower end of the TLC strip was submerged in the mobile phase, 50 mM diethylenetriaminepentaacetic acid (DTPA). When the solvent front had travelled to the top of the TLC strip, it was cut in two slightly above the pencil line to yield the base (the point of application of activity) and the top (migrated activity). The amount of radioactivity on each section of the TLC strip was measured using a CRC-15R radioisotope dose calibrator (Capintec Inc, NJ, USA). The radiolabelling yield for each time point was calculated using Equation 5.1 below.

$$radiolabelling\ yield = \frac{radioactivity\ at\ base}{total\ radioactivity\ (base+top)}\ x\ 100 \qquad \textbf{(5.1)}$$

Following the 24 h incubation period, ^{89}Zr-DOTA-SPIONs were washed 3 times with ultrapure water via spin filtration.

5.2.2 Phantom Preparation

Stock solutions of ^{89}Zr-DOTA-SPIONs were prepared for PET and MR imaging by diluting particles in 1% (w/w) low gelling temperature agarose. The stock solutions were allowed to set in 100 µl microfuge tubes, which were subsequently mounted in a large holder containing 1% agarose.

5.2.3 *In Vivo* Studies

Animals

General animal methods are described in Chapter 2. To assess the pharmacokinetics of Zr-DOTA-SPIONs, 11 week-old healthy male albino C57BL/6 mice from an in-house colony managed by the Biomedical Services Unit of the University of Liverpool received a tail vein injection of ^{Nat}Zr-DOTA-SPIONs (25 µg Fe in 100 µl saline) (n = 4) or ^{89}Zr-DOTA-SPIONs (200 µg Fe, 1 MBq ^{89}Zr in 200 µl PBS) (n = 3).

PET/CT

Immediately (~ 30 minutes) following injection of ^{89}Zr-DOTA-SPIONs and then at days 1, 5 and 7, mice were anaesthetised and whole-body PET/CT scans were performed as described in Chapter 2. 3D ROIs were drawn around the lungs, liver, spleen and kidneys of mice for each time point using VivoQuant™ software (Invicro, MA, USA). This allowed the amount of activity in these organs to be calculated. Because it was difficult to draw ROIs around the spine and joints, the remaining activity that was measured in the animals by the software was labelled 'remaining' and was attributed to the signal seen in the bones.

MRI

MRI studies were performed at days 1, 5 and 7 after injection of ^{89}Zr-DOTA-SPIONs or on day 1 after injection of ^{Nat}Zr-DOTA-SPIONs to acquire T_2*-weighted liver images. MR acquisition parameters are described in Chapter 2. Relaxation times were calculated using Paravision® (Bruker, MA, USA).

5.3 Results

5.3.1 *In Vivo* MR Imaging of ^{Nat}Zr-DOTA-SPIONs

To assess how well animals would tolerate a systemic injection of Zr-labelled SPIONs, and to determine the concentration of particle required to generate contrast in the liver, non-radioactive ^{Nat}Zr-DOTA-SPIONs (25 µg, Fe basis) were first administered to mice intravenously. The abdomens of mice were imaged by MR using a T_2*-weighted sequence prior to receiving the injection and were then imaged 24 h post injection (Figure 5.6a).

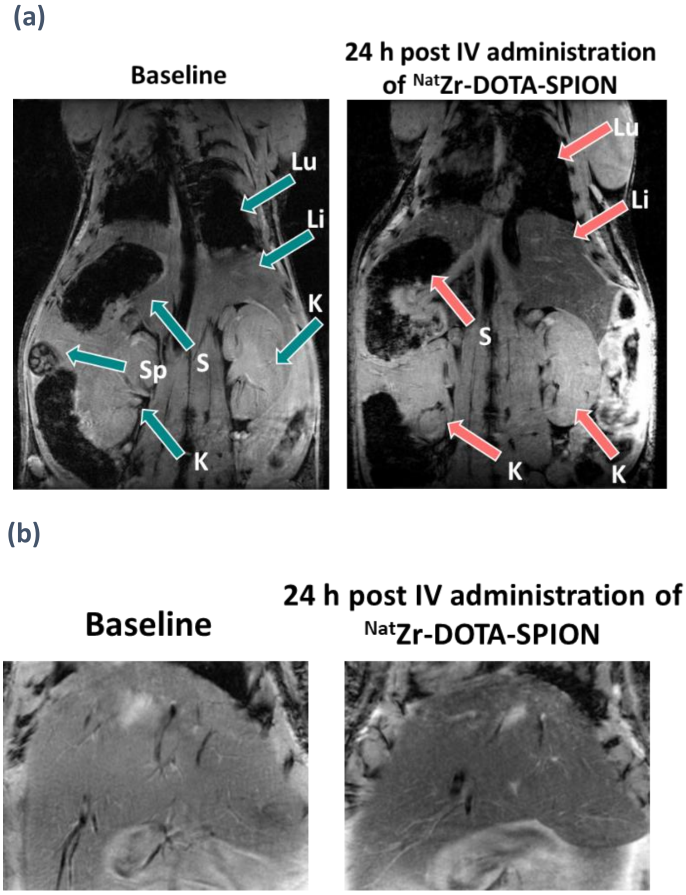

Figure 5.6: (a) T_2*-weighted images of a mouse abdomen at baseline (prior to ^{Nat}Zr-DOTA-SPION injection) and on day 1 (24 h post administration). Labels: Lu = lungs, Li = liver, K = kidneys, Sp = spleen, S = stomach. **(b)** Representative T_2*-weighted MRI of the liver of a mouse at baseline (prior to ^{Nat}Zr-DOTA-SPION injection) and on day 1 (24 h post administration).

Figure 5.6b displays T_2*-weighted images of mice livers at baseline and 24 h after receiving ^{Nat}Zr-DOTA-SPIONs. The latter images showed subtle hypointense contrast due to the presence of SPIONs in the liver. The images shown are selected from MR slices that display a large volume of the liver. The livers of mice were focused on to demonstrate the ability of

^{Nat}Zr-DOTA-SPIONs, which have a hydrodynamic diameter of 140 nm, to generate contrast since it is established in the literature that particles of diameters greater than 100 nm are rapidly sequestered by Kupffer cells of the liver[261]. The spleen was not focused on because the volume of this organ is much smaller than that of the liver and thus, is more difficult to image and calculate relaxation times from.

Changes in the T_2* relaxation times in the livers of mice were measured by drawing ROIs around images of the livers taken at baseline and on day 1 (24 h post administration of ^{Nat}Zr-DOTA-SPIONs). As seen in Figure 5.7, the liver T_2* relaxation time was significantly lower on day 1 (mean = 5.73 ± 0.35 ms) than at baseline (8.90 ± 0.43 ms) ($P = 0.00073$; paired sample t-Test), which is likely due to the accumulation of SPIONs.

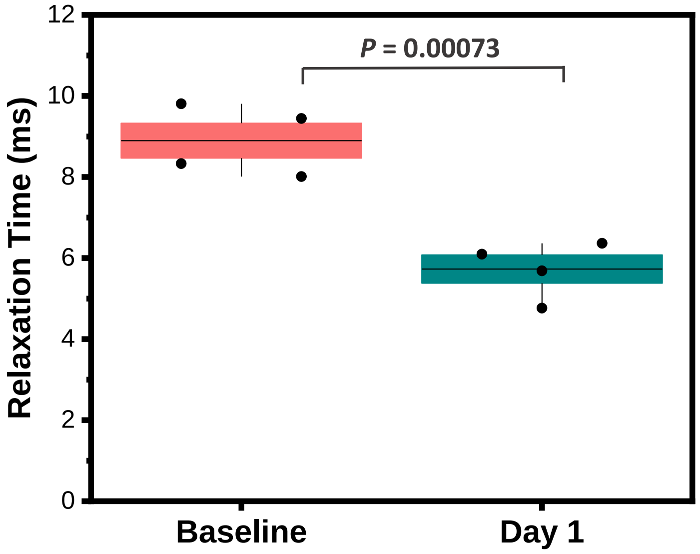

Figure 5.7: T_2* relaxation times of the liver at baseline and on day 1 (24 h post administration of ^{Nat}Zr-DOTA-SPIONs). The two time points are statistically different from one another, $P = 0.00073$ (paired sample t-Test). n = 4.

5.3.2 *In Vitro* Validation of ^{89}Zr-DOTA-SPION Binding

To assess the kinetics and mechanism of ^{89}Zr binding to DOTA-SPIONs, the particles were radiolabelled and the radiolabelling yield was calculated at 0.5, 1, 3, 4 and 24 h after incubation using TLC. Mixed dextran SPIONs, particles that contained no macrocycle, were used as control particles (Figure 5.8a). For DOTA-SPIONs, there was a slow increase in the radiochemical yield as time progressed, with 28% ^{89}Zr bound to the particles after half an hour. This increased to 93% after a 3 h incubation and 96% after the full 24 h time period. Mixed dextran SPIONs, on the other hand, appeared to react almost completely with ^{89}Zr after just 0.5 h, with a measured radiochemical yield of 90% following this incubation period. The radiochemical yield of dextran SPIONs reached 100% after the full 24 h incubation.

Despite the high measured radiochemical yield of ^{89}Zr-DOTA-SPIONs after the 24 h period, a lot of the radioactivity was washed away upon purification. As seen in Figure 5.8b, after two ultrapure water spin filter washes, ^{89}Zr-DOTA-SPIONs lost 85% of the activity that was measured on the particles prior to purification.

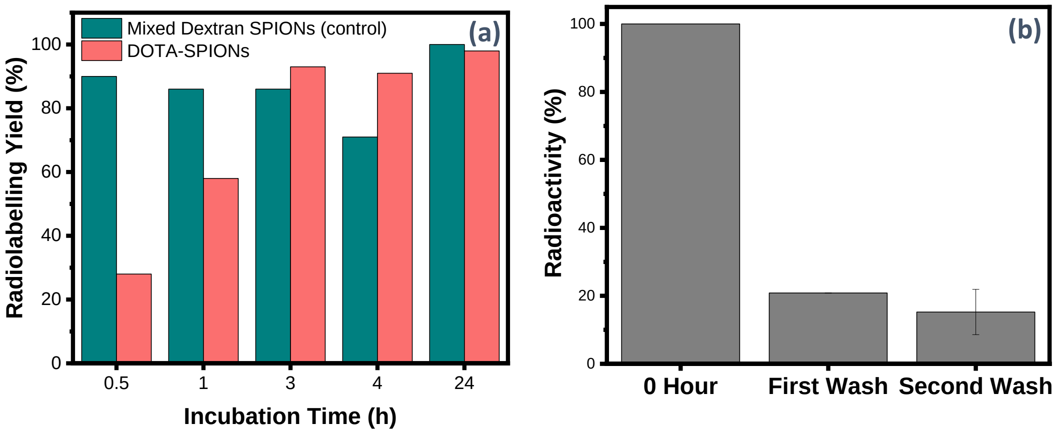

Figure 5.8: *In vitro* validation of ^{89}Zr-DOTA-SPION binding. **(a)** Radiochemical yields of DOTA-SPIONs and mixed dextran SPIONs (control particles) from TLC data following incubation with ^{89}Zr-oxalate after 0.5, 1, 3, 4 and 24 hours. **(b)** The percentage of radioactivity on ^{89}Zr-DOTA-SPIONs following two ultrapure water spin-filtration washes.

5.3.2 *In Vitro* Imaging of ^{89}Zr-DOTA-SPIONs

To demonstrate the ability to image ^{89}Zr-DOTA-SPIONs with PET and MRI, the particles were diluted to different concentrations in agarose, and were then mounted in an agarose phantom and imaged with the two modalities. As seen in Figure 5.9, ^{89}Zr-DOTA-SPIONs displayed a strong signal in PET down to a concentration of 0.1 MBq (^{89}Zr basis) whilst the particles exhibited hypointense contrast in T_2* weighted MR images at all Fe concentrations in a dose-dependent manner.

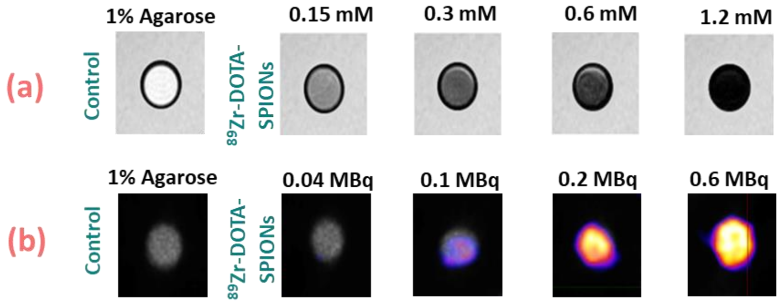

Figure 5.9: ^{89}Zr-DOTA-SPIONs diluted to different concentrations in 1% (w/w) agarose and set in an agarose phantom. **(a)** T_2* weighted MR images of SPIONs compared to control (just agarose). TE = 15.5 ms. **(b)** PET/CT images of ^{89}Zr-DOTA-SPIONs of increasing ^{89}Zr activity compared to agarose control.

5.3.3 *In Vivo* Imaging of ^{89}Zr-DOTA-SPIONs

PET Imaging

To evaluate the pharmacokinetics of ^{89}Zr-DOTA-SPIONs and to assess their *in vivo* stability, mice were injected intravenously (via the tail vein) with the radiolabelled nanoparticles containing ~1 MBq activity. PET imaging displayed activity in the lungs (Lu), liver (Li), spleen (S) and kidneys (K) on day 0 (Figure 5.10). On day 1 onwards, the activity in the lungs and kidneys appeared to decrease, with the liver and spleen signal remaining constant. Activity in the bones (B), particularly at the knee and shoulder joints and down the spine, appeared to become more intense from day 1.

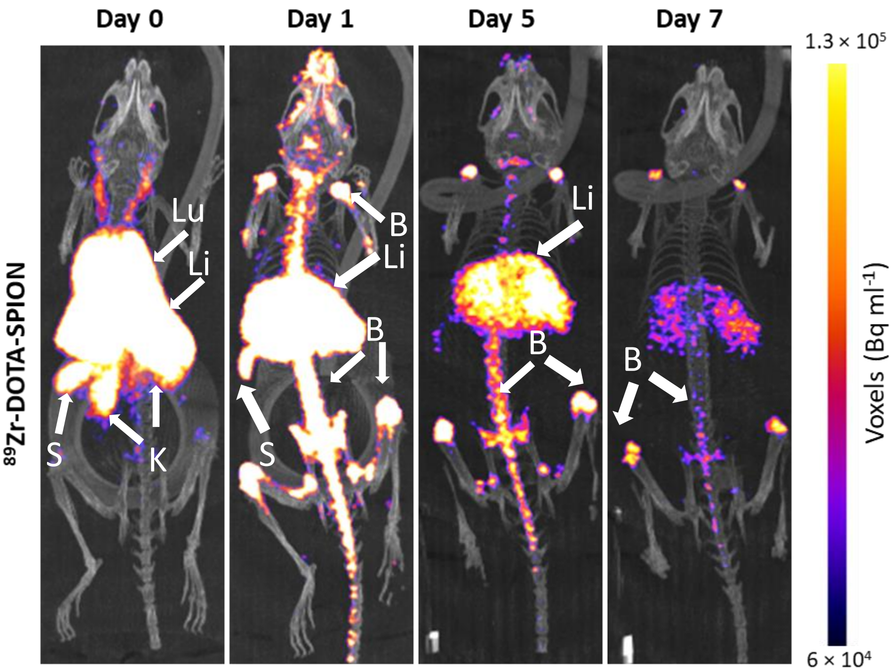

Figure 5.10: Representative whole-body biodistribution of ^{89}Zr-DOTA-SPIONs imaged by PET/CT following IV injection in mice on days 0 (day of injection), 1, 5 and 7. Labels: Lu = lungs, Li = liver, S = spleen, K = kidneys and B = bones. Note that the overall strength of the PET signal reduces over time due to natural decay of the isotope.

Changes in the biodistribution of ^{89}Zr-DOTA-SPIONs were quantified by drawing 3D ROIs around the lungs, liver and spleen of the animals at each time point and calculating the activity signal there. The 'remaining' activity was determined and comes mostly from the signal seen in the bones, as well as the small amount of activity seen in the kidneys on day 0. The whole-body biodistribution of ^{89}Zr-DOTA-SPIONs following systemic administration is seen in Figure 5.11 and is expressed as a percentage of the total body activity. The quantification data revealed that the relative liver signal was constant over the 7-day time course, with the proportion of activity measured on each day being statistically the same. This was also true for the spleen signal. The lung signal; however, dropped from 17 ± 2% to 0% from day 0 to 1, which was statistically significant (P = 0.0000003). On the other hand, the 'remaining' signal, which accounts for the activity seen in the bone, displayed a significant increase in activity from day 0 to 1 (40 ± 3% to 57 ± 3%, P = 0.0006). The measured 'remaining' activity for the rest of the time points (days 1 to 5 to 7) were statistically the same, suggesting that the strong signal seen in the bones from day 1 onwards remained constant.

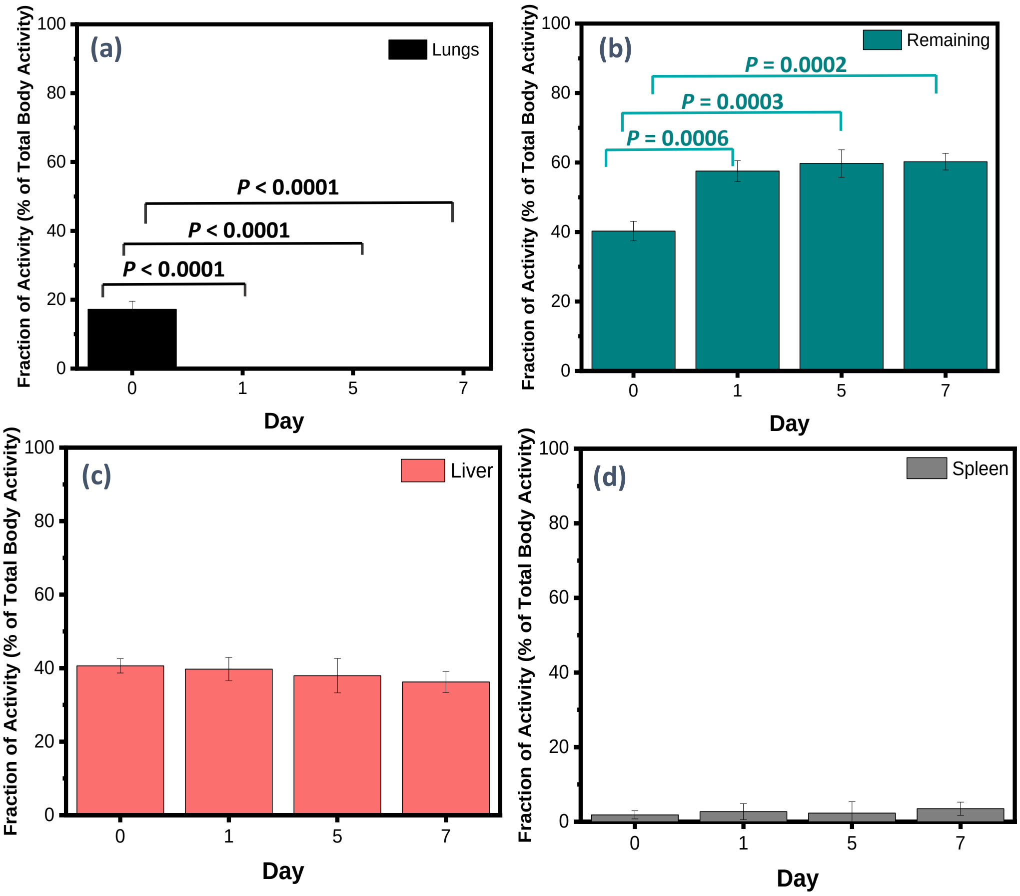

Figure 5.11: 3D ROI quantification of PET signal in **(a)** lungs, **(b)** 'remaining', which accounts for signal in the kidneys and in the bones (spine/joints) **(c)** liver and **(d)** spleen following IV injection of ^{89}Zr-DOTA-SPIONs. Quantification of the PET signal revealed statistically significant differences in the distribution data over the 7-day time course for both the lungs and 'remaining' (one-way ANOVA; $P < 0.001$). As indicated by the black bars **(a)**, there was a significant decrease in lung signal from day 0 (17 ± 2%) to day 1 (0%), day 5 (0%) and day 7 (0%) ($P < 0.0001$; Tukey's post-hoc test). As indicated by the green bars **(b)**, there was also a significant increase in 'remaining' signal due to bone deposition from day 0 (40 ± 3%) to day 1 (57 ± 3%), day 5 (60 ± 4%) and day 7 (60 ± 2%) ($P = 0.0006$; Tukey's post-hoc test). Both the liver **(c)** and spleen signals **(d)** remained statistically the same over the 7-day time course (one-way ANOVA; $P > 0.05$). Data are shown as mean ± SD, n = 3.

MR Imaging

To confirm the findings from PET, MRI was employed 24 h after the IV injection of ^{89}Zr-DOTA-SPIONs (day 1) and then on days 5 and 7. The same mice that were imaged via PET were imaged via MR, and the SPION dose corresponded to ~200 µg iron per mouse. A homogeneous hypointense contrast was seen in the liver on day 1, which was weaker on days 5 and 7 (Figure 5.12). This observation was confirmed through quantification of the hepatic T_2* relaxation time (Figure 5.13a), which revealed a significant decrease from baseline to days 1 and 5 ($P = 0.007$, $P = 0.03$, respectively; one way ANOVA). At the 0.05 level of significance, the baseline hepatic T_2* relaxation time was not different from that of day 7 ($P = 0.057$), which suggests that iron began to clear from the liver between days 5 and 7.

Figure 5.13b displays representative decay curves of T_2* signal of the livers at baseline, day 1, day 5 and day 7 as a function of echo time. The T_2* signal in the liver on day 1 decayed much more rapidly than at baseline due to the presence of a high concentration of ^{89}Zr-DOTA-SPIONs. The signal decay on days 5 and 7 occurred more slowly than on day 1, suggesting clearance of ^{89}Zr-DOTA-SPIONs from the liver. Relaxation times of the livers at each time point were derived from these curves.

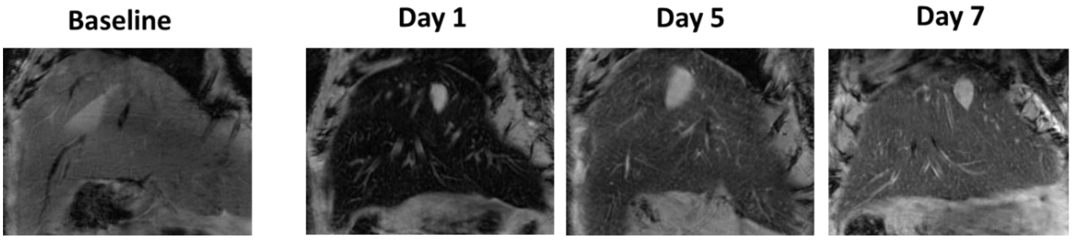

Figure 5.12: Representative T_2* weighted images of mice livers at baseline and following IV injection of ^{89}Zr-DOTA-SPIONs at days 1, 5 and 7. The latter images revealed hypointense contrast compared to baseline due to the presence of ^{89}Zr-DOTA-SPIONs.

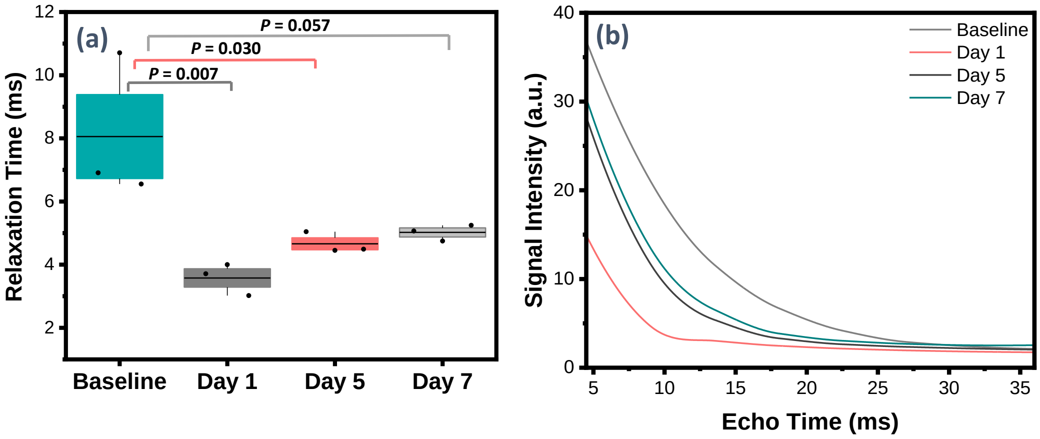

Figure 5.13: (a) The T_2* relaxation time of the liver before (baseline) and up to 7 days post IV administration of ^{89}Zr-DOTA-SPIONs. In the livers, T_2* relaxation times revealed significant differences between baseline and days 1, 5 and 7 (baseline, 8.06 ± 2.30 ms; day 1, 3.58 ± 0.50 ms; day 5, 4.66 ± 0.33 ms; day 7, 5.02 ± 0.25 ms; one-way ANOVA, $P = 0.0096$). Baseline and day 1 and baseline and day 5 are statistically different from one another ($P = 0.007$ and $P = 0.030$, Tukey's post-hoc test). By day 7, the difference in T_2* relaxation time compared with baseline levels was no longer statistically significant ($P = 0.057$). n = 3 **(b)** Representative curves showing changes in signal intensity as a function of echo time at baseline, day 1, day 5 and day 7. Lines represent the exponential fit of the data from where the relaxation time is derived.

5.4 Discussion

The work in this chapter assessed the pharmacokinetic properties of ^{89}Zr-DOTA-SPIONs following a systemic injection in mice. The main aim was to assess the *in vivo* stability of the particles so as to determine whether the hybrid particles would be suitable for labelling and tracking RAW cells *in vivo*.

Radiolabelling of DOTA-SPIONs

DOTA-SPIONs were labelled with the radionuclide, ^{89}Zr, via room temperature incubation with ^{89}Zr-oxalate. The extent of the reaction was monitored by TLC, which revealed an increase in radiolabelling yield with increasing time (Figure 5.8a). At 3 hours after incubation, 93% radiolabelling yield was achieved and this increased to 96% 24 hours after the incubation. On the other hand, the radiolabelling yield of the control particles (mixed dextran SPIONs) reached 90% within 0.5 hours. As discussed in Chapter 3, the high binding of Zr to the control particles is likely due to the non-specific, electrostatic binding of $[^{89}Zr(C_2O_4)_4]^{4-}$ to the polycationic DEAE-dex chains of the SPIONs. The quicker kinetics of the mixed dextran SPION radiolabelling reaction may be attributed to there being more DEAE-dex chains available for $[^{89}Zr(C_2O_4)_4]^{4-}$ to interact with, whereas in DOTA-SPIONs, the polymer shell is decorated with the DOTA macrocycle and thus has fewer DEAE-dex chains available for the radionuclide to electrostatically bind to.

Although DOTA-SPIONs achieved almost 100% binding with ^{89}Zr according to TLC measurements, most of the activity (85%) washed off the particles following 2 x spin filter washes with ultrapure water (Figure 5.8b). This suggests that the electrostatic interaction between ^{89}Zr and DOTA-SPIONs was weak. In Chapter 3, ICP-OES was used to quantify the amount of non-radioactive Zr on DOTA-SPIONs following spin filter washes. Although little to no Zr was measured in the supernatant of the washes in non-radioactive experiments, the amount of Zr that washed off the particles in these experiments was likely below the limit of detection for ICP-OES analysis (1 ppb). On the other hand, the radioactive dose calibrator was able to detect ^{89}Zr at very low concentrations in the supernatant of the washes.

Since a great deal of activity was lost from the particles during purification, phantoms were created to determine the lowest amount of ^{89}Zr required to generate a PET signal. Particles that contained as little as 0.1 MBq ^{89}Zr displayed signal in PET imaging (Figure 5.9b). ^{89}Zr-DOTA-SPION phantoms also displayed hypointense contrast in T_2* weighted images at concentrations as low as 0.15 mM (Figure 5.9a). Since PET imaging of the phantoms provided a strong signal at activities of 0.6 MBq and the activity was detected at activities as low as 0.1 MBq, mice received an IV injection of ^{89}Zr-DOTA-SPIONs containing 1 MBq radioactivity and 200 µg Fe. Because a lot of activity washed off the particles, a much higher iron dose than what is typical (about 25 µg Fe) was given to animals, in order for them to receive sufficient ^{89}Zr activity.

PET Imaging

Mice were imaged by PET immediately after the systemic injection of particles, which revealed high signal in the liver, lungs, spleen and kidneys (day 0, Figure 5.10). The immediate, strong signal in the liver was likely due to the large size of the particles (140 nm, see Chapters 3,4), since particles of diameters over 100 nm are rapidly taken up by Kupffer cells of the liver[260]. The liver signal remained strong and constant over the 7-day time course (Figure 5.11), which suggests that the particles were cleared via hepatobiliary excretion. There was also a small and constant signal in the spleen over the 7-day imaging period, which is due to sequestration of the particles by the MPS. Since ^{89}Zr-oxalate has not been shown to accumulate in high amounts in the spleen[92], the signal there is likely due to the presence of radiolabelled particles and not leached or unbound ^{89}Zr.

There was a strong PET signal seen in the lungs on day 0 (17 ± 2%), which is likely due to the high vascularisation of the lungs and the fact that this organ is highly perfused, meaning that the particles localised there rapidly before moving to other organs in the body. However, the lung signal dropped to 0% on day 1, without there being an increase in liver or spleen signal, which is where we would expect ^{89}Zr-DOTA-SPIONs to localise to. In 2015, Abou *et al.*[92] investigated the behaviour of IV administered ^{89}Zr-oxalate in mice and discovered that within 8 hours post-injection, the radioactive complex accumulated in the heart and lungs. The researchers found that, following the 8 hour period, the activity measured in the heart and lungs was then rapidly cleared in favour of bone deposition. Interestingly, as seen in Figure 5.11, the drop in the proportion of activity in the lungs from day 0 to day 1 (- 17%) is the same as the increase in the proportion of the 'remaining' activity from day 0 to day 1 (+ 17%). This suggests that the activity in the lungs seen on day 0 was, in fact, due to the presence of unbound/free ^{89}Zr, which circulated in the blood, accumulated in the highly vascularised and perfused lungs, then deposited in the bone. This finding confirms that ^{89}Zr-DOTA-SPIONs are not completely stable *in vivo*.

As seen in Figures 5.10 and 5.11, there was an increase in the 'remaining' signal from days 0 to 1, which accounts mostly for the signal accumulation in the bones. This increase was observed qualitatively in Figure 5.10, with a marked increase in signal seen in the joints and down the spine of mice on day 1 compared to day 0. It was also measured quantitatively, with a significant increase between the 'remaining' signal on day 1 compared to day 0 (P = 0.0000003). The accumulation of radioactivity in the bones indicates that ^{89}Zr is no longer bound to its tracer (SPIONs)[283]. As discussed above, we propose that the attachment of ^{89}Zr to DOTA-SPIONs is via a weak electrostatic interaction, hence the lability of the SPION-zirconium-89 bond and the high activity quantified in the bones.

Chen *et al*. reported the synthesis of chelate-free ^{89}Zr labelled silica nanoparticles via the electrostatic binding of $^{89}Zr^{4+}$ to deprotonated silanol groups ($-Si-O^-$) on the surface of spherical silica nanoparticles ($dSiO_2$-NPs)[284]. Following IV injection of $^{89}Zr^{4+}$ labelled $dSiO_2$-NPs in mice, the particles began to display a significant bone uptake on day 1 post-injection, which increased further on day 3 post-injection. This demonstrates the *in vivo* instability of electrostatically radiolabelled nanoparticles and the osteophilicity of $^{89}Zr^{4+}$. No further increase in bone was seen after day 3 and the clearance of ^{89}Zr from the bone was slow. The researchers named the rapid increase in bone signal from day 0 to day 3 the 'burst detachment', which was followed by a period of 'slow clearance'[284].

For ^{89}Zr-DOTA-SPIONs, a similar, rapid increase in bone signal was observed from day 0 to day 1, which may be explained by a 'burst detachment' of ^{89}Zr ions from the particles. On days 1, 5 and 7, the 'remaining' (bone) signals were statistically the same ($P > 0.05$), showing that no further amount of ^{89}Zr detached from DOTA-SPIONs and deposited in the bone. This suggests that, although a large amount of weakly associated ^{89}Zr ions detached from the particles and deposited in the bone, the activity that was more tightly bound with DOTA-SPIONs remained bound to the particles over the 7 day imaging period, and localised predominantly to the liver.

MRI

The stability of the more tightly bound ^{89}Zr-DOTA-SPIONs is further demonstrated in the MRI of mice. The images of mice livers in Figure 5.12 revealed hypointense contrast on days 1, 5 and 7, which signified the presence of ^{89}Zr-DOTA-SPIONs due to the uptake of the particles by Kupffer cells of the MPS. The uptake of particles by the liver was confirmed by T_2* relaxation measurements, which revealed statistically significant reductions in relaxation times on days 1 and 5 compared to baseline. Day 7 was no longer statistically different to baseline but was close ($P = 0.057$), suggesting that the particles had just begun to be eliminated from the liver. The T_2* relaxation times on days 1, 5 and 7; however, were statistically the same ($P > 0.05$). This result matches the PET data for the liver, which revealed a strong and constant signal there over the 7 day time course. The colocalisation of the signals in the liver suggest that the particles that were sequestered there remained bound and were stable.

The liver on day 1 in Figure 5.12 is much darker than the liver on day 1 in Figure 5.6b, where mice received a systemic injection of ^{Nat}Zr-DOTA-SPIONs. This is because in the study involving ^{89}Zr-DOTA-SPIONs, the animals received a much greater dose of iron (200 µg) in order for them to be administered enough radioactivity for PET, whilst in the non-radioactive experiment, animals received just 25 µg iron. In the radioactive experiments, mice tolerated the particles well, despite receiving such a high dose of iron. This demonstrates the biocompatibility of DOTA-SPIONs.

Although it appears that some of the electrostatically bound ^{89}Zr-DOTA-SPIONs remained stable *in vivo* due to the corresponding liver signals observed in PET and MRI, there was still a significant amount of bone uptake of the particles following IV administration. This suggests that ^{89}Zr-DOTA-SPIONs are not completely stable *in vivo*. Having a stably coordinated hybrid PET/MRI tracer is of high importance in the tracking of cells so that their *in vivo* distribution can be qualified without there being any misleading signals (i.e. in the bone). Thus, these particles were not taken forward for cell labelling and tracking studies.

Due to the affinity of ^{89}Zr-DOTA-SPIONs for uptake by Kupffer cells, these particles may be more suited towards the targeting and imaging of the liver. Alcoholic-associated liver disease (ALD) is a major cause of chronic liver injury and is a prominent factor in liver-related mortality in the West[285]. ALD represents a spectrum of liver injuries resulting from the use of alcohol, which includes cirrhosis, fibrosis and steatosis[286]. The activation of Kupffer cells to an M1 phenotype through the secretion of pro-inflammatory cytokines is a key stage in the progression of ALD thus limiting the polarisation of the cells to this pro-inflammatory phenotype is considered an attractive therapeutic strategy[287]. The delivery of anti-inflammatory cytokines, such as IL-10, to the liver can facilitate the re-education of Kupffer macrophages to an M2 phenotype[288], minimising ALD progression. Nanoparticles are an attractive platform for the delivery of cytokines and allow a high payload of such molecules to be delivered to organs of interest[289]. IL-10-functionalised silver nanoparticles (AgNPs) have been developed by Baganizi *et al.*, for the treatment of inflammatory diseases[290]. This was achieved through the EDC coupling of IL-10 proteins onto the poly(vinylpyrolidone) coating of the AgNPs, which contains free carboxylate groups. A similar approach could be applied to functionalise ^{89}Zr-DOTA-SPIONs with IL-10 for the treatment of inflammatory liver disease. The DOTA molecules on these probes contain free carboxylate groups, which can be used to couple with the free amine groups that are on IL-10 using an EDC coupling approach. This would not interfere with radiolabelling since the mechanism of ^{89}Zr attachment to DOTA-SPIONs appears to be via a non-competing, electrostatic mechanism. The advantage of IL-10 functionalised ^{89}Zr-DOTA-SPIONs is that they could offer a *theranostic* approach to the treatment of liver disease: the SPION/MR component could allow for anatomical imaging of liver damage, the ^{89}Zr/PET component could confirm and quantify the localisation of the agent in the liver and the IL-10 component could offer therapeutic capabilities.

5.5 Conclusions

The work presented in this chapter demonstrates that the proposed electrostatically bound ^{89}Zr-DOTA-SPIONs are not completely stable *in vivo* due to demonstrating a high uptake in the bones via PET imaging. Although signal coregistration was observed in the liver with PET and MRI, the major drawback of these particles is that weakly associated ^{89}Zr ions can dissociate *in vivo* and produce signals elsewhere in the body. Because of this, these particles were not used for cell tracking since they could possibly produce confusing signals upon administration of labelled cells, which would prevent their *in vivo* distribution from being accurately monitored and quantified. Instead, ^{89}Zr-PCTA-SPIONs, which have shown the ability to chelate Zr ions[93], were utilised for macrophage tracking and this work is discussed in Chapter 6.

Chapter 6

Multimodal Imaging of ^{89}Zr-PCTA-SPION Labelled RAW 264.7 Cells in a Murine Model of Renal Ischaemia/Reperfusion Injury

6.1 Introduction

Studies have shown that following intravenous (IV) administration, stem and stromal cell-based therapies are unable to traffic to injured organs due to them experiencing the pulmonary first pass effect, whereby cells become entrapped in the lungs and die[291-293]. Macrophages, on the other hand, have demonstrated the capacity to pass through the lungs when administered IV[11] and home to sites of injury[294]. Because of the ability of macrophages to survive and distribute throughout the body, they are a suitable cell type for testing the feasibility of ^{89}Zr-PCTA-SPIONs as cell tracking probes.

This chapter will discuss the biodistribution, fate and persistence of IV injected cells in healthy and injured mice, and will study the homing capabilities of firefly luciferase (FLuc^{+}) expressing macrophage-like RAW 264.7 cells labelled with ^{89}Zr-PCTA-SPIONs in a murine model of kidney injury. This will allow the value of the hybrid probes as cell tracking agents to be assessed, and will help to confirm the homing abilities of macrophage-like cells to injured kidneys.

Fate and Biodistribution of IV Administered Macrophages in Healthy Animals

To understand the *in vivo* behaviour of IV administered macrophages, studies involving the labelling and tracking of the cells have been performed in healthy animals. In 2008, Dou *et al.* reported the use of bone marrow-derived macrophages (BMDMs) as ‘Trojan horse’ vehicles for anti-retroviral drug delivery in mice[295]. To visualise how the macrophages distribute in the body following IV injection, the cells were first labelled with imaging agents and their biodistribution was monitored. Macrophages were labelled with the nuclear imaging agent, ^{111}indium-oxine, and the cells were tracked using single-photon emission computed tomography (SPECT). Radioactivity was mostly detected in the lungs on the day of injection, which is expected, since the lungs are the first vascular bed that cells encounter upon IV injection. However, by day 1, there was a marked reduction in the SPECT signal detected in the lungs, which was concurrent with a significant increase in the amount of radioactivity detected in the liver and spleen.

MRI was employed as a secondary imaging technique to confirm the findings from SPECT imaging, which was achieved through the labelling of macrophages with Feridex® SPIONs. MR revealed strong hypointense contrast in the liver and spleen 24 hours post administration of macrophages, which is in agreement with the SPECT data. The results from this study suggest that macrophages can pass through the lungs and distribute to other organs in the body. However, the work from this report is limited in that the macrophages used did not express genetic reporters for bioluminescence imaging (BLI) thus the proportion of live cells delivered to each organ was not assessed. Since nanoparticles and radiotracers can leach from cells and lead to false-positive signals, it is unclear if the signals and contrast detected in the liver and spleen were due to the administered macrophages themselves, or from SPION and ^{111}indium-oxine debris that were sequestered by resident macrophages of these organs.

A recent report from our group has addressed the issue of gaining information on the viability of administered RAW 264.7 cells by applying a bimodal cell tracking strategy, which comprised BLI and multispectral optoacoustic tomography (MSOT) imaging[11]. The RAWs utilised in this study expressed FLuc, which allowed for BLI, whilst labelling the cells with gold nanorods (GNR) permitted MSOT imaging. Following IV administration into healthy mice, the majority of *in vivo* FLuc-BLI signal was concentrated in the lungs; but some signal was observed more posteriorly. *Ex vivo* BLI was performed within 1 hour of macrophage administration to quantify more accurately the intra-organ distribution of the live cells. This revealed bioluminescence (BL) signal predominantly in the lungs; however, weaker signals were detected in the spleen, liver, kidneys and brain, which again suggests that RAWs, a macrophage-like cell line, can pass through the pulmonary circulation.

MSOT was performed to confirm the findings from BLI, as well as to study the temporal dynamics of macrophage migration. Following IV injection of the GNR-labelled cells, signal intensity in the liver and spleen immediately increased for the first 90 minutes before it began to plateau. Signal intensity in the kidney; however, remained close to basal levels. MSOT data confirmed the findings from BLI and add to the evidence that macrophages and macrophage-like cells have the ability to avoid sequestration by the lungs and can persist in other organs of the body.

Fate and Biodistribution of IV Administered Macrophages in Murine Models of Kidney Injury

When applied in pre-clinical models, macrophages have shown the ability to ameliorate acute kidney injury (AKI)[296], a disease which is estimated to contribute to 1.7 million deaths per year[297]. Since macrophages have been shown to bypass the vascular bed of the lungs following IV administration in healthy animals[11, 295], it has been postulated that macrophages administered in models of kidney injury can also pass through the pulmonary circulation and home to the site of the damaged organ.

Guiteras *et al*. reported the homing capabilities of macrophages in a murine model of unilateral ureteral obstruction (UUO)[294], which was assessed through the labelling of cells with a near-infrared (NIR) fluorescent dye and subsequent cell tracking via fluorescent imaging (FI). Fluorescent labelled macrophages were administered to mice 7 days post UUO injury via tail vein injection, and the animals were imaged by FI 24 hours post administration of the cells. *In vivo* imaging revealed a strong signal exclusively in the liver, whilst *ex vivo* imaging, performed 48 h post administration of macrophages, confirmed the high fluorescence signal intensity in the liver, as well as revealing signal in the spleen, lungs, heart, bowel and, importantly, in the kidneys. The fluorescence signal detected in several organs of the body demonstrates the ability of macrophages to extravasate the lungs.

Closer *ex vivo* analysis of the kidneys revealed a significantly greater fluorescence signal in the obstructed kidney compared to the healthy kidney, which suggests the homing capabilities of macrophages to sites of renal injury[294]. However, there are some problems with the imaging strategy applied in this study. Firstly, the macrophages used were not luciferase expressing thus the proportion of live cells delivered to the kidneys could not be determined using BLI.

Instead, the macrophages were labelled with a lipophilic fluorescent dye, which can transfer to host cells and create false positives during imaging[298]. In addition to this, the kidneys emit intense autofluorescence, which can increase further upon renal injury[299]. Because of these issues, the fluorescence signal detected in the obstructed kidney may not be an accurate reflection of the true number of macrophages that were present there.

A similar study was recently published by our group, which assessed the homing capabilities of IV administered FLuc$^+$ RAW cells in a murine model of unilateral renal ischaemia/reperfusion injury (IRI) using BLI[300]. Mice were imaged by BLI immediately following injection of the cells, which displayed a high signal in the lungs, as well as signal spread posteriorly throughout the body and in the head, again demonstrating the ability of macrophage-like cells to extravasate the pulmonary circulation. By day 1, signal was only observed in the lungs and the liver. *In vivo* findings were confirmed by *ex vivo* BL analysis, a more sensitive technique, which revealed signal in the lungs, liver and spleen, as well as in the kidneys, suggesting that RAW cells can survive and be retained there. The amount of BL signal detected in the injured kidney was significantly greater than that detected in the healthy kidney, which suggests that IV injected RAW cells can home to sites of renal injury. This is possibly due to chemoattraction, since it is established that chemokine-mediated macrophage infiltration occurs during ischaemic AKI[301].

The inability to quantify differences in BL signal in healthy vs injured kidneys *in vivo* is due to a combination of the low spatial resolution of BLI, signal attenuation from surrounding tissues, signal saturation in other organs (e.g. the lungs, liver and spleen), as well as the surgical scar overlying the injured kidney. *Ex vivo* analysis is not an ideal solution since it requires culling animals, which is in direct conflict with the 3 Rs of humane animal research (replacement, reduction and refinement). Better combinations of imaging modalities are required for understanding the biodistribution, persistence, fate and homing capabilities of macrophages *in vivo*.

Imaging Modalities for Tracking Macrophages to the Kidney

As detailed in Chapter 1, there are several imaging modalities that can be applied in the tracking of cell therapies. This section will discuss the advantages and disadvantages of three of the main imaging modalities (MRI, optical and PET) and how they can be used for tracking cells to the kidney, which is displayed schematically in Figure 6.1

MRI

A key advantage of MRI as a modality for cell tracking is that it offers very high spatial resolution, which means that it can provide detailed anatomical information of organs[62]. For tracking cells to the kidney, MRI can offer an insight into the intra-organ distribution of cells, noting their precise location within the renal tissue. An issue with using MRI for cell tracking to the kidney; however, is that cells are often labelled with SPIONs, which create negative (dark) contrast[302]. Thus, it can be difficult to quantify cell numbers within the kidney and the technique can only be used qualitatively, or semi-quantitatively at best with SPIONs as the labelling probe. This problem is compounded by the fact that renal injury models, particularly IRI, produce blood coagulation within the medulla of the kidney[300], which appears as hypointense contrast. To accurately assess the number of cells delivered to the kidney, MRI is best used in conjunction with another imaging modality that has quantification capabilities.

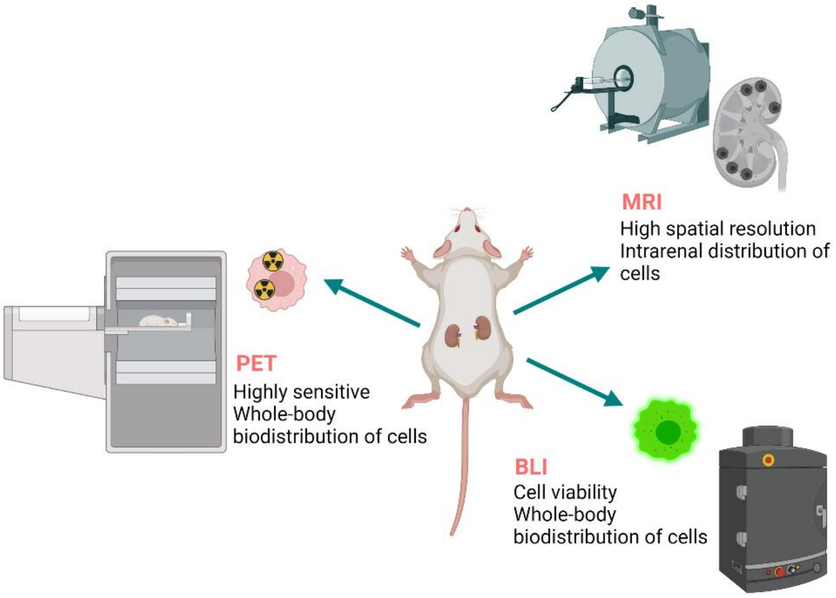

Figure 6.1: A trimodal imaging strategy can help to provide information on whether administered cells can home to an injured organ, for example, a kidney. MRI offers high spatial resolution and can provide detailed information on the intra-renal distribution of cells. PET allows for the whole-body biodistribution of cells to be imaged, is highly sensitive and is fully quantitative so allows for the number of cells within the kidney to be quantified without the requirement of culling animals. BLI can also provide details on the whole-body biodistribution of cells and is an indicator of living cells.

Optical

There is an array of issues associated with using optical imaging (OI), which encompasses FI and BLI, for cell tracking. For instance, light scattering is a common problem because it limits the penetration depth of the modality and reduces its spatial resolution[58]. As discussed earlier in this chapter, tracking cells in the kidney with FI has often relied on the use of fluorescent dyes, which can generate false positives[298], and this issue is heightened by the inherent autofluorescence of the kidneys[299]. Bioluminescence reporter imaging, particularly FLuc-BLI, is a more useful form of OI for cell tracking since BLI is more sensitive and the signals generated are indicators of living cells. However, the technique is still not perfect for *in vivo* cell tracking to the kidney due to the issues of low spatial resolution and signal attenuation, the latter problem meaning that *ex vivo* BL analysis is often required for sensitive detection of small numbers of cells in deep seated organs. To avoid the culling of animals, a more sensitive technique should be applied for tracking cell numbers to the kidney, to corroborate the information provided by BLI.

PET

PET is a highly sensitive nuclear imaging technique that offers excellent temporal resolution, making it ideal for tracking the whole-body biodistribution of administered cells[2]. The modality provides an unlimited penetration depth and is fully quantitative, meaning that following systemic administration, the number of cells that have been delivered to the kidneys can be quantified. PET is limited in its spatial resolution, so the intra-renal distribution of cells cannot be assessed, and a complementary technique such as MRI is required to ascertain such information. Additionally, PET signal is not an indicator of live cells, and can be generated from the leaching of radiotracers from cells, which creates false positives. When applied in cell tracking, it is advantageous to combine PET imaging with BLI, for the detection of live cells expressing genetic reporters such as FLuc.

There are strengths and weaknesses associated with all imaging modalities[303]. Combining BLI, MRI and PET could offer a strong, trimodal imaging strategy that would allow the intra-renal distribution of administered cells to be qualified with MRI, information on the viability of the cells to be ascertained with BLI and the number of cells in the kidneys to be quantified with PET. Used together, this imaging strategy could provide accurate information on the biodistribution, fate and persistence of IV administered cells, as well as on the homing capabilities of the cells to injured kidneys.

Experimental Plan

The aim of this work was to assess the feasibility of ^{89}Zr-PCTA-SPIONs as a cell tracking agent, using RAW 264.7 cells as the cell population, since macrophages and macrophage-like cells have demonstrated the ability to extravasate the lungs and populate other organs of the body following IV administration. Additionally, RAW cells have shown the ability to home to injured kidneys[304]. Because of this, we also aimed to observe and quantify the homing capabilities of FLuc-expressing RAW cells labelled with ^{89}Zr-PCTA-SPIONs to injured kidneys.

To achieve this, PCTA-SPIONs were labelled with zirconium-89 (^{89}Zr). PCTA-SPIONs were synthesised as described in Chapter 3, then were mixed with ^{89}Zr-oxalate overnight at 37°C. Following purification, FLuc^{+} RAW cells were labelled with ^{89}Zr-PCTA-SPIONs for 24 h. Due to time constraints in the project, a free injection of neat ^{89}Zr-PCTA-SPIONs was not administered into healthy animals prior to labelling and tracking the RAW cells. However, we expect the PCTA particles to be much more stable than the DOTA particles since they had shown the ability to specifically chelate zirconium ions. To confirm this, we conducted more rigorous stability challenge tests on ^{89}Zr-PCTA-SPIONs.

Whilst the cells were being labelled, 7-8 week-old male albino C57BL/6 mice underwent a unilateral renal IRI. The following day, labelled RAWs were administered to mice via tail vein injection. Animals were imaged by PET and BLI on day 0, then 24 h later (day 1). Mice were then sacrificed, and their organs were harvested for *ex vivo* analysis using MRI, BLI and PET. The study plan is summarised in Figure 6.2. C57BL/6 mice were selected for this study since the IRI model developed in our group was optimised using this strain of mice. Work from our group has shown that C57BL/6 mice are more sensitive to IRI than BALB/c mice, resulting in an injury that more closely resembles AKI[297]. Additionally, even within the same strain of mouse, different colonies can show different susceptibilities to ischaemic AKI[305]. Thus, it was crucial to use the mice from within our colony for this study, in order to achieve a successful renal injury. Finally, there were excess C57BL/6 mice available in our colony at the time of this study, therefore, in keeping with the NC3Rs, mice that were available were used. The author recognises that the differing genetic backgrounds of the RAW cells and the mice is a limitation of this study.

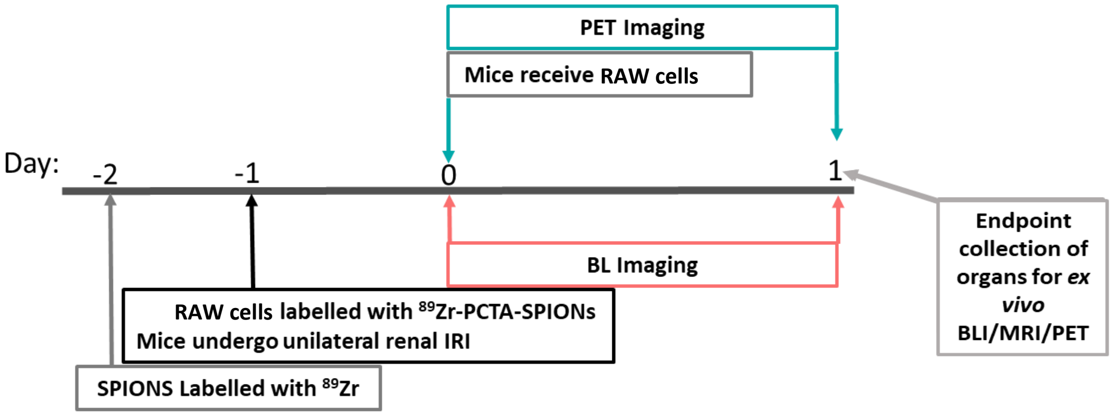

Figure 6.2: Summary of Chapter 6 study plan. PCTA-SPIONs were first radiolabelled with ^{89}Zr to generate ^{89}Zr-PCTA-SPIONs. RAW 264.7 cells were labelled with ^{89}Zr-PCTA-SPIONs overnight. At the same time, mice underwent unilateral renal ischaemia/reperfusion injury (IRI). On day 0, mice received ^{89}Zr-PCTA-SPION^{+}/FLuc^{+} RAW cells and were immediately imaged by PET and BLI. This was repeated on day 1, then the animals were culled and their organs were collected for *ex vivo* imaging.

6.2 Methods

6.2.1 Radiolabelling PCTA-SPIONs with Zirconium-89 Oxalate (^{89}Zr-oxalate)

PCTA-SPIONs and mixed dextran SPIONs were synthesised as described in Chapter 3 and were purified to concentrations of 1 mg ml^{-1}. To both particle types, 20 megabecquerel (MBq, 15 µl) ^{89}Zr-oxalate (Perkin Elmer, Amsterdam, Netherlands) was added, the pH of the particle solutions was adjusted to ~7.0, then 100 µl TRIS buffer (100 mM, pH 7.4) was added.

Both particle mixtures were shaken for 24 hours at 37°C. Following the incubation with ^{89}Zr-oxalate, the particles were washed three times with ultrapure water via spin filtration. The radiolabelling yield was measured using a CRC-15R radioisotope dose calibrator (Capintech Inc, NJ, USA) and was calculated following the three washes using Equation 6.1 below. The particles were sterilised through a 0.22 µm syringe filter with a polyether sulfone (PES) membrane prior to cell labelling.

$$radiolabelling\ yield = \frac{radioactivity\ measured\ on\ particles}{total\ radioactivity\ (on\ particles + in\ \ supernatant\ of washes)}\ x\ 100 \quad \textbf{(6.1)}$$

6.2.2 Phantom Preparation

RAW 264.7 cells were cultured as described in Chapter 2. For imaging cells, RAWs were labelled with ^{89}Zr-PCTA-SPIONs or ^{89}Zr-dex-SPIONs at ^{89}Zr concentrations of 0.3 MBq (^{89}Zr basis) and 12.5 µg ml^{-1} (Fe basis) then were fixed with 4% paraformaldehyde (PFA), resuspended in 1% (w/w) low gelling temperature agarose and loaded into 100 µl polypropylene tubes. The tubes were then mounted in a large holder containing 1% agarose. The phantom was then imaged by PET and MR (parameters found in Chapter 2).

6.3.3 *In Vivo* Studies

Cell Preparation and Administration

For MR and PET tracking, RAW 264.7 cells were labelled with ^{89}Zr-PCTA-SPIONs at a concentration of 12.5 µg ml^{-1} (Fe basis), with the particles containing ~ 8.5 MBq ^{89}Zr, for a period of 24 h. This resulted in an iron concentration of ~ 5 pg Fe cell^{-1} and ~ 0.03 MBq ^{89}Zr per 1 million cells. Following the labelling period, cells were washed with phosphate-buffered saline (PBS) to remove excess particles. Labelled RAWs were scraped, pelleted and resuspended in ice cold PBS and were kept on ice until administration. 200 µl of cell suspension containing ~ 8×10^6 labelled RAWs was administered to each mouse via IV injection.

Animals

General animal methods are described in Chapter 2. To assess the biodistribution, fate and persistence of ^{89}Zr-PCTA-SPION$^+$/FLuc$^+$ RAW cells, 7-8 week-old male albino C57BL/6 mice from an in-house colony managed by the Biomedical Services Unit of the University of Liverpool received a tail vein injection of labelled cells following unilateral renal IRI (n = 5).

Renal Ischaemia/Reperfusion Injury

IRI surgery was performed by Dr Ioana-Roxana Martinas, University of Liverpool. Briefly, mice were anaesthetised and a flank incision was made for unilateral clamping of the renal pedicle for 40 min, using an atraumatic vascular clamp. Following the clamping period, the vascular clamp was removed to allow for restoration of renal blood flow, which was confirmed visually prior to repair of muscle and skin layers. In this model of IRI, renal impairment is observed 24 h post injury[306] thus cells were administered at this time point.

PET/CT

At 30 minutes (day 0) then 24 hours (day 1) after the ^{89}Zr-PCTA-SPION$^+$/FLuc$^+$ RAW cell injection, whole-body PET/CT scans were performed as described in Chapter 2. 3D ROIs were drawn around the lungs, liver, spleen, kidneys and joints of mice for each time point using VivoQuant™ software (Invicro, MA, USA). This allowed the amount of activity, and thus cells, in these organs to be calculated.

BLI

Immediately after PET imaging on day 0 and day 1, mice were administered 150 mg/kg body weight luciferin (Promega, Southampton, UK) intraperitoneally and were imaged 15 min later in a bioluminescence imager. Imaging data were normalised to the acquisition conditions and expressed as radiance (photons/second/cm^2/steradian (p^{-1} s^{-1} cm^{-2} sr^{-1})).

6.3.4 *Ex Vivo* Studies

BLI

For *ex vivo* BLI, mice were culled 10 min post administration of luciferin. Organs were then harvested and immediately imaged. BL signals were quantified by drawing ROIs around the individual organs (lungs, liver, spleen, kidneys). The relative signal intensity per organ was calculated as a percentage of the signal intensity from all organs.

PET

For *ex vivo* imaging of the kidneys, the organs were placed individually in 5 ml flat bottomed centrifuge tubes, which were subsequently secured in a rat bed. The kidneys were then imaged overnight by PET for approximately 12 hours.

MRI

For *ex vivo* imaging of the kidneys, the organs were fixed in 4% PFA then were embedded in 1% (w/w) low gelling temperature agarose for MR imaging. A FLASH T_2^* sequence was applied, the acquisition parameters of which are detailed in Chapter 2.

6.3 Results

6.3.1 *In Vitro* Validation of ^{89}Zr-PCTA-SPION Binding

To assess the efficiency and mechanism of ^{89}Zr binding to PCTA-SPIONs, the particles were radiolabelled overnight with ^{89}Zr-oxalate. The radiolabelling yield was calculated and this was compared with the binding to mixed dextran SPIONs (dex-SPION), as seen in Figure 6.3a. The radiolabelling yield of ^{89}Zr-PCTA-SPIONs following the overnight incubation was 76 ± 5% whilst the radiolabelling yield of ^{89}Zr-dex-SPIONs was 89 ± 5%. To evaluate the binding stability of ^{89}Zr-PCTA-SPIONs and ^{89}Zr-dex-SPIONs, the labelled particles were incubated overnight in either 10% FBS or 50 mM of the chelating agent, DTPA, at 37°C. Following the incubation period, the particles were washed 3 times via spin filtration, using either FBS or DTPA as the washing medium and the amount of radioactivity in the supernatant of each wash was measured. As seen in Figure 6.3b, ^{89}Zr-PCTA-SPIONs lost a small amount of activity (4%) after the first wash in DTPA but no more activity was lost in the second or third washes. ^{89}Zr-dex-SPIONs also lost 4% of the activity after the first wash in DTPA but lost no more activity during the second and third washes. ^{89}Zr-PCTA-SPIONs were completely stable in serum losing no activity after the three washes. However, ^{89}Zr-dex-SPIONs were less stable in serum than ^{89}Zr-PCTA-SPIONs, losing 10% of the activity following 3 serum washes.

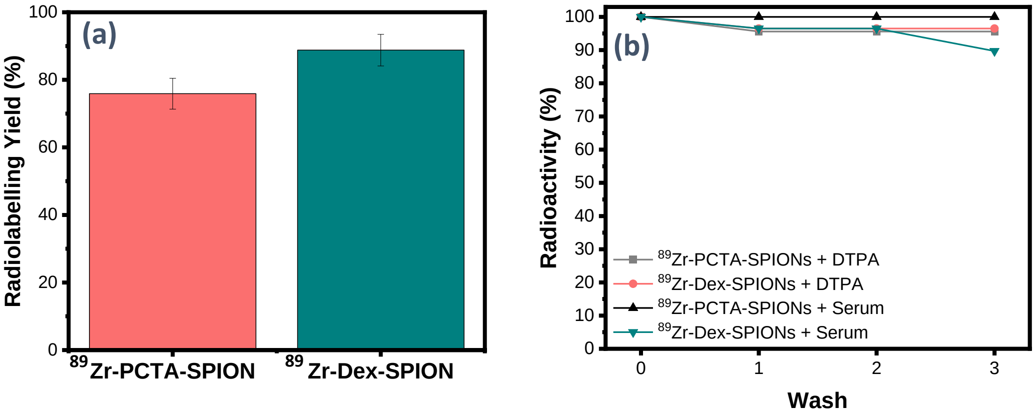

Figure 6.3: (a) Radiolabelling yields of PCTA-SPIONs and dex-SPIONs following overnight incubation with ^{89}Zr. **(b)** Stability challenge studies of ^{89}Zr-PCTA-SPIONs in DTPA (^{89}Zr-PCTA-SPIONs + DTPA) and in serum (^{89}Zr-PCTA-SPIONs + serum) and ^{89}Zr-dex-SPIONs in DTPA (^{89}Zr-Dex-SPIONs + DTPA) and in serum (^{89}Zr-Dex-SPIONs + serum).

To determine whether the macrocycle, PCTA, had chelated $^{89}Zr^{4+}$ under the radiolabelling conditions, q-TOF-MS was performed on radiolabelled PCTA-SPIONs. Figure 6.4 displays the q-TOF-MS of ^{89}Zr-PCTA-SPIONs. There is a mass at *m/z* = 469.3, which corresponds to ^{89}Zr-PCTA (yttrium-PCTA, the product of radioactive decay); however, this peak is very small in intensity. Additionally, there is a large peak at *m/z* = 381.1, corresponding to the unlabelled PCTA macrocycle, which suggests that not a great deal of macrocycle was labelled by $^{89}Zr^{4+}$.

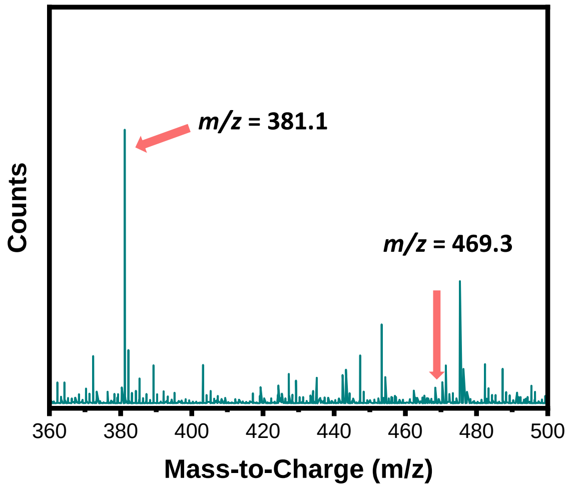

Figure 6.4: q-TOF-MS (positive ion mode) analysis of ^{89}Zr-PCTA-SPIONs in the *m/z* range 360 – 500 displaying a small peak at *m/z* = 469.3, which corresponds to ^{89}Zr-PCTA and a larger peak at *m/z* = 381.1, which corresponds to the unlabelled PCTA macrocycle.

6.3.2 *In Vitro* Imaging of ^{89}Zr-PCTA-SPION Labelled RAW 264.7 Cells

To assess the effect on viability of labelling RAW cells with radioactive SPIONs, the cells were labelled overnight with ^{89}Zr-PCTA-SPIONs and the control particles, ^{89}Zr-dex-SPIONs, at a concentration of 12.5 μg ml^{-1}. The uptake of radiolabelled SPIONs by RAWs was visualised using Prussian blue staining, which displayed blue pigment within the cells compared to control (unlabelled cells). As seen in Figure 6.5, both particle types displayed a similar degree of uptake in RAWs, with blue staining visible in all cells, and the particles displayed minimal extracellular aggregation. Meanwhile, control (unlabelled cells) displayed no staining. RAW cells appeared healthy and were adherent following the incubation with both types of ^{89}Zr-SPIONs, suggesting that the radionuclide has no deleterious effect on cell health.

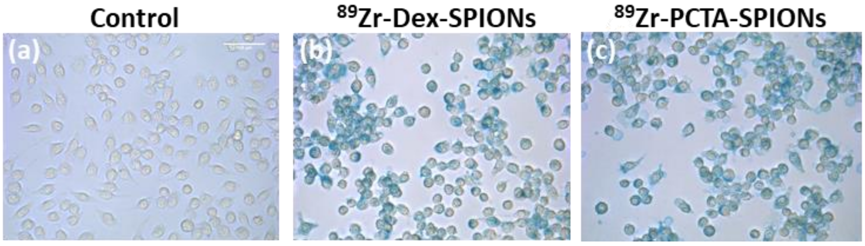

Figure 6.5: Prussian blue staining of RAW 264.7 cells after 24 h labelling with **(a)** just media (no SPIONs), **(b)** ^{89}Zr-dex-SPIONs and **(c)** ^{89}Zr-PCTA-SPIONs at a concentration of 12.5 μg ml^{-1}. Scale bar = 100 μm.

To demonstrate the ability to image ^{89}Zr-PCTA-SPION labelled RAW cells, the cells were fixed and then suspended in agarose at a concentration of 1.3 × 10^{3} cells per μl (Figure 6.6) for combined PET/MR imaging. Cells were labelled with ^{89}Zr-PCTA-SPIONs and the control particles, ^{89}Zr-dex-SPIONs, at concentrations of 0.3 MBq (^{89}Zr basis) and 12.5 μg ml^{-1} (Fe basis). Figure 6.6a displays T_2* weighted images of ^{89}Zr-SPIONs, with RAWs labelled with each particle type exhibiting hypointense contrast, demonstrating the ability of the SPIONs to generate MR contrast when internalised in cells. As seen in Figure 6.6b, RAWs labelled with each particle type also showed a strong signal with PET, displaying the ability of ^{89}Zr-SPIONs to generate nuclear signal while internalised in cells.

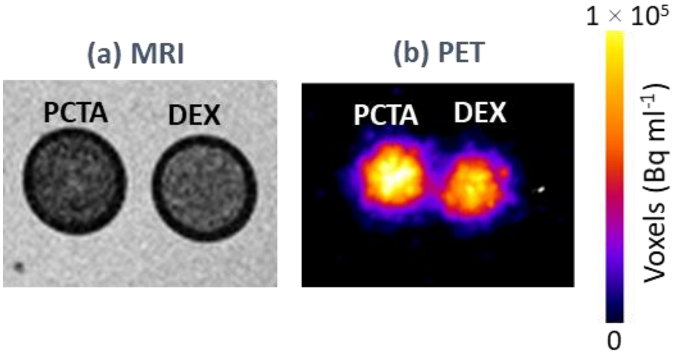

Figure 6.6: (a) Fixed RAW 264.7 cells labelled with ^{89}Zr-PCTA-SPIONS (PCTA) and ^{89}Zr-dex-SPIONs (DEX) at a concentration of 12.5 μg ml^{-1} (Fe basis) that were set in an agarose phantom and imaged via MR with a T_2*-weighted sequence. (**b)** Fixed RAWs labelled by ^{89}Zr-PCTA-SPIONS (PCTA) and ^{89}Zr-dex-SPIONs (DEX) at a concentration of 0.3 MBq that were set in an agarose phantom and imaged by PET/CT. Images correspond to the cross section of two individual tubes, containing the labelled cells and embedded in agarose. Agarose gives a positive (bright) signal in MRI but produces no signal in PET.

6.3.3 *In Vivo* Imaging of ^{89}Zr-PCTA-SPION Labelled RAW 264.7 Cells

PET Imaging

To determine the *in vivo* biodistribution of RAW cells, a combination of PET/CT and BLI was applied. A total of 8×10^6 ^{89}Zr-PCTA-SPION$^+$/FLuc$^+$ cells (containing ~ 0.3 MBq ^{89}Zr) were administered to each mouse via the tail vein 24 hours after the animals had undergone unilateral renal IRI. Mice were imaged by PET 30 minutes after administration of the radiolabelled cells (day 0), which revealed a strong signal exclusively in the lungs, as seen in Figure 6.7. By day 1, the PET signal in the lungs had reduced in intensity, while the signal in the liver and spleen had increased in intensity, with a small amount of signal also visible in the knee and shoulder joints, which was due to the presence of leached/unbound ^{89}Zr.

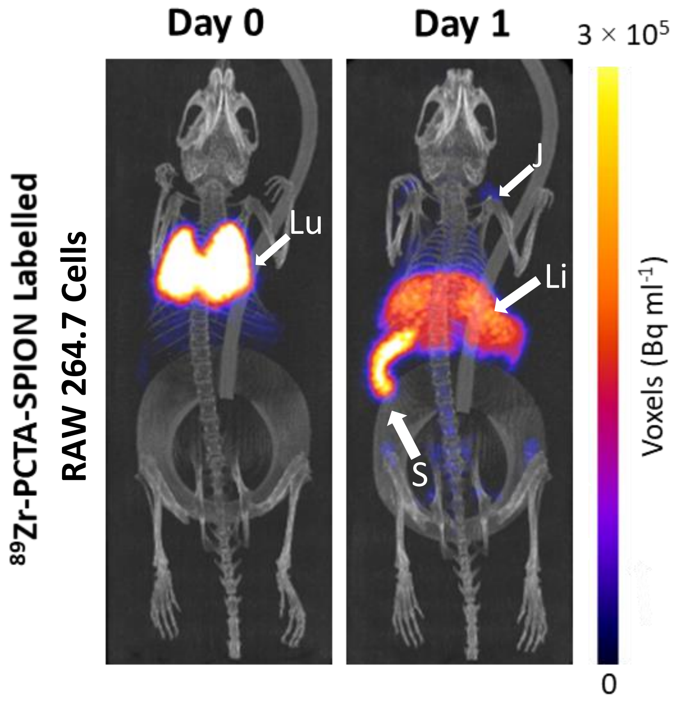

Figure 6.7: Representative whole-body biodistribution of ^{89}Zr-PCTA-SPION labelled RAW 264.7 cells imaged by PET/CT following IV injection in mice that had undergone unilateral renal ischaemia/reperfusion injury (IRI). Animals were imaged on day 0 (day of injection) and day 1. Labels: Lu = lungs, S = spleen, Li = liver, J = joints.

Changes in the biodistribution of ^{89}Zr-PCTA-SPION labelled RAW cells were quantified by drawing 3D ROIs around the lungs, liver, spleen and knee and shoulder joints of the mice at each time point and calculating the signal there. The whole-body biodistribution of the PET signal is seen in Figure 6.8 and is expressed as a percentage of the total body activity. The quantification data revealed a significant reduction in the lung signal from day 0 (87 ± 4%) to day 1 (9 ± 10%, *P* = 0.00007). This was concurrent with significant increases in the liver signal from day 0 (9 ± 2%) to day 1 (44 ± 7%, *P* = 0.0003) and the spleen signal from day 0 (4 ± 1%) to day 1 (43 ± 9%, *P* = 0.0005). There was also a significant increase in the PET signal found in the joints (knees, shoulders) from day 0 (0.2 ± 0.5%) to day 1 (4 ± 2%, *P* = 0.006).

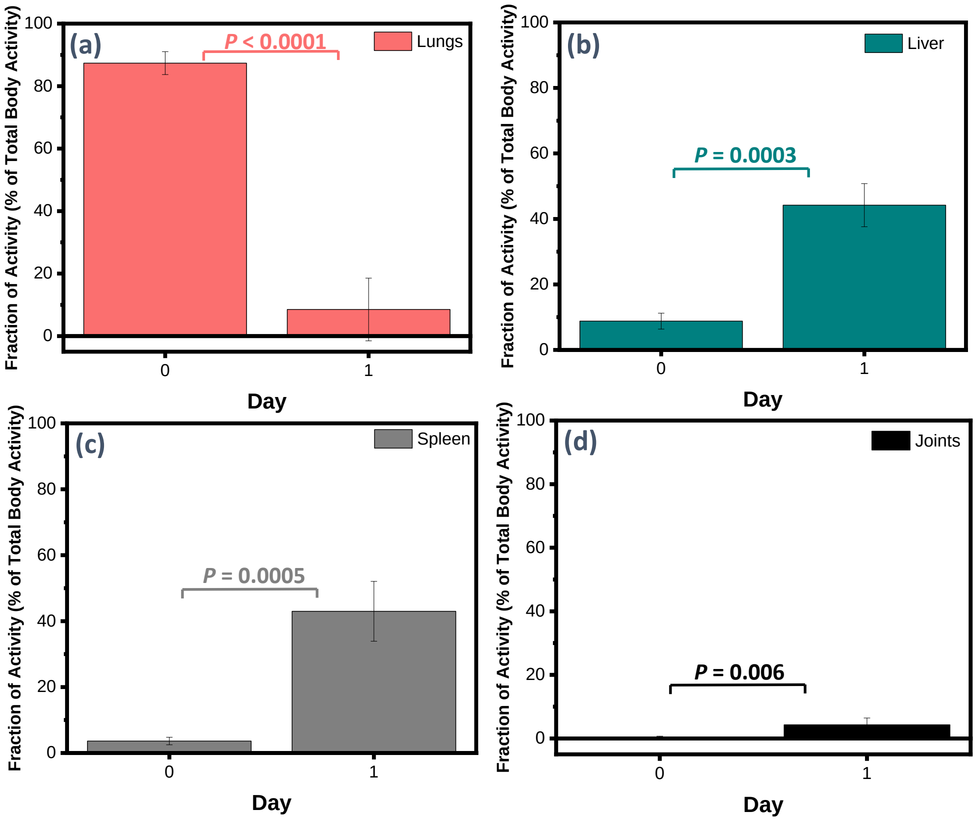

Figure 6.8: 3D ROI quantification of PET signal in **(a)** lungs, **(b)** liver, **(c)** spleen and **(d)** joints following IV injection of ^{89}Zr-PCTA-SPION labelled RAW 264.7 cells. Quantification of the PET signal revealed a statistically significant reduction in the lung signal from day 0 (87 ± 4%) to day 1 (9 ± 10%) (paired t-Test; *P* < 0.0001). There were significant increases in signals in the liver from day 0 (9 ± 2%) to day 1 (44 ± 7%) (paired t-Test; *P* = 0.0003), the spleen from day 0 (4 ± 1%) to day 1 (43 ± 9%) (paired t-Test; *P* = 0.0005) and the joints from day 0 (0.2 ± 0.5%) to day 1 (4 ± 2%)(paired t-Test; *P* = 0.006). Data are shown as mean ± SD, n = 5.

Bioluminescence Imaging

BLI was employed to confirm the findings from PET imaging, as well as to provide information on the viability of the RAWs following IV injection (Figure 6.9a). BL imaging displayed a similar distribution to PET imaging on day 0, with most of the BL signal seen in the lungs. However, by day 1, only a small amount of signal was seen in the lungs for one mouse, with the rest displaying no signal at all, and no signal was observed more posteriorly, i.e. in the liver and spleen, as was seen in PET imaging. The total bioluminescence signal (flux) in the animals was quantified, which revealed a significant reduction in the flux measured on day 1 (5×10^6 p/s) compared to day 0 (2×10^7 p/s) (paired t-Test; $P = 0.019$). This suggested that a significant proportion of cells, approximately 80%, had died within the 24 period.

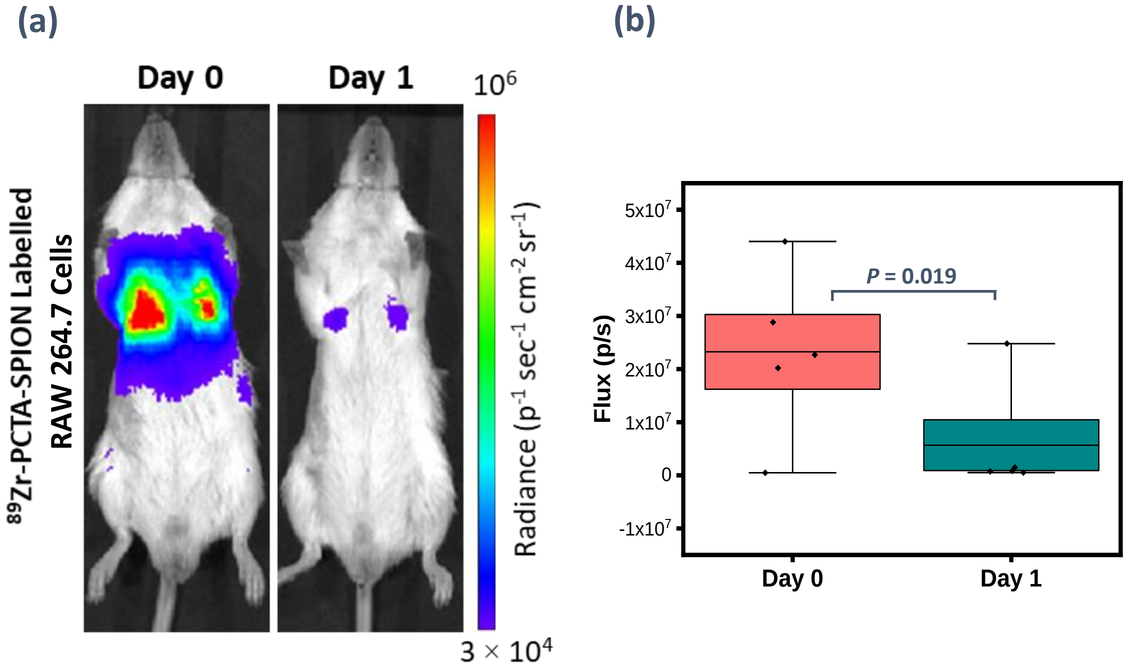

Figure 6.9: (a) Representative biodistribution of RAW 264.7 cells following IV administration, as determined by BLI. Day 0 revealed the biodistribution of RAWs immediately after injection and shows that the cells were confined within the lungs. By day 1, there was only a small amount of signal observed in the lungs in one mouse (shown here), with the rest showing no signal at all. **(b)** Quantification of the total BLI signal revealed a significant reduction in flux (photons per second) from day 0 to day 1 (paired t-Test; $P = 0.019$), which suggested cell death. n = 5.

6.3.3 *Ex Vivo* Imaging of ^{89}Zr-PCTA-SPION Labelled RAW 264.7 Cells

Due to the improved sensitivity of *ex vivo* BLI compared to *in vivo* BLI, the technique was utilised to quantify the proportion of live cells within each organ. Mice were culled 24 hours post administration of RAW cells (day 1) and the individual organs were imaged. As seen in Figures 6.10a and 6.10b, most signal (94 ± 7%) was found in the lungs, followed by the liver (4 ± 5%) and negligible amounts of bioluminescence signal were detected in the spleen (0.8 ± 1%) and kidneys (0.8 ± 1%).

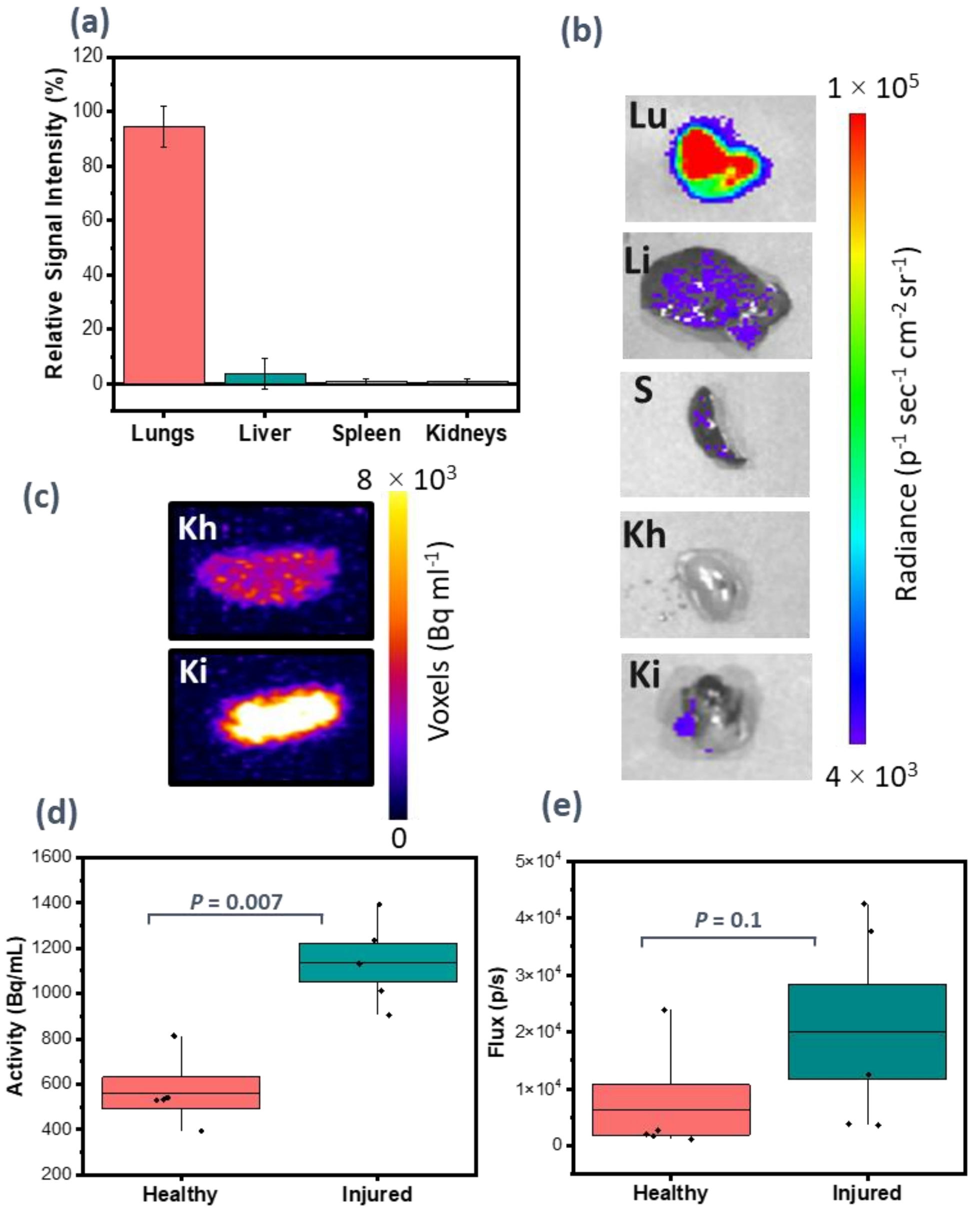

Figure 6.10: (a) *Ex vivo* quantification of the bioluminescence signal intensity of organs 24 h post IV administration of FLuc$^+$ RAW 264.7 cells. Values represent the mean signal intensity measured in each organ and are normalised to the total flux from all organs. Data are shown as mean ± SD (n = 5). **(b)** Representative images of organs imaged *ex vivo* on day 1 post administration of RAW cells. Labels: Lu = lungs, Li = liver, S = spleen, Ki = injured kidney and Kh = healthy kidney. No BL signal was visible in the healthy kidney and only a small amount of BL signal was visible in the injured kidney **(c)** *Ex vivo* PET imaging of a healthy kidney (Kh) and an injured kidney (Ki). There is a greater amount of PET signal present in the injured kidney that underwent IRI. **(d)** Quantification of the PET signal from each of the *ex vivo* kidneys. There was a significantly greater amount of PET signal detected in the injured kidneys that underwent IRI compared to the healthy kidneys (paired t-Test; P = 0.007). **(e)** Quantification of the total BL flux from each of the *ex vivo* kidneys. Whilst there was a greater average amount of flux detected in the injured kidneys that underwent IRI compared to the healthy kidneys, this was not significant (paired t-Test; P = 0.1). n = 5.

Since *in vivo* BLI and PET imaging did not allow differences in the injured and healthy kidney to be determined, *ex vivo* MRI, BLI and PET imaging of the kidneys was employed. As seen in Figure 6.10c, a higher PET signal was detected in the injured kidneys (1100 Bq ml^{-1}) than in the healthy kidneys (600 Bq ml^{-1}) and 3D ROI quantification of the signal revealed this difference to be significant (Figure 6.10d) (P = 0.007). BLI, however, revealed only a small amount of signal in the injured kidney and there appeared to be no signal in the healthy kidney (Figure 6.10b). Closer analyses of the kidneys (Figure 6.10e) revealed a greater amount of flux in the injured kidney (2×10^4 p/s) vs in the healthy kidney (6×10^3 p/s); however, this was not significant ($P > 0.05$).

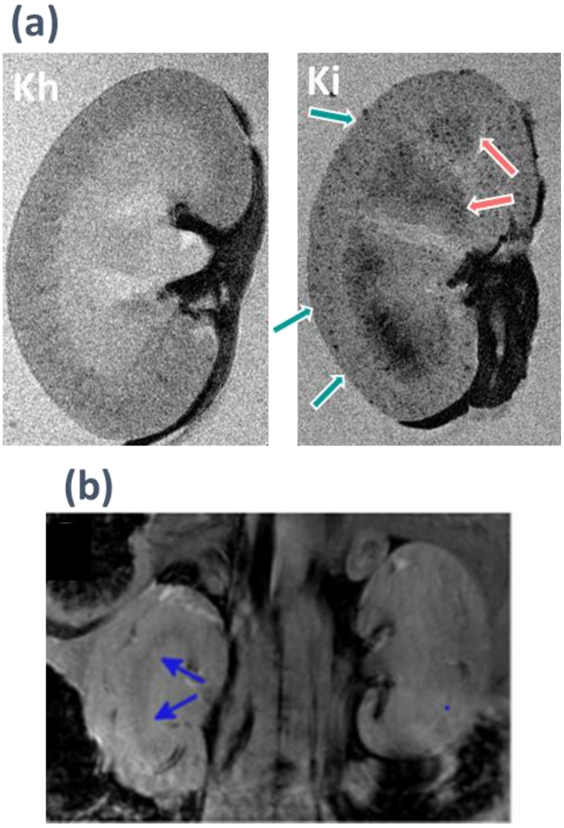

Figure 6.11: (a) *Ex vivo* high-resolution MRI of a healthy mouse kidney (Kh) and an injured mouse kidney (Ki) obtained from applying a T_2^* sequence. More hypointense areas, and therefore cells, appear to be present in the injured kidney that underwent IRI. The green arrows represent hypointense foci, which is due to the presence of RAW cells and the pink arrows represent hypointense contrast due to blood coagulation. **(b)** *In vivo* MR image of a mouse 1 day post IRI that has received no SPION labelled cells. The blue arrows display the hypointense contrast in the medulla, which is a consequence of blood coagulation. This image was not produced from experiments undertaken in this thesis and was reproduced with permission from reference 137.

Ex vivo MRI was employed as a complementary technique to qualitatively confirm any differences between RAW cell distributions in the healthy kidney vs the injured kidney. As seen in Figure 6.11a, there appeared to be a greater deal of hypointense foci located within the cortex of the injured kidney compared to the healthy kidney, which suggests the presence of labelled RAW cells. It is likely that these hypointense foci are due to SPION$^+$ cells (green arrows) and not due to blood coagulation in the injured kidney, which also appears as hypointense contrast (pink arrows), but is localised in the medulla rather than the cortex.

6.4 Discussion

The work in this chapter assessed the biodistribution, persistence and fate of ^{89}Zr-PCTA-SPION^{+}/FLuc^{+} RAW 264.7 cells following IV injection in a murine model of renal IRI. The main aims of this study were to assess the feasibility of the hybrid particles as cell tracking agents. It has been previously shown that RAW cells can home to injured kidneys[304] and so we aimed to apply a trimodal imaging strategy to confirm this observation and to quantify the homing capabilities of the labelled macrophage-like cells to injured kidneys.

Radiolabelling of PCTA-SPIONs

PCTA-SPIONs were labelled with the radionuclide, ^{89}Zr, via incubation with ^{89}Zr-oxalate at 37°C. The radiolabelling yield of ^{89}Zr-PCTA-SPIONs was calculated and this was compared to the radiolabelling yield of the control particles, ^{89}Zr-dex-SPIONs, which gave values of 76 ± 5% and 89 ± 5%, respectively (Figure 6.3a). The higher yield for the control particles compared to the macrocycle-bound SPIONs was also observed in Chapter 5 and is likely to be caused by the high degree of non-specific, electrostatic binding of $[^{89}Zr(C_2O_4)_4]^{4-}$ to the polycationic DEAE-dex chains of the SPIONs. The greater extent of non-specific binding to the control particles may be due to there being more DEAE-dex chains available for the ^{89}Zr ion to interact with, whilst in PCTA-SPIONs, the particles are decorated with macrocycle and so may have fewer polymer chains for $[^{89}Zr(C_2O_4)_4]^{4-}$ to electrostatically bind to.

^{89}Zr-PCTA-SPIONs were characterised by q-TOF-MS, which revealed a peak at $m/z = 469.3$ that corresponds to ^{89}Zr-PCTA (it is actually Y-PCTA since ^{89}Zr decays to yttrium). As seen in Figure 6.4, the peak at $m/z = 469.3$ was small in intensity, which suggests that, although the macrocycle was labelled by ^{89}Zr under the radiolabelling conditions, only a small amount of ^{89}Zr-PCTA formed. This may be because in the non-radioactive Zr labelling studies, a large excess of the Zr source was reacted (micromolar quantities), which may have driven the formation of Zr-PCTA. However, in radiolabelling studies, the amount of ^{89}Zr reacted corresponded to ~ 15 pmol due to the specific activity of the radionuclide.

The respective stabilities of ^{89}Zr-PCTA-SPIONs and ^{89}Zr-dex-SPIONs were compared by incubating and washing both particle types in 10% serum, as well as in the chelating agent, DTPA (Figure 6.3b). ^{89}Zr-PCTA-SPIONs were more stable than ^{89}Zr-dex-SPIONs in serum, losing none of their bound activity after three serum washes, whilst the control particles lost 10% of their bound activity following the same amount of serum washes. The extra degree of stability of ^{89}Zr-PCTA-SPIONs in large, charged serum proteins compared to the control particles may have been due to ^{89}Zr-PCTA-SPIONs having some chelated Zr, whilst the binding of ^{89}Zr to the control particles was only weak and non-specific. Both particles displayed some degree of instability in 50 mM of the chelating agent, DTPA, losing 4% of their bound activity following three DTPA washes. This was likely due to DTPA chelating with non-specifically bound ^{89}Zr and stripping it away. Despite these rigorous washing processes, most of the activity remained bound to both ^{89}Zr-PCTA-SPIONs and ^{89}Zr-dex-SPIONs, suggesting that the non-specific binding of ^{89}Zr to the polycationic SPIONs was fairly stable.

Another radiolabelling mechanism that could be responsible for the observed high stability of ^{89}Zr-PCTA-SPIONs and the control particles is surface radio-mineralisation (SRM), which was described in Chapter 3. Briefly, SRM involves the deposition of ^{89}Zr-oxide onto the surface of SPIONs using heat, and was first reported by Boros *et al*[158]. SRM of ^{89}Zr is not reported to occur at 20 or 30°C but is reported to begin at 40°C. PCTA-SPIONs were labelled at the reduced temperature of 37°C since this is the temperature required to radiolabel the PCTA macrocycle[93]; however, it is possible that some SRM occurred at this temperature. ^{89}Zr-SPIONs produced via the SRM method are reported to be extremely stable to ligand and plasma challenge tests, as well as being extremely stable *in vivo*, displaying very little bone deposition[158]. Since similar *in vitro* stability was observed for ^{89}Zr-PCTA-SPIONs, it is possible that SRM contributed, at least in part, to the binding of ^{89}Zr to PCTA-SPIONs.

In Vitro Imaging

The cellular internalisation of ^{89}Zr-PCTA-SPIONs was studied and was compared to the uptake of ^{89}Zr-dex-SPIONs. Intracellular uptake of the particles by RAW 264.7 cells was confirmed via Prussian blue staining, which revealed no differences in the particles' uptake properties. As seen in Figure 6.5, both ^{89}Zr-PCTA-SPIONs and ^{89}Zr-dex-SPIONs were taken up well by RAW cells, displaying blue pigment within the intracellular space of all cells, with a similar staining pattern and intensity to what was observed for ^{Nat}Zr-PCTA-SPIONs (see Chapter 4). This suggests that the radionuclide, ^{89}Zr, did not exert any deleterious effects on macrophage cell health. Because of this, the labelled cells were next assessed for their ability to show signal/contrast in PET and MRI (Figure 6.6). The cells were labelled with ^{89}Zr-PCTA-SPIONs and ^{89}Zr-dex-SPIONs at concentrations of 0.3 MBq (^{89}Zr basis) and 12.5 µg ml^{-1} (Fe basis). RAWs labelled with either type of particle displayed a similar degree of contrast in MR and signal intensity in PET, suggesting no differences in the binding of ^{89}Zr-PCTA-SPIONs compared to the control particles.

In Vivo Imaging

Due to the good MR contrast and PET signal intensity observed for ^{89}Zr-PCTA-SPION^{+} RAWs, the cells were administered IV to mice following the renal unilateral IRI. Animals were imaged 30 minutes post administration of the cells (day 0) by PET, which revealed a strong signal in the lungs (Figure 6.7). This is expected since the lung microvasculature is the first vascular bed that IV administered cells encounter and become sequestered by. By day 1, the PET signal observed was found mostly in the liver and spleen, with a small amount of signal seen in the shoulder and knee joints. *In vivo* quantification was performed using 3D ROI calculations. As seen in Figure 6.8, quantification of the PET signal confirmed the qualitative observations; a high proportion (87 ± 4%) of the PET signal was measured in the lungs on day 0. By day 1, the proportion of the signal measured in the lungs dropped to 9 ± 10%; meanwhile, the proportion of the signal in the liver increased from day 0 to day 1 (9 ± 2% on day 0 to 44 ± 7% on day 1) and increased in the spleen from day 0 to day 1 (4 ± 1% to

43 ± 9%). This suggests that RAW cells, like macrophages, can bypass the lungs and populate other organs of the body when administered IV, which is consistent with reports in the literature[295, 300].

It was hoped that *in vivo* quantification of the signal within the kidneys could have been obtained; however, no signal intensity was observed in either kidney in the intact animals. Signal was observed in the shoulder and knee joints; however, which occurs when weakly chelated ^{89}Zr separates from its tracer *in vivo* and deposits in these phosphate-rich regions[307]. This suggests that some ^{89}Zr had been released from the cells, which raises the question of whether the PET signals observed in the liver and spleen were due to viable ^{89}Zr-PCTA-SPION^{+} cells or leached ^{89}Zr and/or ^{89}Zr-PCTA-SPION debris. Since mononuclear phagocyte system (MPS) activity is high in the liver and spleen, it is possible that these organs could have sequestered any ^{89}Zr and/or ^{89}Zr-PCTA-SPION debris. However, as we saw in Chapter 5, the spleen activity was very low over the 7 days post IV administration of the similar free particles, ^{89}Zr-DOTA-SPIONs. At the same time, numerous reports have demonstrated that IV administered macrophages typically populate the lungs, then home to the liver and spleen[11, 295, 300], which suggests that the PET signals detected in the liver and spleen in this study were due to ^{89}Zr-PCTA-SPION labelled cells (and not particle debris) that had persisted there.

To address the ambiguity centred on the nature of the PET signals observed in the liver and spleen, BLI was applied, which can provide information on the viability of administered cells. *In vivo* BLI was performed immediately after IV administration of the luciferase expressing RAW cells (day 0), which showed that cells were mostly in the thorax, with a high BL signal intensity observed in the lungs (Figure 6.9a). By day 1, most of the BL signal was no longer visible in the animals, apart from a very weak lung signal in one mouse, which is consistent with reported findings from our group[300]. This was confirmed through quantitative analysis of the total bioluminescence signal (flux, photons/second). As seen in Figure 6.9b, the total whole-body flux of the animals dropped significantly from day 0 to day 1, which suggests that a large proportion of the cells (80%) had died between these time points.

Whilst this excessive cell death could be explained by differences in the genetic backgrounds of the RAW cells and the mice used in this study, remarkably, we have observed similar attrition rates and biodistributions of the RAW cells within BALB/c mice (the correct genetic background) in previous studies conducted in our group. At 24 h-post IV administration of RAW cells in BALB/c mice that had undergone a unilateral IRI, the cells displayed an identical distribution to what was shown in this thesis – with only a small amount of signal remaining in the lungs by day 1[304]. In another study where RAW cells were administered IV to healthy BALB/c mice, 97% of the cells were observed to have died within a 48 hour period[308]. This suggests that other factors, such as the RAW cells themselves or the route of administration, are contributing to the high level of cell death.

Ex Vivo Imaging

Given the poor spatial resolution of *in vivo* BLI, and the significant amount of cell death, it was not possible to assess which organs had been populated by RAWs at day 1. Thus, immediately after *in vivo* imaging on day 1, the animals were sacrificed and their major organs were harvested and imaged via *ex vivo* BLI. Quantification of the BL signal in the individual organs was achieved by drawing ROIs around each of the organs, which revealed that the highest proportion of the BL signal (94 ± 8%) was in the lungs, with a small proportion (4 ± 6%) detected in the liver and negligible amounts detected in the spleen and kidneys (both 1 ± 1%) (Figure 6.10a). This bioluminescence quantification data conflicts directly with the quantification data obtained from PET imaging, the latter of which suggested that very few cells were present in the lungs by day 1, and the majority of the signals/cells were in the liver and spleen. This implies one of two things: (i) following IV administration, the cells encountered the vascular bed of the lungs, where they remained, and a large proportion died. Tissue resident macrophages of the liver, spleen and kidneys then sequestered ^{89}Zr-PCTA-SPION debris. Or (ii) following IV administration, the cells encountered the lungs then distributed in the liver, spleen and kidneys before some of the cells died and released their probe debris there. Since intravenously injected macrophages and macrophage-like cells have been reported to bypass the lung vasculature and populate other organs of the body[11, 294, 295, 300], the second possibility, or a combination of the two possibilities is likely to be true.

To test this eventuality, closer *ex vivo* analysis of the kidneys was employed. A unilateral ischaemia/reperfusion model of kidney injury was utilised in this study since it provides the advantage of an internal control within the same mouse. This allowed for comparison of the differences between the injured and healthy kidneys of each animal. As seen in Figure 6.10c, the injured kidney displayed a much higher PET signal intensity compared to the healthy kidney. Quantification of the PET signal was achieved through drawing 3D ROIs around each kidney. As seen in Figure 6.10d, this revealed a statistically significant difference between the kidneys, with the injured kidneys having a greater PET signal intensity (P = 0.007). Bioluminescence analysis of the kidneys also revealed differences between the injured and healthy kidneys, with the injured kidney displaying a greater average bioluminescence intensity (Figure 6.10e). However, this difference was not significant ($P > 0.05$). As seen in Figure 6.10b, there was only a small amount of visible BL signal in the injured kidney. In previous studies, we have cut the kidneys in half for *ex vivo* BL analysis to improve the sensitivity of the measurement by reducing tissue attenuation. However, in this study, the kidneys were kept whole in order to minimise handling and, therefore, radiation exposure. This may explain why a strong bioluminescence signal was not observed in representative *ex vivo* images of the kidneys, and why the differences between the kidneys were not significant. Noteworthy, BLI is only a semi-quantitative technique, whilst PET is fully quantitative, so the data generated by PET is likely to be more accurate, and may explain why the differences between the kidneys was significant when measured with PET but not BLI.

MRI was used to qualitatively determine whether RAWs home to and persist in the injured kidney, as was suggested by PET and BLI data. High resolution *ex vivo* imaging by MR revealed hypointense contrast in the renal cortex of the injured and healthy kidneys, as well as darkening of the medulla of the injured kidneys (Figure 6.11a). On closer examination, the injured kidneys appeared to exhibit more hypointense foci in the renal cortex compared to healthy kidneys, which suggests the presence of ^{89}Zr-PCTA-SPION labelled RAW cells.

The combined evidence from *ex vivo* BLI, PET and MRI strongly suggests that IV administered RAW cells can home to injured kidneys. Through reporter gene imaging that is specific to viable cells, live RAWs were detected in the injured kidney, which provides unambiguous evidence that RAW cells can bypass the lungs and populate other organs of the body. This implies that the signal observed in the kidneys by PET and MRI was due to cells that had homed there, and not due to tissue resident macrophages of the kidneys that had sequestered debris from cells that had encountered the lung vasculature and died. The higher proportion of signal in the injured kidneys compared to the healthy kidneys suggests that RAW cells can home to sites of injury. However, this information could not be ascertained using *in vivo* imaging techniques. This was partly due to significant cell death, which meant that most of the *in vivo* BL signal had decayed by day 1, and also due to PET signal saturation in the liver and spleen, which meant that the kidneys were not visible on *in vivo* images.

Numerous reports have detailed cell tracking in renal models of IRI using a single modality, namely bioluminescence imaging[309-311]; however, as discussed earlier, this modality has a number of limitations. Studies from our own group have applied *bimodal* imaging strategies for the tracking of cells to injured kidneys[300, 312], however, to the best of our knowledge, the study in this chapter is the first to apply a *trimodal* imaging strategy for tracking cells to the kidney in a pre-clinical injury model. The findings from this study demonstrate the benefits of combining reporter gene imaging (FLuc-BLI) with direct cell labelling methods (^{89}Zr-PCTA-SPIONs for PET/MRI), which can offer information on cell viability and cell localisation within target organs, as well as cell quantification capabilities. Because of this, the triply robust imaging strategy provided solid evidence on the biodistribution, persistence and fate of administered macrophage-like cells, which could help in the development of macrophage therapies. In addition, the developed probes could be utilised for tracking a variety of cell types and could be used to assess the homing capabilities of cells to a variety of injured organs.

6.5 Conclusions

The work presented in this chapter demonstrates that ^{89}Zr-PCTA-SPIONs are stable and effective cell tracking probes. The particles were able to follow the *in vivo* journey of intravenously injected RAW cells and displayed little bone deposition in PET imaging, which suggests that they were stably bound. Using a *trimodal* imaging strategy that comprised PET, BLI and MRI, the RAW cells appeared to home to and accumulate in sites of renal injury. However, it was not possible to observe this through *in vivo* imaging alone due to problems with cell death and sensitivity, which meant that animals had to be sacrificed for the more sensitive *ex vivo* imaging to take place. The difference in genetic background between the RAW cells and the mice used in this study likely contributed to the high level of cell death of the RAW cells, and is a limitation of the study. However, it should be noted that a similar level of cell death was observed in studies where the RAW cells were administered IV into BALB/c mice (the correct genetic background), suggesting that the lung environment and/or cells of the innate immune system might have an adverse effect on the viability of the RAW cells.

Chapter 7

Final Discussion and Conclusions

The aims of this thesis were to:

1. Develop a hybrid imaging agent that could show signal and contrast in both positron emission tomography (PET) and magnetic resonance imaging (MRI), via the attachment of the PET tracer, zirconium-89 (^{89}Zr), to dextran-coated superparamagnetic iron oxide nanoparticles (SPIONs).
2. Optimise the *in vitro* colloidal stability of the hybrid particles, as well as their uptake and toxicity profiles in RAW 264.7 cells.
3. Assess the pharmacokinetics and *in vivo* stability of the hybrid particles following a systemic injection in mice using PET and MRI.
4. Assess the biodistribution, fate and persistence of IV administered luciferase expressing RAW 264.7 cells that are labelled with the hybrid particles using BLI, PET and MRI in a murine model of renal ischaemia/reperfusion injury (IRI).

Hybrid PET/MR imaging agents were developed utilising mixed dextran-coated SPIONs as the MR component and ^{89}Zr as the PET component, with ^{89}Zr attached to SPIONs through the use of tetraazamacrocycles. To achieve this, the polymer, CM-dextran, was functionalised with the small ethylene glycol linker, EDEA, to generate EDEA-CM-dextran. The linker was used to serve as a site for the attachment of the metal chelating macrocycles. Mixed dextran SPIONs were synthesised with the functionalised EDEA-CM-dextran and a second dextran polymer, DEAE-dextran. The latter polymer was kept as part of the polymer stabilising system due to it being polycationic, since SPIONs that carry high positive charges result in very efficient labelling of stem/progenitor cells and macrophages, without the requirement of a transfection agent[125, 313].

It was determined that the optimum ratio of EDEA-CM-dextran to DEAE-dextran was 1:4, since particles of this polymer system remained colloidally stable in 10% FBS-containing serum, displaying no aggregation or sedimentation. Once this was determined, the particles were functionalised with the tetraazamacrocycles, DOTA or PCTA, to generate DOTA-SPIONs or PCTA-SPIONs, which were then labelled with zirconium (Zr). In initial studies, non-radioactive Zr was used to demonstrate that the chemistry was viable, and two different macrocycles were attached to the mixed dextran SPIONs because they require different temperatures to be labelled by Zr/^{89}Zr. As determined by quadrupole time-of-flight mass spectrometry (q-TOF-MS), the DOTA macrocycle was not labelled by Zr at room temperature since DOTA requires high temperatures (> 65°C) to be labelled[98]. Instead, DOTA-SPIONs bound a significant amount of Zr non-specifically, as determined by inductively coupled plasma-optical emission spectrometry (ICP-OES). PCTA-SPIONs, on the other hand, chelated Zr at a mildly elevated temperature of 37°C to generate Zr-PCTA-SPIONs, as determined by q-TOF-MS.

The uptake and toxicity profiles of the hybrid particles, Zr-DOTA-SPIONs and Zr-PCTA-SPIONs were explored in RAW 264.7 cells. Zr-DOTA-SPIONs were found to be non-toxic to RAW cells up to a dosing concentration of 50 µg ml^{-1}, affording an uptake of ~ 7 pg Fe cell^{-1} at this highest dosing concentration. Zr-PCTA-SPIONs were well tolerated by RAWs up to a dosing concentration of 12.5 µg ml^{-1}, but began to cause detachment of the cells at dosing concentrations greater than this. Zr-PCTA-SPIONs afforded an uptake of ~ 5 pg Fe cell^{-1} at the highest dosing concentration, which is a sufficient amount to generate MR contrast[125]. Since both hybrid particle types demonstrated the ability to bind a sufficient amount of Zr, were found to be non-cytotoxic at the labelling concentrations used and afforded sufficient iron uptake, both DOTA-SPIONs and PCTA-SPIONs were taken forward for radiolabelling with ^{89}Zr and *in vivo* testing.

First, DOTA-SPIONs were labelled with ^{89}Zr and were then administered via tail vein injection into healthy mice to determine the pharmacokinetics and *in vivo* stability of ^{89}Zr-DOTA-SPIONs. Animals were imaged by PET immediately following systemic injection (day 0) and then on days 1, 5 and 7. From day 1, there was significant bone deposition (approximately 57% of the total body activity) in the knee and shoulder joints, as well as down the spine, suggesting the instability of ^{89}Zr-DOTA-SPIONs. This was due to the fact that ^{89}Zr was bound non-specifically, and free/weakly bound ^{89}Zr has a preference for depositing in the bone due to being trans-chelated by phosphate compounds that reside there[92]. This is problematic because the PET signals produced in the bone are non-specific, and require the administration of further quantities of ^{89}Zr to produce specific signals in the areas/organs of interest, which can lead to toxicity.

Because of this, and because ^{89}Zr-PCTA-SPIONs had shown the ability to bind Zr more stably via chelation, these particles were utilised for the labelling and tracking of RAW cells *in vivo*. To achieve this, PCTA-SPIONs were radiolabelled with ^{89}Zr and were then used to label RAW cells *in vitro.* The labelled, FLuc-expressing cells were then IV administered to mice that had undergone a unilateral renal IRI. Importantly, although a small amount of bone signal (4% of the total body activity by day 1) was observed following administration of ^{89}Zr-PCTA-SPION labelled RAWs, the extent of the deposition was minor compared to when ^{89}Zr-DOTA-SPIONs were administered. The heightened stability of ^{89}Zr-PCTA-SPIONs, which was confirmed through serum and DTPA washes, could be explained by the higher temperature at which PCTA-SPIONs were labelled with ^{89}Zr (37°C instead of room temperature, as was used for ^{89}Zr-DOTA-SPIONs).

There are three potential mechanisms for labelling SPIONs with ^{89}Zr:

1. A chelator method, which was was attempted for the Zr labelling of PCTA-SPIONs, and was achieved for ^{Nat}Zr-PCTA-SPIONs. In this case, PCTA was labelled with non-radioactive Zr, but as seen in the q-TOF-MS of ^{89}Zr-PCTA-SPIONs, the macrocycle was not properly labelled by ^{89}Zr under the radiolabelling conditions (only a very small peak was observed that corresponds to ^{89}Zr-PCTA). This may be explained by the concentration disparity between non-radioactive and radioactive conditions; in the labelling of ^{Nat}Zr-PCTA-SPIONs, a large excess of the Zr source was used (micromolar quantities), which may have driven the reaction towards labelling. However, in radiolabelling reactions, the amount of activity used corresponded to ~ picomolar quantities of Zr, which may not have been enough to drive the reaction towards labelling PCTA with the radiometal.

2. Physisorption/electrostatic radiolabelling, which is another facile, potential mechanism for the radiolabelling of SPIONs, and is likely the mechanism that occurred for the radiolabelling of ^{89}Zr-DOTA-SPIONs, and partly for the radiolabelling of ^{89}Zr-PCTA-SPIONs. This is because DOTA requires high temperatures to be labelled with metal ions so the binding of ^{89}Zr to DOTA-SPIONs was likely caused by an electrostatic attraction between $[^{89}Zr(C_2O_4)_4]^{4-}$ (the speciation of the radiometal in oxalic acid) and the polycationic chains of DEAE-dextran that coat the mixed dextran SPIONs. Since ^{89}Zr-PCTA-SPIONs experienced such little bone deposition by day 1, this suggests that ^{89}Zr was much more strongly bound to PCTA-SPIONs than to DOTA-SPIONs.
3. A third radiolabelling mechanism exists that involves the heat-induced mineralisation of ^{89}Zr-oxide onto the surface of SPIONs, which was first reported by Boros *et al*[158]. and was further explored and characterised by Patrick *et al.*, with the latter team calling the mechanism ‘surface radio-mineralisation’ (SRM)[159]. Boros *et al.* demonstrated that SRM does not occur at low temperatures (20°C, 30°C), but begins to take place at 40°C. The authors also reported remarkable *in vivo* stability for their SRM synthesised ^{89}Zr-SPIONs following IV administration, which resulted in very little bone uptake in mice (2.3% of administered dose). To label PCTA-SPIONs, a temperature of 37°C was applied, since it has been reported that PCTA requires physiological temperature to be labelled by ^{89}Zr[164]. Since very little bone deposition was observed for ^{89}Zr-PCTA-SPIONs in mice following IV administration, it is possible that this mechanism, at least in part, was responsible for the radiolabelling of PCTA-SPIONs by ^{89}Zr; some SRM may have taken place at 37°C.

Although chelator methods are tried and tested routes for radiolabelling, the difficult aqueous coordination chemistry of ^{89}Zr, which is at risk of hydrolysis and colloid formation, make this method unfavourable and unreliable. For future applications of radiolabelling SPIONs for multimodal imaging, the SRM technique is most valuable since it produces very stable hybrid particles, of which the components do not separate *in vivo*, and can be applied to a range of different radiometals, including $^{111}In^{3+}$ for SPECT and other PET isotopes[158], such as $^{64}Cu^{2+}$. Additionally, it is possible that this mechanism could work for other inorganic nanoparticles, for example, gold nanoparticles (AuNPs), for hybrid nuclear/photoacoustic imaging. Since the SRM mechanism begins to occur at a mild temperature of 40°C, this minimises the risk of thermal decomposition of nanoparticles, particularly polymer-stabilised nanoparticles.

In terms of their ability to track cells *in vivo*, ^{89}Zr-PCTA-SPIONs proved to be capable, generating corroborating signals in PET and MRI, which were complemented by the cell viability information provided by bioluminescence reporter gene imaging, demonstrating the benefits of multimodal imaging approaches. Although it was observed that RAW cells can home to an injured kidney, this was confirmed through *ex vivo* analysis since neither *in vivo* PET nor BLI were sensitive or specific enough to determine this. This was partly due to a significant amount of cells dying (80%) between the day of administration and day 1, which is a common problem with IV administered cells, and partly due to the PET signal saturation that occurred in the lungs due to cell entrapment, as well as in the liver and spleen due to the high mononuclear phagocyte system (MPS) activity in these organs. This meant that any weak signals originating from the kidneys were likely masked by the strong signals in these other organs, when intact animals were imaged.

Another potential application of ^{89}Zr-PCTA-SPIONs, which utilises uptake by resident macrophages to its advantage, is in the tracking of tumour-associated macrophages (TAMs). TAMs are prominent immune cells that make up a major component of the tumour microenvironment and can represent up to 50% of a tumour cell mass[314, 315]. In cancer, circulating monocytes are recruited to tumours where they differentiate into TAMs in response to chemokines and growth factors that are produced by tumour cells. TAMs can become polarised to an M2 phenotype due to the release of cytokines, such as IL-4, by the tumour mass[316]. M2 TAMs secrete high levels of anti-inflammatory cytokines, angiogenic factors and proteases that interact with tumour cells to promote their proliferation, angiogenesis, and metastasis, all of which contribute to tumour progression[317]. Thus, imaging TAMs, especially the M2 phenotype, can serve as an important biomarker for the diagnosis of cancer, and can help to predict tumour progression and outcome in cancer patients[314]. ^{89}Zr-PCTA-SPIONs could be used to selectively target and image TAMs *in vivo,* exploiting the inherent activity of macrophages, which is to phagocytose foreign material. Current strategies for imaging TAMs have utilised PET, due to its high sensitivity, specific targeting and quantification capabilities, with many of the PET tracers used being based on radiolabelled nanoparticles[318-320]. SPIONs have also been used to track and image TAMs *in vivo* with MRI[321] due to the fact that MRI can allow for real-time assessment of nanoparticles and can image their endocytosis[315]. However, to the best of the author's knowledge, there have been no specific reports on the tracking of TAMs using radiolabelled SPIONs and combined PET and MR imaging. Applying ^{89}Zr-PCTA-SPIONs in the targeting and visualisation of TAMs would combine the benefits of the SPION component, which would enable its uptake by TAMs and allow for high spatial resolution imaging by MR, with the ^{89}Zr component, which would provide a long half-life for longitudinal PET imaging and allow for high sensitivity and quantification. Furthermore, to gain more informative data on the state of tumour progression, ^{89}Zr-PCTA-SPIONs could be further functionalised with mannose ligands for the specific targeting of the CD206 mannose receptor that is expressed in high levels on M2-polarised TAMs. ^{89}Zr-DOTA-SPIONs, on the other hand, would not be useful for this application because they are not stable *in vivo*, thus, systemic administration of the particles in cancer models would lead to non-specific signals in the bone, and weaker signals in the tumour environment.

In summary, two types of hybrid PET/MR imaging agent (^{89}Zr-DOTA-SPIONs and ^{89}Zr-PCTA-SPIONs) were developed for the *in vivo* tracking of cells, via the radiolabelling of dextran-coated SPIONs with ^{89}Zr. Although neither particle type appeared to bind ^{89}Zr in the way that was expected (via macrocycle chelation), both bound a significant amount of the radiometal via non-specific mechanisms. Both particle types displayed minimal cytotoxic effects to RAW cells and displayed good uptake in the cells. ^{89}Zr-PCTA-SPIONs were employed to label and track RAW cells *in vivo* in a murine model of unilateral renal IRI, so as to confirm whether macrophage-like cells can home to an injured kidney, as has been demonstrated previously by our group[304]. The particles, when taken up by RAW cells, were extremely stable *in vivo*, displaying little bone deposition and producing corroborating signals in PET, MRI and BLI. However, the imaging strategy could not determine whether RAW cells can home to an injured kidney using *in vivo* methods, and animals had to be sacrificed to ascertain this information. This was due to a combination of significant cell death and signal saturation in organs such as the liver and spleen, where there is high MPS activity. The large degree of cell death is likely attributed to the differing genetic backgrounds between the RAW cells and the mice that were used in this work, which is a large limitation in this study. However, we have observed similar rates of attrition and similar biodistribution profiles of the RAW cells during previous studies involving BALB/c mice in our group[304, 308], suggesting that other factors such as the RAWs themselves and the route of administration may have contributed to the cell death.

Future Work

Future work on this project should address the issues centred on the *in vivo* model applied in the final chapter of this thesis. To do this, the RAW cells could be injected into animals of the correct genetic background, i.e. BALB/c mice. However, since the IRI model used in Chapter 6 was optimised in C57BL/6 mice and we have observed similar rates of attrition of the RAW cells in BALB/c mice anyway, this might not produce much more informative data. Instead, ^{89}Zr-PCTA-SPION labelled primary macrophages could be studied in the IRI model. A study in our group that investigated the behaviour of IV administered bone marrow-derived macrophages (BMDMs) in a murine model of multiple organ dysfunction demonstrated that BMDMs could be detected by BLI 4 days post administration[312]. The total flux detected on day 4 was greater than that on day 1, suggesting that not only did BMDMs not die shortly after their administration, they may have even proliferated. BMDMs isolated from C57BL/6 mice would be the best choice of cell to use in future unilateral renal IRI tracking studies since they will have a better survival rate, which may allow differences in the kidneys to be assessed and quantified using *in vivo* techniques. Other routes of administration, such as intra-arterial injection, could also be trialled to see if this improves the survival rate of the macrophages *in vivo*.

Other experiments that could be performed to strengthen the results reported in this thesis are *in vivo* pharmacokinetics and stability studies on neat, systemically injected ^{89}Zr-PCTA-SPIONs. Due to time constraints in the project, these studies were not performed, but they would help to provide validating information on the *in vivo* stability of the probes and would help to confirm that these probes are, in fact, more stable than ^{89}Zr-DOTA-SPIONs. Additionally, further *in vitro* toxicity studies should be performed on both DOTA and PCTA-SPION-labelled RAW cells, involving longer incubation times, since the free injected ^{89}Zr-DOTA-SPIONs were used *in vivo* for one week. *In vitro* uptake and toxicity studies could also be performed on a variety of cell types, such as mesenchymal stromal cells (MSCs) and dopaminergic neurons, to determine whether the probes could be valuable for the *in vivo* tracking of such cells.

As discussed in earlier chapters, the developed probes could also be used for other biological applications. For example, ^{89}Zr-DOTA-SPIONs could be further functionalised with the anti-inflammatory cytokine, IL-10, via EDC coupling approaches for a *theranostic* approach to treating and imaging inflammatory liver disease. Further, the labile electrostatic bonds between cationic ^{89}Zr-DOTA-SPIONs and negatively charged species could be exploited to deliver such species to the liver. For example, there is much interest in delivering siRNA to Kupffer cells in order to reduce TNF-α production since this cytokine plays a large role in the pathogenesis of inflammatory liver disease[322]. Current strategies for transfecting Kupffer cells use cationic lipid vehicles[323], however, using ^{89}Zr-DOTA-SPIONs for siRNA delivery would benefit from the particles being able to deliver the cargo to the cells, as well as being able to image the liver with both PET and MR.

With respect to the chemistry of the probes, more work could be performed on ^{89}Zr-PCTA-SPIONs to determine whether the mechanism of ^{89}Zr binding at 37°C is via SRM. This could be achieved by applying the characterisation techniques described in the paper published by Patrick *et al.*[159], such as x-ray photoelectron spectroscopy (XPS), to determine whether ^{89}Zr-oxide is mineralised on the surface of the particles following radiolabelling. Finally, PCTA-SPIONs could be used to chelate other radionuclides under mild conditions such as the SPECT tracer, ^{111}In^{3+}, which is much more stable than ^{89}Zr^{4+} in aqueous medium. This means that ^{111}In^{3+} is not at risk of hydrolysing and forming colloids, so can more effectively label macrocycles and chelates. Although PET has the edge over SPECT in that it is fully quantitative whilst SPECT is only semi-quantitative, SPECT is more widely used in the clinic. This is due to the ease at which SPECT isotopes can be generated, compared to PET isotopes, which have to be synthesised off-site and transported. Thus, there will always be a large clinical demand for SPECT tracers, which indium-labelled-PCTA-SPIONs could provide.

The main advantage of both the developed PCTA-SPIONs and DOTA-SPIONs is that they are massively multimodal, meaning that they offer not one but two types of imaging capabilities, as well as having vast potential for further functionalisation with cytokines, antibodies, drugs and more. There are many examples in the literature of nanoparticle systems that have imaging capabilities and there are many examples of nanoparticle systems that can deliver important biomolecule cargo, however, there are few examples of nanoparticle systems that can offer both functionalities. One of the main limitations of the probes developed in this work is the high surface charge on the particles, which meant that competing electrostatic mechanisms dominated the radiolabelling process, producing particles that had a degree of instability *in vivo*. This affinity for electrostatically binding compounds to the probes could be exploited, however, to allow the probes to deliver important cargo to particular organs *in vivo*. In drug delivery, for example, it is important that the drug can load and unload efficiently from the nanoparticle, so a labile interaction between the two entities is necessary. PCTA-SPIONs or DOTA-SPIONs could be excellent candidates for this.

References

1. Buzhor E, Leshansky L, Blumenthal J, Barash H, Warshawsky D, Mazor Y, et al. Cell-based therapy approaches: the hope for incurable diseases. Regenerative medicine. 2014;9(5):649-72.
2. Scarfe L, Brillant N, Kumar JD, Ali N, Alrumayh A, Amali M, et al. Preclinical imaging methods for assessing the safety and efficacy of regenerative medicine therapies. npj Regenerative Medicine. 2017;2(1):28.
3. Nerem RM. Regenerative medicine: the emergence of an industry. Journal of the Royal Society, Interface. 2010;7 Suppl 6(Suppl 6):S771-5.
4. Weiss ML, Troyer DL. Stem cells in the umbilical cord. Stem Cell Rev. 2006;2(2):155-62.
5. Burns CE, Zon LI. Portrait of a stem cell. Developmental cell. 2002;3(5):612-3.
6. Thomson JA, Itskovitz-Eldor J, Shapiro SS, Waknitz MA, Swiergiel JJ, Marshall VS, et al. Embryonic stem cell lines derived from human blastocysts. Science (New York, NY). 1998;282(5391):1145-7.
7. Reubinoff BE, Pera MF, Fong CY, Trounson A, Bongso A. Embryonic stem cell lines from human blastocysts: somatic differentiation in vitro. Nature biotechnology. 2000;18(4):399-404.
8. Schwartz SD, Regillo CD, Lam BL, Eliott D, Rosenfeld PJ, Gregori NZ, et al. Human embryonic stem cell-derived retinal pigment epithelium in patients with age-related macular degeneration and Stargardt's macular dystrophy: follow-up of two open-label phase 1/2 studies. Lancet (London, England). 2015;385(9967):509-16.
9. Schwartz SD, Hubschman JP, Heilwell G, Franco-Cardenas V, Pan CK, Ostrick RM, et al. Embryonic stem cell trials for macular degeneration: a preliminary report. Lancet (London, England). 2012;379(9817):713-20.
10. Lee JE, Lee DR. Human embryonic stem cells: derivation, maintenance and cryopreservation. Int J Stem Cells. 2011;4(1):9-17.
11. Scarfe L, Taylor A, Sharkey J, Harwood R, Barrow M, Comenge J, et al. Non-invasive imaging reveals conditions that impact distribution and persistence of cells after in vivo administration. Stem Cell Research & Therapy. 2018;9(1):332.
12. Torres Crigna A, Daniele C, Gamez C, Medina Balbuena S, Pastene DO, Nardozi D, et al. Stem/Stromal Cells for Treatment of Kidney Injuries With Focus on Preclinical Models. Frontiers in medicine. 2018;5:179.
13. Matthay MA, Goolaerts A, Howard JP, Lee JW. Mesenchymal stem cells for acute lung injury: preclinical evidence. Critical care medicine. 2010;38(10 Suppl):S569-73.
14. Mei SH, McCarter SD, Deng Y, Parker CH, Liles WC, Stewart DJ. Prevention of LPS-induced acute lung injury in mice by mesenchymal stem cells overexpressing angiopoietin 1. PLoS medicine. 2007;4(9):e269.
15. Boyle AJ, McNiece IK, Hare JM. Mesenchymal stem cell therapy for cardiac repair. Methods in molecular biology (Clifton, NJ). 2010;660:65-84.
16. Sage EK, Thakrar RM, Janes SM. Genetically modified mesenchymal stromal cells in cancer therapy. Cytotherapy. 2016;18(11):1435-45.
17. Zeng XM. Human embryonic stem cells: Mechanisms to escape replicative senescence? Stem Cell Rev. 2007;3(4):270-9.
18. Caplan AI. Mesenchymal Stem Cells: Time to Change the Name! STEM CELLS Translational Medicine. 2017;6(6):1445-51.
19. Kuriyan AE, Albini TA, Townsend JH, Rodriguez M, Pandya HK, Leonard RE, 2nd, et al. Vision Loss after Intravitreal Injection of Autologous "Stem Cells" for AMD. N Engl J Med. 2017;376(11):1047-53.
20. Jung JW, Kwon M, Choi JC, Shin JW, Park IW, Choi BW, et al. Familial occurrence of pulmonary embolism after intravenous, adipose tissue-derived stem cell therapy. Yonsei medical journal. 2013;54(5):1293-6.

21. Lee AS, Tang C, Cao F, Xie X, van der Bogt K, Hwang A, et al. Effects of cell number on teratoma formation by human embryonic stem cells. Cell cycle (Georgetown, Tex). 2009;8(16):2608-12.
22. Spees JL, Lee RH, Gregory CA. Mechanisms of mesenchymal stem/stromal cell function. Stem Cell Research & Therapy. 2016;7(1):125.
23. Iso Y, Spees JL, Serrano C, Bakondi B, Pochampally R, Song YH, et al. Multipotent human stromal cells improve cardiac function after myocardial infarction in mice without long-term engraftment. Biochemical and biophysical research communications. 2007;354(3):700-6.
24. Dai W, Hale SL, Martin BJ, Kuang JQ, Dow JS, Wold LE, et al. Allogeneic mesenchymal stem cell transplantation in postinfarcted rat myocardium: short- and long-term effects. Circulation. 2005;112(2):214-23.
25. Lee RH, Pulin AA, Seo MJ, Kota DJ, Ylostalo J, Larson BL, et al. Intravenous hMSCs improve myocardial infarction in mice because cells embolized in lung are activated to secrete the anti-inflammatory protein TSG-6. Cell stem cell. 2009;5(1):54-63.
26. Bi B, Schmitt R, Israilova M, Nishio H, Cantley LG. Stromal cells protect against acute tubular injury via an endocrine effect. Journal of the American Society of Nephrology : JASN. 2007;18(9):2486-96.
27. Geng Y, Zhang L, Fu B, Zhang J, Hong Q, Hu J, et al. Mesenchymal stem cells ameliorate rhabdomyolysis-induced acute kidney injury via the activation of M2 macrophages. Stem Cell Research & Therapy. 2014;5(3):80.
28. Zhou Y, Yamamoto Y, Xiao Z, Ochiya T. The Immunomodulatory Functions of Mesenchymal Stromal/Stem Cells Mediated via Paracrine Activity. J Clin Med. 2019;8(7):1025.
29. Uccelli A, de Rosbo NK. The immunomodulatory function of mesenchymal stem cells: mode of action and pathways. Annals of the New York Academy of Sciences. 2015;1351:114-26.
30. Wang Y, Wang YP, Zheng G, Lee VW, Ouyang L, Chang DH, et al. Ex vivo programmed macrophages ameliorate experimental chronic inflammatory renal disease. Kidney international. 2007;72(3):290-9.
31. Guiteras R, Flaquer M, Cruzado JM. Macrophage in chronic kidney disease. Clinical Kidney Journal. 2016;9(6):765-71.
32. Brennan PN, MacMillan M, Manship T, Moroni F, Glover A, Graham C, et al. Study protocol: a multicentre, open-label, parallel-group, phase 2, randomised controlled trial of autologous macrophage therapy for liver cirrhosis (MATCH). BMJ open. 2021;11(11):e053190.
33. Chernykh ER, Shevela EY, Starostina NM, Morozov SA, Davydova MN, Menyaeva EV, et al. Safety and Therapeutic Potential of M2 Macrophages in Stroke Treatment. Cell transplantation. 2016;25(8):1461-71.
34. Wynn TA, Chawla A, Pollard JW. Macrophage biology in development, homeostasis and disease. Nature. 2013;496(7446):445-55.
35. Franken L, Schiwon M, Kurts C. Macrophages: sentinels and regulators of the immune system. Cellular Microbiology. 2016;18(4):475-87.
36. Martin CJ, Peters KN, Behar SM. Macrophages clean up: efferocytosis and microbial control. Current Opinion in Microbiology. 2014;17:17-23.
37. Soroosh P, Doherty TA, Duan W, Mehta AK, Choi H, Adams YF, et al. Lung-resident tissue macrophages generate Foxp3⁺ regulatory T cells and promote airway tolerance. The Journal of Experimental Medicine. 2013;210(4):775-88.
38. Spiller KL, Koh TJ. Macrophage-based therapeutic strategies in regenerative medicine. Advanced drug delivery reviews. 2017;122:74-83.
39. Wynn TA, Vannella KM. Macrophages in Tissue Repair, Regeneration, and Fibrosis. Immunity. 2016;44(3):450-62.
40. Novak ML, Koh TJ. Phenotypic transitions of macrophages orchestrate tissue repair. American Journal of Pathology. 2013;183(5):1352-63.

41. Lee S, Kivimäe S, Dolor A, Szoka FC. Macrophage-based cell therapies: The long and winding road. J Control Release. 2016;240:527-40.
42. Happle C, Lachmann N, Škuljec J, Wetzke M, Ackermann M, Brennig S, et al. Pulmonary transplantation of macrophage progenitors as effective and long-lasting therapy for hereditary pulmonary alveolar proteinosis. Science translational medicine. 2014;6(250):250ra113.
43. Patel AN, Henry TD, Quyyumi AA, Schaer GL, Anderson RD, Toma C, et al. Ixmyelocel-T for patients with ischaemic heart failure: a prospective randomised double-blind trial. Lancet (London, England). 2016;387(10036):2412-21.
44. Lu J, Cao Q, Zheng D, Sun Y, Wang C, Yu X, et al. Discrete functions of M2a and M2c macrophage subsets determine their relative efficacy in treating chronic kidney disease. Kidney international. 2013;84(4):745-55.
45. Abbasi MA, Chertow GM, Hall YN. End-stage renal disease. BMJ Clin Evid. 2010;2010:2002.
46. Hsu CY. Linking the population epidemiology of acute renal failure, chronic kidney disease and end-stage renal disease. Current opinion in nephrology and hypertension. 2007;16(3):221-6.
47. Faradji A, Bohbot A, Schmitt-Goguel M, Roeslin N, Dumont S, Wiesel ML, et al. Phase I trial of intravenous infusion of ex-vivo-activated autologous blood-derived macrophages in patients with non-small-cell lung cancer: toxicity and immunomodulatory effects. Cancer immunology, immunotherapy : CII. 1991;33(5):319-26.
48. Faradji A, Bohbot A, Frost H, Schmitt-Goguel M, Siffert JC, Dufour P, et al. Phase I study of liposomal MTP-PE-activated autologous monocytes administered intraperitoneally to patients with peritoneal carcinomatosis. Journal of clinical oncology : official journal of the American Society of Clinical Oncology. 1991;9(7):1251-60.
49. Hennemann B, Scheibenbogen C, Schümichen C, Andreesen R. Intrahepatic adoptive immunotherapy with autologous tumorcytotoxic macrophages in patients with cancer. Journal of immunotherapy with emphasis on tumor immunology : official journal of the Society for Biological Therapy. 1995;18(1):19-27.
50. Lesimple T, Moisan A, Guillé F, Leberre C, Audran R, Drenou B, et al. Treatment of metastatic renal cell carcinoma with activated autologous macrophages and granulocyte--macrophage colony-stimulating factor. Journal of immunotherapy (Hagerstown, Md : 1997). 2000;23(6):675-9.
51. Ritchie D, Mileshkin L, Wall D, Bartholeyns J, Thompson M, Coverdale J, et al. In vivo tracking of macrophage activated killer cells to sites of metastatic ovarian carcinoma. Cancer immunology, immunotherapy : CII. 2007;56(2):155-63.
52. Lindvall O, Hyun I. Medical innovation versus stem cell tourism. Science (New York, NY). 2009;324(5935):1664-5.
53. Kiatpongsan S, Sipp D. Medicine. Monitoring and regulating offshore stem cell clinics. Science (New York, NY). 2009;323(5921):1564-5.
54. Naumova AV, Modo M, Moore A, Murry CE, Frank JA. Clinical imaging in regenerative medicine. Nature biotechnology. 2014;32(8):804-18.
55. Mark Tangney KPF. In Vivo Optical Imaging in Gene & Cell Therapy. Current Gene Therapy. 2012;12(1):2-11.
56. James ML, Gambhir SS. A Molecular Imaging Primer: Modalities, Imaging Agents, and Applications. 2012;92(2):897-965.
57. Sakudo A. Near-infrared spectroscopy for medical applications: Current status and future perspectives. Clinica chimica acta; international journal of clinical chemistry. 2016;455:181-8.
58. Kim JE, Kalimuthu S, Ahn B-C. In vivo cell tracking with bioluminescence imaging. Nucl Med Mol Imaging. 2015;49(1):3-10.
59. Beard P. Biomedical photoacoustic imaging. Interface Focus. 2011;1(4):602-31.
60. Yao J, Wang LV. Photoacoustic tomography: fundamentals, advances and prospects. Contrast Media Mol Imaging. 2011;6(5):332-45.

61. Wang LV, Hu S. Photoacoustic tomography: in vivo imaging from organelles to organs. Science (New York, NY). 2012;335(6075):1458-62.
62. Sharkey J, Scarfe L, Santeramo I, Garcia-Finana M, Park BK, Poptani H, et al. Imaging technologies for monitoring the safety, efficacy and mechanisms of action of cell-based regenerative medicine therapies in models of kidney disease. European journal of pharmacology. 2016;790:74-82.
63. Steinberg I, Huland DM, Vermesh O, Frostig HE, Tummers WS, Gambhir SS. Photoacoustic clinical imaging. Photoacoustics. 2019;14:77-98.
64. Francies O. Photoacoustic Imaging of Head and Neck Tumours. ClinicalTrialsgov. 2021.
65. Wang X. Laser-based Photoacoustic Tomography of Human Inflammatory Arthritis. ClinicalTrialsgov. 2008.
66. Medarova Z MA. Imaging of Pancreatic Cancer: A Promise for Early Diagnosis Through Targeted Strategies. Cancer Therapy. 2004;2:329 - 44.
67. Sehl OC, Gevaert JJ, Melo KP, Knier NN, Foster PJ. A Perspective on Cell Tracking with Magnetic Particle Imaging. Tomography (Ann Arbor, Mich). 2020;6(4):315-24.
68. Kiani A, Esquevin A, Lepareur N, Bourguet P, Jeune F, Gauvrit J. Main applications of hybrid PET-MRI contrast agents: A review. Contrast Media Mol Imaging. 2015;11.
69. Hicks R, Lau E, Binns D. Hybrid imaging is the future of molecular imaging. Biomed Imaging Interv J. 2007;3(3):e49-e.
70. Pichler BJ, Judenhofer MS, Pfannenberg C. Multimodal imaging approaches: PET/CT and PET/MRI. Handbook of experimental pharmacology. 2008(185 Pt 1):109-32.
71. Hricak H, Choi BI, Scott AM, Sugimura K, Muellner A, Schulthess GKv, et al. Global Trends in Hybrid Imaging. Radiology. 2010;257(2):498-506.
72. Kraitchman DL, Bulte JWM. In vivo imaging of stem cells and Beta cells using direct cell labeling and reporter gene methods. Arterioscler Thromb Vasc Biol. 2009;29(7):1025-30.
73. Thin MZ. Developing multi-modal imaging agents for stem cell tracking. United Kingdom: University College London; 2018.
74. Yaghoubi SS, Campbell DO, Radu CG, Czernin J. Positron emission tomography reporter genes and reporter probes: gene and cell therapy applications. Theranostics. 2012;2(4):374-91.
75. Yaghoubi SS, Campbell DO, Radu CG, Czernin J. Positron emission tomography reporter genes and reporter probes: gene and cell therapy applications. Theranostics. 2012;2(4):374-91.
76. Jurgielewicz P, Harmsen S, Wei E, Bachmann MH, Ting R, Aras O. New imaging probes to track cell fate: reporter genes in stem cell research. Cell Mol Life Sci. 2017;74(24):4455-69.
77. Patrick PS, Hammersley J, Loizou L, Kettunen M, Rodrigues T, Hu D-E, et al. Dual-modality gene reporter for in vivo imaging. Proceedings of the National Academy of Sciences of the United States of America. 2013;111.
78. Filonov GS, Piatkevich KD, Ting L-M, Zhang J, Kim K, Verkhusha VV. Bright and stable near-infrared fluorescent protein for in vivo imaging. Nature biotechnology. 2011;29(8):757-61.
79. Brunker J, Yao J, Laufer J, Bohndiek SE. Photoacoustic imaging using genetically encoded reporters: a review. Journal of biomedical optics. 2017;22(7).
80. Neefjes M, Housmans BAC, van den Akker GGH, van Rhijn LW, Welting TJM, van der Kraan PM. Reporter gene comparison demonstrates interference of complex body fluids with secreted luciferase activity. Scientific Reports. 2021;11(1):1359.
81. Billinton N, Knight AW. Seeing the Wood through the Trees: A Review of Techniques for Distinguishing Green Fluorescent Protein from Endogenous Autofluorescence. Analytical Biochemistry. 2001;291(2):175-97.
82. de Almeida PE, van Rappard JRM, Wu JC. In vivo bioluminescence for tracking cell fate and function. Am J Physiol Heart Circ Physiol. 2011;301(3):H663-H71.

83. Zhao H, Doyle TC, Wong RJ, Cao Y, Stevenson DK, Piwnica-Worms D, et al. Characterization of coelenterazine analogs for measurements of Renilla luciferase activity in live cells and living animals. Molecular imaging. 2004;3(1):43-54.

84. Zhao H, Doyle T, Coquoz O, Kalish F, Rice B, Contag C. Emission spectra of bioluminescent reporters and interaction with mammalian tissue determine the sensitivity of detection <i>in vivo</i>. Journal of biomedical optics. 2005;10(4):041210.

85. Taylor A, Wilson KM, Murray P, Fernig DG, Lévy R. Long-term tracking of cells using inorganic nanoparticles as contrast agents: are we there yet? Chemical Society Reviews. 2012;41(7):2707-17.

86. Rosado-de-Castro PH, Pimentel-Coelho PM, Gutfilen B, Lopes de Souza SA, de Freitas GR, Mendez-Otero R, et al. Radiopharmaceutical Stem Cell Tracking for Neurological Diseases. BioMed Research International. 2014;2014:417091.

87. Zhang Y, Hong H, Cai W. PET tracers based on Zirconium-89. Curr Radiopharm. 2011;4(2):131-9.

88. Bansal A, Pandey MK, Demirhan YE, Nesbitt JJ, Crespo-Diaz RJ, Terzic A, et al. Novel 89Zr cell labeling approach for PET-based cell trafficking studies. EJNMMI Research. 2015;5(1):19.

89. Sato N, Wu H, Asiedu KO, Szajek LP, Griffiths GL, Choyke PL. (89)Zr-Oxine Complex PET Cell Imaging in Monitoring Cell-based Therapies. Radiology. 2015;275(2):490-500.

90. McConathy JE. Tracking Peripheral Immune Cell Infiltration of the Brain in Central Inflammatory Disorders Using [Zr-89]Oxinate-4-labeled Leukocytes University of Alabama at Birmingham2019 [

91. Friberger I, Jussing E, Han J, Goos JACM, Siikanen J, Kaipe H, et al. Optimisation of the Synthesis and Cell Labelling Conditions for [89Zr]Zr-oxine and [89Zr]Zr-DFO-NCS: a Direct In Vitro Comparison in Cell Types with Distinct Therapeutic Applications. Molecular imaging and biology. 2021;23(6):952-62.

92. Abou DS, Ku T, Smith-Jones PM. In vivo biodistribution and accumulation of 89Zr in mice. Nucl Med Biol. 2011;38(5):675-81.

93. Pandya DN, Henry KE, Day CS, Graves SA, Nagle VL, Dilling TR, et al. Polyazamacrocycle Ligands Facilitate 89Zr Radiochemistry and Yield 89Zr Complexes with Remarkable Stability. Inorganic Chemistry. 2020;59(23):17473-87.

94. Meijs WE, Herscheid JD, Haisma HJ, Pinedo HM. Evaluation of desferal as a bifunctional chelating agent for labeling antibodies with Zr-89. International journal of radiation applications and instrumentation Part A, Applied radiation and isotopes. 1992;43(12):1443-7.

95. Chomet M, Schreurs M, Bolijn MJ, Verlaan M, Beaino W, Brown K, et al. Head-to-head comparison of DFO* and DFO chelators: selection of the best candidate for clinical 89Zr-immuno-PET. European journal of nuclear medicine and molecular imaging. 2021;48(3):694-707.

96. Deri MA, Zeglis BM, Francesconi LC, Lewis JS. PET imaging with ^{89}Zr: from radiochemistry to the clinic. Nucl Med Biol. 2013;40(1):3-14.

97. Bhatt NB, Pandya DN, Wadas TJ. Recent Advances in Zirconium-89 Chelator Development. Molecules (Basel, Switzerland). 2018;23(3).

98. Pandya DN, Bhatt N, Yuan H, Day CS, Ehrmann BM, Wright M, et al. Zirconium tetraazamacrocycle complexes display extraordinary stability and provide a new strategy for zirconium-89-based radiopharmaceutical development. Chemical Science. 2017;8(3):2309-14.

99. Kim MH, Woo S-K, Kim KI, Lee TS, Kim CW, Kang JH, et al. Simple Methods for Tracking Stem Cells with (64)Cu-Labeled DOTA-hexadecyl-benzoate. ACS medicinal chemistry letters. 2015;6 5:528-30.

100. Barrow M, Taylor A, Murray P, Rosseinsky MJ, Adams DJ. Design considerations for the synthesis of polymer coated iron oxide nanoparticles for stem cell labelling and tracking using MRI. Chemical Society Reviews. 2015;44(19):6733-48.

101. Holland GN, Bottomley PA, Hinshaw WS. 19F magnetic resonance imaging. Journal of Magnetic Resonance (1969). 1977;28(1):133-6.

102. Srinivas M, Boehm-Sturm P, Aswendt M, Pracht ED, Figdor CG, de Vries IJ, et al. In vivo 19F MRI for cell tracking. J Vis Exp. 2013(81):e50802-e.

103. Fraum TJ, Ludwig DR, Bashir MR, Fowler KJ. Gadolinium-based contrast agents: A comprehensive risk assessment. Journal of Magnetic Resonance Imaging. 2017;46(2):338-53.

104. Agudelo CA, Tachibana Y, Hurtado AF, Ose T, Iida H, Yamaoka T. The use of magnetic resonance cell tracking to monitor endothelial progenitor cells in a rat hindlimb ischemic model. Biomaterials. 2012;33(8):2439-48.

105. Guenoun J, Koning GA, Doeswijk G, Bosman L, Wielopolski PA, Krestin GP, et al. Cationic Gd-DTPA liposomes for highly efficient labeling of mesenchymal stem cells and cell tracking with MRI. Cell transplantation. 2012;21(1):191-205.

106. Rudelius M, Daldrup-Link HE, Heinzmann U, Piontek G, Settles M, Link TM, et al. Highly efficient paramagnetic labelling of embryonic and neuronal stem cells. European journal of nuclear medicine and molecular imaging. 2003;30(7):1038-44.

107. Thomsen HS. Nephrogenic systemic fibrosis: A serious late adverse reaction to gadodiamide. European radiology. 2006;16(12):2619-21.

108. Silva AC, Bock NA. Manganese-enhanced MRI: an exceptional tool in translational neuroimaging. Schizophr Bull. 2008;34(4):595-604.

109. Aoki I, Takahashi Y, Chuang KH, Silva AC, Igarashi T, Tanaka C, et al. Cell labeling for magnetic resonance imaging with the T1 agent manganese chloride. NMR in biomedicine. 2006;19(1):50-9.

110. Gilad AA, Walczak P, McMahon MT, Na HB, Lee JH, An K, et al. MR tracking of transplanted cells with "positive contrast" using manganese oxide nanoparticles. Magn Reson Med. 2008;60(1):1-7.

111. Srivastava AK, Kadayakkara DK, Bar-Shir A, Gilad AA, McMahon MT, Bulte JWM. Advances in using MRI probes and sensors for in vivo cell tracking as applied to regenerative medicine. Dis Model Mech. 2015;8(4):323-36.

112. Cortajarena AL, Ortega D, Ocampo SM, Gonzalez-García A, Couleaud P, Miranda R, et al. Engineering Iron Oxide Nanoparticles for Clinical Settings. Nanobiomedicine. 2014;1:2.

113. Wahajuddin, Arora S. Superparamagnetic iron oxide nanoparticles: magnetic nanoplatforms as drug carriers. Int J Nanomedicine. 2012;7:3445-71.

114. Schulze F, Dienelt A, Geissler S, Zaslansky P, Schoon J, Henzler K, et al. Amino-polyvinyl alcohol coated superparamagnetic iron oxide nanoparticles are suitable for monitoring of human mesenchymal stromal cells in vivo. Small (Weinheim an der Bergstrasse, Germany). 2014;10(21):4340-51.

115. Babič M, Schmiedtová M, Poledne R, Herynek V, Horák D. In vivo monitoring of rat macrophages labeled with poly(l-lysine)-iron oxide nanoparticles. Journal of Biomedical Materials Research Part B: Applied Biomaterials. 2015;103(6):1141-8.

116. Shi L, Zhang J, Zhao M, Tang S, Cheng X, Zhang W, et al. Effects of polyethylene glycol on the surface of nanoparticles for targeted drug delivery. Nanoscale. 2021;13(24):10748-64.

117. Chung HJ, Lee H, Bae KH, Lee Y, Park J, Cho S-W, et al. Facile synthetic route for surface-functionalized magnetic nanoparticles: cell labeling and magnetic resonance imaging studies. ACS Nano. 2011;5(6):4329-36.

118. Babic M, Schmiedtova M, Poledne R, Herynek V, Horak D. In vivo monitoring of rat macrophages labeled with poly(l-lysine)-iron oxide nanoparticles. Journal of Biomedical Materials Research Part B-Applied Biomaterials. 2015;103(6):1141-8.

119. Reddy AM, Kwak BK, Shim HJ, Ahn C, Lee HS, Suh YJ, et al. In vivo tracking of mesenchymal stem cells labeled with a novel chitosan-coated superparamagnetic iron oxide nanoparticles using 3.0T MRI. Journal of Korean medical science. 2010;25(2):211-9.

120. Shi ZL, Neoh KG, Kang ET, Shuter B, Wang SC, Poh C, et al. (Carboxymethyl)chitosan-Modified Superparamagnetic Iron Oxide Nanoparticles for

Magnetic Resonance Imaging of Stem Cells. Acs Applied Materials & Interfaces. 2009;1(2):328-35.
121. Jo J-i, Aoki I, Tabata Y. Design of iron oxide nanoparticles with different sizes and surface charges for simple and efficient labeling of mesenchymal stem cells. Journal of Controlled Release. 2010;142(3):465-73.
122. Molday RS, MacKenzie D. Immunospecific ferromagnetic iron-dextran reagents for the labeling and magnetic separation of cells. Journal of immunological methods. 1982;52(3):353-67.
123. Barrow M, Taylor A, García Carrión J, Mandal P, Park BK, Poptani H, et al. Co-precipitation of DEAE-dextran coated SPIONs: how synthesis conditions affect particle properties, stem cell labelling and MR contrast. Contrast Media Mol Imaging. 2016;11(5):362-70.
124. Barrow M, Taylor A, Nieves DJ, Bogart LK, Mandal P, Collins CM, et al. Tailoring the surface charge of dextran-based polymer coated SPIONs for modulated stem cell uptake and MRI contrast. Biomaterials Science. 2015;3(4):608-16.
125. Sharkey J, Starkey Lewis PJ, Barrow M, Alwahsh SM, Noble J, Livingstone E, et al. Functionalized superparamagnetic iron oxide nanoparticles provide highly efficient iron-labeling in macrophages for magnetic resonance-based detection in vivo. Cytotherapy. 2017;19(4):555-69.
126. Currie S, Hoggard N, Craven IJ, Hadjivassiliou M, Wilkinson ID. Understanding MRI: basic MR physics for physicians. Postgraduate medical journal. 2013;89(1050):209-23.
127. Scilid H. MRI made easy:(... well almost). Berlin: Schering AG; 1990.
128. Catherine Westbrook CKR, John Talbot. MRI In Practice. Oxford, U.K.: Blackwell Publishing Ltd; 1993.
129. Bashir U. T2* Relaxation [Reference article]. Radiopaedia.org: Radiopaedia.org; 2012 [updated 02/04/2020. 16:[1]. Available from: https://radiopaedia.org/articles/t2-relaxation-1?lang=gb.
130. Moore MM, Chung T. Review of key concepts in magnetic resonance physics. Pediatric Radiology. 2017;47(5):497-506.
131. Holz MJMRiC. L. Banci, L. Bertini and C. Luchinat. Nuclear and electron relaxation. The magnetic nucleus-unpaired electron coupling in solution. VCH, Weinheim, New York, Basel, Cambridge, 1991, pp. 216, DM 118. ISBN 3-527-28306-4. 1993;31(13):S154-S.
132. James ML, Gambhir SS. A Molecular Imaging Primer: Modalities, Imaging Agents, and Applications. Physiological Reviews. 2012;92(2):897-965.
133. Kapoor V, McCook BM, Torok FS. An Introduction to PET-CT Imaging. RadioGraphics. 2004;24(2):523-43.
134. Severin GW, Engle JW, Barnhart TE, Nickles RJ. 89Zr radiochemistry for positron emission tomography. Med Chem. 2011;7(5):389-94.
135. Baldwin TO. Chemiluminescence and Bioluminescence. In: Lennarz WJ, Lane MD, editors. Encyclopedia of Biological Chemistry (Second Edition). Waltham: Academic Press; 2013. p. 461-6.
136. Raschke WC, Baird S, Ralph P, Nakoinz I. Functional macrophage cell lines transformed by abelson leukemia virus. Cell. 1978;15(1):261-7.
137. Taylor A, Sharkey J, Harwood R, Scarfe L, Barrow M, Rosseinsky MJ, et al. Multimodal Imaging Techniques Show Differences in Homing Capacity Between Mesenchymal Stromal Cells and Macrophages in Mouse Renal Injury Models. Molecular Imaging and Biology. 2019.
138. Li L, Jiang W, Luo K, Song H, Lan F, Wu Y, et al. Superparamagnetic iron oxide nanoparticles as MRI contrast agents for non-invasive stem cell labeling and tracking. Theranostics. 2013;3(8):595-615.
139. Singh N, Jenkins G, Asadi R, Doak S. Potential toxicity of superparamagnetic iron oxide nanoparticles (SPION). Nano Reviews. 2010;1.

140. Gautam RK, Chattopadhyaya MC. Chapter 7 - Functionalized Magnetic Nanoparticles: Adsorbents and Applications. In: Gautam RK, Chattopadhyaya MC, editors. Nanomaterials for Wastewater Remediation. Boston: Butterworth-Heinemann; 2016. p. 139-59.
141. Laurent S, Forge D, Port M, Roch A, Robic C, Vander Elst L, et al. Magnetic Iron Oxide Nanoparticles: Synthesis, Stabilization, Vectorization, Physicochemical Characterizations, and Biological Applications. Chemical Reviews. 2008;108(6):2064-110.
142. Lu A-H, Salabas EL, Schüth F. Magnetic Nanoparticles: Synthesis, Protection, Functionalization, and Application. Angewandte Chemie International Edition. 2007;46(8):1222-44.
143. Molday RS, Mackenzie D. Immunospecific ferromagnetic iron-dextran reagents for the labeling and magnetic separation of cells. Journal of Immunological Methods. 1982;52(3):353-67.
144. Paul KG, Frigo TB, Groman JY, Groman EV. Synthesis of Ultrasmall Superparamagnetic Iron Oxides Using Reduced Polysaccharides. Bioconjugate Chemistry. 2004;15(2):394-401.
145. Paul KG, Frigo TB, Groman JY, Groman EV. Synthesis of ultrasmall superparamagnetic iron oxides using reduced polysaccharides. Bioconjug Chem. 2004;15(2):394-401.
146. Barrow M, Taylor A, Fuentes-Caparrós AM, Sharkey J, Daniels LM, Mandal P, et al. SPIONs for cell labelling and tracking using MRI: magnetite or maghemite? Biomaterials Science. 2018;6(1):101-6.
147. Pu YJ, Vaid RK, Boini SK, Towsley RW, Doecke CW, Mitchell D. A Practical Method for Functionalized Peptide or Amide Bond Formation in Aqueous−Ethanol Media with EDC as Activator. Organic Process Research & Development. 2009;13(2):310-4.
148. Kuo JW, Swann DA, Prestwich GD. Chemical modification of hyaluronic acid by carbodiimides. Bioconjugate Chemistry. 1991;2(4):232-41.
149. Valeur E, Bradley M. Amide bond formation: beyond the myth of coupling reagents. Chemical Society Reviews. 2009;38(2):606-31.
150. Konig W, Geiger R. [A new method for synthesis of peptides: activation of the carboxyl group with dicyclohexylcarbodiimide using 1-hydroxybenzotriazoles as additives]. Chemische Berichte. 1970;103(3):788-98.
151. Kiani A, Esquevin A, Lepareur N, Bourguet P, Le Jeune F, Gauvrit J. Main applications of hybrid PET-MRI contrast agents: a review. Contrast media & molecular imaging. 2016;11(2):92-8.
152. Tudisca C, Nasoodi A, Fraioli F. PET-MRI: clinical application of the new hybrid technology. Nuclear medicine communications. 2015;36(7):666-78.
153. Frullano L, Catana C, Benner T, Sherry AD, Caravan P. Bimodal MR-PET agent for quantitative pH imaging. Angewandte Chemie (International ed in English). 2010;49(13):2382-4.
154. Bulte JW, Kraitchman DL. Iron oxide MR contrast agents for molecular and cellular imaging. NMR in biomedicine. 2004;17(7):484-99.
155. Lamb J, Holland JP. Advanced Methods for Radiolabeling Multimodality Nanomedicines for SPECT/MRI and PET/MRI. Journal of Nuclear Medicine. 2018;59(3):382-9.
156. McNeil SE. Nanoparticle therapeutics: a personal perspective. Wiley interdisciplinary reviews Nanomedicine and nanobiotechnology. 2009;1(3):264-71.
157. Abou DS, Thorek DLJ, Ramos NN, Pinkse MWH, Wolterbeek HT, Carlin SD, et al. (89)Zr-labeled paramagnetic octreotide-liposomes for PET-MR imaging of cancer. Pharm Res. 2013;30(3):878-88.
158. Boros E, Bowen AM, Josephson L, Vasdev N, Holland JP. Chelate-free metal ion binding and heat-induced radiolabeling of iron oxide nanoparticles. Chemical Science. 2015;6(1):225-36.

159. Patrick PS, Bogart LK, Macdonald TJ, Southern P, Powell MJ, Zaw-Thin M, et al. Surface radio-mineralisation mediates chelate-free radiolabelling of iron oxide nanoparticles. Chemical Science. 2019;10(9):2592-7.
160. Boros E, Bowen AM, Josephson L, Vasdev N, Holland JP. Chelate-free metal ion binding and heat-induced radiolabeling of iron oxide nanoparticles. Chem Sci. 2015;6(1):225-36.
161. Thorek DLJ, Ulmert D, Diop N-FM, Lupu ME, Doran MG, Huang R, et al. Non-invasive mapping of deep-tissue lymph nodes in live animals using a multimodal PET/MRI nanoparticle. Nature Communications. 2014;5(1):3097.
162. Lamb J, Holland JP. Advanced Methods for Radiolabeling Multimodality Nanomedicines for SPECT/MRI and PET/MRI. Journal of nuclear medicine : official publication, Society of Nuclear Medicine. 2018;59(3):382-9.
163. Ge CC, Tian J, Zhao YL, Chen CY, Zhou RH, Chai ZF. Towards understanding of nanoparticle-protein corona. Archives of Toxicology. 2015;89(4):519-39.
164. Pandya DN, Henry KE, Day CS, Graves SA, Nagle VL, Dilling TR, et al. Polyazamacrocycle Ligands Facilitate (89)Zr Radiochemistry and Yield (89)Zr Complexes with Remarkable Stability. Inorg Chem. 2020;59(23):17473-87.
165. Asti M, Tegoni M, Farioli D, Iori M, Guidotti C, Cutler CS, et al. Influence of cations on the complexation yield of DOTATATE with yttrium and lutetium: a perspective study for enhancing the 90Y and 177Lu labeling conditions. Nuclear Medicine and Biology. 2012;39(4):509-17.
166. Glišić S, Nikolić G, Cakic M, Trutic N. Spectroscopic study of copper(II) complexes with carboxymethyl dextran and dextran sulfate. Russian Journal of Physical Chemistry A. 2015;89:1254-62.
167. Demirbilek C, Dinc CO. Synthesis of diethylaminoethyl dextran hydrogel and its heavy metal ion adsorption characteristics. Carbohydrate Polymers. 2012;90(2):1159-67.
168. Muehe AM, Feng D, von Eyben R, Luna-Fineman S, Link MP, Muthig T, et al. Safety Report of Ferumoxytol for Magnetic Resonance Imaging in Children and Young Adults. Invest Radiol. 2016;51(4):221-7.
169. Zaw Thin M, Allan H, Bofinger R, Kostelec TD, Guillaume S, Connell JJ, et al. Multi-modal imaging probe for assessing the efficiency of stem cell delivery to orthotopic breast tumours. Nanoscale. 2020;12(31):16570-85.
170. Saitô H, Ando I, Naito A. Solid State NMR Spectroscopy for Biopolymers: Principles and Applications. Solid State NMR Spectroscopy for Biopolymers: Principles and Applications. 2006:1-464.
171. Mohammadi MR, Malkovskiy AV, Jothimuthu P, Kim K-M, Parekh M, Inayathullah M, et al. PEG/Dextran Double Layer Influences Fe Ion Release and Colloidal Stability of Iron Oxide Nanoparticles. Scientific Reports. 2018;8(1):4286.
172. Kettler K, Veltman K, van de Meent D, van Wezel A, Hendriks AJ. Cellular uptake of nanoparticles as determined by particle properties, experimental conditions, and cell type. Environmental Toxicology and Chemistry. 2014;33(3):481-92.
173. Moore TL, Rodriguez-Lorenzo L, Hirsch V, Balog S, Urban D, Jud C, et al. Nanoparticle colloidal stability in cell culture media and impact on cellular interactions. Chemical Society Reviews. 2015;44(17):6287-305.
174. Palanisamy S, Wang Y-M. Superparamagnetic iron oxide nanoparticulate system: synthesis, targeting, drug delivery and therapy in cancer. Dalton Transactions. 2019;48(26):9490-515.
175. Basuki JS, Jacquemin A, Esser L, Li Y, Boyer C, Davis TP. A block copolymer-stabilized co-precipitation approach to magnetic iron oxide nanoparticles for potential use as MRI contrast agents. Polymer Chemistry. 2014;5(7):2611-20.
176. Singh N, Jenkins GJS, Asadi R, Doak SH. Potential toxicity of superparamagnetic iron oxide nanoparticles (SPION). Nano Reviews. 2010;1(1):5358.
177. Šimeček J, Schulz M, Notni J, Plutnar J, Kubíček V, Havlíčková J, et al. Complexation of Metal Ions with TRAP (1,4,7-Triazacyclononane Phosphinic Acid)

Ligands and 1,4,7-Triazacyclononane-1,4,7-triacetic Acid: Phosphinate-Containing Ligands as Unique Chelators for Trivalent Gallium. Inorganic Chemistry. 2012;51(1):577-90.
178. Tsionou MI, Knapp CE, Foley CA, Munteanu CR, Cakebread A, Imberti C, et al. Comparison of macrocyclic and acyclic chelators for gallium-68 radiolabelling. RSC Advances. 2017;7(78):49586-99.
179. Boros E, Holland JP. Chemical aspects of metal ion chelation in the synthesis and application antibody-based radiotracers. Journal of labelled compounds & radiopharmaceuticals. 2018;61(9):652-71.
180. Tircsó G, Kovács Z, Sherry AD. Equilibrium and Formation/Dissociation Kinetics of Some LnIIIPCTA Complexes. Inorganic Chemistry. 2006;45(23):9269-80.
181. Ferreira CL, Yapp DT, Lamsa E, Gleave M, Bensimon C, Jurek P, et al. Evaluation of novel bifunctional chelates for the development of Cu-64-based radiopharmaceuticals. Nucl Med Biol. 2008;35(8):875-82.
182. Ferreira CL, Lamsa E, Woods M, Duan Y, Fernando P, Bensimon C, et al. Evaluation of Bifunctional Chelates for the Development of Gallium-Based Radiopharmaceuticals. Bioconjugate Chemistry. 2010;21(3):531-6.
183. Davydov YP, Davydov DY, Zemskova L. Speciation of Zr(IV) radionuclides in solutions. Radiochemistry. 2006;48:358-64.
184. Sasaki T, Kobayashi T, Takagi I, Moriyama H. Hydrolysis Constant and Coordination Geometry of Zirconium(IV). Journal of Nuclear Science and Technology. 2008;45(8):735-9.
185. Kobayashi T, Sasaki T, Takagi I, Moriyama H. Solubility of Zirconium(IV) Hydrous Oxides. Journal of Nuclear Science and Technology. 2007;44(1):90-4.
186. Holland JP. The Radiochemistry of Zirconium. Handbook of Radiopharmaceuticals2020. p. 343-74.
187. Holland JP, Sheh Y, Lewis JS. Standardized methods for the production of high specific-activity zirconium-89. Nucl Med Biol. 2009;36(7):729-39.
188. Wulfsberg G. Inorganic Chemistry: University Science Books; 2000.
189. Rausch K, Reuter A, Fischer K, Schmidt M. Evaluation of nanoparticle aggregation in human blood serum. Biomacromolecules. 2010;11(11):2836-9.
190. Gregory J. Approximate expressions for retarded van der waals interaction. Journal of Colloid and Interface Science. 1981;83(1):138-45.
191. Sader JE, Carnie SL, Chan DYC. Accurate Analytic Formulas for the Double-Layer Interaction between Spheres. Journal of Colloid and Interface Science. 1995;171(1):46-54.
192. Verwey EJW. Theory of the Stability of Lyophobic Colloids. The Journal of Physical and Colloid Chemistry. 1947;51(3):631-6.
193. Tripathy N, Hong T-K, Ha K-T, Jeong H-S, Hahn Y-B. Effect of ZnO nanoparticles aggregation on the toxicity in RAW 264.7 murine macrophage. Journal of Hazardous Materials. 2014;270:110-7.
194. Bouissou C, Potter U, Altroff H, Mardon H, van der Walle C. Controlled release of the fibronectin central cell binding domain from polymeric microspheres. Journal of Controlled Release. 2004;95(3):557-66.
195. Nel A, Xia T, Madler L, Li N. Toxic potential of materials at the nanolevel. Science. 2006;311(5761):622-7.
196. Liu X, Yang Z, Sun J, Ma T, Hua F, Shen Z. A brief review of cytotoxicity of nanoparticles on mesenchymal stem cells in regenerative medicine. Int J Nanomedicine. 2019;14:3875-92.
197. Nel A, Xia T, Mädler L, Li N. Toxic Potential of Materials at the Nanolevel. Science. 2006;311(5761):622.
198. Pisanic TR, Blackwell JD, Shubayev VI, Fiñones RR, Jin S. Nanotoxicity of iron oxide nanoparticle internalization in growing neurons. Biomaterials. 2007;28(16):2572-81.
199. Singh N, Manshian B, Jenkins GJS, Griffiths SM, Williams PM, Maffeis TGG, et al. NanoGenotoxicology: The DNA damaging potential of engineered nanomaterials. Biomaterials. 2009;30(23):3891-914.

200. Vakili-Ghartavol R, Momtazi-Borojeni AA, Vakili-Ghartavol Z, Aiyelabegan HT, Jaafari MR, Rezayat SM, et al. Toxicity assessment of superparamagnetic iron oxide nanoparticles in different tissues. Artificial Cells, Nanomedicine, and Biotechnology. 2020;48(1):443-51.
201. Schweiger C, Hartmann R, Zhang F, Parak WJ, Kissel TH, Rivera_Gil P. Quantification of the internalization patterns of superparamagnetic iron oxide nanoparticles with opposite charge. Journal of Nanobiotechnology. 2012;10(1):28.
202. Wang T, Bai J, Jiang X, Nienhaus GU. Cellular Uptake of Nanoparticles by Membrane Penetration: A Study Combining Confocal Microscopy with FTIR Spectroelectrochemistry. ACS Nano. 2012;6(2):1251-9.
203. Kehrer JP. The Haber–Weiss reaction and mechanisms of toxicity. Toxicology. 2000;149(1):43-50.
204. Sarkar A, Sil PC. Iron oxide nanoparticles mediated cytotoxicity via PI3K/AKT pathway: Role of quercetin. Food and Chemical Toxicology. 2014;71:106-15.
205. Chen Y-C, Hsiao J-K, Liu H-M, Lai IY, Yao M, Hsu S-C, et al. The inhibitory effect of superparamagnetic iron oxide nanoparticle (Ferucarbotran) on osteogenic differentiation and its signaling mechanism in human mesenchymal stem cells. Toxicology and Applied Pharmacology. 2010;245(2):272-9.
206. Chou LY, Ming K, Chan WC. Strategies for the intracellular delivery of nanoparticles. Chem Soc Rev. 2011;40(1):233-45.
207. Mahmoudi M, Meng J, Xue X, Liang XJ, Rahman M, Pfeiffer C, et al. Interaction of stable colloidal nanoparticles with cellular membranes. Biotechnology advances. 2014;32(4):679-92.
208. Makaraci P, Kim K. trans-Golgi network-bound cargo traffic. European journal of cell biology. 2018;97(3):137-49.
209. Foroozandeh P, Aziz AA. Insight into Cellular Uptake and Intracellular Trafficking of Nanoparticles. Nanoscale Res Lett. 2018;13(1):339-.
210. Zhao F, Zhao Y, Liu Y, Chang X, Chen C, Zhao Y. Cellular uptake, intracellular trafficking, and cytotoxicity of nanomaterials. Small (Weinheim an der Bergstrasse, Germany). 2011;7(10):1322-37.
211. Litwack G. Human biochemistry: Academic Press; 2017.
212. Ramsden J. The Safety of Nanofacture and Nanomaterials. 2018. p. 205-23.
213. Hirota K, Terada H. Endocytosis of Particle Formulations by Macrophages and Its Application to Clinical Treatment. Ceresa B, editor2012. 413-28 p.
214. Yu Y. Resolving Endosome Rotation in Intracellular Trafficking. Biophysical Journal. 2018;114(3):630A-A.
215. Kuhn DA, Vanhecke D, Michen B, Blank F, Gehr P, Petri-Fink A, et al. Different endocytotic uptake mechanisms for nanoparticles in epithelial cells and macrophages. Beilstein Journal of Nanotechnology. 2014;5:1625-36.
216. Parton RG, Simons K. The multiple faces of caveolae. Nature reviews Molecular cell biology. 2007;8(3):185-94.
217. Wang Z, Tiruppathi C, Cho J, Minshall RD, Malik AB. Delivery of nanoparticle: complexed drugs across the vascular endothelial barrier via caveolae. IUBMB life. 2011;63(8):659-67.
218. Lim JP, Gleeson PA. Macropinocytosis: an endocytic pathway for internalising large gulps. Immunology and cell biology. 2011;89(8):836-43.
219. Zhu M, Nie G, Meng H, Xia T, Nel A, Zhao Y. Physicochemical properties determine nanomaterial cellular uptake, transport, and fate. Accounts of chemical research. 2013;46(3):622-31.
220. Rejman J, Oberle V, Zuhorn IS, Hoekstra D. Size-dependent internalization of particles via the pathways of clathrin- and caveolae-mediated endocytosis. The Biochemical journal. 2004;377(Pt 1):159-69.
221. Lu F, Wu SH, Hung Y, Mou CY. Size effect on cell uptake in well-suspended, uniform mesoporous silica nanoparticles. Small (Weinheim an der Bergstrasse, Germany). 2009;5(12):1408-13.

222. Chaffey N. Alberts, B., Johnson, A., Lewis, J., Raff, M., Roberts, K. and Walter, P. Molecular biology of the cell. 4th edn. Ann Bot. 2003;91(3):401-.
223. Marano F, Hussain S, Rodrigues-Lima F, Baeza-Squiban A, Boland S. Nanoparticles: molecular targets and cell signalling. Archives of toxicology. 2011;85(7):733-41.
224. Panariti A, Miserocchi G, Rivolta I. The effect of nanoparticle uptake on cellular behavior: disrupting or enabling functions? Nanotechnol Sci Appl. 2012;5:87-100.
225. Dausend J, Musyanovych A, Dass M, Walther P, Schrezenmeier H, Landfester K, et al. Uptake mechanism of oppositely charged fluorescent nanoparticles in HeLa cells. Macromolecular bioscience. 2008;8(12):1135-43.
226. Walkey CD, Chan WCW. Understanding and controlling the interaction of nanomaterials with proteins in a physiological environment. Chemical Society Reviews. 2012;41(7):2780-99.
227. Vroman L, Adams AL, Fischer GC, Munoz PC. Interaction of high molecular weight kininogen, factor XII, and fibrinogen in plasma at interfaces. Blood. 1980;55(1):156-9.
228. Falahati M, Attar F, Sharifi M, Haertlé T, Berret J-F, Khan RH, et al. A health concern regarding the protein corona, aggregation and disaggregation. Biochimica et Biophysica Acta (BBA) - General Subjects. 2019;1863(5):971-91.
229. Cheng X, Tian X, Wu A, Li J, Tian J, Chong Y, et al. Protein Corona Influences Cellular Uptake of Gold Nanoparticles by Phagocytic and Nonphagocytic Cells in a Size-Dependent Manner. ACS Applied Materials & Interfaces. 2015;7(37):20568-75.
230. Boström M, Williams DRM, Ninham BW. Specific Ion Effects: Why DLVO Theory Fails for Biology and Colloid Systems. Physical Review Letters. 2001;87(16):168103.
231. Edwards SA, Williams DRM. Double Layers and Interparticle Forces in Colloid Science and Biology: Analytic Results for the Effect of Ionic Dispersion Forces. Physical Review Letters. 2004;92(24):248303.
232. Safi M, Courtois J, Seigneuret M, Conjeaud H, Berret JF. The effects of aggregation and protein corona on the cellular internalization of iron oxide nanoparticles. Biomaterials. 2011;32(35):9353-63.
233. Dobrovolskaia MA, Patri AK, Zheng J, Clogston JD, Ayub N, Aggarwal P, et al. Interaction of colloidal gold nanoparticles with human blood: effects on particle size and analysis of plasma protein binding profiles. Nanomedicine: Nanotechnology, Biology and Medicine. 2009;5(2):106-17.
234. Kittler S, Greulich C, Gebauer JS, Diendorf J, Treuel L, Ruiz L, et al. The influence of proteins on the dispersability and cell-biological activity of silver nanoparticles. Journal of Materials Chemistry. 2010;20(3):512-8.
235. Fish WW. Rapid colorimetric micromethod for the quantitation of complexed iron in biological samples. Methods in enzymology. 1988;158:357-64.
236. Mahl D, Greulich C, Meyer-Zaika W, Köller M, Epple M. Gold nanoparticles: dispersibility in biological media and cell-biological effect. Journal of Materials Chemistry. 2010;20(29):6176-81.
237. Chen ZP, Zhang Y, Zhang S, Xia JG, Liu JW, Xu K, et al. Preparation and characterization of water-soluble monodisperse magnetic iron oxide nanoparticles via surface double-exchange with DMSA. Colloids and Surfaces A: Physicochemical and Engineering Aspects. 2008;316(1):210-6.
238. Ji Z, Jin X, George S, Xia T, Meng H, Wang X, et al. Dispersion and Stability Optimization of TiO2 Nanoparticles in Cell Culture Media. Environmental Science & Technology. 2010;44(19):7309-14.
239. Böhmert L, Voß L, Stock V, Braeuning A, Lampen A, Sieg H. Isolation methods for particle protein corona complexes from protein-rich matrices. Nanoscale Advances. 2020;2(2):563-82.
240. Veiseh O, Gunn JW, Zhang M. Design and fabrication of magnetic nanoparticles for targeted drug delivery and imaging. Advanced drug delivery reviews. 2010;62(3):284-304.

241. Ramos S, Campos-Terán J, Mas-Oliva J, Nylander T, Castillo R. Forces between Hydrophilic Surfaces Adsorbed with Apolipoprotein AII Alpha Helices. Langmuir. 2008;24(16):8568-75.
242. Huang D-M, Hsiao J-K, Chen Y-C, Chien L-Y, Yao M, Chen Y-K, et al. The promotion of human mesenchymal stem cell proliferation by superparamagnetic iron oxide nanoparticles. Biomaterials. 2009;30(22):3645-51.
243. Gao L, Zhuang J, Nie L, Zhang J, Zhang Y, Gu N, et al. Intrinsic peroxidase-like activity of ferromagnetic nanoparticles. Nature nanotechnology. 2007;2(9):577-83.
244. Ye M, Shi B. Zirconia Nanoparticles-Induced Toxic Effects in Osteoblast-Like 3T3-E1 Cells. Nanoscale Res Lett. 2018;13(1):353-.
245. Yang Y, Bao H, Chai Q, Wang Z, Sun Z, Fu C, et al. Toxicity, biodistribution and oxidative damage caused by zirconia nanoparticles after intravenous injection. Int J Nanomedicine. 2019;14:5175-86.
246. Au C, Mutkus L, Dobson A, Riffle J, Lalli J, Aschner M. Effects of nanoparticles on the adhesion and cell viability on astrocytes. Biological trace element research. 2007;120(1-3):248-56.
247. Pöttler M, Fliedner A, Schreiber E, Janko C, Friedrich R, Bohr C, et al. Impact of Superparamagnetic Iron Oxide Nanoparticles on Vocal Fold Fibroblasts: Cell Behavior and Cellular Iron Kinetics. Nanoscale Res Lett. 2017;12.
248. Guggenheim EJ, Rappoport JZ, Lynch I. Mechanisms for cellular uptake of nanosized clinical MRI contrast agents. Nanotoxicology. 2020;14(4):504-32.
249. Gu J, Xu H, Han Y, Dai W, Hao W, Wang C, et al. The internalization pathway, metabolic fate and biological effect of superparamagnetic iron oxide nanoparticles in the macrophage-like RAW264.7 cell. Science China Life sciences. 2011;54(9):793-805.
250. Ferris TJ, Charoenphun P, Meszaros LK, Mullen GED, Blower PJ, Went MJ. Synthesis and characterisation of zirconium complexes for cell tracking with Zr-89 by positron emission tomography. Dalton Transactions. 2014;43(39):14851-7.
251. Lans C, van Asseldonk T. Dr. Duke's Phytochemical and Ethnobotanical Databases, a Cornerstone in the Validation of Ethnoveterinary Medicinal Plants, as Demonstrated by Data on Pets in British Columbia. In: Máthé Á, editor. Medicinal and Aromatic Plants of North America. Cham: Springer International Publishing; 2020. p. 219-46.
252. Deri MA, Zeglis BM, Francesconi LC, Lewis JS. PET imaging with ^{89}Zr: from radiochemistry to the clinic. Nucl Med Biol. 2013;40(1):3-14.
253. Lee DB, Roberts M, Bluchel CG, Odell RA. Zirconium: biomedical and nephrological applications. ASAIO journal (American Society for Artificial Internal Organs : 1992). 2010;56(6):550-6.
254. Gofman JW. STUDIES WITH COLLOIDS CONTAINING RADIOISOTOPES OF YTTRIUM, ZIRCONIUM, COLUMBIUM, AND LANTHANUM .1. THE CHEMICAL PRINCIPLES AND METHODS INVOLVED IN PREPARATION OF COLLOIDS OF YTTRIUM, ZIRCONIUM, COLUMBIUM, AND LANTHANUM. J Lab Clin Med. 1949;34(3):297-304.
255. Meijs WE, Haisma HJ, Van der Schors R, Wijbrandts R, Van den Oever K, Klok RP, et al. A facile method for the labeling of proteins with zirconium isotopes. Nucl Med Biol. 1996;23(4):439-48.
256. Sun C, Lee JSH, Zhang M. Magnetic nanoparticles in MR imaging and drug delivery. Adv Drug Deliv Rev. 2008;60(11):1252-65.
257. Wáng YXJ, Idée J-M. A comprehensive literatures update of clinical researches of superparamagnetic resonance iron oxide nanoparticles for magnetic resonance imaging. Quant Imaging Med Surg. 2017;7(1):88-122.
258. Crețu BE-B, Dodi G, Shavandi A, Gardikiotis I, Șerban IL, Balan V. Imaging Constructs: The Rise of Iron Oxide Nanoparticles. 2021;26(11):3437.
259. Leal MP, Muñoz-Hernández C, Berry CC, García-Martín ML. In vivo pharmacokinetics of T2 contrast agents based on iron oxide nanoparticles: optimization of blood circulation times. RSC Advances. 2015;5(94):76883-91.

260. Barry SE. Challenges in the development of magnetic particles for therapeutic applications. International Journal of Hyperthermia. 2008;24(6):451-66.
261. Arami H, Khandhar A, Liggitt D, Krishnan KM. In vivo delivery, pharmacokinetics, biodistribution and toxicity of iron oxide nanoparticles. Chemical Society Reviews. 2015;44(23):8576-607.
262. Alexis F, Pridgen E, Molnar LK, Farokhzad OC. Factors affecting the clearance and biodistribution of polymeric nanoparticles. Mol Pharm. 2008;5(4):505-15.
263. Wang J, Chen Y, Chen B, Ding J, Xia G, Gao C, et al. Pharmacokinetic parameters and tissue distribution of magnetic Fe(3)O(4) nanoparticles in mice. Int J Nanomedicine. 2010;5:861-6.
264. Kaufman CL, Williams M, Madison Ryle L, Smith TL, Tanner M, Ho C. Superparamagnetic iron oxide particles transactivator protein-fluorescein isothiocyanate particle labeling for in vivo magnetic resonance imaging detection of cell migration: uptake and durability. Transplantation. 2003;76(7).
265. Kohyama M, Ise W, Edelson BT, Wilker PR, Hildner K, Mejia C, et al. Role for Spi-C in the development of red pulp macrophages and splenic iron homeostasis. Nature. 2009;457(7227):318-21.
266. Sun S, Zeng H, Robinson DB, Raoux S, Rice PM, Wang SX, et al. Monodisperse MFe_2O_4 (M = Fe, Co, Mn) nanoparticles. Journal of the American Chemical Society. 2004;126(1):273-9.
267. Jing M, Liu XQ, Liang P, Li CY, Zhang XT, Wang D, et al. [Labeling neural stem cells with superparamagnetic iron oxide in vitro and tracking after implantation with MRI in vivo]. Zhonghua yi xue za zhi. 2004;84(16):1386-9.
268. Ahrens ET, Feili-Hariri M, Xu H, Genove G, Morel PA. Receptor-mediated endocytosis of iron-oxide particles provides efficient labeling of dendritic cells for in vivo MR imaging. Magnetic resonance in medicine. 2003;49(6):1006-13.
269. Arbab AS, Wilson LB, Ashari P, Jordan EK, Lewis BK, Frank JA. A model of lysosomal metabolism of dextran coated superparamagnetic iron oxide (SPIO) nanoparticles: implications for cellular magnetic resonance imaging. Nmr in Biomedicine. 2005;18(6):383-9.
270. Bao Y, Wen T, Samia ACS, Khandhar A, Krishnan KM. Magnetic Nanoparticles: Material Engineering and Emerging Applications in Lithography and Biomedicine. J Mater Sci. 2016;51(1):513-53.
271. Taylor A, Herrmann A, Moss D, Sée V, Davies K, Williams SR, et al. Assessing the efficacy of nano- and micro-sized magnetic particles as contrast agents for MRI cell tracking. PLoS One. 2014;9(6):e100259-e.
272. Nelson NR, Port JD, Pandey MK. Use of Superparamagnetic Iron Oxide Nanoparticles (SPIONs) via Multiple Imaging Modalities and Modifications to Reduce Cytotoxicity: An Educational Review. 2020;1(1):105-35.
273. Bourrinet P, Bengele HH, Bonnemain B, Dencausse A, Idee JM, Jacobs PM, et al. Preclinical safety and pharmacokinetic profile of ferumoxtran-10, an ultrasmall superparamagnetic iron oxide magnetic resonance contrast agent. Investigative Radiology. 2006;41(3):313-24.
274. Choi HS, Liu W, Misra P, Tanaka E, Zimmer JP, Ipe BI, et al. Renal clearance of quantum dots. 2007;25(10):1165-70.
275. Sarin HJJoar. Physiologic upper limits of pore size of different blood capillary types and another perspective on the dual pore theory of microvascular permeability. 2010;2(1):1-19.
276. Longmire M, Choyke PL, Kobayashi H. Clearance properties of nano-sized particles and molecules as imaging agents: considerations and caveats. Nanomedicine (Lond). 2008;3(5):703-17.
277. McDonagh PR, Sundaresan G, Yang L, Sun M, Mikkelsen R, Zweit J. Biodistribution and PET imaging of 89-zirconium labeled cerium oxide nanoparticles synthesized with several surface coatings. Nanomedicine. 2018;14(4):1429-40.

278. Zhan Y, Ehlerding EB, Shi S, Graves SA, Goel S, Engle JW, et al. Intrinsically Zirconium-89-Labeled Manganese Oxide Nanoparticles for In Vivo Dual-Modality Positron Emission Tomography and Magnetic Resonance Imaging. J Biomed Nanotechnol. 2018;14(5):900-9.
279. Thorek DL, Ulmert D, Diop NF, Lupu ME, Doran MG, Huang R, et al. Non-invasive mapping of deep-tissue lymph nodes in live animals using a multimodal PET/MRI nanoparticle. Nature communications. 2014;5:3097.
280. Balakrishnan VS, Rao M, Kausz AT, Brenner L, Pereira BJ, Frigo TB, et al. Physicochemical properties of ferumoxytol, a new intravenous iron preparation. European journal of clinical investigation. 2009;39(6):489-96.
281. Bengele HH, Palmacci S, Rogers J, Jung CW, Crenshaw J, Josphson L. Biodistribution of an ultrasmall superparamagnetic iron oxide colloid, BMS 180549, by different routes of administration. Magnetic Resonance Imaging. 1994;12(3):433-42.
282. Nakamura A, Osonoi T, Terauchi Y. Relationship between urinary sodium excretion and pioglitazone-induced edema. Journal of diabetes investigation. 2010;1(5):208-11.
283. Severin GW, Jørgensen JT, Wiehr S, Rolle AM, Hansen AE, Maurer A, et al. The impact of weakly bound ^{89}Zr on preclinical studies: non-specific accumulation in solid tumors and aspergillus infection. Nucl Med Biol. 2015;42(4):360-8.
284. Chen F, Goel S, Valdovinos HF, Luo H, Hernandez R, Barnhart TE, et al. In Vivo Integrity and Biological Fate of Chelator-Free Zirconium-89-Labeled Mesoporous Silica Nanoparticles. ACS Nano. 2015;9(8):7950-9.
285. Slevin E, Baiocchi L, Wu N, Ekser B, Sato K, Lin E, et al. Kupffer Cells: Inflammation Pathways and Cell-Cell Interactions in Alcohol-Associated Liver Disease. The American Journal of Pathology. 2020;190(11):2185-93.
286. Crabb DW, Im GY, Szabo G, Mellinger JL, Lucey MR. Diagnosis and Treatment of Alcohol-Associated Liver Diseases: 2019 Practice Guidance From the American Association for the Study of Liver Diseases. Hepatology. 2020;71(1):306-33.
287. Wan J, Benkdane M, Teixeira-Clerc F, Bonnafous S, Louvet A, Lafdil F, et al. M2 Kupffer cells promote M1 Kupffer cell apoptosis: a protective mechanism against alcoholic and nonalcoholic fatty liver disease. Hepatology. 2014;59(1):130-42.
288. Zhang J-x, Yang Y, Huang H, Xie H-b, Huang M, Jiang W, et al. TNF-α/TNFR1 regulates the polarization of Kupffer cells to mediate trichloroethylene-induced liver injury. Ecotoxicology and Environmental Safety. 2022;230:113141.
289. Almer G, Summers KL, Scheicher B, Kellner J, Stelzer I, Leitinger G, et al. Interleukin 10-coated nanoparticle systems compared for molecular imaging of atherosclerotic lesions. Int J Nanomedicine. 2014;9:4211-22.
290. Baganizi D, Nyairo E, Duncan S, Singh S, Dennis V. Interleukin-10 Conjugation to Carboxylated PVP-Coated Silver Nanoparticles for Improved Stability and Therapeutic Efficacy. Nanomaterials. 2017;7.
291. Schrepfer S, Deuse T, Reichenspurner H, Fischbein MP, Robbins RC, Pelletier MP. Stem cell transplantation: the lung barrier. Transplantation proceedings. 2007;39(2):573-6.
292. Eggenhofer E, Benseler V, Kroemer A, Popp FC, Geissler EK, Schlitt HJ, et al. Mesenchymal stem cells are short-lived and do not migrate beyond the lungs after intravenous infusion. Frontiers in immunology. 2012;3:297.
293. Fischer UM, Harting MT, Jimenez F, Monzon-Posadas WO, Xue H, Savitz SI, et al. Pulmonary passage is a major obstacle for intravenous stem cell delivery: the pulmonary first-pass effect. Stem cells and development. 2009;18(5):683-92.
294. Guiteras R, Sola A, Flaquer M, Hotter G, Torras J, Grinyó JM, et al. Macrophage Overexpressing NGAL Ameliorated Kidney Fibrosis in the UUO Mice Model. Cellular Physiology and Biochemistry. 2017;42(5):1945-60.
295. Dou H, Destache CJ, Morehead JR, Mosley RL, Boska MD, Kingsley J, et al. Development of a macrophage-based nanoparticle platform for antiretroviral drug delivery. Blood. 2006;108(8):2827-35.

296. Geng Y, Zhang L, Fu B, Zhang J, Hong Q, Hu J, et al. Mesenchymal stem cells ameliorate rhabdomyolysis-induced acute kidney injury via the activation of M2 macrophages. Stem cell research & therapy. 2014;5(3):80.
297. Harwood R. Investigating the physiology of ischaemia reperfusion injury of the mouse kidney and the efficacy of regenerative medicine therapies after acute kidney injury. United Kingdom: Liverpool University 2021.
298. Santeramo I, Herrera Perez Z, Illera A, Taylor A, Kenny S, Murray P, et al. Human Kidney-Derived Cells Ameliorate Acute Kidney Injury Without Engrafting into Renal Tissue. Stem cells translational medicine. 2017;6(5):1373-84.
299. Sun Y, Yu H, Zheng D, Cao Q, Wang Y, Harris D, et al. Sudan black B reduces autofluorescence in murine renal tissue. Archives of pathology & laboratory medicine. 2011;135(10):1335-42.
300. Taylor A, Sharkey J, Harwood R, Scarfe L, Barrow M, Rosseinsky MJ, et al. Multimodal Imaging Techniques Show Differences in Homing Capacity Between Mesenchymal Stromal Cells and Macrophages in Mouse Renal Injury Models. Molecular Imaging and Biology. 2020;22(4):904-13.
301. Furuichi K, Kaneko S, Wada T. Chemokine/chemokine receptor-mediated inflammation regulates pathologic changes from acute kidney injury to chronic kidney disease. Clinical and experimental nephrology. 2009;13(1):9-14.
302. Zaw Thin M, Ogunlade O, Comenge J, Patrick PS, Stuckey DJ, David AL, et al. Stem cell delivery to kidney via minimally invasive ultrasound-guided renal artery injection in mice. Scientific Reports. 2020;10(1):7514.
303. James ML, Gambhir SS. A molecular imaging primer: modalities, imaging agents, and applications. Physiological reviews. 2012;92(2):897-965.
304. Taylor A, Sharkey J, Harwood R, Scarfe L, Barrow M, Rosseinsky MJ, et al. Multimodal Imaging Techniques Show Differences in Homing Capacity Between Mesenchymal Stromal Cells and Macrophages in Mouse Renal Injury Models. Molecular imaging and biology. 2020;22(4):904-13.
305. Wei Q, Dong Z. Mouse model of ischemic acute kidney injury: technical notes and tricks. Am J Physiol Renal Physiol. 2012;303(11):F1487-F94.
306. Hesketh EE, Czopek A, Clay M, Borthwick G, Ferenbach D, Kluth D, et al. Renal ischaemia reperfusion injury: a mouse model of injury and regeneration. Journal of visualized experiments : JoVE. 2014(88).
307. Abou DS, Ku T, Smith-Jones PM. In vivo biodistribution and accumulation of 89Zr in mice. Nuclear medicine and biology. 2011;38(5):675-81.
308. Taylor A, Sharkey J, Plagge A, Wilm B, Murray P. Multicolour In Vivo Bioluminescence Imaging Using a NanoLuc-Based BRET Reporter in Combination with Firefly Luciferase. Contrast Media & Molecular Imaging. 2018;2018:2514796.
309. Wise AF, Williams TM, Kiewiet MBG, Payne NL, Siatskas C, Samuel CS, et al. Human mesenchymal stem cells alter macrophage phenotype and promote regeneration via homing to the kidney following ischemia-reperfusion injury. American Journal of Physiology-Renal Physiology. 2014;306(10):F1222-F35.
310. Zhuo W, Liao L, Fu Y, Xu T, Wu W, Yang S, et al. Efficiency of Endovenous Versus Arterial Administration of Mesenchymal Stem Cells for Ischemia-Reperfusion–Induced Renal Dysfunction in Rats. Transplantation proceedings. 2013;45(2):503-10.
311. Tögel F, Yang Y, Zhang P, Hu Z, Westenfelder C. Bioluminescence imaging to monitor the in vivo distribution of administered mesenchymal stem cells in acute kidney injury. Am J Physiol Renal Physiol. 2008;295(1):F315-F21.
312. Sharkey J, Ressel L, Brillant N, Scarfe L, Wilm B, Park BK, et al. A Noninvasive Imaging Toolbox Indicates Limited Therapeutic Potential of Conditionally Activated Macrophages in a Mouse Model of Multiple Organ Dysfunction. Stem Cells Int. 2019;2019:7386954-.
313. Barrow M, Taylor A, Nieves DJ, Bogart LK, Mandal P, Collins CM, et al. Tailoring the surface charge of dextran-based polymer coated SPIONs for modulated stem cell uptake and MRI contrast. Biomaterials science. 2015;3(4):608-16.

314. Yang L, Zhang Y. Tumor-associated macrophages: from basic research to clinical application. J Hematol Oncol. 2017;10(1):58-.

315. Mukherjee S, Sonanini D, Maurer A, Daldrup-Link HE. The yin and yang of imaging tumor associated macrophages with PET and MRI. Theranostics. 2019;9(25):7730-48.

316. Yang L, Zhang Y. Tumor-associated macrophages: from basic research to clinical application. Journal of Hematology & Oncology. 2017;10(1):58.

317. Grivennikov SI, Greten FR, Karin M. Immunity, inflammation, and cancer. Cell. 2010;140(6):883-99.

318. Kim H-Y, Li R, Ng TS, Courties G, Rodell CB, Prytyskach M, et al. Quantitative imaging of tumor-associated macrophages and their response to therapy using 64Cu-labeled macrin. ACS nano. 2018;12(12):12015-29.

319. Locke LW, Mayo MW, Yoo AD, Williams MB, Berr SS. PET imaging of tumor associated macrophages using mannose coated 64Cu liposomes. Biomaterials. 2012;33(31):7785-93.

320. Pérez-Medina C, Tang J, Abdel-Atti D, Hogstad B, Merad M, Fisher EA, et al. PET imaging of tumor-associated macrophages with 89Zr-labeled high-density lipoprotein nanoparticles. Journal of nuclear medicine. 2015;56(8):1272-7.

321. Daldrup-Link HE, Golovko D, Ruffell B, DeNardo DG, Castaneda R, Ansari C, et al. MRI of tumor-associated macrophages with clinically applicable iron oxide nanoparticles. Clinical Cancer Research. 2011;17(17):5695-704.

322. Pichu S, Krishnamoorthy S, Zhang B, Jing Y, Shishkov A, Ponnappa BC. Dicer-substrate siRNA inhibits tumor necrosis factor alpha secretion in Kupffer cells in vitro: In vivo targeting of Kupffer cells by siRNA-liposomes. Pharmacological Research. 2012;65(1):48-55.

323. Colino CI, Lanao JM, Gutierrez-Millan C. Targeting of Hepatic Macrophages by Therapeutic Nanoparticles. Front Immunol. 2020;11:218-.

Appendix

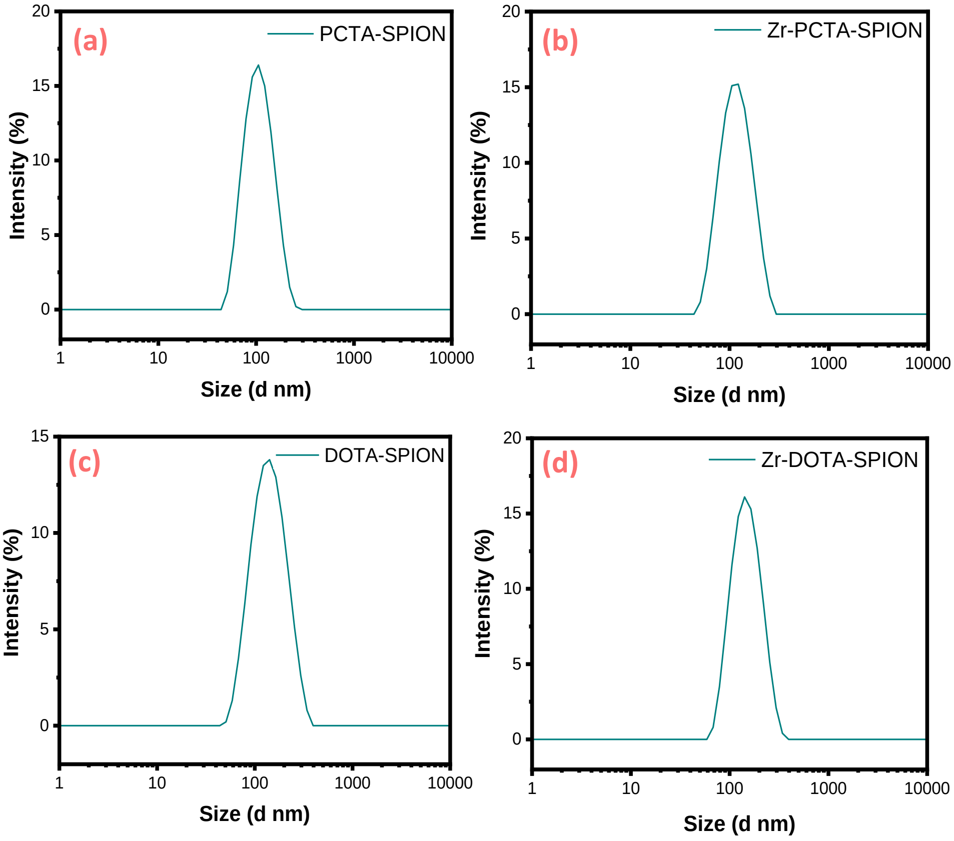

Figure A3.1: (a) Particle size distribution of PCTA-SPIONs **(b)** Particle size distribution of Zr-PCTA-SPIONs **(c)** Particle size distribution of DOTA-SPIONs **(d)** Particle size distribution of Zr-DOTA-SPIONs.

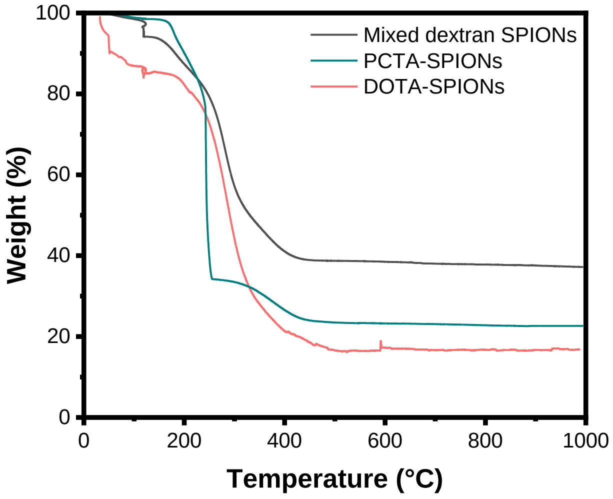

Figure A3.2: Thermogravimetric analysis (TGA) weight loss curves for mixed dextran SPIONs, PCTA-SPIONs and DOTA-SPIONs measured under a constant air flow.

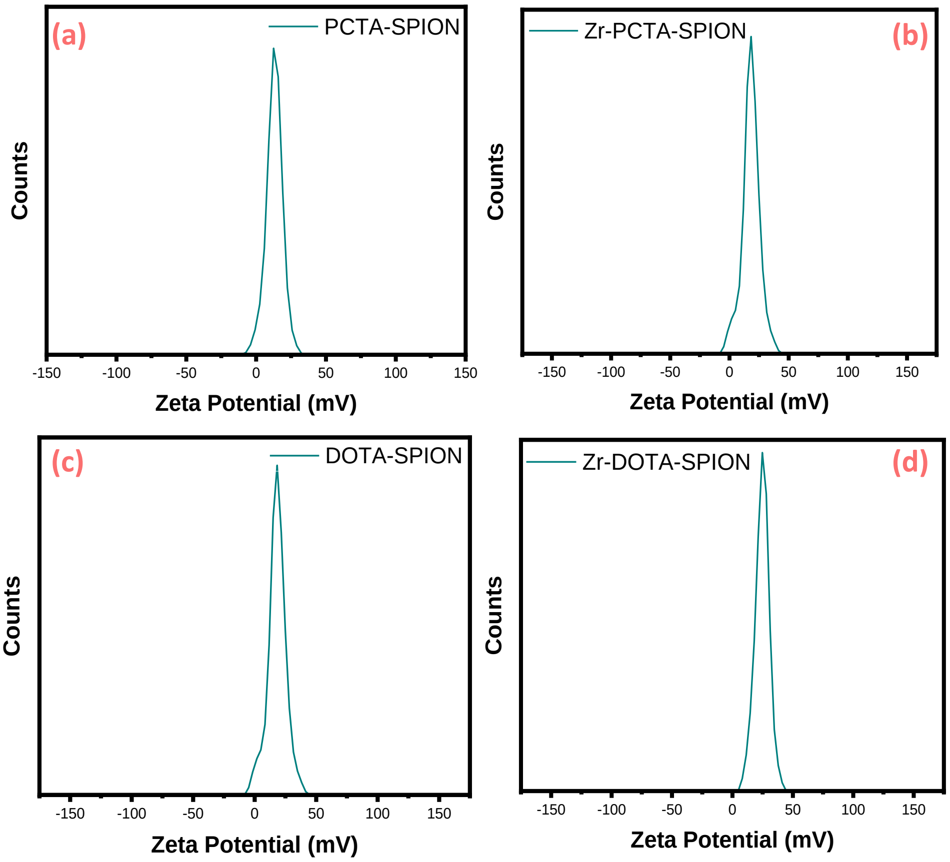

Figure A3.3: (a) Zeta potential distribution of PCTA-SPIONs **(b)** Zeta potential distribution of Zr-PCTA-SPIONs **(c)** Zeta potential distribution of DOTA-SPIONs **(d)** Zeta potential distribution of Zr-DOTA-SPIONs.

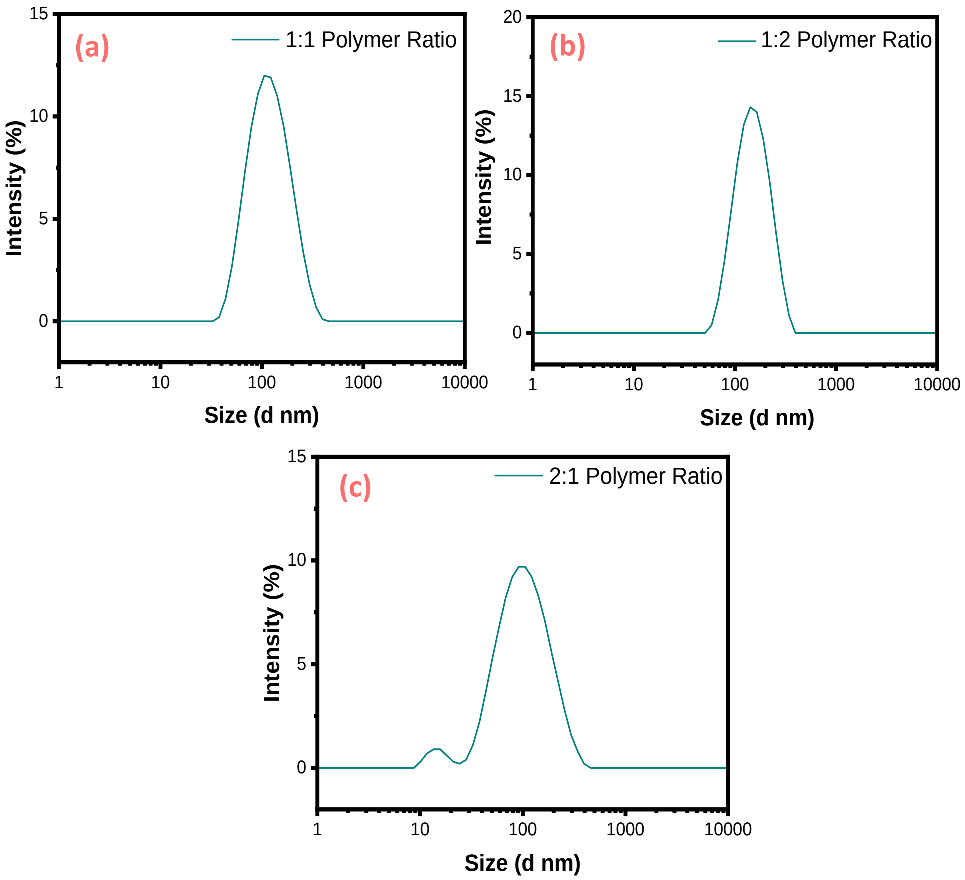

Figure A4.1: **(a)** Particle size distribution of mixed dextran SPIONs synthesised with a 1:1 ratio (by mass) of the polymers, EDEA-CM-dextran to DEAE-dextran **(b)** Particle size distribution of mixed dextran SPIONs synthesised with a 1:2 ratio (by mass) of the polymers, EDEA-CM-dextran to DEAE-dextran **(c)** Particle size distribution of mixed dextran SPIONs synthesised with a 2:1 ratio (by mass) of the polymers, EDEA-CM-dextran to DEAE-dextran.

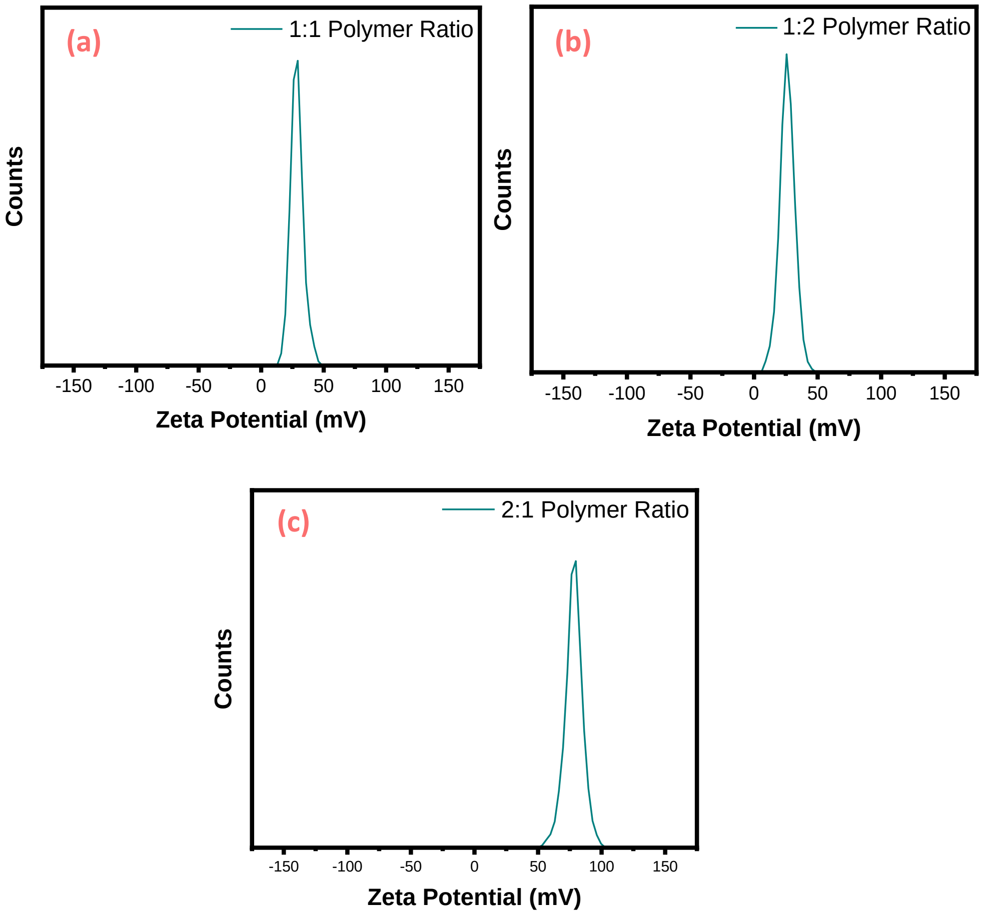

Figure A4.2: (a) Zeta potential distribution of mixed dextran SPIONs synthesised with a 1:1 ratio (by mass) of the polymers, EDEA-CM-dextran to DEAE-dextran **(b)** Zeta potential distribution of mixed dextran SPIONs synthesised with a 1:2 ratio (by mass) of the polymers, EDEA-CM-dextran to DEAE-dextran **(c)** Zeta potential distribution of mixed dextran SPIONs synthesised with a 2:1 ratio (by mass) of the polymers, EDEA-CM-dextran to DEAE-dextran.